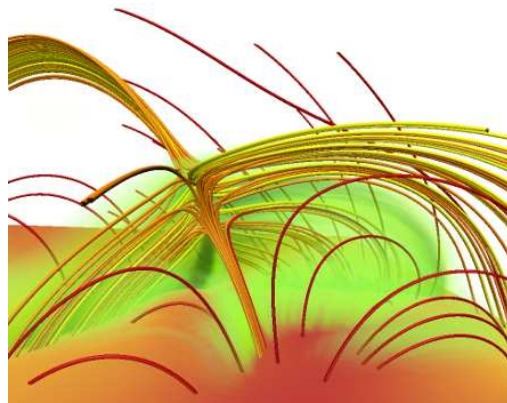University of Copenhagen
Faculty of Science

Particle Dynamics
in Solar Coronal Magnetic Reconnection Regions

by Gisela Baumann

A thesis submitted for the degree of Doctor of Philosophy in natural science

Niels Bohr Institute, University of Copenhagen
&
Theoretische Physik I, Ruhr-Universität Bochum

The PhD School of Science, Faculty of Science, University of Copenhagen, Denmark

May 2012

Contents

List of Figures

ii

List of Tables

ACKNOWLEDGMENTS

Abstract

Numerous multiscale eruptions and flux emergence events on its surface define the every day activity of the Sun. Investigations of these events are observationally limited due to the state-of-art of today's instruments and the perspicuous lack of in-situ observations in the close proximity of the solar surface. However, numerical simulations provide a sandbox for theoretical studies of the underlying physical processes of such events, the results and consequences of which may be compared to constraints given by spectral observations, to the amount of total released energy, or to the size and time scales of structures.

The theory specifying the solar plasma motion fairly accurately is a combination of a fluid description, representing the conductive behavior, and electromagnetism, affecting charged particles. The resulting global theory is called magnetohydrodynamics (MHD), which is a macroscopic description of a plasma. In order to investigate particle kinetics, a microscopic particle tracing method is needed to describe the motion of single particles (unlike the bulk motion used in MHD) in a self-consistent electromagnetic field. One numerical kinetic approach is the use of Particle-In-Cell simulations (PIC). The numerical plasma description of MHD and PIC methods are joined in the presented research, introducing one of the first models successfully interconnecting microscopic and macroscopic scales. For this purpose microscopic plasma parameters are modified to run a kinetic simulation based on a dataset from an MHD simulation. Although this technique is still in the early stages and the heavy numerical constraints limit the parameter choices, it marks the birth of a promising new numerical tool for investigations of systems covering a vast range of scales.

Most of the energy released through particle eruptions originates from the process of magnetic reconnection, which transforms magnetic energy into charged particle acceleration, bulk flow and heat. There is an entire zoo of solar eruption phenomena triggered by magnetic reconnection, among which the best known ones are solar jets, solar flares and coronal mass ejections (CMEs). The present studies focus on the acceleration mechanism of particles in 3D reconnection regions of an active region in a pre-flare phase, and on a coronal hole region producing a solar jet. In both cases the acceleration happens on account of a systematic, slowly evolving ('DC') electric field, which builds up at the electric current sheet that separates two different magnetic connectivity domains. Such electric fields are a consequence of magnetic reconnection, and are shown here to be able to persist, even under collionless conditions, since particles remain in the accelerating electric field only for a limited time, being gradually replaced by new particles, which also need to be accelerated. The relatively small fraction of highly accelerated particles is not able to completely short-circuit the electric field through a polarization electric field. The acceleration results in a power law distribution of non-thermal particles, with a dN/dE power law index of about -1.6 ro -1.8, extending in the numerical simulations only to a few tens of keV. We speculate that the DC electric field acceleration in the Sun is responsible for the part of the energy distribution extending to a few hundred keV, while stochastic particle acceleration is a likely candidate for acceleration particles with a steeper power law index, extending to hundreds of Mev for electrons and to the Gev range for ions.

1 OBJECTIVES

What accelerates electrons in the solar corona to non-thermal energies?
Where are they primarily accelerated?

How can micro- and macroscopic scales of the Sun be unified into one
consistent numerical model?
And what are the physical consequences of such an interlocked formulation?

One of the main questions addressed over and over again in solar physics research is the coronal heating problem; why does the systematic decrease in temperature from the solar interior out to the solar surface suddenly change into a rapid temperature increase in the solar corona? The most plausible explanation is nowadays believed to be magnetic reconnection, which may be described as a restructuring of magnetic field during which magnetic energy is transferred into kinetic energy and heat. Magnetic reconnection (in the course of this dissertation simply called reconnection) may be locally efficient, but globally seen the volume affected by a single reconnection event is microscopic, compared to the extent of the Sun. This deficiency is thought to be compensated by the abundance of reconnection events taking place in the solar atmosphere.

Detecting reconnection events in the solar atmosphere is a tremendous challenge for observers, not only due to their tiny dimensions, much smaller than the spatial resolution of current instruments, but also as a result of the requirements on the sensitivity of the instruments, which are exceptional for phenomena taking place in this very tenuous environment. However, the large scale behavior of the plasma at the surface of the Sun as well as large scale emission spectra, as a result of particle acceleration, can be obtained more or less directly from observations.

Numerical simulations, on the other hand, offer a unique playground to train our understanding and expectations of what should be seen by the instruments directed to the Sun — both on large scales, on the order of Mm (1 Mm = 1000 km), as well as on small scales of the size of a reconnection region. Yet this method does not come without its challenge. The main reason, which has so far prevented a direct comparison with observational results, is a consequence of reconnection being a multi-scale process; the global reconnection event locations are determined by the large scale magnetic field, while the actual process of energy transfer into heat and particle acceleration takes

place on microscopic/kinetic scales. Macroscopic scales are accurately described by magnetohydrodynamics (MHD), while microscopic plasma behavior is well reproduced by kinetic simulations, such as particle-in-cell simulations (PIC). Hardly any attempt to combine these two model descriptions exists, although we know that during reconnection energy exchange takes place over a large range of length scales and supposedly provides the key to understanding the particle acceleration mechanism associated with several of the observed eruptive phenomena on the Sun.

The objectives of this dissertation is therefore to investigate the dynamics of fully three dimensional reconnection regions, and to study their associated particle acceleration mechanism, by interconnecting MHD and PIC computer models.

The thesis is structured in the following way: The first two chapters provide general background knowledge. Chapter 2 contains an introduction to the research field (coronal environment, 3D reconnection and acceleration mechanisms). Chapter 3 describes the numerical implementation of solar corona simulations — its restrictions and constraints. The following two chapters 4 and 5 provide an overview of the results from two solar simulation experiments, one from an active region prior to an observed flare occurrence and one from an open magnetic field coronal hole region. Chapter 4 builds on the articles Baumann, Galsgaard, and Nordlund (2012) and Baumann, Haugbølle, and Nordlund (2012), while Chapter 5 relates to Baumann and Nordlund (2012). In these Chapters I also provide additional material not included in the articles which can be found in the appendix. The appendix further contains a list of the kinetic plasma equations and fundamental numerical values. Finally I draw conclusions and summarize the perspectives for future research in Chapter 6.

2   SOLAR ATMOSPHERIC ENVIRONMENT

2.1   Overview of the Sun

The Sun is a giant ball of gas, with a diameter of 1.4 million km (1400 Mm), emitting each day a vast amount of energetic particles into its surroundings. The energetic particles carry some of the energy originally produced in its interior into the interplanetary medium. Depending on its level of activity, the energy released from the Sun during a solar flare event, lasting from only a few seconds up to minutes, can be as high as 10^{25} Joule. This amount of released energy is comparable to the *yearly* average heat flow from the interior of the Earth (Kanamori, 1978). The main two sources for energetic particles are *solar flares* and *coronal mass ejections* (CMEs), which accelerate electrons from $10 \, \text{keV}$ ($1.6 \times 10^{-15} \, \text{J}$) up to at least $100 \, \text{MeV}$ ($1.6 \times 10^{-11} \, \text{J}$) (Aschwanden, 1999).

Reconnection is thought to be a fundamental process in these solar plasma energy releases taking place in the solar atmosphere. The solar atmosphere consists of the photosphere (the 'surface' of the Sun), the chromosphere and the corona, sketched in Figure 2.1. The photosphere lies on top of the turbulent convection zone, in which magnetic flux tubes rise buoyantly until they encounter the cool photosphere. Further out lies the chromosphere which is hotter and more tenuous and is partially ionized. Finally follows — via a thin transition region where the temperature rises sharply — the highly ionized corona, with thermal speeds of about $4000 \, \text{km/s}$. The corona is the focus of this thesis.

Particle eruptions from reconnection regions in the optically thin corona happen as so-called *free magnetic energy*, stored on top of the *potential energy* (which is the lowest energy state of the magnetic field for a given photospheric boundary condition) is released. Free magnetic energy is generated for example by twisting and shearing motions at the photospheric boundary, which reorder the magnetic field lines. Drivers of this dynamics of photospheric sources are the motions of convection cells, which also cause magnetic flux emergence from the photosphere into the corona and thus create active regions consisting of groups of sunspots. Particles are most efficiently accelerated in regions with high temperatures and low densities, such as in the corona above solar active regions.

The magnetic field strength varies from several thousand Gauss below the solar surface to a few Gauss in the corona (away from active regions). Despite the high magnetic field strength in lower layers, it is the immense gas pressure that dominates the plasma motion in these regions. Looking at the plasma beta β (ratio of gas pressure and magnetic pressure), β is generally larger than unity below the solar surface and changes to values below one at the photosphere, decreasing rapidly in the chromospheric layer. The magnetic field strength varies

Figure 2.1: The atmospheric layers of the Sun (not to scale)

over several orders of magnitude at any one height, depending on the horizontal location. In active regions the magnetic field reaches up to a few thousand Gauss, while the background field is estimated to be a few tens of Gauss. The corona shows mainly two characteristic magnetic field topologies; zones where both 'ends' of the magnetic field lines are attached to the Sun and zones where field lines reach far out into space, interacting with the interplanetary magnetic field before returning to the opposite polarity at the Sun. Locally the latter type seems to be field lines of a magnetic monopole, hence 'open'. Such field lines are predominantly found in polar regions and are a typical feature of 'coronal holes'. From open field line regions fast solar wind constantly emerges, featuring velocities of $400 - 800 \, \mathrm{km \, s^{-1}}$, while closed magnetic field line regions produce a slower solar wind, with velocities on the order of $200 - 400 \, \mathrm{km \, s^{-1}}$.

2.2 3D Reconnection

The basic concept of 3D reconnection in connection with solar eruptions has been introduced by Giovanelli (1946), who pointed out the likely existence of neutral points in the chromosphere. Reconnection is a process that restructures the magnetic field and converts stored magnetic energy into kinetic energy (particle acceleration), bulk flow and heat, with the purpose of transferring the system into a lower energy state.

Reconnection is fundamentally different in 2D and 3D. One of the most significant differences between these two cases is that 3D reconnection can occur in entire volumes (called *diffusion regions*) and does not require that the magnetic field vanishes at a so-called X-type null-point, in contrast to 2D reconnection. Studies of 3D reconnection have changed the understanding and definition of reconnection. It is now defined as a non-ideal process in which

$$\mathbf{B} \times (\nabla \times \mathbf{R}) \neq 0, \tag{2.1}$$

4

where **B** is the magnetic field and **R** symbolizes the violation term of the ideal Ohm's law (Schindler, Hesse, and Birn, 1988), which contains all possible contributions from the Hall effect, the Petersen effect, as well as normal and anomalous resistivity. Schindler, Hesse, and Birn (1988) describe this requirement as 'breakdown of magnetic connection due to a localized non-idealness'. Magnetic connection had been defined many years before by Newcomb (1958), who called it the necessary and sufficient condition for magnetic field line-preservation. Equation (2.1) states that reconnection occurs if field lines do not follow the plasma. Note that this is a weaker constraint than flux conservation, as shown in Kulsrud (2005). Equivalent to Equation (2.1) Hesse and Schindler (1988) define reconnection as

$$\int E_\parallel ds \neq 0, \tag{2.2}$$

where $E_\parallel$ is the parallel electric field component with respect to the magnetic field direction. In reconnection regions the electric field is hence no longer zero in the frame co-moving with the plasma, but there is a local electric field present. Locally the plasma is said to be non-ideal, which implies that the frozen-in flux theorem is no longer valid. The reconnection rate, which describes how violent a reconnection process is, is directly deduced from the reconnection definition as the maximum value of the integral over the parallel electric field along a magnetic field line (Hesse, Forbes, and Birn, 2005). $E_\parallel$ is of high importance for the acceleration of particles. It can arise for example from instabilities in the reconnection region, which set in as a result of flows that lead to a thinning of the current sheet, which consequently goes unstable. Such a process could for instance be triggered by shearing of photospheric magnetic field lines or by magnetic flux emergence from below the photosphere.

Another difference between 2D and 3D reconnection is the types of instabilities that are possible. 2D instabilities can suddenly get overwhelmed by 3D instabilities in a 3D experiment (e.g. Dahlburg and Einaudi, 2002).

For these reasons I focus in the course of this thesis on 3D reconnection, which is still heavily under investigation, while the 2D case is more well established.

Reconnection is happening over an immense range of different scales; the large scales, on the order of tens of Mm, which can be described by magnetohydrodynamics (MHD), determine the overall magnetic field structure and thus the locations of reconnection. At the small, kinetic scales, on the order of mm to cm, the mechanism of particle acceleration and energy transfer is specified. Numerically this latter scale may be represented by particle-in-cell (PIC) simulations. Thin, unstable current sheets with typical thicknesses on the order of kinetic scales may then provide important sites of reconnection.

Numerical studies of reconnection have shown that there are mainly three different reconnection scenarios possible in 3D: non-null reconnection, null-point reconnection and separator reconnection (Pontin, 2011). In the first paper of this thesis (Baumann, Galsgaard, and Nordlund, 2012), referred to as active region experiment, reconnection takes place in the vicinity of a magnetic null-point. The general geometry is sketched in Figure 2.2. Such null-points are part of the magnetic skeleton, which also includes the spine and fan-plane (Priest and Titov, 1996a). The spine passes through the null-point, where the fan-plane separates the two connectivity domains. The fan-plane is therefore also called a separatrix surface. Spine- and fan-reconnection are defined according to

Figure 2.2: Magnetic 3D reconnection null-point topology

where a current builds up during reconnection; in spine-reconnection a current is present in the spine, while fan-reconnection shows a current in the fan-plane. The orientation of the fan and spine is defined by the eigenvectors of ∇B_{null}, where B_{null} can be estimated to lowest order using a Taylor expansion at the null-point

$$B_{null} = B_{Jacobi}(\mathbf{s_0} - \mathbf{s}) \tag{2.3}$$

where B_{Jacobi} is the Jacobi matrix of the magnetic field at the null-point s_0. In case that the eigenvalues of the fan-plane are equal the field lines in the fan-plane are isotropically distributed, while unequal eigenvalues results in an anisotropy of the field lines, which concentrate towards the eigenvector with the largest eigenvalue. A summary of the different types of 3D null-points can be found in Parnell *et al.* (1996).

In case that a magnetic skeleton experiences for instance shearing, a current can build up either in the fan-plane or along the spine. If the current forms along the spine the field lines in the fan-plane form spirals and the fan and spine are inclined towards each other by 90 degrees. If a current is present in the fan-plane the inclination will no longer be 90 degrees (Birn and Priest, 2007, pg. 63 – 64). Combinations of these two cases are possible as well. In the active region experiment of this thesis the fan current dominates and therefore the spine and the fan surface are not orthogonal to each other.

2.2.1 Observational Signatures of Reconnection

As the magnetic field in the solar corona is weak compared to the photosphere, direct measurements of the coronal magnetic field are generally difficult. One possibility to extract information is by conducting extrapolations of the magnetic field of the photosphere into the corona. The photospheric magnetic field is usually measured by making use of the Zeemann effect. The longitudinal Zeeman effect can be turned directly into images of the component of the magnetic field along the line of sight by using circular polarization filters, and by utilizing in addition the linear polarization caused by the transverse Zeeman effect one can create vector magnetograms. In order to carry out a magnetic field extrapolation one needs to first make an assumption of what magnetic field one expects in this particular environment; e.g. a current free (potential) or a force free magnetic field.

The lack of exact measurements makes it difficult to confront observations directly with concepts from the theory of magnetic reconnection, such as magnetic null-points or magnetic separatrices. Hence there are also no direct observations of reconnection. The reason is the small scales of the dissipation regions as well as the low densities that are making emissions very weak and hence difficult to detect (van Driel-Gesztelyi, 2009). However, applying the previously mentioned extrapolation techniques it became apparent from the resulting magnetic field topologies that magnetic null-points are abundant in the solar corona (e.g. Régnier, Parnell, and Haynes, 2008; Longcope and Parnell, 2009). There are also various indirect evidences of reconnection, as associated processes leave direct footprints on its environment that can be observed; e.g. hot loop top emissions (Masuda *et al.*, 1994), the separation of flare ribbons (Wang *et al.*, 2003), outflow shocks and bi-directional jets (Wang, Sui, and Qiu, 2007), radio type III bursts (Manoharan *et al.*, 1996), plasmoid and plasma blob eruptions (Ohyama and Shibata, 1998; Kumar *et al.*, 2012), among numerous others (cf. van Driel-Gesztelyi (2003)).

2.3 Resistivity and Collisions in Solar Plasmas

The global coronal magnetic field is mostly force-free and well frozen into the plasma. But locally resistivity—or analogous processes leading to magnetic dissipation—must be present, since it is a requirement for reconnection to happen. Resistivity is indirectly also linked to particle acceleration, as it allows parallel electric fields to develop during the reconnection process.

Resistivity in plasmas is mainly representing particle collisions, or more precisely collisions between electrons (e) and ions (i), because the collision frequency and the cross-section for such collisions is highest, as mentioned for example by Boyd and Sanderson (2003, p.316):

$$\nu_{ei} \sim Z\nu_{ee} \gg \nu_{ii} \gg \nu_{ie}, \tag{2.4}$$

where ν are the collision frequencies and Z is the charge state (equals unity for ionized hydrogen). In a fully ionized plasma, completely dominated by Coulomb collisions, the electric resistivity, defined as the reciprocal of the conductivity σ, is the *Spitzer resistivity*.

The corona is close to being fully ionized, so the mean molecular weight μ is often assumed to be ≈ 0.6 (differing from 0.5 because of the presence of helium and heavier elements). In such a plasma the particles interact primarily via Coulomb fields (and only little via collisions with neutrals), which leads to a majority experiencing small angle scatterings. As the electron-ion collision frequency ν_{ei} goes as the particle density n_e and the electron temperature $T_e^{-3/2}$, a hot rare plasma like the corona is almost collisionless, since the collision frequency is much smaller than the plasma frequency. However, electric resistivity and hence magnetic diffusion may nevertheless occur, since there are other mechanisms than Coulomb collisions that may generate non-ideality. Anomalous resistivity is one candidate (or candidate group). Anomalous resistivity is a result of kinetic instabilities, for example in turbulent current sheets. The resistivity is then a locally variable quantity, generally depending on the local current density (Birn and Priest, 2007, p.144). But there is still little known

about this type of plasma behavior and more numerical kinetic simulations are required. However, anomalous resistivity goes beyond the scope of this thesis.

2.4 Particle Acceleration

2.4.1 Basic Equations of Particle Acceleration

The relativistic equation of motion for a charged particle in an electric field $\mathbf{E}$, a magnetic field $\mathbf{B}$, and a gravitational field giving rise to a force of gravity $\mathbf{g}$ may be written as

$$m\frac{d(\gamma \mathbf{v})}{dt} = \mathbf{g} + q(\mathbf{E} + \mathbf{v} \times \mathbf{B}), \tag{2.5}$$

where $\frac{d\mathbf{x}}{dt} = \mathbf{v}$ is the particle velocity, m its mass and γ is the Lorentz factor. Since the effect of gravity is negligible small in the solar corona over time scales of a few seconds it can be ignored for this discussion of sources of particle acceleration. The acceleration must hence be caused by the electric field $\mathbf{E}$ or the Lorentz force $\mathbf{v} \times \mathbf{B}$. To look at the kinetic energy gain of a particle with time, we take the scalar product of Equation (2.5) with $\mathbf{v}$ and receive

$$m\gamma \cdot \frac{d}{dt}(v^2) = q\mathbf{v}\mathbf{E} + \mathbf{v} \cdot (\mathbf{v} \times \mathbf{B}), \tag{2.6}$$

where the second term is zero, since $\mathbf{v} \cdot (\mathbf{v} \times \mathbf{B}) = \mathbf{B} \cdot (\mathbf{v} \times \mathbf{v})$. So we are left with

$$m\gamma \cdot \frac{d}{dt}(v^2) = q\mathbf{v}\mathbf{E} \tag{2.7}$$

which reveals that a charged particle gains (or loses) energy only if its velocity has a component along the electric field. So the amount of acceleration of a particle depends on the strength of the electric field and the angle between $\mathbf{v}$ and $\mathbf{E}$. In a magnetic field, a particle undergoes a circular motion, perpendicular to $\mathbf{B}$, called the gyro motion. The radius of the gyration is known as the gyro radius or Larmor radius and is defined by

$$r_g = \frac{v_\perp}{\omega_c} \approx \frac{v_{th}}{\omega_c} \tag{2.8}$$

where ω_c is the gyro frequency of a particle around $\mathbf{B}$, $v_\perp$ is the particle velocity component perpendicular to the magnetic field and v_{th} represents the thermal speed. A force along the magnetic field can thus accelerate particles without any interaction with the gyro motion of the particle and is thus most efficient. Hence the $E_\parallel$ is the major accelerator of particles in plasmas.

Next I give a short overview over the different sources of electric fields in the corona.

2.4.2 Particle Acceleration Mechanisms and Observational Constraints

It is widely accepted that reconnection is where particle acceleration events have their roots - both in solar flares (active region experiment) and in X-ray jets (coronal hole experiment). But besides DC electric fields, turbulence and shocks

may also contribute their share to the acceleration of particles in reconnection regions.

The energy build-up phase of the pre-eruptive fields is a process that takes many hours or even days, while the actual eruption happens on time scales of seconds or minutes. The build-up phase is likely a phase where the system is in quasi-static equilibrium, with free magnetic energy either growing or, alternatively, coming closer and closer to a state where it can be released. It is during the release phase that particle acceleration becomes most apparent, but in principle some (much lower) level of particle acceleration may take place also during the build-up phase.

With respect to particle acceleration during eruptive solar events there are several observational constraints that need to be incorporated. Here are some of the most important ones:

- Energy releases during the most powerful solar flares are on the order of 10^{25} J (10^{32} erg) (Woods, Kopp, and Chamberlin, 2006). X-ray jets show energy releases on the order of 10^{20}–10^{22} J (Shimojo and Shibata, 2000).

- Electrons are accelerated up to at least 100 MeV (Aschwanden, 1999) in solar flares.

- Electron acceleration happens on time scales on the order of seconds or tens of seconds (Aschwanden, 1999) in flares and on the order of minutes in coronal jet events (Filippov, Golub, and Koutchmy, 2009).

- The electron energy distribution features a power-law above thermal energies (Kane and Anderson, 1970), sometimes it shows a broken power-law.

- The energy release often happens in sub-steps and not continuously and on time scales much shorter than that for energy injection into the corona (Aschwanden, 2002). In the case of X-ray jets, this shows up as recurring events (Chifor *et al.*, 2008).

- The impact locations of non-thermal electrons in a certain magnetic field geometry are mainly revealed by hard X-ray observations, as non-thermal particles impact dense plasma regions and radiate hard X-rays through bremsstrahlung (thick target model (Brown, 1971; Brown *et al.*, 2009)).

- The spectral index in flare events evolves according to the soft-hard-soft rule, by Parks and Winckler (1969); Kane and Anderson (1970)

A possible acceleration mechanism of particles in reconnection regions is based on large-scale DC electric fields. Particles are, at the same time as they feel the force by the electric field, also subjected to collisions with ambient particles. Dreicer (1960) defined a critical electric field value E_D, the so-called Dreicer field, for which the force resulting from the electric field and the frictional force balance. The Dreicer field is typically around 10^{-2} V m^{-1} (Anastasiadis, 2002) in the solar corona and provides a reference point for distinction between 'weak' and 'strong' electric fields.

If the frictional force is smaller than the acceleration force the associated electric field is called a super-Dreicer electric field and has $E > E_D$. Retaining

only the acceleration and collision terms the equation of motion for an electron in an external electric field may be rewritten as (Zharkova *et al.*, 2011)

$$\frac{d\mathbf{v}}{dt} = \frac{q\mathbf{E}}{m_e} - \nu_c\mathbf{v},$$
(2.9)

where ν_c is the collision frequency. As previously mentioned, the electron ion collisions dominate the collision frequency, so that $\nu_c \approx \nu_{ei}$. And since ν_{ei} is $\propto v^{-3}$, this leads to

$$m_e\frac{d\mathbf{v}}{dt} = q\left(\mathbf{E} - \mathbf{E_D}\left[\frac{v_{th,e}}{v}\right]^2\right),$$
(2.10)

where $v_{th,e}$ is the electron thermal speed. Litvinenko (1996) applied this case to a simple magnetic configuration of a current sheet.

On the other hand in the sub-Dreicer regime, where $E < E_D$, only the particles in the thermal velocity distribution with $v > \sqrt{\frac{E_D}{E}} \cdot v_{th,e}$ experience a velocity increase, which then reduces the electric drag force further and thus leads to electrons being accelerated freely out of the thermal distribution. This process is known as *runaway acceleration*. Particles with velocities smaller than $\sqrt{\frac{E_D}{E}} \cdot v_{th,e}$ are slowed down and remain part of the thermal velocity distribution function. In the marginal super-Dreicer case the critical velocity is at the thermal speed, meaning that all electrons with speed higher than the thermal speed are accelerated.

Although sub-Dreicer electric fields, applied to solar eruptions (e.g. Holman, 1985), can in principal explain the velocity distribution of non-thermal particles, the major problem with considering this acceleration source as the main particle accelerator in solar eruptive events is the large spatial scales required to reach the observed energy gain, which has not found support in observations.

Super-Dreicer fields are discussed in Litvinenko (1996). They are believed to be more realistic when considering particle acceleration in powerful solar eruptions.

There are two other models, which do not rely on large-scale electric fields, but in which acceleration takes place due to small scale electric fields in shocks and turbulent regions. Shocks are often seen in connection with reconnection of magnetic field lines, but it is still not known what part they play in the particle acceleration. The underlying process of shock acceleration are the first- and second-order Fermi shock acceleration mechanism (Fermi, 1949). An important constraint of shock acceleration models is the requirement for turbulence or plasma waves, which serve as a tool to get a repetitive passage of particles through the shock front. Shock acceleration in solar flares has been studied by among others Cargill (1991).

The other particle acceleration model to be considered is stochastic particle acceleration, reviewed by Miller *et al.* (1997). In general stochastic processes utilize the fact that particles gain energy in average over a certain period of time during which they are exposed to several acceleration/deacceleration sites in a turbulent environment. A frequently discussed stochastic acceleration mechanism is due to wave-particle interaction, where one idea is to use the resonance between the particles gyro radius and the wave frequency (Miller *et al.*, 1997), where the time it takes a particle to make one gyro orbit is equal to the period

of a wave. The accumulated particle energy is taken from the turbulent energy pool, which thus decreases with time if not replenished. For an overview of the different acceleration mechanism, see Miller (2000).

It is likely that in reality DC electric fields, turbulence and shocks are simultaneously present in reconnection regions, and contribute in different ways to the overall picture. Different acceleration mechanisms could dominate in different energy intervals, and for different particle species, for example.

Observations provide certain hints concerning the acceleration mechanism present. But the resolution as well as the measurement techniques set limits to the extent of understanding of the underlying physics. What we can see are mainly the consequences of accelerated particles, such as bremsstrahlung, cyclotron radiation, synchrotron radiation, and Thomson scattering. But we are not able to directly observe what leads to these energetic particles. This is why numerical simulations are very handy. They provide a way to study the physical processes in particle acceleration regions using different models whose results may then be compared to observations, and thus the underlying mechanism can be inferred.

The most common approach for particle acceleration investigations is the test particle approach (Chapter 3.2). The trajectories of test particles in a 3D reconnection topology given by Priest and Titov (1996b) has been studied for fan-reconnection as well as spine-reconnection by Dalla and Browning (2005) and Dalla and Browning (2008), respectively. Their initial conditions are coronal. They found a strong dependence of the energy gain of a test particle on its starting position. The highest acceleration appeared near the null-point, where the particles are unmagnetized and free to move according to the imposed electric field. In these studies spine-reconnection produces more high-energy particles than fan-reconnection and the steady-state is reached more quickly. On the other hand spine-reconnection did not produce jets emitted along the spine axis as they found during fan-reconnection.

These studies indicate that the DC electric field is a viable mechanism for particle acceleration in solar eruptions. But such collisionless test particle approached are only valid if on the one hand the particles speeds are high enough, so that collisions are rare, and on the other hand there is only a small particle population accelerated, so the effect of the charged particles on their accelerating electric fields is negligible. Dalla and Browning (2006) further investigated spine-reconnection, using the same potential field null-point reconnection configuration, finding two reconnection jets traveling in both directions along the spine. The initial velocity distribution is chosen to be Maxwellian. Highly accelerated particles show a strong velocity component along the magnetic field and the quasi-steady state energy distribution features a power-law tail index of -0.92. The authors conclude that the level of acceleration of these particles is strongly dependent on their angle of injection and hence on their position inside the reconnection region. It can therefore be surmised that their power-law index must be somehow dependent on the number of particles in the optimal injection position and the geometry of the magnetic field. This is what is found as well in the work presented here (see Baumann, Haugbølle, and Nordlund, 2012; Baumann and Nordlund, 2012): The magnetic field geometry, its magnitude, and the particle density are essentially the main factors to determine the power-law distribution. It is crucial though to note here that the publications by Dalla et al. use a potential magnetic field geometry (no currents), and as they require

the initially potential magnetic field to be static $\frac{dB}{dt} = 0$, there will never be currents (unlike in the experiments presented here). They do drive the boundaries in order to build up electric fields. At the locations where these electric fields are discontinuous, reconnection is assumed to take place, although non-ideal effects are not included in the model. This approach is a simplified version of solving the MHD equations, and is equivalent to saying that reconnection is taking place with infinite velocity. This may be a dangerous approach if one is interested in short timescale processes, such as the instant powerful particle acceleration in solar eruptions evidenced by hard X-ray and radio wavelength.

Another approach was taken by Rosdahl and Galsgaard (2010), who also conducted test particle simulations in connection with the formation of a solar jet., but starting from a flux emergence experiment. Further Turkmani *et al.* (2005, 2006) used an evolved MHD simulation snapshot of an MHD model in which a straight stratified coronal magnetic loop reacts to photospheric driving, together with test particles to study particle acceleration in such a turbulent environment. They showed that the applied photospheric random motion causes small scale current sheets at which particles are stochastically accelerated to relativistic energies in only a fraction of a second. Despite neglecting resistivity outside the current sheets in the MHD snapshot they conclude that the particle acceleration is clearly too high, due to the ignored back reaction of the particles onto the fields, which in fact breaks the conservation of energy; particles gain energy from the fields, but the field energy remains constant, see also the discussion of the test particle approach in Chapter 3.2.

As previously mentioned, electrons are found to be accelerated up to at least 100 MeV in solar flares, which, assuming a purely thermal source would mean that they escaped from regions with temperatures of approximately 7×10^{11} K. There have been some observations of very hot regions, such as by Masuda *et al.* (1994), but such regions are very rare and are unlikely to be the reason for the observed highly energetic particles. In fact, Lin *et al.* (2003) estimated from observations that $10\% - 50\%$ of the total released energy in eruptive solar events is contained in non-thermal electrons, while the rest is shared between non-thermal protons, plasma flow (bulk flow) and heating. MHD simulations (see Chapter 3.1) are limited to a thermal particle distribution, meaning that they cannot explain the production of non-thermal highly energetic particles. But the theory of MHD can of course account for the energy released by the plasma flow coming from a region covering several Mm or more, which kinetic effects can hardly account for. Plasma particle velocities in 3D reconnection outflow regions in MHD are a superposition of a bulk flow, accelerated by the Lorentz force ($\mathbf{j} \times \mathbf{B}$, where $\mathbf{j}$ is the electric current density) and thermal velocities, which are the result of mainly Joule dissipation in the non-ideal dissipation region, giving further rise to a high gas pressure capable of helping to accelerate plasma out of the reconnection region. Another contribution comes from slow shock structures, which are sometimes found in reconnection scenarios. But shocks are not expected to be the major accelerators of plasma in 3D reconnection regions.

To summarize, MHD simulations are an excellent choice to describe the overall magnetic field structures of a reconnection region, or in other words to provide the active region environment, but they cannot cover the entire story, down to non-ideal dissipative scales. A kinetic description is needed to understand the non-thermal part of the observed particle energies. Therefore the

approach developed in this thesis of using an MHD code to set up the 3D reconnection environment and then pass the state on to a PIC code is a new and promising way to understand solar eruptive events.

Particle Acceleration in Current Sheets

Current sheets form where magnetic field lines in adjacent regions are inclined at some angle (Ampére's law). In the corona current sheets build as a result of photospheric motions; when flux tubes emerge into pre-existing magnetic fields, or when translational motions in the photosphere push magnetic flux of different orientations towards each other. Current sheets are only maintained if there is a flow or the magnetic field is continuously deformed; otherwise the current sheets eventually diffuse away.

Assuming that reconnection is responsible for particle acceleration in eruptive coronal events and that reconnection occurs in current sheets links current sheets directly to particle acceleration. Instabilities in current sheets can trigger non-ideal plasma processes and thus lead to reconnection. But the overall current density inferred from magnetic field measurements in solar flare regions cannot, via classical resistivity, account for high enough resistive electric field to induce a reconnection event. Therefore, to drive reconnection, current sheets must consist of clusters of much smaller current sheets, providing locally a higher resistivity that then enables reconnection.

Additionally thin current sheets are prone to various instabilities, which also lead to enhancements of the resistivity. The fragmentation of current sheets, offering a possibility for multiple reconnection sites, has been investigated by using numerical experiments, leading to the conclusion that one or several governing small scale instabilities, such as the tearing instability (Shibata and Tanuma, 2001), are responsible for the suggested fragmentation. A concurrent process is the formation of magnetic islands, which may later merge by the coalescence instability (reconnection between magnetic islands). Islands shrink due to magnetic tension and finally lead to first-order Fermi acceleration of particles (Drake *et al.*, 2006a). One example of current sheet fragmentation simulations is summarized in the papers by Bárta, Büchner, and Karlický (2010) and Karlický and Bárta (2011). They show that coalescence and fragmentation of plasmoids can cause fragmentation of current sheets, which furthermore may lead to acceleration of electrons up to non-thermal energies. Further investigations on kinetic scales have been undertaken by Drake *et al.* (2006a). Such models may explain the periodic energy release seen in some solar flares, but most of the simulations performed so far showing a fragmentation of the current sheet are 2- or 2.5-dimensional. There have only been little work done in a fully 3D realistic setup. But future studies will certainly reveal the importance of plasmoids for particle acceleration.

3   COMPUTATIONAL MODELING

There is an immense range of different scales interacting in the solar atmosphere and there is still no clear understanding of how the complex non-ideal feedback from small to large scales is taking place. Magnetic reconnection is a typical example of a multi-scale process; magnetic diffusion takes place on kinetic scales (order of mm), while the overall magnetic field of the reconnection region feeding flux to the reconnection area as well as the scale of energy inflow are on the order of Mm, as illustrated in Figure 3.1. Next I provide an overview of the re-

Figure 3.1: From the gyro radius to the coronal loop size

strictions of different numerical codes when used for solar atmosphere modeling. I concentrate on the three most popular theoretical descriptions; magnetohydrodynamics (MHD) single-fluid models, test particle models, and particle-in-cell (PIC) models. There are of course numerous others, such as multi-fluid approaches and alternative kinetic descriptions, e.g. the hybrid method (where electrons are described as a fluid and ions as single particles).

3.1 The MHD Approach

MHD is basically a fluid description, with an actively evolving magnetic field, while the electric field is derived from an approximate 'generalized Ohm's law'. The main constraints of this description are (e.g. Baumjohann and Treumann, 1996):

- The time scales must be much longer than characteristic time scales of individual particle motions

- The length scales of plasma variations are much larger than characteristic length scales of individual particles, such as the gyro radius

- Relativistic effects are negligible. As by point 1), only long time scales are considered, so the displacement current can be neglected.

- The plasma is in thermodynamic equilibrium, hence collision-dominated

- The plasma is treated as one fluid and single particle aspects are neglected

Although MHD codes assume collisions to be abundantly present, MHD works astonishingly well also for collisionless plasmas in low density environment, such as in the solar corona, as has been extensively demonstrated.

3.2 Test Particle Approach

The test particle approach is one way to get a first order estimate of kinetic plasma behavior on macroscopic scales. It is hence something in-between a kinetic description and a macroscopic description. It normally starts out from electromagnetic fields from an MHD simulation, or possibly an analytic expression or observations. The idea is to position charged test particles in an electromagnetic field and to integrate their trajectories, by solving their equation of motion. This method for studying the particle acceleration mechanisms is very popular. Its main requirements are (Rosdahl and Galsgaard, 2010):

- The number of accelerated particles needs to be small, so that the magnetic and electric fields associated with the moving charges are negligible.

- Collisions and other particle interactions (e.g. charge attraction or repulsion) can be neglected

- low plasma densities, so that the polarization field is weak (Siversky and Zharkova, 2009)

In test particle simulations there is, unlike in kinetic simulations, no immediate back-reaction from the particles onto the field. Siversky and Zharkova (2009) compared the test particle approach with a kinetic simulation and concluded that the magnetic field induced by moving charged particles is negligible, while the electric field induced by accelerated particles is large compared to the background field induced by reconnection. Therefore particle trajectories and energy spectra may be substantially altered even for a small number of simulated particles. Ignoring the back-reaction from particles onto the fields also means that the energy gained by the particles is not lost from the fields. An exaggerated acceleration is the consequence, as noted also by Rosdahl and Galsgaard (2010).

3.3 The Kinetic Approach

A popular kinetic approach is to use particle-in-cell (PIC) codes. PIC codes, such as the *PhotonPlasma* code, solve the Maxwell equations, containing external and self-consistent fields arising from the plasma motion,

$$-\frac{\partial \mathbf{B}}{\partial t} = \nabla \times \mathbf{E} \qquad (3.1)$$

$$\epsilon_0 \mu_0 \frac{\partial \mathbf{E}}{\partial t} = \nabla \times \mathbf{B} - \mu_0 \mathbf{j}, \qquad (3.2)$$

together with the relativistic equation of motion for charged particles

$$m\frac{d(\gamma \mathbf{v})}{dt} = q(\mathbf{E} + \mathbf{v} \times \mathbf{B}), \qquad (3.3)$$

where ϵ_0 is the vacuum permittivity and μ_0 the vacuum permeability. PIC simulations use the phase space to describe a plasma and its temporal evolution, unlike the MHD description of a fluid, which ignores all information related to the velocity distribution. Every classical particle can be completely described by its position and momentum. In the PIC description we therefore give every particle a set of seven coordinates including its position, momentum and time. Instead of densities like in the MHD approach, distribution functions are used in kinetic simulations. This enables one to look at the statistical, kinetic information of a plasma, which is why the MHD description is also known as macroscopic and the PIC description as kinetic. MHD simulations further assume transport coefficients, while PIC codes directly allow for particle and wave particle interactions. In addition to the usual MHD wave modes PIC simulations provide the transverse electromagnetic waves / light waves. Note that PIC simulations in principle contain the complete MHD description, but that in practice the MHD limit may be prohibitively expensive.

Kinetic approaches are in principle the most exact descriptions. But there are, as well as in the other approaches, assumptions and approximations relative to the real case. Some of the general assumptions / properties of PIC codes are:

- Particles are considered to be so-called 'pseudo particles' representing many real particles, keeping the same charge to mass ratio as its components have in total.

- A particle position is represented by a probability function, a so called shape function, in order to smoothen out the charge distribution to avoid aliasing problems. Hence particles are not defined at only one position, but over about one cell.

- The positions of the fields are discrete although in reality they are continuous. However, field values can be computed at continuous locations, using interpolation between the discrete points.

In addition to these there are stability and similar constraints for explicit PIC codes, such as the *PhotonPlasma* PIC code:

- the Debye length λ_D[1] should not be smaller than about 0.3 grid cells, Δs. If the ratio of $\lambda_D/\Delta s$ is smaller, *aliasing effects* may become disturbing —

---

[1]The Debye sphere is the distance at which the thermal particle energy and the electrostatic potential energy are in balance (Baumjohann and Treumann, 1996) - see definition in appendix

depending on the shape function of the particle; the smoother the shape function, the less of a problem there is. Aliasing effects are side effects of the spatial discretization, causing artificial plasma perturbations, the result of which is heating of the plasma, leading to a growth of λ_D. This constraint for PIC simulations was introduced by Birdsall (1991) and has been widely used since (e.g. Siversky and Zharkova, 2009; Tsiklauri and Haruki, 2007; Pritchett, 2003). But already Okuda (1972) noted that depending on the ratio of the Debye sphere to the grid size numerical instabilities do or do no occur. If the Debye sphere is resolved by the computational grid there should not occur any numerical instabilities and kinetic effects can be correctly represented.

- Another requirement on the cell size is that the propagation of electromagnetic (light-) waves should be resolved, meaning that $c\Delta t < \Delta s$, where Δt is the time step.

- Δt must be smaller than (some fraction of) the orbit period of a particle (Tajima, 1986, p.59): $\omega_{ce}\Delta t < 0.35$, where ω_{ce} is the electron gyro frequency.

- A second recommendation concerning the time step is that it should resolve the Langmuir wave (plasma oscillation) evolution: $\omega_{pe}\Delta t < 1$, where ω_{pe} is the electron plasma frequency[2].

- One also needs to make sure to stay in the kinetic range and do not simulate MHD; A few grid cells Δs need to be contained in one electron skin depth δ_{skin}. Too few Δs per δ_{skin} lead to an MHD-like fluid behavior of the plasma, while too many Δs per δ_{skin} may result in uncoupling kinetic scales from the MHD behavior and hence a loss of the ability to match the large scale plasma behavior to MHD boundary and initial conditions.

- Additionally the number of particles per cell is often considered as a restrictive parameter of PIC simulations. A minimum number of 10 particles per cell turns out to be a reasonable limit in the case of the *PhotonPlasma* code – this constraint also depends on the smoothness of the shape function. Having too few particles per cell in a simulation results in single particles scattering against each other through the mechanism of the charge collection on the grid; fluctuations in the total charge per cell caused by low number statistics leads to artificial small scale electric field fluctuations.

All these recommendations and requirements have the purpose to ensure the dominance of the physical forces over the numerical (Monte Carlo) noise in PIC simulations. The noise mainly comes from the following factors: the reduced number of particles compared to reality by using pseudo-particles, the discrete spatial scale introduced by the grid, the order of the particle distribution shape function representing the particle spatially, and finally the interpolation from the particles to the grid as well as the time integration. Most requirements

---

[2]The plasma frequency is the frequency of charge oscillations in an ionized plasma, describing the time it takes for electrons to restore charge neutrality after a perturbation of any kind (Baumjohann and Treumann, 1996).

concern the electrons, as they are lighter and faster, they determine the time step and the cell size in the simulation.

λ_D is on the order of millimeters in the corona. The physical extents of the computational box in PIC experiments would hence be very tiny if they had to conform with the true scale requirements. On the other hand typical length scales of solar events are on the order of Mm. To study solar flares using PIC codes would thus require an immense number of cells. Additionally, the huge density and temperature ranges from below the solar surface out into the solar corona are impossible for PIC codes to cover, hence flux emergence is essentially impossible to model solely by a PIC simulation. To face the tremendous challenge of covering solar event length scales one is forced to scale the fundamental physical parameters, so that the hierarchy of (order of) length scales and velocities is retained, keeping different scales reasonably separated, but making the dynamical span small enough so that it can be resolved. This is done by modifications of the constants of nature, as discussed in the next Section.

3.4 Coupling the Different Approaches by Modifications of the Constants of Nature

One approach to combine macroscopic with microscopic scales is the test particle approach. But as previously mentioned, this approach has very tight validity limits. In order to assure self-consistent modeling of particle acceleration in solar eruptive events, a kinetic description of the plasma motion is needed. But how can we couple all the scales, from the size of a solar flare down to the electron skin depth or the current sheet width, using a single numerical code? There has so far been mainly one attempt, by Sugiyama and Kusano (2007), to couple MHD and kinetic codes into a so-called interlocked model. But including small scale kinetic domains in an MHD simulation faces several problems; among these that a low-pass filter is needed in the interface between the two domains, as only low-frequency waves may propagate in the MHD domain. These combined models are still under development as it is numerically a highly complex problem. In the present study we introduce a new method to meet the challenge of multi-scale simulations and use the method to investigate particle acceleration mechanisms in coronal reconnection regions.

The avoid confusion with respect to the term 'scaling', we make the following clear distinction:

Unit Scaling

We use the term *unit scaling* about the technique of converting physical units into units suitable for numerical codes. This is partly done with the purpose to avoid under- and overflows, partly to reveal the extent to which the results are, in a certain sense, independent of the exact physical size. The experiments hence become 'dimensionless'. Typical choices are for instance to choose the scalings of length, time and density. Fixing these three, we describe a certain physical system, and the scalings of any other physical quantity can be recovered by requiring the relation between physical quantities to remain the same. Requiring, for example, the relation between dynamic pressure, and magnetic pressure to be the same fixes the scaling of magnetic field strength. Any other

three variables may be chosen as the basis for unit scaling. In coronal MHD simulations, for example, one often chooses a typical coronal Alfvén speed, length scale and density as a basis for the scaling.

System Modifications

On the other hand there are system *modifications*, which can be performed by modifications of the constants of nature or, equivalently, modifications of the physical properties of the experiment. Here, in order to reduce the large range between microscopic and macroscopic scales, two sets of modifications are introduced. In doing so, we choose to maintain pressure equilibrium, which implies keeping the plasma beta constant:

$$\beta = \frac{P}{P_m} = \frac{2k_B \rho_m T \mu_0}{\mu m_u B^2}, \tag{3.4}$$

where m_u is the atomic mass constant, P_m the magnetic pressure, k_B the Boltzmann constant, ρ_m the mass density, T the temperature and μ the mean molecular weight.

Modification I: Micro Scales

With this modification the previously mentioned restrictions on the kinetic scales (λ_D, δ_{skin}, ω_{pe} and ω_{ce}) are loosened.
     In terms of changes of the constants of nature modification I amounts to reducing the fundamental charge per particle; this increases all micro scales in proportion to the inverse of the charge per particle.
     The same effect may be produced by changing physical properties of the system in the following way: First the magnetic field strength is changed by a factor $b < 1$. This changes the gyro frequency ω_{ce}. A change in the magnetic field strength must be balanced by reducing the mass density by a factor b^2, to keep the plasma beta (Equation (3.4)) constant, while keeping the temperature constant. This then leads to a change in λ_D and δ_{skin} by a factor of b^{-1} and a change in ω_{pe} by a factor of b. The ratios of the gyro and plasma frequency as well as the ratio between the skin depth and the Debye length are kept constant. These modifications further keep the acceleration of gravity unchanged, since the scale height is proportional to T/g. Also the velocities stay untouched.

Modification II: Velocities

With this modification the previously mentioned restriction on the time step by the speed of light c is loosened.
     In terms of changes of the constants of nature modification II amounts to reducing the speed of light; this increases the time step allowed in numerical simulations correspondingly. A similar effect — reducing the gap between the speed of light and other speeds — may be obtained by changing the physical properties in the following way:
     The temperature is increased by a factor t^2, with a corresponding increase in the acceleration of gravitation g by t^2 and a change of the sound speed v_s and thermal speed v_{th} by t. In order to keep the pressure equilibrium (Equation (3.4)), the magnetic field strength needs to be increased by a factor t. This

further leads to a change of the Alfvén speed by t. Increasing also the material speed with a factor of t one has thus reduced the gap between the speed of light and other speeds with the factor t. The kinetic scales are not left completely unchanged by this modification, as a change in the magnetic field strength has an influence on the gyro frequency, and a change of the temperature changes the Debye length. The skin depth and plasma frequency on the other hand stay constant. The bottom line is that the ratio of the skin depth to the Debye length and gyro radii is modified in exactly the same way as when changing the speed of light.

Adopted Modifications

To summarize, the spans in speed and physical scales may be reduced by changing two of the fundamental constants of nature; the speed of light and the fundamental charge per particle.

Both modifications have in fact at least partially been used before; Drake *et al.* (2005, 2006a,b) changed the speed of light to be 20 times the Alfvén speed. Siversky and Zharkova (2009) on the other hand reduced (often by a factor of 100) the particle density, which is essentially equivalent to reducing the charge per particle.

Another assumption that is often used, and which we also adopt, is a reduction of the mass ratio between ions and electrons from its normal value $m_i/m_e \approx 1836$. This decreases the range between the ion and electron micro scales (skin depths and plasma frequencies), and also reduces the electron thermal velocities. Therefore this approach is often used together with a speed of light decrease, in order to rescale the ratio of the speeds to the speed of light accordingly.

A crucial point to keep in mind when using these types of modifications is to ensure that the hierarchy of characteristic speeds, times and length scales is, to the largest extent possible, maintained. In the solar corona this hierarchy is

$$v_J < v_{th,i} \sim v_s < v_{th,e} < v_A < c, \tag{3.5}$$

where v_J is the average electron drift speed, which arises due to the electric current, $v_{th,i,e}$ is the thermal speed of protons/electrons, v_s is the speed of sound and v_A is the Alfvén speed.

For our simulations of a solar active region as well as for the coronal hole experiment we use a combination of these modifications compared to the real Sun:

- The ratio of proton mass to electron mass is changed to 18, by increasing the electron mass

- ϵ_0 is increased - thus lowering c to of the order 3800 km s^{-1}. μ_0 is kept constant to leave the magnetic pressure the same.

- The elementary charge is reduced with a factor of about 10^6, in order to be able to resolve the micro scales.

In the active region experiment we additionally increase the number density: Instead of the typically used coronal value of $1 \times 10^9 \text{ cm}^{-3}$ (Aschwanden, 2005), we use $128 \times 10^9 \text{ cm}^{-3}$, in order to reduce the Alfvén speed (a value on the order of $1 \times 10^9 \text{ cm}^{-3}$ is probably also too low in an active region).

3.5   Intersection MHD - PIC Simulation

In general the basic macroscopic moments for a one-fluid theory are: the number density n, the plasma bulk flow velocity v, the pressure tensor P and the thermal temperature T. In the *Stagger* code, the simulation provides the mass density (ρ_m) the 3-dimensional momentum (px, py, pz), the thermal energy per unit volume (e) and finally the magnetic field components (Bx, By, Bz). For the initialization of the kinetic parameters in the PIC code we make the following assumptions

$$n_{e,i} = \frac{\rho_m}{(m_e + m_i)} \tag{3.6}$$

$$P_{e,i} = \frac{e}{\rho_m}(\gamma - 1) \tag{3.7}$$

$$\equiv n_{e,i} \cdot k_B \cdot T_{e,i} \tag{3.8}$$

$$T_{e,i} = \frac{P_{e,i}}{n_{e,i}k_B} \tag{3.9}$$

$$= \frac{P_{e,i}(m_e + m_i)}{\rho_m k_B} \tag{3.10}$$

$$v_{th,e,i} = \sqrt{\frac{k_B T_{e,i}}{m_{e,i}}} \tag{3.11}$$

$$\mathbf{u}_{\mathrm{MHD}} = \frac{\mathbf{p}_{\mathrm{MHD}}}{\rho_m} \tag{3.12}$$

$$\mathbf{v}_J = \frac{1}{\mu_0} \cdot \frac{\nabla \times \mathbf{B}}{q n_e} \tag{3.13}$$

$$\mathbf{V}_e = \mathbf{u}_{\mathrm{MHD}} + \mathbf{v}_{th,e} + \mathbf{v}_J \tag{3.14}$$

$$\mathbf{V}_i = \mathbf{u}_{\mathrm{MHD}} + \mathbf{v}_{th,i} \tag{3.15}$$

$$\mathbf{E} = -\mathbf{u}_{\mathrm{MHD}} \times \mathbf{B} \tag{3.16}$$

where $n_{e,i}$ is the electron and ion density, P is the gas pressure, p_{MHD} are the MHD bulk momenta, u_{MHD} the MHD bulk speeds and $T_{e,i}$ the electron and ion temperatures. v_J is the average electron speed required to carry the electric current (to simplify the initialization the electric current is assumed to initially be carried only be the electrons).

For the PIC simulations an initially Maxwellian plasma is assumed, due to the MHD assumption of a collisional system (system time is long compared with the collision time $\frac{1}{\nu}$). The velocity distribution function $f(\mathbf{v})$ is therefore the general Maxwell distribution function

$$f(\mathbf{r}, \mathbf{v}) = n(\mathbf{r}) \left(\frac{m}{2\pi k_B T(\mathbf{r})} \right)^{3/2} \exp \left(\frac{-m(\mathbf{v} - \mathbf{u}_{\mathrm{MHD}})^2}{2k_B T(\mathbf{r})} \right) \tag{3.17}$$

$$\propto \exp \left(-\frac{(\mathbf{v} - \mathbf{u}_{\mathrm{MHD}})^2}{v_{th}(\mathbf{r})^2} \right), \tag{3.18}$$

which thus gives a measure of the spread of the Maxwellian.

The dependence on the position $\mathbf{r}$ arises due to the chosen photosphere-corona temperature and density profile from the MHD simulations. If the electrons and ions were given the same initial bulk velocity there would be no initial
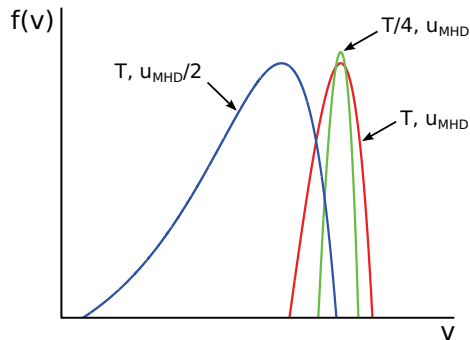
Figure 3.2: Maxwell distribution in a log-log plot: With changing bulk speed the peak shifts sidewards and changes the shape of the distribution, while a change in temperature changes the width and hence shape of the distribution function.

electric current, and there would be a large initial imbalance in Ampere's law, with a transient electric field causing a rapid increase in electric current and with the current carried mainly by the electrons, since the electrons move much faster than the heavier ions. To avoid this artificial perturbation in the beginning of the experiment, the electron velocity is initialized including an electric current speed:

$$\mathbf{j} = n_e q_e \mathbf{V_e} + n_i q_i \mathbf{V_i} \tag{3.19}$$
$$\nabla \times \mathbf{B} \approx \mu_0 \mathbf{j}, \tag{3.20}$$

where q_i is the ion charge. Assuming that $n_e = n_i$ and that, because of the larger inertia of the ions, $V_i \approx \mathbf{u}_{\mathrm{MHD}}$ we are left with

$$\mathbf{V_e} = \mathbf{u}_{\mathrm{MHD}} + \frac{\nabla \times \mathbf{B}}{\mu_0 n_e q_e}. \tag{3.21}$$

This setup provides an electric current from the very beginning of the simulation. A similar velocity initiation has been used in the interlocked model by Sugiyama and Kusano (2007). In principal one should also give ions a weak opposite speed component, but since the initial state inherited from MHD can never be completely consistent with the PIC model we do not bother to do this.

In addition to the setup parameters mentioned so far, in case of a stratified MHD simulation snapshot the densest part is removed, for the sake of code stability, as well as for the fact that we are only interested in the reconnection region in the solar corona. It is of course of high importance to still cover MHD scales with the PIC cut-out, so the experiment does not lose its relation to the solar active region environment.

The magnetic field is directly taken from the MHD snapshot. But the electric field of the PIC simulation is initialized using only the advective electric field $-\mathbf{u}_{\mathrm{MHD}} \times \mathbf{B}$ from the MHD snapshot, for the following reason:

$E_{\parallel}$ can only build up in non-ideal processes. In MHD simulations this parallel electric field is included as a resistivity term $\mathbf{E}_{\mathrm{res}} = \eta \mathbf{j}$. The resistivity η in numerical MHD simulations is imposed to handle instabilities which are caused by the high order operators in steep gradient areas such as current sheets and

shocks, while the real physical viscosity and resistivity length scales and hence the scales at which the parallel electric fields forms in diffusion regions, are taking place on kinetic length scales. These real solar diffusion scales are NOT resolved by MHD length scales. So the resistivity in MHD simulations is artificially high, and should not be directly incorporated into the PIC simulations. This ensures that any $E_\parallel$ that develops in the PIC simulations is created self-consistently.

In particle-in-cell codes (PIC) codes steep gradients also occur, but are automatically limited by the smoothing caused by the interpolations to and from the grid to the particle positions. This can also be seen as a non-ideal term, since particles are moved according to the Lorentz force, which is a result of the electric and magnetic fields produced by the weighted charge and current distribution of the neighboring particles. Hence particles feel each other indirectly over the grid, but two particles in the same cell do not interact directly with each other. Hence the only real physical resistivity in PIC simulations are the particle collisions as implemented in the *PhotonPlasma* PIC code as part of this thesis in the Coulomb scattering routine.

3.6 Initialization of the Magnetic Field in Numerical Experiments

As mentioned earlier in this document, only the photospheric magnetic field can routinely be measured at high resolution. The highly complex coronal field hence needs to be reconstructed. In general there are three fairly different approaches to simulate the magnetic field of pre-eruptive regions of the corona. One is to use a simplified magnetic field geometry, which resembles the observations on large scales. Such a numerical models in regard to solar active regions have been introduced by Baum and Bratenahl (1980), who positioned four flux cells in the photosphere, essentially four point magnetic charges or monopoles. These represent cuts through magnetic flux tubes emerging into the atmosphere. The magnetic field resulting from this construct show separator and separatrix field lines. More recent, improved studies that have used the model of sub-photospheric sources are Demoulin, Henoux, and Mandrini (1994) or Priest, Bungey, and Titov (1997); Aulanier, Pariat, and Démoulin (2005); Santos, Büchner, and Otto (2011). Santos, Büchner, and Otto (2011), for example, started from a force-free potential field and imposed photospheric boundary motions in order to build up currents.

A more elaborated way is magnetic field extrapolation from magnetograms obtained from observations. The simplest approach here is the potential field extrapolation, assuming $\nabla \times \mathbf{B} = 0$, or force-free field extrapolations[3], assuming $\nabla \times \mathbf{B} = \alpha \mathbf{B}$ (and called *linear force-free* if α is constant in space). The potential field extrapolations employed for the active region experiment were performed by using a Fast Fourier Transform potential extrapolation method. Numerical studies of solar flare events in the solar corona making use of this technique have been performed by Masson *et al.* (2009); this was one of the first MHD simulations to use realistic boundary and initial conditions in order

---

[3]Force-free, because the magnetic force on the plasma is zero $\mathbf{j} \times \mathbf{B} = 0$, hence there are only field-aligned currents possible.

to simulate a solar flare event. The active region experiment presented here (Baumann, Galsgaard, and Nordlund, 2012) uses the same technique of extrapolation of the magnetic field from an observed magnetogram. In cases where vector magnetograms are available, a related approach can be to make a linear or non-linear force-free field extrapolation, as done by Baker *et al.* (2009), who investigated the resulting magnetic topology in comparison with observations.

The third method I would like to mention here is one where results are extracted from a flux emergence simulation. The simulation is for example initiated with a twisted and unstable flux tube, initially positioned below the photosphere, which then emerges into the solar corona and interacts with a constant, pre-existing coronal magnetic field. This approach is used in the coronal hole experiment presented in this thesis. It has previously been used by e.g. Archontis *et al.* (2004, 2005) and Moreno-Insertis, Galsgaard, and Ugarte-Urra (2008). Archontis and Hood (2008); Gontikakis, Archontis, and Tsinganos (2009) went even a step closer to reality and simulated first the flux emergence of one flux tube to get a more realistic coronal magnetic field, into which then a second magnetic flux tube emerged.

3.7 The *PhotonPlasma* Particle-In-Cell Code

For all performed PIC simulations discussed in this thesis the *Photon-Plasma* code (Haugbølle, 2005; Hededal, 2005) has been used. The Photon-Plasma code solves the Maxwell equations

$$-\frac{\partial \mathbf{B}}{\partial t} = \nabla \times \mathbf{E} \tag{3.22}$$

$$\epsilon_0 \mu_0 \frac{\partial \mathbf{E}}{\partial t} = \nabla \times \mathbf{B} - \mu_0 \mathbf{j}, \tag{3.23}$$

together with the relativistic equation of motion for charged particles

$$m\frac{d(\gamma \mathbf{v})}{dt} = q(\mathbf{E} + \mathbf{v} \times \mathbf{B}) \tag{3.24}$$

on a staggered Yee lattice (Yee, 1966). The code is fully three-dimensional and uses a 2nd order leapfrog scheme for the progression in time, with 6th order spatial differencing. The electric and magnetic fields on the grid are interpolated to the particle positions using a cubic scheme that involves the 64 nearest mesh points. The particle positions and velocities are updated using the Vay particle-pusher (Vay, 2008). The electric currents are calculated using a new 6th order version of the Esirkepov charge conservation method (Esirkepov, 2001).

There is an option in the code to include particle-interactions via Coulomb scattering, which is especially valuable in the solar chromosphere. As the two main experiments introduced here are both taking place in a coronal environment, the scattering option has generally not been used, except in control experiments that showed only marginal differences. Additional code options (also not used here) are Compton scattering, pair creation and annihilation, multiple species treatment, e.g. to include neutrals and heavier ions.

We use SI units, scaled so the unit of length is $1\,\mathrm{km}$, the unit of time is $0.1\,\mathrm{s}$, and the unit of density is $10^{-12}\,\mathrm{kg\ m^{-3}}$. The same code units are used for the active region as well as the coronal hole experiment.

3.8 The *Stagger* MHD Code

The MHD *Stagger* code is a compressible MHD code, which solves the resistive MHD equations

$$\frac{\partial \rho_m}{\partial t} = -\nabla \cdot (\rho_m \mathbf{u}) \tag{3.25}$$

$$\frac{\partial (\rho_m \mathbf{u})}{\partial t} = -\nabla \cdot (\rho_m \mathbf{uu} + \underline{\underline{\tau}}) - \nabla P$$
$$+ \mathbf{j} \times \mathbf{B} + \rho_m \mathbf{g} \tag{3.26}$$

$$\frac{\partial e}{\partial t} = -\nabla \cdot (e\mathbf{u} + \mathbf{f_e}) - P\nabla \cdot \mathbf{u}$$
$$+ Q_J + Q_\nu \tag{3.27}$$

$$\frac{\partial \mathbf{B}}{\partial t} = -\nabla \times \mathbf{E} \tag{3.28}$$

$$\mathbf{j} = \nabla \times \mathbf{B} \tag{3.29}$$

$$\mathbf{E} = -\mathbf{u} \times \mathbf{B} + \eta \mathbf{j} \tag{3.30}$$

$$Q_J = \eta j^2 \tag{3.31}$$

$$\nabla \cdot \mathbf{B} = 0 \tag{3.32}$$

$$P = (\gamma - 1)e \tag{3.33}$$

$$\tau_{ij} = -\nu_{ij} \rho_m S_{ij} \tag{3.34}$$

$$S_{ij} = \frac{1}{2}\left(\frac{\partial u_i}{\partial x_j} + \frac{\partial u_j}{\partial x_i}\right) \tag{3.35}$$

$$Q_\nu = \rho_m \sum_{ij} \nu_{ij} S_{ij}^2 \tag{3.36}$$

$$\mathbf{f_e} = -\nu_e \rho_m \nabla(e/\rho_m) \tag{3.37}$$

where $\mathbf{u}$ is the bulk velocity, e the thermal energy per unit volume and ν_{ij} represents coefficient of viscosity, symmetric in ij. In some MHD codes the viscosity is assumed to be constant while in others the viscosity is supplied implicitly, through the methods used to ensure numerical stability. In the *Stagger* code the viscosity is instead defined explicitly by

$$\nu = \Delta s \left(\nu_1 c_f + \nu_2 |\mathbf{u}| + \nu_3 \Delta s \, | - \nabla \cdot \mathbf{u}|_+\right), \tag{3.38}$$

where $\nu_1 = 0.005 - 0.02$, $\nu_2 = 0.005 - 0.02$, and $\nu_3 = 0.2 - 0.4$ are dimensionless coefficients that provide dissipation for fast mode waves (ν_1), advective motions (ν_2), and shocks (ν_3). $| - \nabla \cdot \mathbf{u}|_+$ denotes the positive part of the rate of compression $-\nabla \cdot \mathbf{u}$. c_f is the fast mode speed defined by $c_f = \sqrt{(B^2 + \gamma P)/\rho_m}$.

The resistivity η is analogously defined by

$$\eta = \Delta s \left(\nu_1 c_f + \nu_2 |\mathbf{u}| + \nu_3 \Delta s \, | - \nabla \cdot \mathbf{u}_\perp|_+\right), \tag{3.39}$$

where $\mathbf{u}_\perp$ is the component of the velocity perpendicular to $\mathbf{B}$, and where the expression scaled by ν_3 prevents electric current sheets from becoming numerically unresolved. The resulting magnetic grid Reynolds numbers are on the order of a few in current sheets, as required to keep such structures marginally resolved. η is very small in the solar corona, but is still present, in particular in
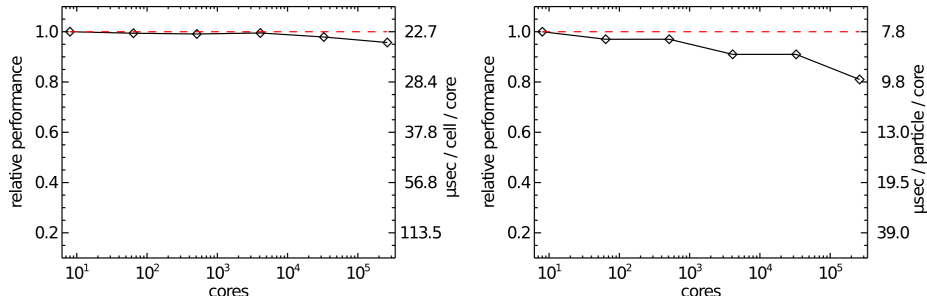
Figure 3.3: Weak Scaling plot for the MHD *Stagger* code (left) and the PIC *PhotonPlasma* code (right) for up to 262 k cores on the JUGENE supercomputer (see also Table 3.1).

reconnection regions. The overall scaling with Δs makes sure that advection, waves, shocks and current sheets are resolved by a few grids cells, independent of the mesh size. Handing resistivity this way minimizes the resistivity overall, as in smooth regions the resistivity is very small and only in steep gradient regions it is enhanced. Further in these MHD Equations S_{ij} is the shear tensor, τ_{ij} the viscous stress tensor and $\mathbf{f_e}$ is a weak diffusive flux of thermal energy needed for numerical stability. The term Q_v represents viscous dissipation, turning kinetic energy into heat, while Q_J is the Joule dissipation, responsible for converting magnetic energy into heat. And finally γ represents the ratio of specific heats, being 5/3 in our simulations, which means that we assume a monoatomic, ionized plasma (no neutrals or molecules included). This is a common approach for coronal plasma, since the temperature is very high and the density is low, the formation of neutral atoms and molecules is unimportant.

The high conductivity and the low plasma beta (10^{-3}, Aschwanden, 2005) lead, together with Equation (3.26) to the conclusion, that in most of the corona electric currents are flowing in directions nearly parallel to the magnetic field.

We include the force of gravity in both the MHD and PIC experiments.

3.9 The Performance of the *Stagger* and the *PhotonPlasma* Codes

Almost all simulations have been run in parallel on the JUGENE IBM Blue-Gene/P supercomputer at Forschungs-Zentrum Jülich (F-ZJ) in Germany. The *Stagger* code uses 23 microseconds per zone update per core on JUGENE, almost independently of the number of cores, as shown in Figure 3.3. The *PhotonPlasma* code uses 7 microseconds per particle update per core on JUGENE. Generally it can be said that the codes show good strong scaling (scaling at constant total problem size) and excellent weak scaling (scaling at constant problem size per core) on the JUGENE cluster. On JUGENE the code scales from 8 to 262 k cores with 82% efficiency, while the *Stagger* code scales with 96% efficiency from 8 to 262 k cores, at constant problem size per core.

Extensive scaling tests were performed. More information can be found at http://comp.astro.ku.dk/Twiki/view/CompAstro/JugeneNotes

Table 3.1: Scaling results

Cores	1	8	64	512	4096	32768	262144
sec/cell (MHD)		22.71	22.84	22.91	22.82	23.19	23.73
sec/particle (PIC)	7.04	7.81	8.09	8.05	8.61	8.57	9.70

4 ACTIVE REGION PLASMA ACCELERATION

The active region experiment consists of two parts: An MHD simulation and an associated PIC simulation. The goal of this active region experiment is to investigate the acceleration mechanism responsible for the particle acceleration in solar flares and other solar eruptive events. The numerical experimental setup is illustrated in Figure 4.1.

4.1 MHD Simulation

We choose a solar flare event which has previously been investigated both observationally as well as numerically by Masson *et al.* (2009). As a vector magnetogram was not available for this solar C-flare[1] event on 16th November 2002, and hence a nonlinear force-free extrapolation not possible, the numerical experiment starts out from a potential magnetic field extrapolation of a magnetogram from the Michelson Doppler Imager (MDI) instrument on The Solar and Heliospheric Observatory (SOHO) satellite (Scherrer *et al.*, 1995)[2]. The cut-out contains 185 x 110 data points. Each horizontal Fourier transform component of the potential is set to be exponentially decreasing in the direction away from the boundary, with amplitude factors of the form $\exp{(-zk_{x,y})}$, where z is the vertical coordinate. The magnetic field is then computed from the gradient of the potential, using the same differential operators as in the MHD code. This ensures that the magnetic field numerically satisfies $\nabla \times \mathbf{B} = 0$; i.e., that it is current free. Subsequently the numerical divergence $\nabla \cdot \mathbf{B}$ is computed; while analytically this should vanish numerically there is generally a small residual. This is iteratively removed by solving for a correction $\delta\Phi$ of the potential which has $\Delta(\delta\Phi) = \nabla \cdot \mathbf{B}$. This ensures that we start with a numerically $\nabla \cdot \mathbf{B}$ clean magnetic field (apart from some small scale noise due to truncation errors). Although the magnetic field in the coronal region is clearly non-potential, a potential field configuration is in most cases a reasonable representation of the overall topology of the magnetic field, while variations in for instance the magnetic field line loop height or the connectivity in weak magnetic field regions may occur (Régnier, 2012).

---

[1] C-flares typically release energies of about 3.6×10^{30} ergs (Kretzschmar, 2011).

[2] The MDI instrument is looking at the Doppler shift in right and left circularly polarized light from the Ni I $\lambda6768$ Å absorption line which forms in about $200 - 300$ km above the photosphere (Georgobiani *et al.*, 2000). These MDI measurements provide a full-disk line-of-sight magnetic field every 96 minutes with a resolution of 4 arcseconds and a total field of view of 34 x 34 arcminutes (Scherrer *et al.*, 1995). The accuracy of the magnetic field data is about about 20 G.
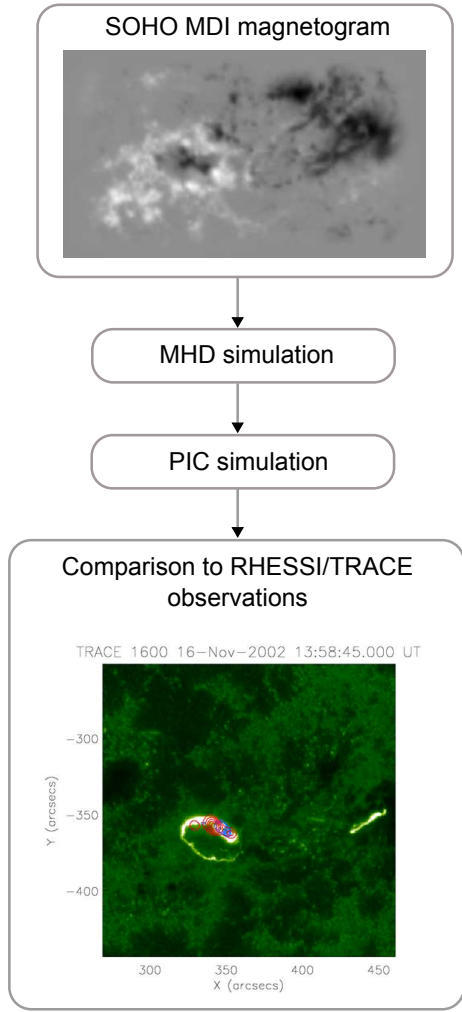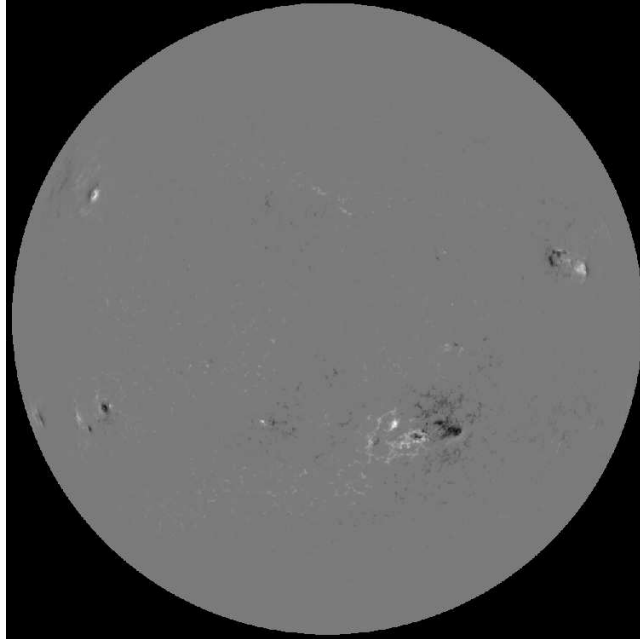
Figure 4.1: Active region experiment sketch

In case that the magnetic field is derived from a magnetogram, as in the active region experiment, the simulation setup is fully defined, with zero initial electric current (because the magnetic field is potential) and zero bulk velocity (since we have no other information). We used a magnetogram (see Figure 4.2a) taken at about 8 hours before the flare occurrence observed by the Transition Region and Coronal Explorer (TRACE), SOHO (Masson *et al.*, 2009) and RHESSI (Reid, 2011) (Figure 4.3a). This gives the simulation time to build up currents as a result of the driving motion we apply after some initial relaxation phase at the photospheric boundary. The applied driving motion at the bottom boundary represents the horizontal photospheric motions in the chosen active region observed by SOHO during the given time period. Driving is needed in order to build up currents and free magnetic energy in the system. The pattern used — deliberately chosen identical to the one used by Masson *et al.* (2009) — is shown in Figure 4.2b. Note that using the line-of-sight data of an active region which is away from the solar meridian causes a projection effect, which may cause some differences in the magnetic fields geometry. This is partially taken into account in the setup of the simulation, using a deprojection that cancels the foreshortening and skewing of the magnetogram. The contamination of the line of sight magnetic field by horizontal components cannot easily be removed.
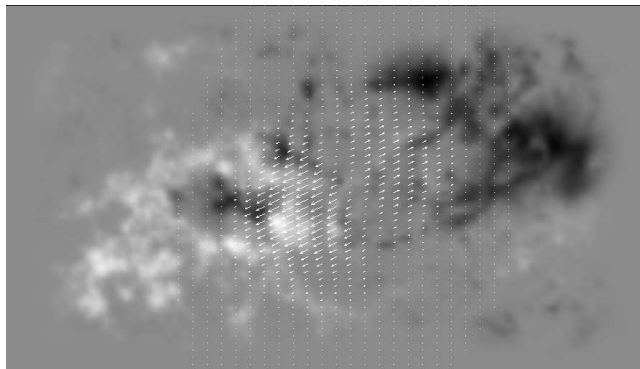
The magnetic feature seen in the solar observatory magnetogram in Figure 4.2a are thought to be a result of emerging flux tubes which rise up to the photosphere from the convection region (Caligari, Moreno-Insertis, and Schussler, 1995) due to the convection and the gas pressure. The hard X-rays emission shown in Figure 4.3b is most probably a result of electrons accelerated to nonthermal energies, which impact the much denser chromosphere and therewith produce bremsstrahlung. Soft X-rays on the other hand are thought to be from bremsstrahlung of electrons with thermal speeds as well as from atomic lines. In the non-thermal thick target model by Brown (1971) it is assumed that the soft X-ray spectra electrons are a consequence of the evaporation of hot plasma, which is heated by electrons that have previously been accelerated at the reconnection region and then impacted the chromosphere at the foot-points of the coronal loops. The model was subsequently improved and an update was published in Brown *et al.* (2009). Even if the electrons collide with thermal protons in the surrounding already before impacting the denser chromosphere the chromospheric emission will dominate because of the proportionality of bremsstrahlung to the ambient density.

Due to a 'parasitic' magnetic field polarity (the small region of black polarity immersed in the larger scale region with white polarity in the left hand side part of the magnetogram) the extrapolation of our chosen magnetogram leads to a 3D magnetic null-point topology, containing a fan-plane with a dome-shaped structure and a spine, surrounded by a much stronger magnetic field that extends to larger heights in the corona.

The 3D MHD simulations using the *Stagger* MHD code are performed on a box size of 175 x 100 x 62 Mm, covered by a stretched mesh of dimensions 896 x 512 x 320, with a cell size of about 80 km covering a reasonably larger region around the null-point. The boundaries at top and bottom are mainly chosen to be closed, while they are periodic on the sides. We conduct two kind of numerical MHD simulations: Stratified atmosphere experiments and constant temperature-density experiments. Additionally we modify the driving speed

(a) MDI full-disk image, 16th November 2002, 06:27 UT

(b) Lowest boundary vertical magnetic field after 0.001 sec after start of an active region experiment MHD run. A windowing function is initially employed, which conduced to have periodic boundary conditions for the Fast Fourier Transform potential extrapolation. Overplotted is the driving velocity pattern applied to photospheric boundary.

Figure 4.2: Full-disk SOHO magnetogram and applied velocity driving pattern

(a) TRACE observations at 1600 Å combined with the SOHO magnetogram (Masson *et al.*, 2009). Reproduced by permission of the AAS and the author.

(b) RHESSI X-ray observations at energies of (blue - soft) 12–25 keV (> 50%) and (red - hard) 25–100 keV (> 50%) overplotted on a TRACE image (Reid, 2011).

Figure 4.3: Observations of the solar C-flare event in AR 10191 on 16th November 2002

and look into its influence on the results. The driving speed is varied by a factor of 6 and even its smallest magnitude is at least 6.6 times larger than the corresponding, observed plasma motions ($\approx 0.5\,\mathrm{km\,s^{-1}}$), for reasons of limited computing time. It is of high importance to keep the driving speed well below the Alfvén velocity v_A and the sound speed v_s, because the magnetic structure and the plasma needs to have enough time to adapt to the new magnetic geometry and should not be haled by the driver. With this we assure an almost force free state at all times in the simulation, meaning that the current is well aligned with the magnetic field.

The driving velocity distribution at the bottom boundary leads to a relative shear of the main two different magnetic flux domains — inside and outside the dome-shaped fan-plane — and gives rise to a thin current sheet in the fan-plane separating these domains. This is the location at which also the diffusive electric field peaks. Reconnection takes place close to the null-point in the separatrix surface. The null-point itself is disrupted with increasing displacement (product of simulation time and amplitude of the average applied driving velocity) by the shearing motion and stretches into a 'weak magnetic field region'. The distortion of the magnetic field further leads to an electric field buildup. The advective electric field, $\mathbf{u} \times \mathbf{B}$, shows generally a higher magnitude than its diffusive counterpart $\eta\mathbf{j}$. With increasing boundary displacement the diffusive electric field close to the null-point increases in a characteristic run with a driving speed of $v_{drive} = 10\,\mathrm{km\,s^{-1}}$ up to around $50\,\mathrm{V\,m^{-1}}$, which corresponds to about $20\,\mathrm{V\,m^{-1}}$ with solar amplitude driving, since the diffusive electric field in current sheets relates as

$$E_{\mathrm{CS}} \propto \phi \propto v^{1/2}. \tag{4.1}$$

to the speed v (Baumann, Galsgaard, and Nordlund, 2012), where Φ is the angle formed by the field lines on each side of the current sheet, while the experimental driving speed is estimated to be 20 times larger than the real photospheric plasma motions. The advective electric field on the other hand experiences a much stronger increase, reaching values of about $900\,\mathrm{V\,m^{-1}}$, which, under the assumption of slow enough driving ($v_{drive} < v_A$), corresponds to $45\,\mathrm{V\,m^{-1}}$. Hence the electric field increase can be traced back to the energy input brought into the system by the boundary motion.

The systems in the presented experiments goes through different near-potential states, so that the evolution of the magnetic energy versus the boundary displacement is nearly perfectly identical for all stratified as well as non-stratified runs and the dissipation represents only a small fraction of the magnetic energy input rate. The rate of change of magnetic energy is almost constant in the beginning of the simulation, but as the work input from the lower boundary looses efficiency due to the angle between the boundary and the magnetic field lines approaching 90 degrees as well as a reduced amount of flux available for displacement, it begins to decrease. The system only stores a tiny amount of free magnetic energy on top of the potential energy, which cannot be counter-vailed by dissipation. The dissipation is shown in Baumann, Galsgaard, and Nordlund (2012) to be to lowest order proportional to the driving speed. Dissipation itself is suggestive of parallel electric fields, as the current in the corona is well aligned with the magnetic field. The parallel electric field $E_\parallel$ is of high interest in conjunction with particle acceleration.

Comparing the evolution with increasing boundary displacement of the non-

stratified and stratified cases leads to the following observation: The density profiles of all non-stratified simulation runs develop congruently with increasing displacement, independent of the driving speed as long as it is well below the Alfvén and sound speed, in which case also the dissipation normalized to the average driving speed at a given boundary displacement is almost superposable. Otherwise, if the ratio between Alfvén and driving speed is approaching unity, the dissipation level deviates perceptibly from the asymptotic behavior of the non-stratified runs. Advancing in time, the null-point in the stratified case moves up faster than in the non-stratified runs, due to dense material (over 1000 times denser than in the non-stratified cases) slowly rising from the lower boundary through the transition region into the corona. This behavior is physical as long as the driving at the photospheric boundary is sufficiently slow. If it is comparable to or faster than the sound speed the global plasma motion changes significantly and discrepancies from the common asymptotic behavior of all other conducted runs occur, in the magnetic dissipation behavior as well as in the magnetic energy evolution. In conclusion, the stratified simulation runs are much more sensitive to the driving speed than non-stratified runs, which initially have a constant density.

In Baumann, Galsgaard, and Nordlund (2012) it is further shown that the total dissipation is approximately independent of the thickness ΔL of the current sheet and hence approximately independent of the grid size, as the numerical models generally resolve current sheets down to a few grid cells. The total dissipation only depends on the change in magnetic field across the current sheet and the current sheet extent A_{CS}, where the current sheet covers a volume of $V_{CS} = \Delta L \cdot A_{CS}$. This results in the important conclusion, that the diffusive electric field as well as the total amount of dissipation is to a lowest order independent of the amount of numerical resistivity.

3D MHD simulations based on observed solar magnetogram of active regions have previously been performed by Masson *et al.* (2009), on a mesh of 237 x 201 x 201, which in fact inspired the MHD part of the experiment presented here. Javadi *et al.* (2011) investigated the heating mechanism of the corona in bright points using an potential field extrapolation of a SOHO magnetogram. But in general simulations based on extrapolations of photospheric magnetic fields are rare, although magnetograms have been used extensively to investigate 3D reconnection topologies (Close *et al.*, 2003; des Jardins *et al.*, 2009), as well as in test particle studies (Arzner and Vlahos, 2006). Arzner and Vlahos (2006) performed a linear force-free magnetic field extrapolation and traced electrons in this time-independent field configuration in order to deduce from their energy spectra the emission spectra. They used a test particle approach (see Section 3.2), where again no back-reactions from the particles onto the fields was included, unlike the experiment introduced in the next Section.

4.2   PIC Simulation

For the *Photon-Plasma* PIC code simulations an evolved (2 h 40 min of real solar time into an MHD simulation) and scaled (according to the guidelines in Section 3.4) MHD simulation dataset with a driving speed of $20\,\mathrm{km\,s^{-1}}$ serves as a starting point. A set of PIC simulations utilizing an MHD simulation data cut-out of size 44 x 25 16 Mm on a uniform mesh with up to 2518 x 1438 x 923
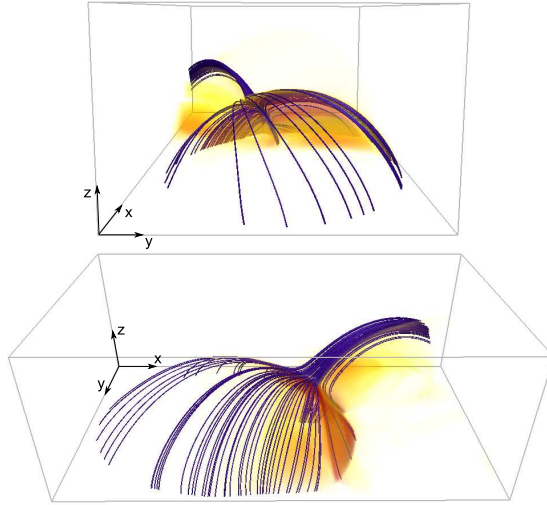
Figure 4.4: Initial PIC simulation snapshot. The blue lines represent the magnetic field lines and the semitransparent volume illustrates the highest electric current density (yellow-lower and orange-highest)

grid points and cell sizes down to $17.5\,\mathrm{km}$ are performed. About 30 real time solar seconds are covered. The velocities of the 20 electrons and 20 protons per cell and the fields are initialized as described in Section 3.5. The boundaries of the computational box are fixed for the fields and open for particles. The initial magnetic field configuration carried over from the MHD simulation is shown in Figure 4.4. A strong current sheet can be seen on the side of the dome, where the driving motion in the MHD simulation has been applied.

Systematic electric fields build up in the fan-plane, where the current sheet is located and the electric current density peaks. The current sheet is a consequence of the shearing of the outer and inner fan-plane magnetic field lines, which arose mainly from the applied boundary motion during the MHD simulations, which is still partially maintained by the chosen boundary conditions; new particles created in the ghost cells are specified according to the MHD snapshot parameters. Similar to the diffusive electric field in the MHD simulation, which is not inherited by the PIC simulation, an $\mathrm{E}_{\parallel}$ component builds up quickly, with peak values in the current sheet, equivalent to the location of the diffusive electric field in the MHD simulations. The overall magnitudes of the electric field, being on the order of $20 - 200\,\mathrm{mV\,m^{-1}}$, are generally far below the one from the MHD simulations, after the modifications described in Section 3.4 have been rescaled according to the following equation, providing the energy-charge relation of a particles that experiences a DC electric field acceleration

$$q\,E\,L = \mu_0^{-2}\left(\frac{\Delta B}{\Delta L}\right)^2\frac{m_e}{2n^2q^2},\tag{4.2}$$

where L is the distance covered by the electron with mass m_e. The right hand side of Equation (4.2) can be reformulated by replacing the ΔL with the typical current sheet thickness and expressing the magnetic field change ΔB with help

of the Alfvén speed to show that all its parameters are determined by macroscopic quantities. This leads to the conclusion that the electric field is inversely proportional to the elementary charge per particle, which was the main modified natural constant in the different simulation runs. The systematic DC electric field, which is mostly parallel to the magnetic field inside the current sheet, causes particles to experience a strong acceleration parallel to the magnetic field as long as they remain inside the current sheet. Most non-thermal particles are located inside the current sheet and win energies of about $4\,\text{keV}$ in just a few seconds, as a result of the DC electric field. Their energy distribution converges in only a couple of seconds to a stable power-law with $dN/dE \sim E^{-1.75}$ (N is the number of particles per unit energy), showing the efficiency of the acceleration. This is a somewhat harder electron distribution compared to what is observed in the real Sun, where the (absolute value of the) index is reported to be ≥ 2 (Krucker $et\ al.$, 2010).

As the current sheet area only makes up a small fraction of the domain, most particles are not significantly accelerated. The thermal electron distribution is preserved by (the majority of) the particles which do not enter the acceleration region of the current sheet and hence remain in the Maxwellian distribution, as they were initialized. The current sheet is mainly maintained by the particles in the lowest part of the non-thermal particle energy distribution. On the other hand up to 50% of the total energy resides in the power-law tail of the energy distribution, while there is only a fraction of 5% of all particles. This low particle number assures that the polarization electric field does not become large.

The power-law index is presumably a consequence of the DC systematic electric field in the fan-plane and is just as the energy cut-off likely determined by the magnetic field geometry. The fastest electrons reach velocities on the order of $10\,\text{keV}$. As the simulation takes place several hours before the C-flare occurrence in this particular active region, we expect higher particle energies during the flare event. Additionally one needs to keep in mind that we simulate 'quiescent' times, which becomes clear from the MHD simulations that did not result in a solar flare, due to the insufficient amounts of free energy available to the system. Nevertheless, the nature of the particle acceleration mechanism is likely to be the same also during the solar flare event. In fact, the lower boundary impact area of non-thermal particles in the simulation collected over a time interval of five seconds is shown in Figure 4.5. Non-thermal electrons are to a large extent responsible for the observed hard X-ray signatures, shown as red contours for this specific solar flare event in Figure 4.3, which correlates rather well with the impact area of the non-thermal particles in our numerical experiment.

The different modifications of the natural constants turn out to result in similar electric fields in the current sheet as well as nearly equivalent power-law indices, as long as the initial temperature is kept sufficiently low. Their thermal distributions are almost congruent, independent of the type of modifications applied. Increasing the temperature drowns the non-thermal distribution, although the electric field range in the current sheet remains about the same.

Solar flares are in general believed to be triggered by shearing and twisting motions (Amari $et\ al.$, 1996) at the photospheric boundary or by MHD instabilities, such as the kink instability (Kliem, Titov, and Török, 2004). But it is also known from observations that the $photospheric$ flux distribution does not change much during the eruptive event itself, which implies that the coronal

Figure 4.5: Impact area of non-thermal electrons in a cut-out of the simulation box. Additionally magnetic field lines passing close to the null-point are overplotted.

magnetic field must be in a highly non-potential state before the flare starts.

We used the method of applying shearing motions at the boundary and although the applied speeds are exaggerated compared to the observed photospheric speeds the system could not reach a state in which a solar eruption is possible. However, this does not prevent us from studying the particle acceleration mechanism, since the overall magnetic structures during the flare event are already established several hours prior to the eruption. And, as shown, the impact area of the particles accelerated to non-thermal energies in our simulations are similar to what is observed for this particular event.

5 CORONAL HOLE PLASMA ACCELERATION

The solar jet experiment presented in this Chapter is similarly to the active region experiment a continuation of an MHD simulation using the *Photonplasma* PIC code. Instead of starting from a magnetogram as in the previous experiment, the second of the mentioned main approaches (see Chapter 3.6) to simulate the coronal magnetic field is used: A flux emergence simulation.

Simulating a flux emergence process from several Mm below the photosphere to several tens of Mm into the corona is computationally a challenging task, as the density changes by a factor of more than 1×10^8. The low density in the corona directly constrains the time-step through the Alfvén speed for explicit MHD codes and hence leads to expensive simulations. In addition to these constraints, the presence of shocks often observed in such simulations provokes the necessity to handle the resistivity and viscosity accordingly to keep the simulation stable.

There has been a lot of work done in the context of simulating flux emergence events. I do not want to go into a detailed review of this work here, as we mostly concentrate on the particle acceleration aspect of the PIC simulation and use the emerging flux rope method more as a tool to create a characteristic arrangement of the coronal magnetic field. I refer to the two reviews of Hood, Archontis, and MacTaggart (2011) and Moreno-Insertis (2007) for further details on flux emergence simulations.

The jet experiment presented here is similar to the flux emergence simulation conducted by Moreno-Insertis, Galsgaard, and Ugarte-Urra (2008), whose setup is motivated by observations on March 10, 2007, by the HINODE satellite in a coronal hole region. Solar eruptive events are often associated with emerging photospheric flux (e.g. Jiang *et al.*, 2007). In this case a jet appeared in the EIS and XRT observations simultaneously to an emergence of a magnetic bipole at the photosphere. The EIS instrument is capable of providing information on velocity and density and therefore gives a convenient occasion for comparisons to and setting of initial conditions of numerical simulations.

The main difference to the simulation by Moreno-Insertis, Galsgaard, and Ugarte-Urra (2008) is the much higher spatial resolution, partly due to the implementation of a stretched mesh in all three directions. The results of the flux emergence experiment by Moreno-Insertis, Galsgaard, and Ugarte-Urra (2008) are briefly summarized in the next section.

5.1 Emerging Flux Tube as Initiator of a Coronal Jet

The jet experiment makes use of the emergence of a buoyant subphotospheric magnetic flux tube to form bipolar magnetic spots, leading to the formation of arch-shaped current sheets containing reconnection sites from which high velocity plasma outflows — so-called hot plasma jets — emerge. The flux tube, positioned in the solar interior at the start of the simulation, is cylindrical and twisted, analogously to the one defined in Fan (2001). The twist of the flux tube is a necessity, in order to allow the flux tube to retain its form, as shown by Abbett, Fisher, and Fan (2000). The twisted property of magnetic flux tubes is also confirmed by observations (e.g. Caligari, Moreno-Insertis, and Schussler, 1995). The magnetic flux tube is initially in pressure equilibrium with its surrounding. As the magnetic field of the tube (internal) is much stronger than the background magnetic field (external), we may write

$$P_{ext} = P_{int} + P_{m,int} = P_{int} + \frac{B^2}{2\mu_0}. \tag{5.1}$$

Assuming an ideal gas law $P = \frac{\rho_m k_B T}{\mu m_u}$ and $T_{ext} = T_{int}$, we conclude that, because of the additional magnetic pressure term, the gas density inside the tube must be lower than in its surrounding. Hence there is a buoyancy force acting against the tension force of the magnetic field of the flux tube. If a density perturbation at the center of the flux tube is introduced, the tube rises due to the gas pressure difference between the inside and outside of the flux rope and extends against the force of gravity and the tension force from the bending magnetic field of the flux tube, as discussed in Archontis *et al.* (2004).

When approaching the photosphere the flux tube slows down. Here the plasma beta becomes of the order of unity, which suddenly causes the magnetic pressure to win in importance. The magnetic pressure of the tube acts now against the gas and magnetic pressure of the surrounding, and the tube expands rapidly into the rare corona. The penetrating emerging flux at the photosphere causes a destabilization of the coronal magnetic field, which leads to the formation of current sheets and reconnection regions at the interface of the two connectivity domains. The background magnetic field and the flux tube magnetic field are chosen to become almost exactly anti-parallel at their first encounter. Subsequent flux emergence of the twisted magnetic field leads to several reconnection events. From the main reconnection region two hot plasma jets are expelled as a result of the gas pressure gradient (causing velocities on the order of the local sound speed) and as a result of the Lorentz force (causing velocities on the order of the local Alfvén speed).

5.2 The MHD Experiment

The fully 3D resistive, compressible MHD simulation, is performed using the *Stagger* code, including gravity, but not taking into account radiative cooling and heat conduction effects. The experiment covers a vertical physical height of 32.5 Mm and horizontally extends to 33.8 Mm and 38.1 Mm in the x and y directions respectively. The numerical grid, of size 512^3, is non-uniform in all
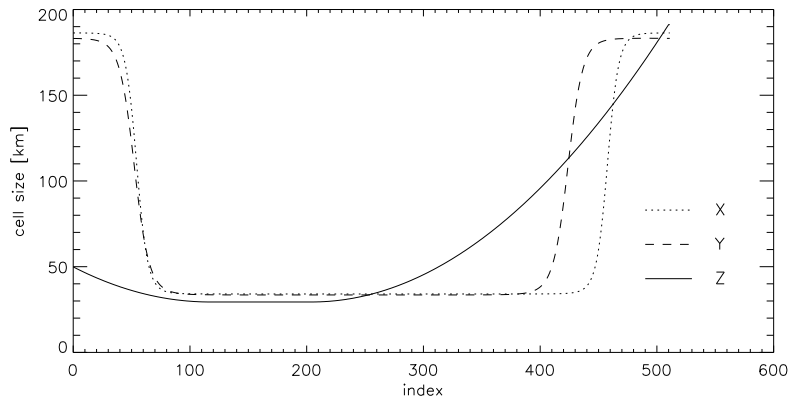
Figure 5.1: Cell sizes in km for all three axis against the indices. The z axis is the height.

three directions. Its minimal grid spacing of (x_{min}, y_{min}, z_{min})=(34.1, 33.5, 29.4) km is centered around the region, in which later in the experiment reconnection will take place. Figure 5.1 visualized the stretching of the mesh. The boundaries are periodic in x and y and closed/damped in the vertical direction.

A simple, stratified atmospheric profile is imposed, see Figure 5.2, in which the lowest 3.7 Mm of the total computational box height are still below the photosphere. From the lower boundary of the photosphere to the transition region extends a 2 Mm "chromosphere", in which the temperature is assumed to be constant at $\approx 5.6 \times 10^4$ K. Above that there is a steep temperature gradient, representing the transition region, with a physical height of 2 Mm. On top of that resides the corona, covering about 24.8 Mm with an initially constant temperature of around 2.2×10^6 K. The density of the corona is about $6 \times 10^8 \mathrm{cm}^{-3}$, an order of magnitude smaller than what is estimated from active regions (Aschwanden, 2005), consistent with the fact that the model represents a coronal hole region of the Sun.

In order to obtain a hydrostatic background profile we start by setting a one dimensional temperature profile as a function of height. From

$$\frac{dP}{dz} = -\rho_m g \tag{5.2}$$

and

$$\rho_m = \mu \cdot m_u \cdot \frac{P}{k_b \cdot T} \tag{5.3}$$

we integrate Equation (5.2) to obtain the pressure and further receive from Equation (5.3) the density. On top of that we define a constant background magnetic field of magnitude 3.3 Gauss, featuring an inclination of 65 degrees in the yz-plane. The flux tube is positioned along the y-axis, 1.7 Mm below the photosphere and has a maximum magnetic field strength of 1000 Gauss. The imposed background magnetic field is present throughout the entire box, representing the open magnetic field in which plasma can actually reach into the interplanetary space; i.e., a typical magnetic field configuration of coronal holes.
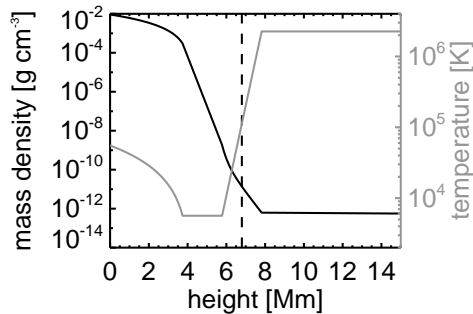
Figure 5.2: Atmospheric profile. The mass density (black) and the temperature (gray) are plotted against the box height in Mm. The dashed line represents the lower end of the cut-out used for the PIC simulation.

This overall field does not significantly influence the flux tube motion below the photosphere, since it is much below the magnetic field strength of the flux tube and the plasma motion is dominated by the gas pressure.

In addition to the high density plasma emerging into the corona from lower heights, rendering the particle densities horizontally highly inhomogeneous, there is a steep vertical particle density gradient, due to the initial stratification profile applied. Passing such an evolved MHD dataset to the PIC code would result in strong fluctuations in the electric field, as pseudo-particles with different weights move into low density regions, causing sudden increases in the charge density, which hence lead to strong fluctuations of the electric field. These kind of numerical fluctuations would disturb the investigation of the acceleration mechanism at work. We therefore cut away the lower, very dense parts of the MHD simulation domain (see dashed line in Figure 5.2[1]) before passing a subregion of the MHD dataset of extent 22 x 22 x 22 Mm to the PIC code. Even after cutting away the lower parts of the MHD dataset this experiment is, due to the highly varying number densities in the horizontal direction, numerically more challenging with respect to keeping numerical noise low, in comparison to the active region experiment discussed before.

At the specific time of the MHD simulation where a snapshot is passed on to the PIC code the dense plasma enclosed in the flux rope has almost completely been reconnected and ejected out of the reconnection region. Some of it also drained off along the magnetic field lines as a result of gravity. The jet velocities are of the order $400 - 800 \, \mathrm{km \, s^{-1}}$.

The interface between the MHD and PIC simulation is again treated as described in Chapter 3.5. The boundaries are left open for particles and fixed for the fields. Figure 5.3 shows the initial magnetic field configuration, together with the current sheet that extents along the flux rope, where reconnection with the overlying (green) magnetic field is taking place. To the left of the flux rope in the left hand side panel of Figure 5.3 a turbulent area has developed as a consequence of down flowing material interacting with material ejected from the reconnection site. To the right of the flux rope a new connectivity

---

[1]Note, that Figure 5.2 shows the initial atmospheric profile, while an evolved state of the MHD simulation is used as PIC simulation input.
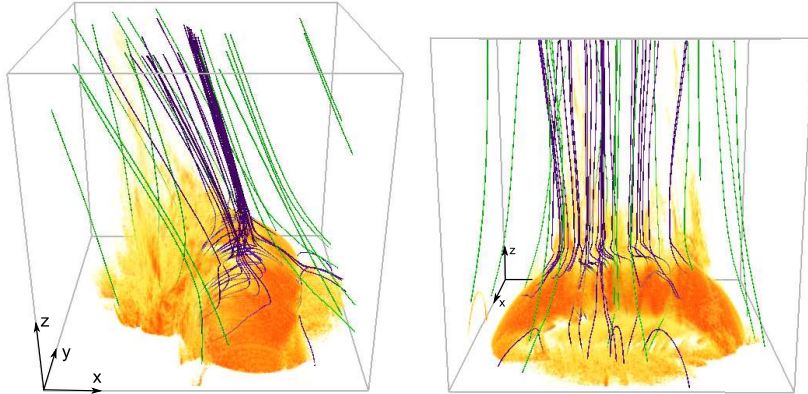
Figure 5.3: PIC simulation initial state. Magnetic field lines in blue are chosen to be close to the low magnetic field region, while the green field lines highlight the overlying coronal magnetic field. The electric current sheet density is shown in a semitransparent volume covering from yellow (low) to red (high) in intensity.

domain has formed by newly reconnected magnetic field lines, as described in Moreno-Insertis, Galsgaard, and Ugarte-Urra (2008, region 3, Figure 2).

Mainly two different grid dimensions are used; 400^3 and 800^3. The mesh is uniform and the cell sizes are 55 km and 27.5 km. Up to 7.5 seconds of solar time are simulated, with 20 particles per cell per species. In order to resolve microscopic scales of the plasma, the charge density, the speed of light as well as the proton-to-electron mass ratio have been modified, see Chapter 3.4. Two modification sets are introduced here, which differ by a factor of two in the choice of the elementary charge. The Debye length and skin depth are resolved by four cells in the current sheet, while one gyro radius contains several tens of cells in that area. The diffusive electric field ($E_{res} = \eta \mathbf{j}$ from the MHD simulation, where η is the locally defined resistivity and $\mathbf{j}$ the current density) contains the $E_{\parallel}$. A comparison of the locations of E_{res} and the self-consistently established $E_{\parallel}$ in the PIC simulation shows that both peak in the dome-shaped current sheet between the two connectivity domains. As a consequence, a non-thermal electron energy tail distribution builds up in the reconnection region, featuring a power-law index of $\frac{dN}{dln(E)}$ in the range -0.6 – -0.7. The overall distribution shows several peaks already from the beginning, mainly as a result of the two different plasmas flowing into the reconnection region; on one hand there is the low density but high temperature coronal plasma and on the other hand there is the cool, dense plasma contained in the flux rope. These are transferred to the PIC simulation through the bulk flow. In addition to that, the distribution coming from the currents in the MHD snapshot is added to this superposition of energy distribution functions (current drift velocity, as in Equation (3.20)).

The main acceleration mechanism is found to, also in this case, be a systematic, slowly fluctuating electric field peaking in the current sheet. The electric field is mainly directed along the magnetic field. The current sheet thickness is hence determining in particular the shape of the non-thermal energy distribution, by limiting the number of particles that can enter it. Particles which have once reached the current sheet are accelerated and therefore contribute a

share to the current density required by the magnetic field geometry. Due to the low magnetic field strength, their gyro radius is increased, so that they may feel differently oriented electric field areas during one gyration period. This may drop them out of the current sheet, which gives rise to a need for new particles entering this region to become accelerated, in order to maintain the electric current.

Jets have been observed in several different wavelengths, of which X-ray jets are the largest jet events. Jets are in general following magnetic field lines and there is an entire zoo of different jets reaching speeds from about $10\,\mathrm{km\,s^{-1}}$ to about $1000\,\mathrm{km\,s^{-1}}$, with an average of 150–$200\,\mathrm{km\,s^{-1}}$, and releasing energies on the order of 10^{27}–10^{29} ergs (e.g. Shimojo *et al.*, 1996; Shimojo and Shibata, 2000; Bain and Fletcher, 2009; Savcheva *et al.*, 2007). Shibata *et al.* (1994) concluded from observations of an active region that, similarly to solar flare plasma eruptions, solar jets must be driven by reconnecting magnetic fields. PIC simulations of reconnection region which give rise to strong outflow jets have been previously performed by Karimabadi, Daughton, and Scudder (2007) and Shay, Drake, and Swisdak (2007)), who focused their simulations on the small diffusion region. On large scales, using the test particles approach, Rosdahl and Galsgaard (2010) investigated the charged particle motion in a dataset of a flux emergence experiment. Apart from the already mentioned studies by Archontis *et al.* (2005) and Moreno-Insertis, Galsgaard, and Ugarte-Urra (2008), Gontikakis, Archontis, and Tsinganos (2009) conducted a similar simulation, but with two successive flux emergence events, spatially close enough that reconnection takes place between them. A current sheet formed, at which outer edge reconnection jets with local Alfvén velocities on the order of $100\,\mathrm{km\,s^{-1}}$ occur, which nicely compare with the presented TRACE observations. Pariat, Antiochos, and DeVore (2009) introduced a model for solar polar jets with a follow-up article (Pariat, Antiochos, and DeVore, 2010) explaining among numerous simulation outcomes, the intermittency of jets.

6 SUMMARY AND CONCLUSIONS

This work has focused on providing the first steps towards bridging the immense gap between microscopic scales (generation of resistivity) and macroscopic scales (generation of magnetic eruptive phenomena) on the Sun. A primary goal has been to study the mechanism of particle acceleration in different magnetic environments of the solar atmosphere. Hence, offering a method for coupling MHD and PIC models is one of the novel cornerstones of this project.

Kinetic simulations covering fully realistic scales of solar phenomena will never be possible, even on the largest supercomputer ever to be built. However, as shown in the present thesis, this challenge can be faced by making the dynamical span small enough to be resolved, while still keeping the different scales reasonably well separated, and retaining as much as possible of the ordering in the hierarchy of length and times scales.

Nonetheless, in the process of obtaining the results presented here over 50 million BlueGene/P core hours were spent, in simulations with up to 136 billion particles and 3.5 billion cells. A single simulation produced up to 5 Terabytes of data, the analysis of which was naturally a challenge, also from the hardware point of view. The access to such extensive resources was rendered possible through a John von Neumann Institute for Computing (NIC) grant, and through a subsequent Partnership for Advanced Computing in Europe (PRACE) grant. Due to the very successful scaling results obtained on the current system (with up to 2^{18} processors being used in parallel), it is expected that the performance of the simulation codes remains excellent even on systems with millions of cores, allowing investigations with even higher resolutions in the future.

The MHD active region experiment made use of an increase in driving speed when compared to reality, saving large amounts of computing power and making it possible to simulate the long buildup phase ahead of large solar eruptions. It was demonstrated that, as long as the driving speed remains smaller than the local Alfvén speed and sound speed, the results are essentially equivalent, and can be scaled to solar values. The restriction on velocities was shown to be more severe in simulations with a stratified atmosphere than in simulations with an initially constant density. However, if the constraints are complied with, stratified and non-stratified simulation runs show striking similarities.

The experiments were started from a potential extrapolation of a SOHO magnetogram, providing the main aspects of the magnetic topology of this particular solar active region. Despite the exaggerated driving, no flare like event emerged. It can be concluded that with the applied boundary driving, with only horizontal motions, and with a mainly compressive character, not enough free energy can be stored in the system to cause a sudden and powerful energy release. Therefore, flux emergence or twisting motions must have been present

in the real Sun, simultaneously with the observed horizontal motion.

The level of dissipation in the current sheet was shown to be, to lowest order, independent of the numerical resolution. Within the limits of the resolution we can afford the currents sheets we obtain are essentially monolithic, but we assume that at higher resolutions large scale current sheets will tend to fragment and break up.

The subsequent PIC simulations of this solar active region event are the first of a kind to study self-consistent particle acceleration in a realistic topology. The specifically chosen active region has been used because of its well defined topology, which has previously been investigated by Masson *et al.* (2009). The coupling between MHD and PIC simulations was implemented by using the magnetic fields from the MHD dataset, while only the advective electric field was passed on to the PIC setup. The fields were held fixed at the boundaries. Particles were initially given velocities that consist of the MHD bulk speed, a random thermal velocity, and component related to the electric current. The boundaries were chosen to be open for particles, so they can leave and enter the computational domain freely from a surrounding layer where the initial values are maintained.

A major finding from these investigations is the formation of a power-law of accelerated electrons, which turned out to be the result of a systematic ('DC') electric field particle acceleration mechanism, predominantly present in the current sheet of the fan-plane. A similar result was obtained in the coronal hole experiment, even though the magnetic field geometries are quite different. While the low magnetic field region in the active region experiment is localized to a small volume near a magnetic null-point, in the coronal hole experiment it extends over the entire reconnection region, as reflected by the occurrence of several null-points. The guide field in this reconnection geometry is very small, unlike in the active region experiment, where the guide field is dominating in the fan-plane current sheet. Another difference between the experiments is the enormous density contrasts related to the emergence of dense material from sub-photospheric layers in the coronal hole experiment, which leads to numerical noise, especially in the electric field. The coronal hole experiment further includes a turbulent region, which we speculate, given sufficiently high spatial resolution and sufficiently long simulation times, might be able to host stochastic acceleration sites.

Despite the diverseness, the two types of experiments investigated showed a similar behavior with respect to particle acceleration. We take that as evidence indicating that the power-law nature of the non-thermal particle distribution is very robust, and that the DC acceleration mechanism may be a generic source of at least the lower energy part of the non-thermal particle distribution, independent of the drastic modifications of natural constants applied to the parameter setup of the PIC simulations.

The modifications change the magnitudes of the simulation quantities in a way which can be subjected to scaling arguments, in order to estimate the corresponding solar values. Further investigations are needed to test more carefully to what extent such modification leave the underlying physics qualitatively unchanged. However, some results seem to be of such a fundamental nature that they are likely to be true, independent of the physical modifications.

It was shown, for example, that significant DC electric fields can exist, even in a collisionless environment, without being completely short-circuited by feed-

back effects (polarization electric field). This is due to the limited time particles can stay in the accelerating electric field and hence due to the limited number of particles accelerated to non-thermal energies. The reason for this is that particles get lost from the current sheet, either by following magnetic field lines that do not stay in the current sheet — this is particularly the case in the active region experiment — or because they enter a region with a very weak magnetic field, as they do in the coronal hole experiment.

In the Sun (and in numerical experiments with sufficient resolution) the thickness of current sheets is likely to be controlled by kinetic effects on micro-scales, and that, together with the small scale magnetic field topology and its evolution then sets constraints on how many, how much and how long particles are accelerated in the current sheet electric field. The electric field itself is a necessity, as it ensures a net charged particle flux in the current sheet, as required by the associated magnetic field configuration. The power-law is hence presumably a consequence of the probability for a particle to stay in the current sheet for a certain time.

In Section 2.4.2 the most important observational constraints for solar eruptions were listed. Some of them are consistent with the results obtained in the numerical experiments; e.g. the non-thermal energy-tail featuring a power-law electron energy distribution, a fast electron acceleration process, and the correlation of the impact regions of non-thermal particles with the X-ray emission images. However, the energies of the non-thermal electrons obtained in the two PIC simulations are rather at the lower end of the observed non-thermal distributions, hence contain only a fraction of the high-energy particles estimates of solar flares.

We speculate that the DC electric field explains the lower energy power-law, up to energies of a few hundred keV in the Sun, while its steeper extension part is presumably of another origin, such as stochastic acceleration. The current study is, despite the huge resources that have been available, still bound by numerical constraints that necessarily limit the explorations of parameter space, and basically prevent a study of stochastic particle acceleration mechanisms. Higher resolution and longer duration simulations are needed to resolve turbulent structures.

We expect that particular care must be taken when choosing the mass ratio between electrons and ions when studying stochastic acceleration, since the mass ratio probably plays an important role in producing the observed differences in energy gain. Studying stochastic acceleration is furthermore difficult because a larger number of particles are needed. The steeper power-laws observed at high energies means a very tiny probability of finding particles in this energy domain.

For now it can be concluded that the low energy part of the power-law electron distribution in eruptive solar events is very likely due to DC electric field acceleration.

BIBLIOGRAPHY

Abbett, W.P., Fisher, G.H., Fan, Y.: 2000, The Three-dimensional Evolution of Rising, Twisted Magnetic Flux Tubes in a Gravitationally Stratified Model Convection Zone. *Astrophys. J.* **540**, 548 – 562. doi:10.1086/309316.

Amari, T., Luciani, J.F., Aly, J.J., Tagger, M.: 1996, Very Fast Opening of a Three-dimensional Twisted Magnetic Flux Tube. *Astrophys. J. Lett.* **466**, L39. doi:10.1086/310158.

Anastasiadis, A.: 2002, Acceleration of solar energetic particles: the case of solar flares. *Journal of Atmospheric and Solar-Terrestrial Physics* **64**, 481 – 488. doi:10.1016/S1364-6826(02)00003-2.

Archontis, V., Hood, A.W.: 2008, A Flux Emergence Model for Solar Eruptions. *Astrophys. J. Lett.* **674**, L113 – L116. doi:10.1086/529377.

Archontis, V., Moreno-Insertis, F., Galsgaard, K., Hood, A., O'Shea, E.: 2004, Emergence of magnetic flux from the convection zone into the corona. *Astron. Astrophys.* **426**, 1047 – 1063. doi:10.1051/0004-6361:20035934.

Archontis, V., Moreno-Insertis, F., Galsgaard, K., Hood, A.W.: 2005, The Three-dimensional Interaction between Emerging Magnetic Flux and a Large-Scale Coronal Field: Reconnection, Current Sheets, and Jets. *Astrophys. J.* **635**, 1299 – 1318. doi:10.1086/497533.

Arzner, K., Vlahos, L.: 2006, Gyrokinetic electron acceleration in the force-free corona with anomalous resistivity. *Astron. Astrophys.* **454**, 957 – 967. doi:10.1051/0004-6361:20064953.

Aschwanden, M.J.: 1999, Particle Acceleration and Kinematics in Solar Flares and the Solar Corona. In: Wilson, A., *et al.*(eds.) *Magnetic Fields and Solar Processes*, *ESA Special Publication* **448**, 1015.

Aschwanden, M.J.: 2002, Particle acceleration and kinematics in solar flares - A Synthesis of Recent Observations and Theoretical Concepts (Invited Review). *Space Sci. Rev.* **101**, 1 – 227. doi:10.1023/A:1019712124366.

Aschwanden, M.J.: 2005, *Physics of the Solar Corona. An Introduction with Problems and Solutions (2nd edition)*.

Aulanier, G., Pariat, E., Démoulin, P.: 2005, Current sheet formation in quasi-separatrix layers and hyperbolic flux tubes. *Astron. Astrophys.* **444**, 961 – 976. doi:10.1051/0004-6361:20053600.

Bain, H.M., Fletcher, L.: 2009, Hard X-ray emission from a flare-related jet. *Astron. Astrophys.* **508**, 1443 − 1452. doi:10.1051/0004-6361/200911876.

Baker, D., van Driel-Gesztelyi, L., Mandrini, C.H., Démoulin, P., Murray, M.J.: 2009, Magnetic Reconnection along Quasi-separatrix Layers as a Driver of Ubiquitous Active Region Outflows. *Astrophys. J.* **705**, 926 − 935. doi:10.1088/0004-637X/705/1/926.

Bárta, M., Büchner, J., Karlický, M.: 2010, Multi-scale MHD approach to the current sheet filamentation in solar coronal reconnection. *Advances in Space Research* **45**, 10 − 17. doi:10.1016/j.asr.2009.07.025.

Baum, P.J., Bratenahl, A.: 1980, Flux linkages of bipolar sunspot groups - A computer study. *Solar Phys.* **67**, 245 − 258. doi:10.1007/BF00149805.

Baumann, G., Nordlund, Å.: 2012, Particle-In-Cell Simulation of Electron Acceleration in Solar Coronal Jets. *ArXiv e-prints.*

Baumann, G., Galsgaard, K., Nordlund, Å.: 2012, 3D Solar Null Point Reconnection MHD Simulations. *ArXiv e-prints.*

Baumann, G., Haugbølle, T., Nordlund, Å.: 2012, Kinetic modeling of particle acceleration in a solar null point reconnection region. *ArXiv e-prints.*

Baumjohann, W., Treumann, R.A.: 1996, *Basic space plasma physics.*

Birdsall, C.K.: 1991, Particle-in-cell charged-particle simulations, plus Monte Carlo collisions with neutral atoms, PIC-MCC. *IEEE Transactions on Plasma Science* **19**, 65 − 85. doi:10.1109/27.106800.

Birn, J., Priest, E.R.: 2007, *Reconnection of magnetic fields : magnetohydrodynamics and collisionless theory and observations.*

Boyd, T.J.M., Sanderson, J.J.: 2003, *The Physics of Plasmas.*

Brown, J.C.: 1971, The Deduction of Energy Spectra of Non-Thermal Electrons in Flares from the Observed Dynamic Spectra of Hard X-Ray Bursts. *Solar Phys.* **18**, 489 − 502. doi:10.1007/BF00149070.

Brown, J.C., Turkmani, R., Kontar, E.P., MacKinnon, A.L., Vlahos, L.: 2009, Local re-acceleration and a modified thick target model of solar flare electrons. *Astron. Astrophys.* **508**, 993 − 1000. doi:10.1051/0004-6361/200913145.

Caligari, P., Moreno-Insertis, F., Schussler, M.: 1995, Emerging flux tubes in the solar convection zone. 1: Asymmetry, tilt, and emergence latitude. *Astrophys. J.* **441**, 886 − 902. doi:10.1086/175410.

Cargill, P.J.: 1991, The interaction of collisionless shocks in astrophysical plasmas. *Astrophys. J.* **376**, 771 − 781. doi:10.1086/170325.

Chifor, C., Young, P.R., Isobe, H., Mason, H.E., Tripathi, D., Hara, H., Yokoyama, T.: 2008, An active region jet observed with Hinode. *Astron. Astrophys.* **481**, L57 − L60. doi:10.1051/0004-6361:20079081.

Close, R.M., Parnell, C.E., Mackay, D.H., Priest, E.R.: 2003, Statistical Flux Tube Properties of 3D Magnetic Carpet Fields. *Solar Phys.* **212**, 251 − 275.

Dahlburg, R.B., Einaudi, G.: 2002, MHD unstable modes in the 3D evolution of 2D MHD structures and the diminished role of coalescence instabilities. *Physics Letters A* **294**, 101 − 107. doi:10.1016/S0375-9601(02)00027-0.

Dalla, S., Browning, P.K.: 2005, Particle acceleration at a three-dimensional reconnection site in the solar corona. *Astron. Astrophys.* **436**, 1103 − 1111. doi:10.1051/0004-6361:20042589.

Dalla, S., Browning, P.K.: 2006, Jets of Energetic Particles Generated by Magnetic Reconnection at a Three-dimensional Magnetic Null. *Astrophys. J. Lett.* **640**, L99 − L102. doi:10.1086/503302.

Dalla, S., Browning, P.K.: 2008, Particle trajectories and acceleration during 3D fan reconnection. *Astron. Astrophys.* **491**, 289 − 295. doi:10.1051/0004-6361:200809771.

Demoulin, P., Henoux, J.C., Mandrini, C.H.: 1994, Are magnetic null points important in solar flares ? *Astron. Astrophys.* **285**, 1023 − 1037.

des Jardins, A., Canfield, R., Longcope, D., McLinden, E., Dillman, A.: 2009, Signatures of Magnetic Stress Prior to Three Solar Flares Observed by RHESSI. *Astrophys. J.* **693**, 886 − 893. doi:10.1088/0004-637X/693/1/886.

Drake, J.F., Shay, M.A., Thongthai, W., Swisdak, M.: 2005, Production of Energetic Electrons during Magnetic Reconnection. *Physical Review Letters* **94**(9), 095001. doi:10.1103/PhysRevLett.94.095001.

Drake, J.F., Swisdak, M., Che, H., Shay, M.A.: 2006a, Electron acceleration from contracting magnetic islands during reconnection. *Nature* **443**, 553 − 556. doi:10.1038/nature05116.

Drake, J.F., Swisdak, M., Schoeffler, K.M., Rogers, B.N., Kobayashi, S.: 2006b, Formation of secondary islands during magnetic reconnection. *Geophys. Res. Lett.* **33**, 13105. doi:10.1029/2006GL025957.

Dreicer, H.: 1960, Electron and Ion Runaway in a Fully Ionized Gas. II. *Physical Review* **117**, 329 − 342. doi:10.1103/PhysRev.117.329.

Esirkepov, T.Z.: 2001, Exact charge conservation scheme for Particle-in-Cell simulation with an arbitrary form-factor. *Computer Physics Communications* **135**, 144 − 153. doi:10.1016/S0010-4655(00)00228-9.

Fan, Y.: 2001, The Emergence of a Twisted Ω-Tube into the Solar Atmosphere. *Astrophys. J. Lett.* **554**, L111 − L114. doi:10.1086/320935.

Fermi, E.: 1949, On the Origin of the Cosmic Radiation. *Physical Review* **75**, 1169 − 1174. doi:10.1103/PhysRev.75.1169.

Filippov, B., Golub, L., Koutchmy, S.: 2009, X-Ray Jet Dynamics in a Polar Coronal Hole Region. *Solar Phys.* **254**, 259 − 269. doi:10.1007/s11207-008-9305-6.

Georgobiani, D., Kosovichev, A.G., Nigam, R., Nordlund, Å., Stein, R.F.: 2000, Numerical Simulations of Oscillation Modes of the Solar Convection Zone. *Astrophys. J. Lett.* **530**, L139 − L142. doi:10.1086/312490.

Giovanelli, R.G.: 1946, A Theory of Chromospheric Flares. *Nature* **158**, 81–82. doi:10.1038/158081a0.

Gontikakis, C., Archontis, V., Tsinganos, K.: 2009, Observations and 3D MHD simulations of a solar active region jet. *Astron. Astrophys.* **506**, L45–L48. doi:10.1051/0004-6361/200913026.

Haugbølle, T.: 2005, Modelling Relativistic Astrophysics at the Large and Small Scale. PhD thesis, Niels Bohr Institute [astro-ph/0510292].

Hededal, C.: 2005, Gamma-Ray Bursts, Collisionless Shocks and Synthetic Spectra. PhD thesis, Niels Bohr Institute [astro-ph/0506559].

Hesse, M., Schindler, K.: 1988, A theoretical foundation of general magnetic reconnection. *J. Geophys. Res.* **93**, 5559–5567. doi:10.1029/JA093iA06p05559.

Hesse, M., Forbes, T.G., Birn, J.: 2005, On the Relation between Reconnected Magnetic Flux and Parallel Electric Fields in the Solar Corona. *Astrophys. J.* **631**, 1227–1238. doi:10.1086/432677.

Holman, G.D.: 1985, Acceleration of runaway electrons and Joule heating in solar flares. *Astrophys. J.* **293**, 584–594. doi:10.1086/163263.

Hood, A.W., Archontis, V., MacTaggart, D.: 2011, 3D MHD Flux Emergence Experiments: Idealized models and coronal interactions. *ArXiv e-prints*.

Javadi, S., Büchner, J., Otto, A., Santos, J.C.: 2011, About the relative importance of compressional heating and current dissipation for the formation of coronal X-ray bright points. *Astron. Astrophys.* **529**, A114. doi:10.1051/0004-6361/201015614.

Jiang, Y.C., Chen, H.D., Li, K.J., Shen, Y.D., Yang, L.H.: 2007, The Hα surges and EUV jets from magnetic flux emergences and cancellations. *Astron. Astrophys.* **469**, 331–337. doi:10.1051/0004-6361:20053954.

Kanamori, H.: 1978, Quantification of Earthquakes. *Nature* **271**, 411–414. doi:10.1038/271411a0.

Kane, S.R., Anderson, K.A.: 1970, Spectral Characteristics of Impulsive Solar-Flare X-Rays ???? 10 KeV. *Astrophys. J.* **162**, 1003. doi:10.1086/150732.

Karimabadi, H., Daughton, W., Scudder, J.: 2007, Multi-scale structure of the electron diffusion region. *Geophys. Res. Lett.* **34**, 13104. doi:10.1029/2007GL030306.

Karlický, M., Bárta, M.: 2011, Successive Merging of Plasmoids and Fragmentation in a Flare Current Sheet and Their X-Ray and Radio Signatures. *Astrophys. J.* **733**, 107. doi:10.1088/0004-637X/733/2/107.

Kliem, B., Titov, V.S., Török, T.: 2004, Formation of current sheets and sigmoidal structure by the kink instability of a magnetic loop. *Astron. Astrophys.* **413**, L23–L26. doi:10.1051/0004-6361:20031690.

Kretzschmar, M.: 2011, The Sun as a star: observations of white-light flares. *Astron. Astrophys.* **530**, A84. doi:10.1051/0004-6361/201015930.

Krucker, S., Hudson, H.S., Glesener, L., White, S.M., Masuda, S., Wuelser, J.-P., Lin, R.P.: 2010, Measurements of the Coronal Acceleration Region of a Solar Flare. *Astrophys. J.* **714**, 1108 – 1119. doi:10.1088/0004-637X/714/2/1108.

Kulsrud, R.M.: 2005, *Plasma physics for astrophysics.*

Kumar, P., Cho, K.-S., Bong, S.-C., Park, S.-H., Kim, Y.H.: 2012, Initiation of Coronal Mass Ejection and Associated Flare Caused by Helical Kink Instability Observed by SDO/AIA. *Astrophys. J.* **746**, 67. doi:10.1088/0004-637X/746/1/67.

Lin, R.P., Krucker, S., Hurford, G.J., Smith, D.M., Hudson, H.S., Holman, G.D., Schwartz, R.A., Dennis, B.R., Share, G.H., Murphy, R.J., Emslie, A.G., Johns-Krull, C., Vilmer, N.: 2003, RHESSI Observations of Particle Acceleration and Energy Release in an Intense Solar Gamma-Ray Line Flare. *Astrophys. J. Lett.* **595**, L69 – L76. doi:10.1086/378932.

Litvinenko, Y.E.: 1996, Particle Acceleration in Reconnecting Current Sheets with a Nonzero Magnetic Field. *Astrophys. J.* **462**, 997. doi:10.1086/177213.

Longcope, D.W., Parnell, C.E.: 2009, The Number of Magnetic Null Points in the Quiet Sun Corona. *Solar Phys.* **254**, 51 – 75. doi:10.1007/s11207-008-9281-x.

Manoharan, P.K., van Driel-Gesztelyi, L., Pick, M., Demoulin, P.: 1996, Evidence for Large-Scale Solar Magnetic Reconnection from Radio and X-Ray Measurements. *Astrophys. J. Lett.* **468**, L73. doi:10.1086/310221.

Masson, S., Pariat, E., Aulanier, G., Schrijver, C.J.: 2009, The Nature of Flare Ribbons in Coronal Null-Point Topology. *Astrophys. J.* **700**, 559 – 578. doi:10.1088/0004-637X/700/1/559.

Masuda, S., Kosugi, T., Hara, H., Tsuneta, S., Ogawara, Y.: 1994, A loop-top hard X-ray source in a compact solar flare as evidence for magnetic reconnection. *Nature* **371**, 495 – 497. doi:10.1038/371495a0.

Miller, J.A.: 2000, Particle Acceleration in Solar Flares. In: Martens, P.C.H., Tsuruta, S., Weber, M.A. (eds.) *Highly Energetic Physical Processes and Mechanisms for Emission from Astrophysical Plasmas*, *IAU Symposium* **195**, 277.

Miller, J.A., Cargill, P.J., Emslie, A.G., Holman, G.D., Dennis, B.R., LaRosa, T.N., Winglee, R.M., Benka, S.G., Tsuneta, S.: 1997, Critical issues for understanding particle acceleration in impulsive solar flares. *J. Geophys. Res.* **102**, 14631 – 14660. doi:10.1029/97JA00976.

Moreno-Insertis, F.: 2007, Three-dimensional numerical experiments of flux emergence into the corona. In: Shibata, K., Nagata, S., Sakurai, T. (eds.) *New Solar Physics with Solar-B Mission*, *Astronomical Society of the Pacific Conference Series* **369**, 335.

Moreno-Insertis, F., Galsgaard, K., Ugarte-Urra, I.: 2008, Jets in Coronal Holes: Hinode Observations and Three-dimensional Computer Modeling. *Astrophys. J. Lett.* **673**, L211 – L214. doi:10.1086/527560.

Newcomb, W.A.: 1958, Motion of magnetic lines of force. *Annals of Physics* **3**, 347 − 385. doi:10.1016/0003-4916(58)90024-1.

Ohyama, M., Shibata, K.: 1998, X-Ray Plasma Ejection Associated with an Impulsive Flare on 1992 October 5: Physical Conditions of X-Ray Plasma Ejection. *Astrophys. J.* **499**, 934. doi:10.1086/305652.

Okuda, H.: 1972, Nonphysical Noises and Instabilities in Plasma Simulation due to a Spatial Grid. *Journal of Computational Physics* **10**, 475. doi:10.1016/0021-9991(72)90048-4.

Pariat, E., Antiochos, S.K., DeVore, C.R.: 2009, A Model for Solar Polar Jets. *Astrophys. J.* **691**, 61 − 74. doi:10.1088/0004-637X/691/1/61.

Pariat, E., Antiochos, S.K., DeVore, C.R.: 2010, Three-dimensional Modeling of Quasi-homologous Solar Jets. *Astrophys. J.* **714**, 1762 − 1778. doi:10.1088/0004-637X/714/2/1762.

Parks, G.K., Winckler, J.R.: 1969, Sixteen-Second Periodic Pulsations Observed in the Correlated Microwave and Energetic X-Ray Emission from a Solar Flare. *Astrophys. J. Lett.* **155**, L117. doi:10.1086/180315.

Parnell, C.E., Smith, J.M., Neukirch, T., Priest, E.R.: 1996, The structure of three-dimensional magnetic neutral points. *Physics of Plasmas* **3**, 759 − 770. doi:10.1063/1.871810.

Pontin, D.I.: 2011, Three-dimensional magnetic reconnection regimes: A review. *Advances in Space Research* **47**, 1508 − 1522. doi:10.1016/j.asr.2010.12.022.

Priest, E.R., Titov, V.S.: 1996a, Magnetic Reconnection at Three-Dimensional Null Points. *Royal Society of London Philosophical Transactions Series A* **354**, 2951 − 2992. doi:10.1098/rsta.1996.0136.

Priest, E.R., Titov, V.S.: 1996b, Magnetic Reconnection at Three-Dimensional Null Points. *Royal Society of London Proceedings Series A* **354**, 2951 − 2992.

Priest, E.R., Bungey, T.N., Titov, V.S.: 1997, The 3D topology and interaction of complex magnetic flux systems. *Geophysical and Astrophysical Fluid Dynamics* **84**, 127 − 163. doi:10.1080/03091929708208976.

Pritchett, P.L.: 2003, Particle-in-Cell Simulation of Plasmas - A Tutorial. In: Büchner, J., Dum, C., Scholer, M. (eds.) *Space Plasma Simulation, Lecture Notes in Physics, Berlin Springer Verlag* **615**, 1 − 24.

Régnier, S.: 2012, Magnetic Energy Storage and Current Density Distributions for Different Force-Free Models. *Solar Phys.* **277**, 131 − 151. doi:10.1007/s11207-011-9830-6.

Régnier, S., Parnell, C.E., Haynes, A.L.: 2008, A new view of quiet-Sun topology from Hinode/SOT. *Astron. Astrophys.* **484**, L47 − L50. doi:10.1051/0004-6361:200809826.

Reid, H.: 2011, private communication. In: *private communication.*

Rosdahl, K.J., Galsgaard, K.: 2010, Test particle acceleration in a numerical MHD experiment of an anemone jet. *Astron. Astrophys.* **511**, A73. doi:10.1051/0004-6361/200913541.

Santos, J.C., Büchner, J., Otto, A.: 2011, Development of electric currents in a magnetic field configuration containing a magnetic null point. *Astron. Astrophys.* **525**, A3. doi:10.1051/0004-6361/201014758.

Savcheva, A., Cirtain, J., Deluca, E.E., Lundquist, L.L., Golub, L., Weber, M., Shimojo, M., Shibasaki, K., Sakao, T., Narukage, N., Tsuneta, S., Kano, R.: 2007, A Study of Polar Jet Parameters Based on Hinode XRT Observations. *PASJ* **59**, 771.

Scherrer, P.H., Bogart, R.S., Bush, R.I., Hoeksema, J.T., Kosovichev, A.G., Schou, J., Rosenberg, W., Springer, L., Tarbell, T.D., Title, A., Wolfson, C.J., Zayer, I., MDI Engineering Team: 1995, The Solar Oscillations Investigation - Michelson Doppler Imager. *Solar Phys.* **162**, 129−188. doi:10.1007/BF00733429.

Schindler, K., Hesse, M., Birn, J.: 1988, General magnetic reconnection, parallel electric fields, and helicity. *J. Geophys. Res.* **93**, 5547−5557. doi:10.1029/JA093iA06p05547.

Shay, M.A., Drake, J.F., Swisdak, M.: 2007, Two-Scale Structure of the Electron Dissipation Region during Collisionless Magnetic Reconnection. *Physical Review Letters* **99**(15), 155002. doi:10.1103/PhysRevLett.99.155002.

Shibata, K., Tanuma, S.: 2001, Plasmoid-induced-reconnection and fractal reconnection. *Earth, Planets, and Space* **53**, 473−482.

Shibata, K., Nitta, N., Strong, K.T., Matsumoto, R., Yokoyama, T., Hirayama, T., Hudson, H., Ogawara, Y.: 1994, A gigantic coronal jet ejected from a compact active region in a coronal hole. *Astrophys. J. Lett.* **431**, L51−L53. doi:10.1086/187470.

Shimojo, M., Shibata, K.: 2000, Physical Parameters of Solar X-Ray Jets. *Astrophys. J.* **542**, 1100−1108. doi:10.1086/317024.

Shimojo, M., Hashimoto, S., Shibata, K., Hirayama, T., Hudson, H.S., Acton, L.W.: 1996, Statistical Study of Solar X-Ray Jets Observed with the YOHKOH Soft X-Ray Telescope. *PASJ* **48**, 123−136.

Siversky, T.V., Zharkova, V.V.: 2009, Particle acceleration in a reconnecting current sheet: PIC simulation. *Journal of Plasma Physics* **75**, 619. doi:10.1017/S0022377809008009.

Sugiyama, T., Kusano, K.: 2007, Multi-scale plasma simulation by the interlocking of magnetohydrodynamic model and particle-in-cell kinetic model. *Journal of Computational Physics* **227**, 1340−1352. doi:10.1016/j.jcp.2007.09.011.

Tajima, T.: 1986, Plasma physics via computer simulation C.K. Birdsall and A.B. Langdon, McGraw-Hill, New York, 1985. xxiii + 479 pages. US $45. *Computer Physics Communications* **42**, 151−152. doi:10.1016/0010-4655(86)90240-7.

Tsiklauri, D., Haruki, T.: 2007, Magnetic reconnection during collisionless, stressed, X-point collapse using particle-in-cell simulation. *Physics of Plasmas* **14**(11), 112905. doi:10.1063/1.2800854.

Turkmani, R., Vlahos, L., Galsgaard, K., Cargill, P.J., Isliker, H.: 2005, Particle Acceleration in Stressed Coronal Magnetic Fields. *Astrophys. J. Lett.* **620**, L59−L62. doi:10.1086/428395.

Turkmani, R., Cargill, P.J., Galsgaard, K., Vlahos, L., Isliker, H.: 2006, Particle acceleration in stochastic current sheets in stressed coronal active regions. *Astron. Astrophys.* **449**, 749−757. doi:10.1051/0004-6361:20053548.

van Driel-Gesztelyi: 2003, *Observational signatures of magnetic reconnection.*

van Driel-Gesztelyi, L.: 2009, Magnetic reconnection and energy release on the Sun and solar-like stars. In: *IAU Symposium*, *IAU Symposium* **259**, 191−200. doi:10.1017/S1743921309030440.

Vay, J.-L.: 2008, Simulation of beams or plasmas crossing at relativistic velocity. *Physics of Plasmas* **15**(5), 056701. doi:10.1063/1.2837054.

Wang, H., Qiu, J., Jing, J., Zhang, H.: 2003, Study of Ribbon Separation of a Flare Associated with a Quiescent Filament Eruption. *Astrophys. J.* **593**, 564−570. doi:10.1086/376360.

Wang, T., Sui, L., Qiu, J.: 2007, Direct Observation of High-Speed Plasma Outflows Produced by Magnetic Reconnection in Solar Impulsive Events. *Astrophys. J. Lett.* **661**, L207−L210. doi:10.1086/519004.

Woods, T.N., Kopp, G., Chamberlin, P.C.: 2006, Contributions of the solar ultraviolet irradiance to the total solar irradiance during large flares. *Journal of Geophysical Research (Space Physics)* **111**, 10. doi:10.1029/2005JA011507.

Yee, K.: 1966, Numerical solution of inital boundary value problems involving maxwell's equations in isotropic media. *IEEE Transactions on Antennas and Propagation* **14**, 302−307. doi:10.1109/TAP.1966.1138693.

Zharkova, V.V., Arzner, K., Benz, A.O., Browning, P., Dauphin, C., Emslie, A.G., Fletcher, L., Kontar, E.P., Mann, G., Onofri, M., Petrosian, V., Turkmani, R., Vilmer, N., Vlahos, L.: 2011, Recent Advances in Understanding Particle Acceleration Processes in Solar Flares. *ArXiv e-prints.*

A APPENDIX: NOTATION AND DEFINITIONS

Notation

$\mathbf{B}$	magnetic field
c	speed of light
$\mathbf{E}$	electric field
$\mathbf{E_D}$	Dreicer electric field
$E_{\parallel}$	electric field component parallel to the magnetic field
$\mathbf{E_{res}}$	resistive electric field
E_{CS}	electric field in current sheet
e	thermal energy per volume
$\mathbf{g}$	gravitational field
$\mathbf{j}$	electric current density
k_B	Boltzmann constant
$m_{e,i}$	electron and proton mass
m_u	atomic mass constant
N	number of particles
$n_{e,i}$	electron and proton particle density
P	gas pressure
P_m	magnetic pressure
p_{MHD}	MHD bulk momenta
$-q_e = q_i$	electron and proton charge
Q_J	Joule dissipation
Q_v	viscous dissipation
Z	charge state
$r_{g,e,i}$	electron and ion gyro radius
S_{ij}	shear tensor
$T_{e,i}$	electron and proton temperature
t	time
u_{MHD}	MHD bulk speed
$V_{e,i}$	PIC average speed
$\mathbf{v}$	particle velocity
v_A	Alfvén speed
v_J	electric current drift speed
v_s	sound speed
v_{drive}	driving speed of boundary motion
$v_{th,e,i}$	electron and proton thermal speed

β	plasma beta
γ	adiabatic index or Lorentz factor
$\delta_{skin,e,i}$	electron and proton skin depth
Δs	cell size
Δt	time step in simulations
ΔL	current sheet thickness
ϵ_0	vacuum permittivity
η	resistivity
λ_D	Debye length
μ	mean molecular weight
μ_0	vacuum permeability
ν_{ij}	viscosity
ν_c	collision frequency
ν_{ei}	electron-ion collision frequency
ρ_m	mass density
ρ_q	charge density
σ	plasma conductivity
τ_{ij}	viscous stress tensor
Φ	angle between field lines on each side of the current sheet
$\omega_{c,e,i}$	electron and proton gyro frequency
$\omega_{p,e,i}$	electron and proton plasma frequency

Definitions and Equations (SI units)

$$c = \frac{1}{\sqrt{\epsilon_0 \cdot \mu_0}}$$

$$\rho_m = n_e m_e + n_i m_i$$

$$\rho_q = q_i n_i + q_e n_e$$

$$P_m = \frac{B^2}{2\mu_0}$$

$$P = n k_B T$$

$$= \frac{\rho_m k_B T}{\mu \, m_u}$$

$$= \rho_m R T$$

$$T = \frac{m \, v_{th}^2}{3 k_B}$$

$$\mathbf{j} = q_e n_e \mathbf{V_e} + q_i n_i \mathbf{V_i}$$

$$\beta = \frac{P}{P_m}$$

$$= \frac{2\mu_0 n k_B T}{B^2}$$

$$\lambda_{D,e} = \sqrt{\frac{\epsilon_0 k_B T_e}{n_e \cdot q_e^2}}$$

$$= \frac{v_{th,e}}{\omega_{pe}}$$

$$v_s = \sqrt{\gamma \cdot \frac{P}{\rho_m}}$$

$$= \sqrt{\gamma \cdot \frac{k_B T}{m}}$$

$$v_A = \frac{B}{\sqrt{\mu_0 \cdot \rho_m}}$$

$$\omega_{ce,ci} = \frac{q_{e,i} \cdot B}{m_{e,i}}$$

$$\omega_{pe,pi} = \sqrt{\frac{n_{e,i} \cdot q^2}{m_{e,i} \cdot \epsilon_0}}$$

$$\delta_{skin,e} = \frac{c}{\omega_{pe}}$$

$$= \sqrt{\frac{m_e \epsilon_0 c^2}{n_e q_e^2}}$$

$$= \sqrt{\frac{m_e}{\mu_0 n_e q_e^2}}$$

$$\text{(A.1)}$$

$$v_{th,e,i} = \sqrt{\frac{3k_B \cdot T_{e,i}}{m_{e,i}}}$$

$$\mathbf{v}_J = \frac{\nabla \times \mathbf{B}}{\mu_0 n_e q_e}$$

$$r_{g,e,i} = \frac{m_{e,i} \cdot v_\perp}{|q_{e,i} \cdot B|}$$

$$\approx \frac{v_{th,i}}{\omega_{ci}}$$

Maxwell equations

$$\nabla \times \mathbf{B} = \mu_0 \mathbf{j} + \mu_0 \epsilon_0 \frac{\partial \mathbf{E}}{\partial t}$$

$$\nabla \times \mathbf{E} = -\frac{\partial \mathbf{B}}{\partial t}$$

$$\nabla \cdot \mathbf{B} = 0$$

$$\nabla \cdot \mathbf{E} = \frac{\rho_q}{\epsilon_0}$$

B   APPENDIX: PUBLICATIONS

Article 1: Active region MHD experiment

3D Solar Null Point Reconnection MHD Simulations

G. Baumann[1] · K. Galsgaard[1] · Å. Nordlund[1]

Abstract Numerical MHD simulations of 3D reconnection events in the solar corona have improved enormously over the last few years, not only in resolution, but also in their complexity, enabling more and more realistic modeling. Various ways to obtain the initial magnetic field, different forms of solar atmospheric models as well as diverse driving speeds and patterns have been employed. This study considers differences between simulations with stratified and non-stratified solar atmospheres, addresses the influence of the driving speed on the plasma flow and energetics, and provides quantitative formulae for mapping electric fields and dissipation levels obtained in numerical simulations to the corresponding solar quantities. The simulations start out from a potential magnetic field containing a null-point, obtained from a Solar and Heliospheric Observatory (SOHO) magnetogram extrapolation approximately 8 hours before a C-class flare was observed. The magnetic field is stressed with a boundary motion pattern similar to — although simpler than — horizontal motions observed by SOHO during the period preceding the flare. The general behavior is nearly independent of the driving speed, and is also very similar in stratified and non-stratified models, provided only that the boundary motions are slow enough. The boundary motions cause a build-up of current sheets, mainly in the fan-plane of the magnetic null-point, but does not result in a flare-like energy release. We conclude that the most likely reason for the flare energy release was the additional flux emergence that occurred near the flare site.

Keywords: Sun — corona — magnetic reconnection — magnetic null-point

1. Introduction

There have been different attempts to initialize the magnetic field of the photosphere and corona for numerical simulations; amongst others by elimination of the complex observed small scale structure by the use of several photospheric magnetic monopole sources (Priest, Bungey, and Titov, 1997), by flux emergence experiments (Archontis *et al.*, 2004), as well as by extrapolation (e.g. Masson *et al.*, 2009) of solar observatory magnetograms, e.g. from SOHO. The latter type has typically been used together with potential extrapolations, for simplicity

---

[1] Niels Bohr Institute, Juliane Maries Vej 30, 2100
København Ø, Denmark email: gbaumann@nbi.ku.dk

reasons as well as due to the limited availability of vector magnetograms. As potential magnetic fields contain no free magnetic energy, these cannot directly be used for explaining how flare events take place and where the released energy arises from. Therefore, to use a potential magnetic field as the basis for an investigation of a flare event, the field must be stressed into a state where it contains sufficient free magnetic energy to account for the energy release event. There are different ways by which this may be accomplished. A simple approach is to impose boundary motions that resemble the ones derived from observations (Bingert and Peter, 2011; Gudiksen and Nordlund, 2002). An alternative, more challenging approach is to stress the system by allowing additional magnetic flux to enter through photospheric magnetic flux emergence (Fan and Gibson, 2003). In the solar context both of these process take place simultaneously, while experiments typically concentrate on a single type of stressing, in order to investigate in detail its influence on the dynamical evolution of the magnetic field.

The present investigation is an extension of the work done by Masson *et al.* (2009). They studied the evolution preceding a specific flare event observed with SOHO, starting by taking a magnetogram from about 8 hours before the flare and deriving a potential magnetic field. Due to the presence of a 'parasitic' magnetic polarity, the resulting magnetic field contains a magnetic null-point. From the motions of observed magnetic fragments a schematic photospheric velocity flow was constructed, and was used to stress this initially potential magnetic field. The imposed stress distorts the magnetic field, causing electric currents to build up in the vicinity of the magnetic null-point. The magnetic dissipation associated with the electric current allows a continuous reconnection to take place. The boundary driving together with the reconnection causes the null-point to move. The locations of the magnetic dissipation agree qualitatively with the locations of flare emission in various wavelength bands, which may be seen as evidence supporting a close association between reconnection at the magnetic null-point and the observed C-class flare.

The Masson *et al.* (2009) paper raises many interesting questions, some of which we attempt to answer in the present paper. We therefore let the same observations provide the basis for deriving a potential initial magnetic field, and employ the same imposed boundary stressing of the magnetic field, using the setup to investigate the impact of varying the amplitude of the driving speed, as well as the impact of allowing the experiment to take place in a gravitationally stratified setting.

The paper is organized as follows: In Section 2 we list the equations we solve, and briefly describe the numerical methods used to solve them. In Section 3 we give an overview of the different numerical experiments, in Section 4 we present and discuss the results, and finally in Section 5 we summarize the main results and conclusions.

2. Methods

The simulations have been performed using the fully 3D resistive and compressible *Stagger* MHD code (Nordlund and Galsgaard, 1997a).

The following form of the resistive MHD equations are solved in the code:

$$\frac{\partial \rho}{\partial t} = -\nabla \cdot (\rho \mathbf{u}) \tag{1}$$

$$\frac{\partial (\rho \mathbf{u})}{\partial t} = -\nabla \cdot (\rho \mathbf{u}\mathbf{u} + \underline{\underline{\tau}}) - \nabla p$$
$$+\mathbf{j} \times \mathbf{B} + \rho \mathbf{g} \tag{2}$$

$$\frac{\partial e}{\partial t} = -\nabla \cdot (e\mathbf{u} + \mathbf{f_e}) - p\nabla \cdot \mathbf{u}$$
$$+Q_J + Q_\nu \tag{3}$$

$$\frac{\partial \mathbf{B}}{\partial t} = -\nabla \times \mathbf{E} \tag{4}$$

$$\mathbf{j} = \nabla \times \mathbf{B} \tag{5}$$

$$\mathbf{E} = -\mathbf{u} \times \mathbf{B} + \eta \mathbf{j} \tag{6}$$

$$Q_J = \eta j^2 \tag{7}$$

$$\nabla \cdot \mathbf{B} = 0 \tag{8}$$

$$p = (\gamma - 1)e \tag{9}$$

$$\tau_{ij} = -\nu_{ij}\rho S_{ij} \tag{10}$$

$$S_{ij} = \frac{1}{2}\left(\frac{\partial u_i}{\partial x_j} + \frac{\partial u_j}{\partial x_i}\right) \tag{11}$$

$$Q_\nu = \rho \sum_{ij} \nu_{ij} S_{ij}^2 \tag{12}$$

$$\mathbf{f_e} = -\nu_e \rho \nabla (e/\rho) \tag{13}$$

where ρ is the mass density, $\mathbf{u}$ the bulk velocity, p the pressure, $\mathbf{j}$ the current density, $\mathbf{B}$ the magnetic field, g the acceleration of gravity, e the thermal energy per unit volume and η the resistivity. S_{ij} is the shear tensor, τ_{ij} the viscous stress tensor and $\mathbf{f_e}$ is a weak diffusive flux of thermal energy needed for numerical stability. The term Q_v represents viscous dissipation, turning kinetic energy into heat, while Q_J is the Joule dissipation, responsible for converting magnetic energy into heat.

The solution to the MHD equations is advanced in time using an explicit 3rd order predictor-corrector procedure (Hyman, 1979).

The version of the Stagger MHD code used here assumes an ideal gas law and includes no radiative cooling and heat conduction. The variables are located on different staggered grids, which allows for conservation of various quantities to machine precision. The staggering of variables has been chosen so $\nabla \cdot \mathbf{B}$ is among the quantities conserved to machine precision. Interpolation of variables between different staggered grids is handled by using 5th order interpolation. In a similar way spatial derivatives are computed using expressions accurate to 6th order. To minimize the influence of numerical diffusion dedicated operators are used for calculating both viscosity and resistivity. The viscosity is given by

$$\nu = \Delta d \left(\nu_1 c_f + \nu_2 |\mathbf{u}| + \nu_3 \Delta d \, |-\nabla \cdot \mathbf{u}|_+\right), \tag{14}$$

where Δd is the mesh size and $\nu_1 = 0.005 - 0.02$, $\nu_2 = 0.005 - 0.02$, and $\nu_3 = 0.2 - 0.4$ are dimensionless coefficients that provide a suitable amount of dissipation of fast mode waves (ν_1), advective motions (ν_2), and shocks (ν_3). The expression $|-\nabla \cdot \mathbf{u}|_+$ denotes the positive part of the rate of compression $-\nabla \cdot \mathbf{u}$. c_f is the fast mode speed defined by $c_f = \sqrt{(B^2 + \gamma p) \cdot \rho^{-1}}$.

The resulting grid Reynolds numbers, $\Delta d\, c_f / \nu$, are on the order of $50 - 200$ in regions with smooth variations, while in the neighborhood of shocks they are of the order of a few. The corresponding expression for the resistivity is

$$\eta = \Delta d \left(\nu_1 c_f + \nu_2 |\mathbf{u}| + \nu_3 \Delta d \,| - \nabla \cdot \mathbf{u}_\perp |_+ \right), \qquad (15)$$

where $\mathbf{u}_\perp$ is the component of the velocity perpendicular to $\mathbf{B}$, and where the expression scaled by ν_3 prevents electric current sheets from becoming numerically unresolved. The resulting magnetic grid Reynolds numbers are of the order a few in current sheets, as required to keep such structures marginally resolved.

The overall scaling with Δd ensures that advection patterns, waves, shocks and current sheets remain resolved by a few grids, independent of the mesh size.

The advantage of these three-part expressions for the viscosity and the resistivity, compared to having constant viscosity and resistivity is that constant values would have to be chosen on the order of the largest of these three term, in order to handle shocks and current sheets. In the rest of the volume the viscosity and resistivity would then be orders of magnitude larger than needed. As demonstrated in (Kritsuk *et al.*, 2011) the results are quite similar to state of the art codes that use local Riemann solvers. Such codes also have dissipative behavior on the scale of individual cells – no numerical code is 'ideal' in the sense that it presents solutions corresponding to zero resistivity.

In this article we refer to the $-\mathbf{u} \times \mathbf{B}$-term in the induction equation as the advective electric field, while its counterpart $\eta \mathbf{j}$ is referred to as the diffusive electric field.

3. Simulations

The experimental setup is inspired by the work by Masson *et al.* (2009). Our study sets out from a Fast Fourier Transform potential extrapolation applied to a level 1.8 SOHO/Michelson Doppler Imager magnetogram (Scherrer *et al.*, 1995) from November 16, 2002 at 06:27 UT, 8 hour prior to a C-class flare occurrence in the AR10191 active region. The extrapolation leads to a 3D magnetic null-point topology with a clear fan and spine structure (Green, 1989; Priest and Titov, 1996). In order to allow periodic boundary conditions in the potential field extrapolation we applied a windowing function to the SOHO cut-out of the active region AR10191, which decreases the field close to the boundary towards zero. This cut-out from the complete solar disk SOHO data differs slightly from the one used by Masson *et al.* (2009). As a result, in our case the null-point is initially located at a height of about 4 Mm above the magnetogram, while in their case the null-point is located at a height of only 1.5 Mm above the magnetogram. The change in null position places our null-point in the corona proper and allows

Table 1. Simulation runs. In the stratified runs min and max values are given in brackets. 'Boundary' refers to the plasma flow boundary condition at the lower boundary. Runs with a stratified atmosphere are denoted with an 'S', while 'O' stands for open boundary.

Run	boundary	max. driving [$\mathrm{km\,s^{-1}}$]	density [$\mathrm{cm^{-3}}$]	temperature [K]
1	closed	3.33	6.8×10^{12}	5.0×10^5
1O	open	3.33	6.8×10^{12}	5.0×10^5
2	closed	6.67	6.8×10^{12}	5.0×10^5
3	closed	10	6.8×10^{12}	5.0×10^5
4	closed	20	6.8×10^{12}	5.0×10^5
1S	closed	3.33	$[4.5 \times 10^{10},\ 9.1 \times 10^{15}]$	$[8000, 1 \times 10^6]$
3S	closed	10	$[4.5 \times 10^{10},\ 9.1 \times 10^{15}]$	$[8000, 1 \times 10^6]$
4S	closed	20	$[4.5 \times 10^{10},\ 9.1 \times 10^{15}]$	$[8000, 1 \times 10^6]$

us to perform affordable simulations with stratified atmospheres, while at the same time it does not influence the nature of the current sheet formation, and still successfully describes a typical solar-like magnetic field geometry.

Numerically, a magnetic field derived from a potential extrapolation is not necessarily divergence free, and we therefore initially apply a divergence cleaning procedure, which removes the divergence (as measured by our specific numerical stretched mesh derivative operators) by iteratively applying a correction obtained from solving the Poisson equation
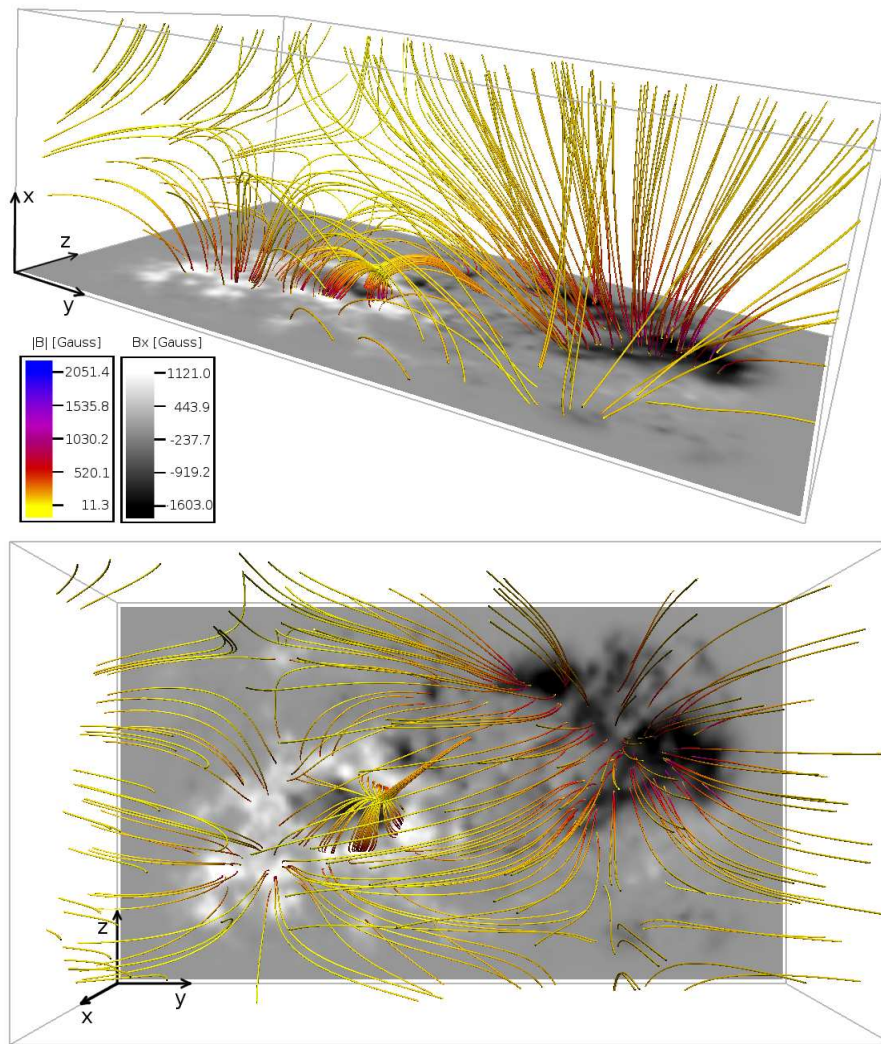
$$\Delta \delta \Phi = -\nabla \cdot \mathbf{B}. \qquad (16)$$

The structure of the resulting initial magnetic field is illustrated in Figure 1a and 1b, showing a strong overall magnetic field and a weaker fan-spine structure close to the photospheric boundary, which is separately illustrated in Figure 2. Note, that the field lines of the fan-spine topology were selected specifically to show the topology, and that the density of the field lines is therefore not representative of the magnetic flux density.
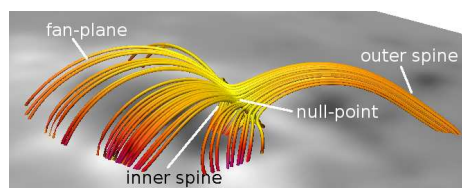
We performed two types of simulations; one type in which we imposed a 1-D gravitationally stratified atmosphere profile, and a second type with constant density and temperature. The density and temperature profiles are shown in Figure 3, and a summary of the simulation runs may be found in Table 1.

The magnetic fields are in all cases anchored at the vertical boundaries, which due to boundary conditions also prevent plasma from flowing in and out. The exception to this is run 1O, in which instead constant pressure is assumed at the lower boundary, and plasma flows through the boundary are allowed. Only minor differences were found between the open and closed boundary cases.
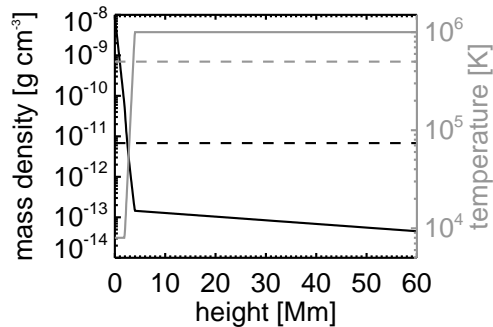
An imposed horizontal velocity field is introduced at the lower boundary of the computational box. This schematic velocity field is based on the motions of magnetic fragments observed by SOHO in the active region. These fragments

Figure 1. Magnetic field resulting from the FFT extrapolation of the SOHO magnetogram taken on November 16, 2002. The region shown here is the entire computational box, having an extent of $60 \times 175 \times 100 \, \text{Mm}$. The slice represents the vertical component of the magnetic field. Black is the negative polarity, white is positive.

Figure 2. Zoom in of Figure 1 (upper drawing) to the fan-spine topology, excluding the large scale field. The volume below the fan-plane is referred to as 'the dome'.

Figure 3. Mass densities are presented in black, temperatures in gray. The solid line shows the 1D mass density and temperature profiles as a function of height x [Mm] of all stratified runs. The dashed line illustrates the constant mass density and temperature of run 1, run 1O, run 2 run 3 and run 4.

outline the fast relative motions observed prior to the flare in the active region and correlate with the observed flux emergence process described by Masson *et al.* (2009). We used and implemented the description of the velocity pattern provided in this reference. In order not to produce initial transients the velocity field at the bottom boundary is slowly ramped up, over a period of about 100 s, by using a hyperbolic tangent function, and is afterwards kept constant. A variety of driving speeds have been employed, ranging from values similar to those used by Masson *et al.* (2009) to values about 6 times lower. We compare and discuss their influence in Section 4.

In general, it is important to keep the driver velocity well below the Alfvén velocity of the magnetic concentrations, because the magnetic structure and the plasma need to have enough time to adapt to the changing positions of the magnetic field lines at the boundary. Ideally, to allow gas pressure to equalize along magnetic fields, in response to compressions and expansions imposed by the boundary motions, the driver velocity should also be small compared to the sound speed in the coronal part of the model. This condition is generally fulfilled in all experiments, since the coronal sound speed is on the order of $100\,\mathrm{km\,s^{-1}}$, while our driving speeds are considerably smaller than that.

With these conditions we assure an almost force free state at all times in the simulation, which implies that the electric current is well aligned with the magnetic field. Nevertheless, the line-tied motions of magnetic field lines imposed by the lower boundary motions causes the creation of a current sheet in which magnetic reconnection takes place.

The maximal velocity of around $20\,\mathrm{km\,s^{-1}}$ that we applied exceeds the actual velocities measured in the active region by a factor of about 40, while it is at the same time clearly sub-Alfvénic. This speed up, which is similar to the one used by Masson *et al.* (2009), has the desirable effect that we can cover a larger solar time interval; a simulated time interval of 12 minutes then corresponds to 8 hours of real solar time. In our slowest cases (1S, 1, and 1O), the simulated time is more than an hour, and the driving speed ($3.33\,\mathrm{km\,s^{-1}}$) is approaching realistic solar values.

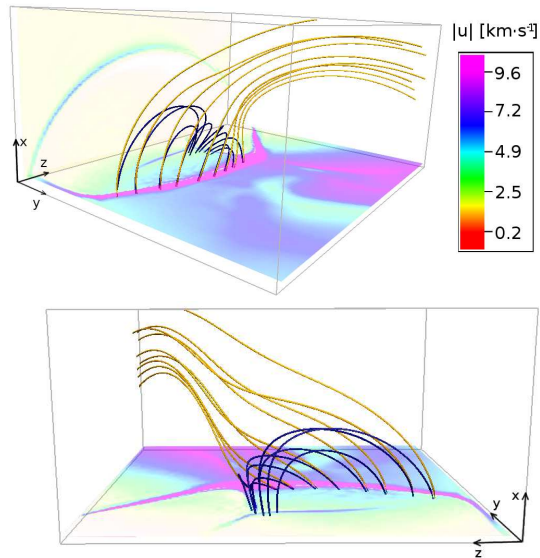**Figure 4.** Cell sizes in km for all three axis plotted against the grid indices. X is the height.

The simulated region has a size of $62 \times 175 \times 100 \,\mathrm{Mm}$, where our x axis points in the direction normal to the solar surface. The computational box is covered by a stretched grid of dimensions $320 \times 896 \times 512$, with a minimum cell size of $\approx 80 \,\mathrm{km}$ maintained in a relatively large region around the null-point. The grid size is smaller than 85 km over a $8 \,\mathrm{x} 50 \,\mathrm{x} 30 \,\mathrm{Mm}$ region, which includes the entire fan-plane and its intersection with the lower boundary. The distributions of cell sizes over grid indices are illustrated in Figure 4. In the initial setup, the null-point is located at height index x = 50.

4. Results and Discussions

As mentioned above, the field extrapolation based on the SOHO magnetogram leads to a fan-spine topology of the magnetic field, illustrated in Figure 2. This structure is surrounded by a stronger magnetic field, which extents to much larger heights into the corona. We concentrate in the present study on the small fan-spine structure, which forms as a consequence of a generally positive polarity in the active region AR10191 hosting a small ('parasitic') negative polarity region. The overlying magnetic field lines, including the ones forming the fan-plane, are anchored in the photosphere and build together with the spine a rather stable magnetic field structure, keeping the plasma from expanding into the upper corona.

We simulate the motion of magnetic field lines located between the large scale negative and positive polarity — hence outside the fan-spine structure — which on November 16, 2002 moved a large amount of magnetic flux towards the east side[1] (left hand side in Figure 1) of the dome, which we define as the volume confined by the fan-plane. This translational motion at the photospheric boundary is represented in our experiment by a boundary motion ('driver'), which is applied at the lower boundary of our computational box. The boundary motions lead to an eastward directed motion of the magnetic field lines outside

---

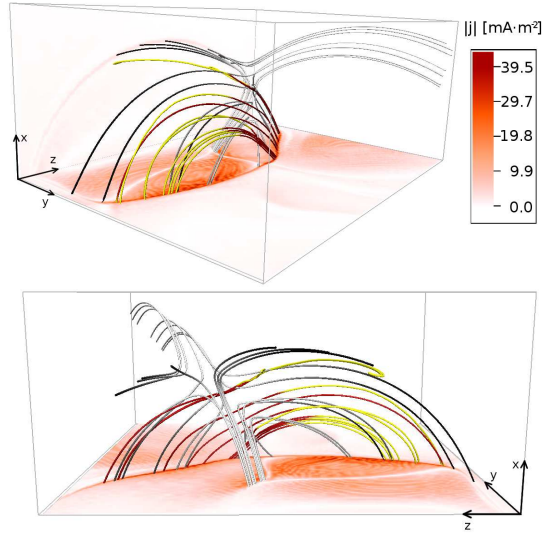[1]We use as reference system the solar coordinate system.

Figure 5. Magnetic field lines connecting to the inside (dark blue) and to the outside (orange) of the fan-plane. The bottom slice shows the bulk speed at a height of about 1.4 Mm. The snapshot is taken at a displacement D = 2.12 Mm in the experiment run 3. The box size is $10 \times 16 \times 22$ Mm.

the dome and to magnetic plasma being pushed against the west periphery of the fan-spine structure. Especially in the stratified case, a part of this flow extends upward along the magnetic field lines toward the neighborhood of the null-point and the outer spine.

The displacement of field lines, particularly outside of the fan-plane, introduces a misalignment between the inner and outer spine (see also Figure 2). Figure 5 shows the field line shear at a nominal 'boundary displacement' (simulation time times the amplitude of the average applied boundary velocity), D = 2.12 Mm after the start of run 3, which has a driving speed of about $10 \, \mathrm{km \, s^{-1}}$. Choosing the displacement instead of the simulation time has the advantage that at a given displacement, all runs have experienced about the same energy input from the work introduced by the boundary driving and are hence comparable. The angle ϕ, designating the difference of the direction between the inner magnetic field lines (in dark blue) and the outer magnetic field lines (in orange) with respect to the fan-plane, is still quite small. The quasi-transparent slices show the bulk speed, which is high just outside the fan-plane, where plasma is pushed up by the driver. Magnetic field lines closely approaching the null-point run just below this high bulk flow layer.

The applied photospheric driving motion indirectly moves the fan-plane foot points at the west side of the fan-spine structure, causing a slight shear between the inner and the outer field lines of the fan-plane to arise due to a different stress level of these two flux systems. The magnetic flux system inside the dome experiences a compression of about 5 times the surrounding gas pressure when the magnetic flux system west to the dome has moved towards it. This leads to
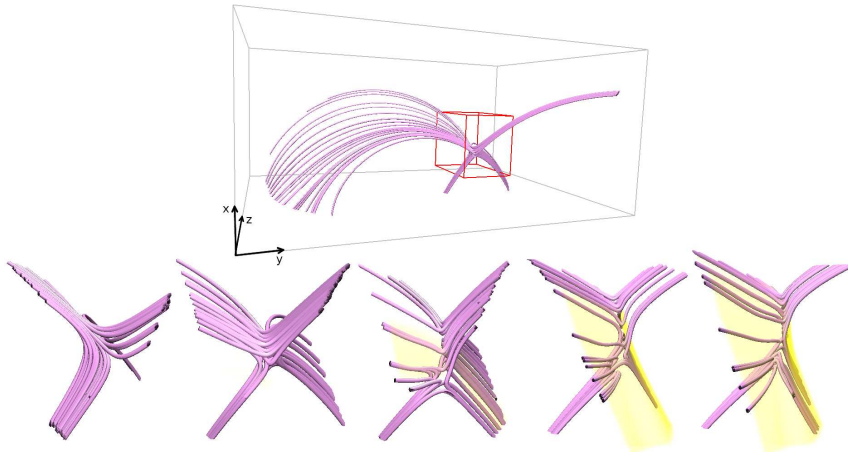
Figure 6. The electric current (red–yellow) flowing antiparallel to the magnetic field lines (black–gray). The color gradient along the streamlines indicates the flow direction (going from red to yellow) and the magnetic field orientation (going from black to gray). The slices show the electric current density of run 3. D = 2.66 Mm and the box size is $10 \times 16 \times 22$ Mm.

a large stress close to the null-point, on the east side of the outer spine, where the magnetic field as a consequence reconnects with the surrounding field in order to reach a lower energy state. A thin current sheet forms in the fan-plane, with the largest electric current densities occurring closest to the driver, where the shear of the field lines is largest. The magnitude of the electric current is lower in the neighborhood of the null-point. At the null-point itself the effect is to disrupt the structure of the null in such a way that the two spine axes move apart, as seen also in other single null investigations (Pontin, Bhattacharjee, and Galsgaard, 2007; Galsgaard and Pontin, 2011). Figure 6 shows the streamlines and direction of the highest electric current in run 3 at D = 2.66 Mm. We find that the electric current is mostly anti-parallel to the magnetic field lines in the fan-plane.

A partial outcome of the reconnection is seen in the motion of the inner spine, which is not being moved directly by the applied photospheric driver, but nevertheless moves at the photospheric level a significant absolute distance of about 4.5 Mm in the simulation, corresponding to a speed of about $4.7\,\mathrm{km\,s^{-1}}$. The motion is nearly linear in space and time. A second signature is the character of the displacement of the outer spine relative to the position of the inner spine.

The initial null-point area, connecting the inner and outer spine, stretches with increasing displacement into a 'weak field region', where the magnetic field strength is very low. This initiates an electric current that passes through the fan-plane, causing the ratio of the smallest to largest fan-eigenvalues to decrease (Parnell *et al.*, 1996). In this case the null almost adopts a 2D structure. This is illustrated in Figure 7. We discuss the relation of this inner and outer spine distance to the electric field at the end of section 4.1.
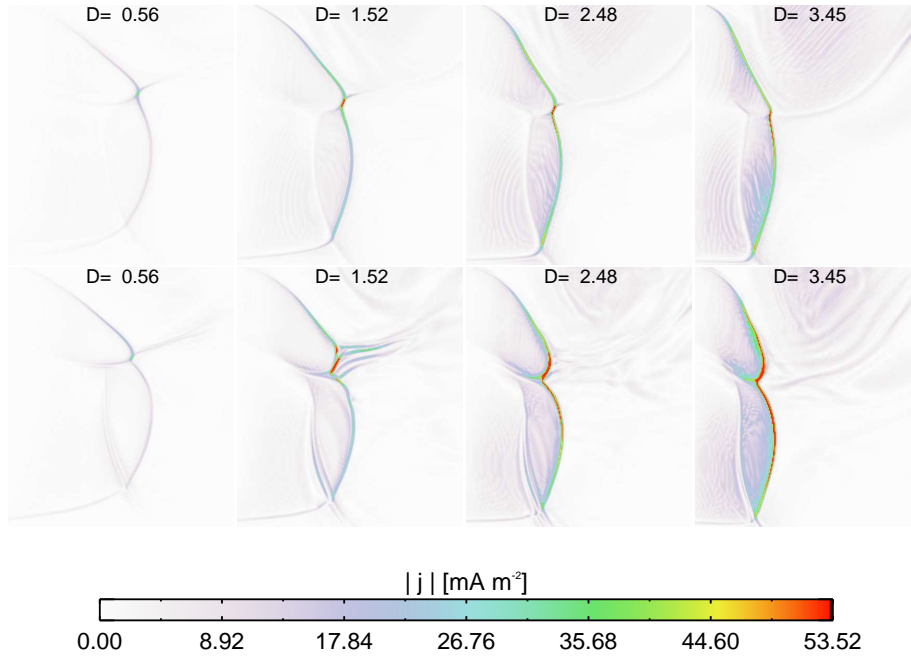
Figure 7. Relative motion of inner and outer spine for run 3. The top panel shows the cutout region for D = 0.02 Mm and the lower panel shows approximately the same selected region for D = 0.02, 0.52, 1.05, 1.59, 2.12 Mm. The yellow volume shows the highest electric current density, which is located in the fan-plane.
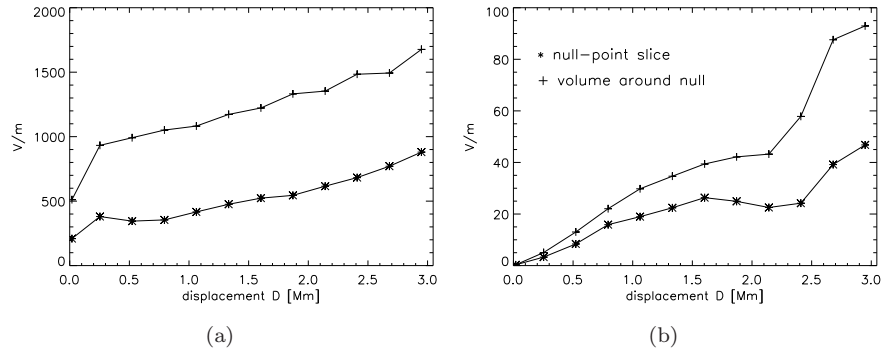
4.1. Time evolution of the diffusive electric field

The diffusive part of the electric field ($\eta\mathbf{j}$) included in the induction equation is responsible for both changing the magnetic field topology and for transforming magnetic energy into Joule dissipation in the MHD picture. In the Sun the diffusive electric field component parallel to the magnetic field is responsible for particle acceleration (Arzner and Vlahos, 2006). It is therefore of particular interest to see how this field evolves with the boundary displacement, and to find out where it concentrates and how large values it reaches. Figure 8 illustrates the electric current accumulation in the fan-plane and along the spine axes of the magnetic null. This behavior is representative for all stratified and non-stratified runs. In the code the resistivity is not a simple constant, as specified by Equation 14, allowing diffusion to be locally increased where dissipation is needed to keep structures from becoming unresolved, while at the same time allowing a minimal amount of diffusion in regions where the magnetic field is smooth. Images of the diffusive electric field are therefore not exact replicas of images of the electric current, but since the resistivity is generally near its largest value in current sheets there is a close correspondence.

The diffusive electric field is found to be concentrated in the fan-plane and to have its local peak in the region where the fan-spine intersection is distorted. However, large values occur over a significant fraction of the fan-plane, as is the case for the electric current density. It is only the parallel diffusive electric field that gives rise to both magnetic reconnection and particle acceleration and its magnitude indicates how violent these processes can be (Schindler, Hesse, and Birn, 1988). In our simulations the advective electric field ($-\mathbf{u} \times \mathbf{B}$), associated with the bulk plasma motion in the fan-plane and along the spine axis is much stronger (Figure 9a) than its diffusive counterpart, but since it is perpendicular

Figure 8. Current density in y-z slice for constant density run 4 (upper row) and stratified atmosphere run 4S (lower row) at a height of x = 3.22 Mm and different displacements D.

to the magnetic field this component causes no magnetic dissipation, and cannot be associated with particle acceleration.
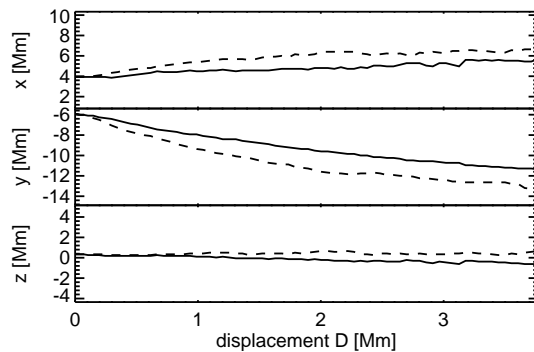

(a)   (b)

Figure 9. Maximum advective electric field (a) and average diffusive electric field calculated over those grid points, at which the electric field amplitude is within 10 percent of the maximum field in a slice of 2 grid cells thickness (b) of the cutout region at the respective height of the null-point (*) and in the total cutout region $10 \times 16 \times 22$ Mm around the null-point, including the fan-plane (+) in run 3.

When determining the values of the diffusive electric field one finds that the peak values in the vicinity of the null-point are increasing with growing displacement (see Figure 9b), going from initially zero to on the order of $50\,\mathrm{V\,m^{-1}}$, while in the fan-plane the diffusive electric field reaches more than $90\,\mathrm{V\,m^{-1}}$ at D = $2.92\,\mathrm{Mm}$. However, as shown below (cf. Equation 22), to estimate the analogous solar electric field, the simulation value should be reduced with a factor equal to the square root of the factor (about 20 for run 3) by which the boundary driving is exaggerated; here we obtain $E \approx 90/\sqrt{20}$, or about $20\,\mathrm{V\,m^{-1}}$. Considering our more benign conditions, this is consistent with Pudovkin *et al.* (1998), who find typical electric fields to be of the order of $100 - 300\,\mathrm{V\,m^{-1}}$ under flaring conditions. Electrons accelerated along the entire current sheet, with an extent of about $15\,\mathrm{Mm}$ (see Figure 6), could nevertheless gain energies of up to about $300\,\mathrm{MeV}$ in our case. Of interest is also the shape of the average diffusive electric field increase in the vicinity of the null-point, plotted in Figure 9b as a (*)-line. Its progression shows an almost identical behavior as a plot of the increasing distance between the inner and outer spine (see Figure 7) plotted against the displacement (plot not presented here).

4.2. Comparison of stratified and non-stratified simulations

Since the null-point is an essential node of the magnetic skeleton, we use it as a reference point for our investigation of the influence of the density profile on the temporal changes of the magnetic field. Here we compare simulation run 4S, which has a stratified atmosphere, with simulation run 4, which has a constant chromosphere-like density and temperature atmosphere (see, Table 1). Figure 10 shows the position of the null-point, connecting the fan-plane and spine magnetic field lines, in all three directions versus the boundary displacement D. In the

Figure 10. Null-point position in Mm in the coordinate system of the experiment. The vertical coordinate is x, and the two horizontal coordinates are y and z. The solid line shows the constant density run 4, while the dashed line represents the stratified run 4S.

stratified case the very dense plasma (9×10^{15} cm^{-3}) at the bottom of the box gives rise to a low Alfvén speed ($v_A = B/\sqrt{\mu_0 \rho_m}$), meaning that the higher density impedes the propagation of the boundary disturbance into the box. But once the disturbances reach beyond the transition region the ambient density

has fallen drastically, and the dense plasma from the lower atmosphere starts spreading out faster and pushes the null-point up. The velocity gradient induced by the large density change causes strong dissipation and in some regions a disruption into multiple smaller current sheets, which can also be seen in the electric current density comparison in Figure 8, showing $|\mathbf{j}|$ for runs 4 and 4S.

In the non-stratified runs the amount of plasma that moves upwards along the magnetic field lines into the corona and contributes to pushing the null-point upwards is much reduced, as seen in Figure 10.

For all runs we find a significant null-point motion (about 1–2 Mm in x, 6 Mm in y and 1 Mm in z) due to the applied driving motion on the bottom boundary, which is comparable to the relative motion of the inner spine.

4.3. The influence of boundary conditions

The driver of the magnetic field evolution is the boundary motion. The magnetic field displacements imposed by the boundary motions have a large influence on the spatial structure of the magnetic skeleton, consisting of null-points, separatrix surfaces (such as the fan-plane), separators, sources and flux domains (e.g. Parnell, Haynes, and Galsgaard, 2008, and references therein). The skeleton itself is a very robust structure, which does not change from a topological point of view, but the detailed appearance of it changes with boundary displacement, as already shown by the analysis of the null-point motion.
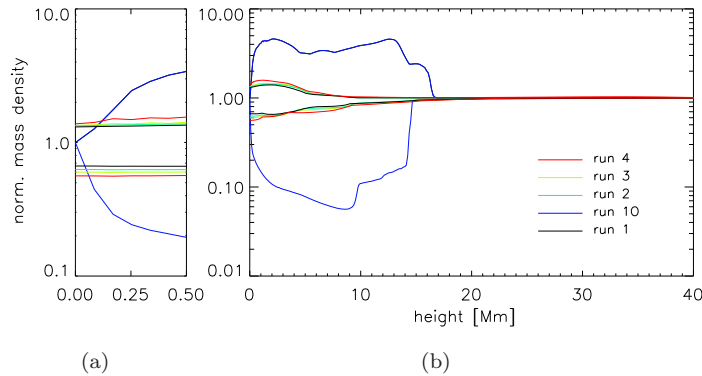
In Figure 11b we compare the density profiles of the closed runs 1, 2, 3 and 4 and the open boundary run 1O. The figure shows that all non-stratified closed flow boundary runs develop a similar density profile: A certain expansion or compression of a region connected to the closed boundary leads to the same density profile, regardless of the driving speed.

The initial sound speed is about $83\,\mathrm{km\,s^{-1}}$ for the non-stratified runs, while being much lower—on the order of $10\,\mathrm{km\,s^{-1}}$—in the lower parts of the stratified runs. The sound speed influences among other things the in- and outflows at open boundaries.

Figure 11a illustrates that the closed boundary conditions influence particularly the lowest density layer, where regions with low and high density build up and cannot be emptied nor filled by plasma out- and inflow. This is not very important for the dynamics of the system, but is also not very solar-like. In the open case, there is a continuous mass exchange and pressure equalization at the boundaries, in which case it is crucial that the sound speed is well above the driving speed, so that the system has time to approach pressure balance.

The low sound speed in the stratified case poses a very tight restriction on the driving speed, in order to avoid exaggerating the effects of inertia. On the other hand there is a clear advantage of having stratification: it provides a pool of mass for the corona to communicate with; the large amount of mass at low temperature acts as a buffer, due to the low Alfvén and sound speed.

Overall, Figure 11b confirms that the density contrast is mainly caused by volume changes, which arise from the imposed boundary motions. If these volume changes happen sufficiently slowly relative to the Alfvén and sound speed, the driving speed loses its importance for the results (but not for the computational cost of obtaining them!).

Figure 11. Density profile min and max over each slice in height for the closed non-stratified simulations, normalized to the asymptote: run 1, run 2, run 3 and run 4 and the open non-s-tratified run 1O. (a) is a zoom in of the first 0.5 Mm of plot (b). The displacement of each run is taken to be from the snapshot closest to D = 1.02 Mm.

4.4. Energy dissipation

Magnetic energy brought into the system by photospheric driving cannot only move the system into another potential state but can also be stored on top of the evolving potential configuration, in case that the integrated dissipation rate cannot compensate for the work done on the system that goes into non-potential energy.
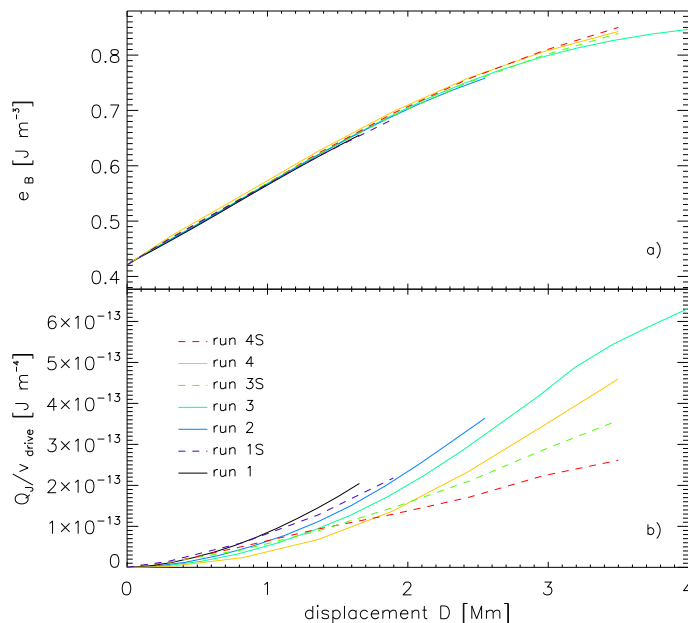
The rate of change of magnetic energy density $e_B = B^2/2$ is described by Equation 17. A change of electromagnetic energy can be caused by a divergence of the Poynting flux F_P, a conversion into bulk kinetic energy by the Lorentz work W_L, or by conversion to heat through Joule dissipation Q_J.

$$\frac{\partial e_B}{\partial t} = -\nabla \cdot (F_P) - W_L - Q_J. \tag{17}$$

The Lorentz work is defined by $W_L = -\mathbf{u} \cdot (\mathbf{j} \times \mathbf{B})$. Joule dissipation, $Q_J = \mathbf{E}_\eta \cdot \mathbf{j} = \eta \mathbf{j}^2$, primarily takes place in the strong current sheets. Electric currents flow mainly along the magnetic field in the corona and therefore Q_J is a suitable indicator for locations at which a significant component of the electric field parallel to the magnetic field may form. This parallel electric field can accelerate charged particles along the magnetic field lines, resulting e.g. in the brightening of flare ribbons.

The evolutions of the magnetic energy and the Joule dissipation normalized to the average driving speed are summarized in a plot covering several simulation runs in Figure 12. The first thing to notice is that the evolution of the magnetic energy, when expressed in terms of the boundary displacement D, is practically identical in all of the runs. The reason for this is that most of the boundary work goes directly into increasing the potential magnetic energy, while only a small amount goes into free magnetic energy. From Figure 12b is seen that the dissipation increases with increasing displacement. This shows that an increasing amount of free energy becomes available through the build up of current
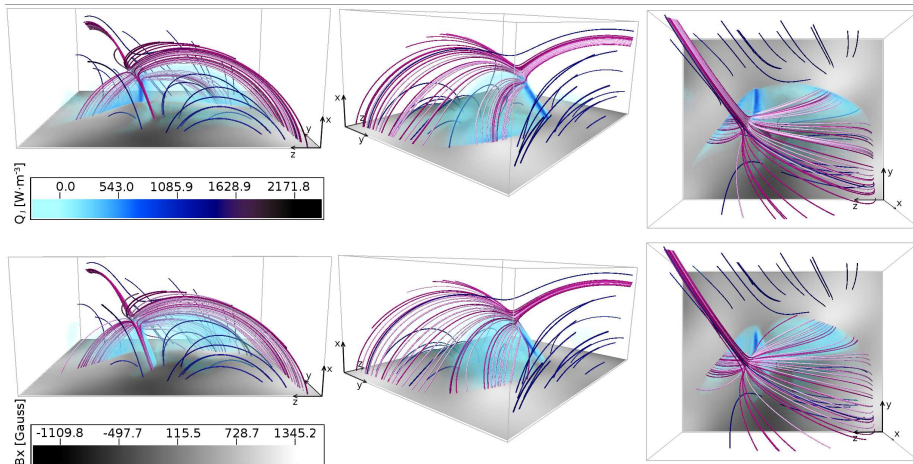
Figure 12. Comparison of the average magnetic energy a) and average magnetic dissipation normalized by the average boundary driving speed of each run b) for constant density runs (solid lines) and stratified runs (dashed lines) in the cutout of approximate size 10 x 16 x 22 Mm.

structures in the null-point fan-plane as the experiment progresses. The small amount of dissipation also hints that the total free energy in the system is small in comparison to the change of energy in the changed potential magnetic field.

The normalization of the magnetic dissipation by average driving speed employed in Figure 12b brings the curves showing the evolution of magnetic dissipation for all the different runs together into a relatively tight set of parallel relations. This illustrates that, to lowest order, the rate of magnetic dissipation, at any given value of the displacement, is proportional to the driving velocity and to the rate of boundary displacement.

The dissipation curves corresponding to the different experiments follow the same general trend, although with some differences, in particular between the stratified and non-stratified cases. The dissipation is generally higher for the stratified cases than for the non-stratified runs during early times and lower during late times. The exception is run 1S, the run with the lowest driving speed, which agrees closely with the non-stratified cases with the slowest driving speed.

The deviations from this common asymptotic behavior are likely consequences of the low Alfvén speeds in the dense layers of the stratified models, causing the dissipation in the stratified runs to be initially high due to their higher densities at low heights compared to the constant density cases. Later, when the motions

Figure 13. The highest joule dissipation of run 1 in the top row and run 1S in the lower row is shown as a semitransparent volume rendering at about D = 0.82 Mm. The box size is $10 \times 16 \times 22$ Mm. The field lines represent magnetic field lines passing closest to the null point (purple), in the close surrounding of the null-point (magenta) and the overlying strong magnetic field (dark blue). The slice on the lower boundary shows the bx magnetic field component.

introduced by the driver reach greater heights, where the mass density is lower than in the constant density runs, the stratified runs generally display a lower dissipation.

We note in this context also that the viscous dissipation in the system is much smaller than the Joule dissipation, as is expected in a coronal environment.

The results summarized in Figure 12 illustrate that for a quantitatively accurate estimate of properties related to the magnetic dissipation it is essential to drive in a way which is compatible with the ordering of characteristic speeds in the Sun; i.e., to keep the boundary speed smaller than the Alfvén speed, and to scale the quantities down in proportion to the speed-up factor used in the driving.

For the non-stratified runs we compute initial Alfvén speeds of $70 - 1400 \, \mathrm{km \, s^{-1}}$ at the lower boundary, which is clearly higher than the driving speed of all runs. So we expect, as is also shown by Figure 12, a similar dissipation increase with increasing displacement, after some initial differences due to the driving speed differences.

In the stratified atmosphere runs the Alfvén speed increases with height. At the lower boundary the initial Alfvén speed is approximately $5 - 200 \, \mathrm{km \, s^{-1}}$, where the minimum value falls below the driving speed used in runs 3S and 4S. Run 1S is just at the edge of being driven slower than the minimum Alfvén speed and indeed gives results which are similar to the non-stratified case run 1. Figure 13 shows that the stratified and non-stratified cases are nevertheless distinguishable. The volume renderings show the Joule dissipation normalized by the driving speed, for run 1 (upper panel) and run 1S (lower panel). The locations of the dissipation maxima agree nicely, but the dissipation maxima differ by a factor of about 1.8, being higher in the stratified run 1S.

In summary, we find that the ratio of the driving speed to the Alfvén speed has a noticeable impact on the dissipation level and, as Figure 12 illustrates, that the stratified simulations tend to display a progressive growth of deviations from the common asymptotic relations defined by the non-stratified runs, unless the driving speed is small compared to both the local Alfvén speed and the sound speed.

However, these are relatively small deviations, compared to the lowest order effect, which is a proportionality of the magnetic dissipation and the driving speed. The reason for this proportionality lies in the scaling behavior of dissipation in current sheets, which is explored in the next subsection.

4.5. Scaling of magnetic dissipation in the current sheet

As illustrated by Figure 5, the magnetic field line orientations on the two sides of the fan-plane only differ by a small amount. This means that the electric current carried by the current sheet, whose thickness (on the order of a few grid cells in the present numerical model) we denote with Δs, is much less than the maximal electric current density $2B/\Delta s$ that would result from a complete reversal of the magnetic field orientation across the current sheet. The electric current density in the current sheet (CS) is in fact on the order of

$$j_{\mathrm{CS}} \sim \Delta B\ \Delta s^{-1} \approx sin(\phi)B_{\mathrm{CS}}\Delta s^{-1} \approx \phi B_{\mathrm{CS}}\Delta s^{-1}, \qquad (18)$$

for small ϕ, where B_{CS} is a typical strength of the magnetic field just outside the current sheet, and ϕ is an angle characterizing the difference of direction of field lines on the two sides of the current sheet.

A fundamental question is now how the total dissipation in the current sheet, and hence the average rate of reconnection in the structure, depends on factors such as the numerical resolution and rate of work done at the boundary. By construction the code keeps current sheets just barely resolved. A change in numerical resolution is thus directly mapped into a proportional change of the current sheet thickness Δs. This behavior is obtained by making η essentially proportional to the grid size (cf. Equation 15). To a first order approximation both B_{CS} and ϕ are independent of Δs. By Equation 18 the electric current density is inversely proportional to Δs, and the magnetic dissipation rate per unit volume Q_J therefore scales as

$$Q_{\mathrm{CS}} = \eta j_{CS}^2 \sim \Delta B^2 \Delta s^{-1} = \phi^2 B_{CS}^2 \Delta s^{-1}. \qquad (19)$$

To obtain the total dissipation in the current sheet this needs to be multiplied with the volume of the current sheet,

$$V_{\mathrm{CS}} \sim A_{\mathrm{CS}}\Delta s. \qquad (20)$$

where we denote by A_{CS} the total area of the current sheet. We thus conclude that the total dissipation is

$$Q_{\mathrm{CS}}V_{\mathrm{CS}} \sim \Delta B^2 A_{\mathrm{CS}}, \qquad (21)$$

and hence is, to lowest order, *independent of* Δs and the resistivity in the current sheet. Note that, as a consequence of ϕ being small, reconnection in the current sheet can proceed without requiring super-Alfvénic outflow velocities from the current sheet.

Estimating now the diffusive electric field in the current sheet we find that it scales as

$$E_{\rm CS} = \eta_{\rm CS} j_{\rm CS} \propto \Delta B = \phi B_{\rm CS}, \qquad (22)$$

again independent of Δs, but proportional to the change of magnetic field direction across the current sheet and hence proportional to ϕ.

Generally the work done by the boundary must go into an increase in magnetic energy (potential plus free magnetic energy), or into kinetic energy or ohmic dissipation. In the present case the magnetic dissipation is able to keep up with the free energy input, and the system essentially goes through a series of equilibrium states. As Figure 12 shows, the total magnetic energy only depends on the displacement and not on the driving speed itself, while the dissipation is essentially proportional to how fast we drive at the boundary, thus $Q_{\rm CS} \propto v$ (Equation 19) and hence $v \propto \phi^2$. So we conclude with the help of Equation 22 that the magnitude of the parallel electric field along the current sheet is essentially proportional to the square-root of the driving speed,

$$E_{\rm CS} \propto \phi \propto v^{1/2}. \qquad (23)$$

This dissipation-driving speed relation is not an artifact of the chosen numerical method; the scaling of η with Δs is generic to all numerical methods, and serves to ensure that higher numerical resolution can be used to reach larger magnetic Reynolds and Lundquist numbers.

With much higher rates of stressing, or with much higher numerical resolution, the current sheet may need to fragment and enter a turbulent regime, in order to support the required amounts of dissipation and reconnection in the face of increasing constraints by the thinness of the current sheets. This is a process that is by now well understood to be able to take over when the need arises (Galsgaard and Nordlund, 1996; Nordlund and Galsgaard, 1997b; Gudiksen and Nordlund, 2005; Berger and Asgari-Targhi, 2009; Bingert and Peter, 2011; Ng, Lin, and Bhattacharjee, 2011; Pontin, 2011).

We thus conclude that, provided that conditions that apply equally to both numerical simulations and the Sun are fulfilled, neither the total magnetic dissipation in a current sheet structure, nor the diffusive part of the electric field depend, to lowest order, on the electrical resistivity—or for that matter on the precise mechanism that sets the level of the electrical resistivity.

4.6. Triggering of rapid energy release

As in Masson *et al.* (2009) there is no significant and sudden relaxation of the system, with an energy release that could correspond to a flare, even though the simulations cover enough solar time to get across the observed flaring event. Looking at the potential part of the magnetic field at different displacement

steps in the simulations, we find steadily increasing magnetic potential energies, and most of the build-up of magnetic energy seen in the experiment actually goes into increasing the potential rather than the non-potential part of the magnetic energy. As discussed above, the magnetic dissipation is able to keep up with varying levels of boundary work, with a residual amount of free energy scaling approximately linearly with the driving speed. The stress in the system is demonstrably moderate, even with our exaggerated driving speed, and we therefore cannot expect boundary motions of the type applied here to be able to explain violent events similar to the observed solar flare.

We consider three possibilities for this difference in behavior between these MHD simulations and the Sun:

i) The limited resolution of the numerical experiment is preventing an instability from occurring that would otherwise trigger a flare-like event

ii) A flare-like event would occur if taking into account kinetic effects (e.g. by using particle-in-cell simulations)

iii) A flare-like event could take place, with MHD alone, but would require for instance an additional flux emergence event in addition to the slow and systematic boundary motion implemented here and in Masson *et al.* (2009)

As demonstrated above, numerical resolution does not to a first order determine the level of dissipation in current sheets, once they are reasonably well resolved. Indeed, by the arguments in the preceding subsection we expect the level of stress (as measured for example by the angle ϕ) caused by the type of motions we employ in the current investigation to be *smaller* in the Sun (by a factor of e.g. $\approx \sqrt{7} \approx 2.5$ relative to our runs 1, 1O and 1S, and it is thus very unlikely that the flare was triggered by accumulation of stress from this type of boundary motion.

An MHD-instability could in principle occur at a later point in time than to where our runs go; but as demonstrated by our experiments even a driving speed that is highly exaggerated relative to the solar value is not able to build up sufficient free energy to account for a C-class flare: The maximum *total* magnetic energy in the entire simulated domain of our experiment is on the order of 2×10^{30} ergs, of which only a very small fraction is free energy. Estimates of C-flare emission are larger than even our potential energy (Kretzschmar, 2011), and hence the free energy available in our model is not sufficient to power a C-class flare. As discussed above, the level of stress is expected to be essentially proportional to the driving speed, and is expected to be largely independent of the level of resistivity, and hence it is unlikely that more stress would build up in the Sun than in these numerical simulations.

Figure 14, which is representative of all runs, illustrates that the rate of change of magnetic energy increases in the beginning, as a result of the work done by the lower boundary. This energy input looses efficiency as the angle between the field lines and the driving boundary approaches 90 degrees. Additionally, since the driving pattern location is fixed, the applied stress becomes less and less efficient, as the flux in this particular region is gradually removed. The dissipation is small compared to the rate of change of magnetic energy, implying that the dissipated free energy only makes up a tiny fraction compared to the

Figure 14. The average rate of change of magnetic energy for run 3 is plotted as a solid line, and the dissipation divided by the average driving speed is shown as a dashed line. Both are restricted to the cutout of approximate size 10 x 16 x 22 Mm used previously

potential energy. This is in agreement with Figure 5, which illustrates that the shear of the magnetic field lines in the current sheet is not very large, even with our exaggerated driving speed. Hence the reconnection is rapid enough to keep the boundary work at a given displacement at an approximately constant level, and to keep the system in a near potential state. We are thus far away from an instability to occur and it is improbable to achieve one at a later point of the experiment.

By similar arguments kinetic effects are not expected to have a major influence on the macroscopic dissipation behavior and reconnection rate. This is consistent with the findings by Birn *et al.* (2005), which show that the same amounts of energy release take place for the same type of reconnection event, independent of the dissipation mechanism. It also shows that there are only small differences in the time scales of the event going from MHD to PIC simulations. These results are entirely consistent with the current sheet scaling arguments presented above, since they hold true independent of the nature of the dissipation mechanism.

We thus conclude that additional external forcing, such as the additional flux emergence mentioned in the third alternative above, is the most likely explanation for the observed solar flare. This conclusion is consistent with the fact that all observational evidence associates flaring either with new flux emergence, or with magnetic configurations that evolve into states that are decidedly MHD-unstable; i.e., ones in which lower energy states become accessible and where dissipative effects make it possible to reach those lower energy states and dynamic instabilities therefore develop. In such dynamic events both of the above two points are still true; things are really kinetic on a small scale, but evolve essentially according to MHD on large scales.

5. Conclusions

The main topic of the presented work is a study of the influence of the driving speed for stratified and non-stratified atmosphere models used to simulate 3D reconnection events in the solar corona. The major findings are:

- Sufficiently low driving speeds lead to similar plasma behavior, including similar evolution of the magnetic energy density and the Joule dissipation (after compensating for the expected effects of the different driving speeds).
- The magnetic dissipation and the diffusive electric field — capable of accelerating charged particles — are both, to lowest order, independent of the plasma resistivity, and hence depend only weakly on the grid resolution in numerical experiments.
- When driving is taking place sufficiently slowly the rate of magnetic dissipation increases linearly with the boundary driving speed while the diffusive electric field increases as the square root of the driving speed.
- The driving speed has a larger impact on the general plasma behavior in the cases with stratified atmospheres, while its influence is minor for non-stratified runs with closed flow boundary conditions, if compared at the same boundary motion displacements.
- The sound speed compared to the driving speed determines the exchange of plasma at the boundaries. Voids can be filled in open boundary runs, while pressure differences at the boundary are carried along in the closed boundary cases. This is not an issue in the stratified runs, due to the large reservoirs of relatively cold gas in the vicinity of the lower boundary. On the other hand the lower information speeds there set severe restrictions on the driving speed.

Our investigations suggest that the applied driver is unlikely to be able to provide a flare-like energy release in the simulations (as well as in the Sun). In fact, based on a comparison of the available free energy in our model with estimates from observations of C-class flares we anticipate that additional magnetic flux emergence served as the triggering mechanism of the observed sudden energy release in the C-class flare that occurred here.

References

Archontis, V., Moreno-Insertis, F., Galsgaard, K., Hood, A., O'Shea, E.: 2004, Emergence of magnetic flux from the convection zone into the corona. *Astron. Astrophys.* **426**, 1047 – 1063. doi:10.1051/0004-6361:20035934.

Arzner, K., Vlahos, L.: 2006, Gyrokinetic electron acceleration in the force-free corona with anomalous resistivity. *Astron. Astrophys.* **454**, 957 – 967. doi:10.1051/0004-6361:20064953.

Berger, M.A., Asgari-Targhi, M.: 2009, Self-organized Braiding and the Structure of Coronal Loops. *Astrophys. J.* **705**, 347 – 355. doi:10.1088/0004-637X/705/1/347.

Bingert, S., Peter, H.: 2011, Intermittent heating in the solar corona employing a 3D MHD model. *Astron. Astrophys.* **530**, A112. doi:10.1051/0004-6361/201016019.

Birn, J., Galsgaard, K., Hesse, M., Hoshino, M., Huba, J., Lapenta, G., Pritchett, P.L., Schindler, K., Yin, L., Büchner, J., Neukirch, T., Priest, E.R.: 2005, Forced magnetic reconnection. *Geophys. Res. Lett.* **32**, 6105. doi:10.1029/2004GL022058.

Fan, Y., Gibson, S.E.: 2003, The Emergence of a Twisted Magnetic Flux Tube into a Preexisting Coronal Arcade. *Astrophys. J. Lett.* **589**, L105 – L108. doi:10.1086/375834.

Galsgaard, K., Nordlund, Å.: 1996, Heating and activity of the solar corona 1. Boundary shearing of an initially homogeneous magnetic field. *J. Geophys. Res.* **101**, 13445 – 13460. doi:10.1029/96JA00428.

Galsgaard, K., Pontin, D.I.: 2011, Steady state reconnection at a single 3D magnetic null point. *Astron. Astrophys.* **529**, A20. doi:10.1051/0004-6361/201014359.

Green, J.M.: 1989, Geometrical properties of 3d reconnecting magnetic fields with nulls. *J. Geophys. Res.* **93**, 8583.

Gudiksen, B.V., Nordlund, Å.: 2002, Bulk Heating and Slender Magnetic Loops in the Solar Corona. *Astrophys. J. Lett.* **572**, L113 – L116. doi:10.1086/341600.

Gudiksen, B.V., Nordlund, Å.: 2005, An Ab Initio Approach to the Solar Coronal Heating Problem. *Astrophys. J.* **618**, 1020 – 1030. doi:10.1086/426063.

Hyman, J.M.: 1979, A method of lines approach to the numerical solution of conservation laws. In: *Advances in Computer Methods for Partial Differential Equations - III*, 313 – 321.

Kretzschmar, M.: 2011, The Sun as a star: observations of white-light flares. *Astron. Astrophys.* **530**, A84. doi:10.1051/0004-6361/201015930.

Kritsuk, A.G., Nordlund, Å., Collins, D., Padoan, P., Norman, M.L., Abel, T., Banerjee, R., Federrath, C., Flock, M., Lee, D., Li, P.S., Müller, W.-C., Teyssier, R., Ustyugov, S.D., Vogel, C., Xu, H.: 2011, Comparing Numerical Methods for Isothermal Magnetized Supersonic Turbulence. *Astrophys. J.* **737**, 13. doi:10.1088/0004-637X/737/1/13.

Masson, S., Pariat, E., Aulanier, G., Schrijver, C.J.: 2009, The Nature of Flare Ribbons in Coronal Null-Point Topology. *Astrophys. J.* **700**, 559 – 578. doi:10.1088/0004-637X/700/1/559.

Ng, C.S., Lin, L., Bhattacharjee, A.: 2011, High-Lundquist Number Scaling in Three-Dimensional Simulations of Parker's Model of Coronal Heating. *ArXiv e-prints*.

Nordlund, A., Galsgaard, K.: 1997a, A 3D MHD code for Parallel Computers. Technical report, Niels Bohr Institute.

Nordlund, A., Galsgaard, K.: 1997b, Topologically Forced Reconnection. In: Simnett, G.M., Alissandrakis, C.E., Vlahos, L. (eds.) *European Meeting on Solar Physics*, *Lecture Notes in Physics, Berlin Springer Verlag* **489**, 179. doi:10.1007/BFb0105676.

Parnell, C.E., Haynes, A.L., Galsgaard, K.: 2008, Recursive Reconnection and Magnetic Skeletons. *Astrophys. J.* **675**, 1656 – 1665. doi:10.1086/527532.

Parnell, C.E., Smith, J.M., Neukirch, T., Priest, E.R.: 1996, The structure of three-dimensional magnetic neutral points. *Physics of Plasmas* **3**, 759 – 770. doi:10.1063/1.871810.

Pontin, D.I.: 2011, Three-dimensional magnetic reconnection regimes: A review. *Advances in Space Research* **47**, 1508 – 1522. doi:10.1016/j.asr.2010.12.022.

Pontin, D.I., Bhattacharjee, A., Galsgaard, K.: 2007, Current sheet formation and nonideal behavior at three-dimensional magnetic null points. *Physics of Plasmas* **14**(5), 052106. doi:10.1063/1.2722300.

Priest, E.R., Titov, V.S.: 1996, Magnetic Reconnection at Three-Dimensional Null Points. *Royal Society of London Philosophical Transactions Series A* **354**, 2951 – 2992. doi:10.1098/rsta.1996.0136.

Priest, E.R., Bungey, T.N., Titov, V.S.: 1997, The 3D topology and interaction of complex magnetic flux systems. *Geophysical and Astrophysical Fluid Dynamics* **84**, 127 – 163. doi:10.1080/03091929708208976.

Pudovkin, M.I., Zaitseva, S.A., Shumilov, N.O., Meister, C.-V.: 1998, Large-Scale Electric Fields in Solar Flare Regions. *Solar Phys.* **178**, 125 – 136.
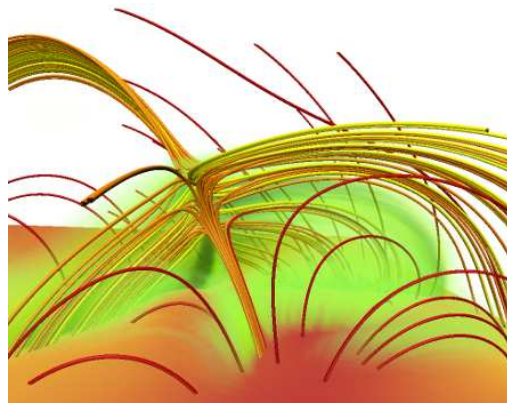
Scherrer, P.H., Bogart, R.S., Bush, R.I., Hoeksema, J.T., Kosovichev, A.G., Schou, J., Rosen-
berg, W., Springer, L., Tarbell, T.D., Title, A., Wolfson, C.J., Zayer, I., MDI Engineering
Team: 1995, The Solar Oscillations Investigation - Michelson Doppler Imager. *Solar Phys.*
162, 129 – 188. doi:10.1007/BF00733429.

Schindler, K., Hesse, M., Birn, J.: 1988, General magnetic reconnection, parallel electric fields,
and helicity. *J. Geophys. Res.* **93**, 5547 – 5557. doi:10.1029/JA093iA06p05547.

Particle Dynamics

in Solar Coronal Magnetic Reconnection Regions

by Gisela Baumann

A thesis submitted for the degree of Doctor of Philosophy in natural science

Niels Bohr Institute, University of Copenhagen
&
Theoretische Physik I, Ruhr-Universität Bochum

The PhD School of Science, Faculty of Science, University of Copenhagen, Denmark

May 2012

Contents

List of Figures

List of Tables

ACKNOWLEDGMENTS

Abstract

Numerous multiscale eruptions and flux emergence events on its surface define the every day activity of the Sun. Investigations of these events are observationally limited due to the state-of-art of today's instruments and the perspicuous lack of in-situ observations in the close proximity of the solar surface. However, numerical simulations provide a sandbox for theoretical studies of the underlying physical processes of such events, the results and consequences of which may be compared to constraints given by spectral observations, to the amount of total released energy, or to the size and time scales of structures.

The theory specifying the solar plasma motion fairly accurately is a combination of a fluid description, representing the conductive behavior, and electromagnetism, affecting charged particles. The resulting global theory is called magnetohydrodynamics (MHD), which is a macroscopic description of a plasma. In order to investigate particle kinetics, a microscopic particle tracing method is needed to describe the motion of single particles (unlike the bulk motion used in MHD) in a self-consistent electromagnetic field. One numerical kinetic approach is the use of Particle-In-Cell simulations (PIC). The numerical plasma description of MHD and PIC methods are joined in the presented research, introducing one of the first models successfully interconnecting microscopic and macroscopic scales. For this purpose microscopic plasma parameters are modified to run a kinetic simulation based on a dataset from an MHD simulation. Although this technique is still in the early stages and the heavy numerical constraints limit the parameter choices, it marks the birth of a promising new numerical tool for investigations of systems covering a vast range of scales.

Most of the energy released through particle eruptions originates from the process of magnetic reconnection, which transforms magnetic energy into charged particle acceleration, bulk flow and heat. There is an entire zoo of solar eruption phenomena triggered by magnetic reconnection, among which the best known ones are solar jets, solar flares and coronal mass ejections (CMEs). The present studies focus on the acceleration mechanism of particles in 3D reconnection regions of an active region in a pre-flare phase, and on a coronal hole region producing a solar jet. In both cases the acceleration happens on account of a systematic, slowly evolving ('DC') electric field, which builds up at the electric current sheet that separates two different magnetic connectivity domains. Such electric fields are a consequence of magnetic reconnection, and are shown here to be able to persist, even under collionless conditions, since particles remain in the accelerating electric field only for a limited time, being gradually replaced by new particles, which also need to be accelerated. The relatively small fraction of highly accelerated particles is not able to completely short-circuit the electric field through a polarization electric field. The acceleration results in a power law distribution of non-thermal particles, with a dN/dE power law index of about -1.6 ro -1.8, extending in the numerical simulations only to a few tens of keV. We speculate that the DC electric field acceleration in the Sun is responsible for the part of the energy distribution extending to a few hundred keV, while stochastic particle acceleration is a likely candidate for acceleration particles with a steeper power law index, extending to hundreds of Mev for electrons and to the Gev range for ions.

1 OBJECTIVES

What accelerates electrons in the solar corona to non-thermal energies?
Where are they primarily accelerated?

How can micro- and macroscopic scales of the Sun be unified into one
consistent numerical model?
And what are the physical consequences of such an interlocked formulation?

One of the main questions addressed over and over again in solar physics research is the coronal heating problem; why does the systematic decrease in temperature from the solar interior out to the solar surface suddenly change into a rapid temperature increase in the solar corona? The most plausible explanation is nowadays believed to be magnetic reconnection, which may be described as a restructuring of magnetic field during which magnetic energy is transferred into kinetic energy and heat. Magnetic reconnection (in the course of this dissertation simply called reconnection) may be locally efficient, but globally seen the volume affected by a single reconnection event is microscopic, compared to the extent of the Sun. This deficiency is thought to be compensated by the abundance of reconnection events taking place in the solar atmosphere.

Detecting reconnection events in the solar atmosphere is a tremendous challenge for observers, not only due to their tiny dimensions, much smaller than the spatial resolution of current instruments, but also as a result of the requirements on the sensitivity of the instruments, which are exceptional for phenomena taking place in this very tenuous environment. However, the large scale behavior of the plasma at the surface of the Sun as well as large scale emission spectra, as a result of particle acceleration, can be obtained more or less directly from observations.

Numerical simulations, on the other hand, offer a unique playground to train our understanding and expectations of what should be seen by the instruments directed to the Sun — both on large scales, on the order of Mm (1 Mm = 1000 km), as well as on small scales of the size of a reconnection region. Yet this method does not come without its challenge. The main reason, which has so far prevented a direct comparison with observational results, is a consequence of reconnection being a multi-scale process; the global reconnection event locations are determined by the large scale magnetic field, while the actual process of energy transfer into heat and particle acceleration takes

place on microscopic/kinetic scales. Macroscopic scales are accurately described by magnetohydrodynamics (MHD), while microscopic plasma behavior is well reproduced by kinetic simulations, such as particle-in-cell simulations (PIC). Hardly any attempt to combine these two model descriptions exists, although we know that during reconnection energy exchange takes place over a large range of length scales and supposedly provides the key to understanding the particle acceleration mechanism associated with several of the observed eruptive phenomena on the Sun.

The objectives of this dissertation is therefore to investigate the dynamics of fully three dimensional reconnection regions, and to study their associated particle acceleration mechanism, by interconnecting MHD and PIC computer models.

The thesis is structured in the following way: The first two chapters provide general background knowledge. Chapter 2 contains an introduction to the research field (coronal environment, 3D reconnection and acceleration mechanisms). Chapter 3 describes the numerical implementation of solar corona simulations — its restrictions and constraints. The following two chapters 4 and 5 provide an overview of the results from two solar simulation experiments, one from an active region prior to an observed flare occurrence and one from an open magnetic field coronal hole region. Chapter 4 builds on the articles Baumann, Galsgaard, and Nordlund (2012) and Baumann, Haugbølle, and Nordlund (2012), while Chapter 5 relates to Baumann and Nordlund (2012). In these Chapters I also provide additional material not included in the articles which can be found in the appendix. The appendix further contains a list of the kinetic plasma equations and fundamental numerical values. Finally I draw conclusions and summarize the perspectives for future research in Chapter 6.

2 SOLAR ATMOSPHERIC ENVIRONMENT

2.1 Overview of the Sun

The Sun is a giant ball of gas, with a diameter of 1.4 million km (1400 Mm), emitting each day a vast amount of energetic particles into its surroundings. The energetic particles carry some of the energy originally produced in its interior into the interplanetary medium. Depending on its level of activity, the energy released from the Sun during a solar flare event, lasting from only a few seconds up to minutes, can be as high as 10^{25} Joule. This amount of released energy is comparable to the *yearly* average heat flow from the interior of the Earth (Kanamori, 1978). The main two sources for energetic particles are *solar flares* and *coronal mass ejections* (CMEs), which accelerate electrons from 10 keV (1.6×10^{-15} J) up to at least 100 MeV (1.6×10^{-11} J) (Aschwanden, 1999).

Reconnection is thought to be a fundamental process in these solar plasma energy releases taking place in the solar atmosphere. The solar atmosphere consists of the photosphere (the 'surface' of the Sun), the chromosphere and the corona, sketched in Figure 2.1. The photosphere lies on top of the turbulent convection zone, in which magnetic flux tubes rise buoyantly until they encounter the cool photosphere. Further out lies the chromosphere which is hotter and more tenuous and is partially ionized. Finally follows — via a thin transition region where the temperature rises sharply — the highly ionized corona, with thermal speeds of about 4000 km/s. The corona is the focus of this thesis.

Particle eruptions from reconnection regions in the optically thin corona happen as so-called *free magnetic energy*, stored on top of the *potential energy* (which is the lowest energy state of the magnetic field for a given photospheric boundary condition) is released. Free magnetic energy is generated for example by twisting and shearing motions at the photospheric boundary, which reorder the magnetic field lines. Drivers of this dynamics of photospheric sources are the motions of convection cells, which also cause magnetic flux emergence from the photosphere into the corona and thus create active regions consisting of groups of sunspots. Particles are most efficiently accelerated in regions with high temperatures and low densities, such as in the corona above solar active regions.

The magnetic field strength varies from several thousand Gauss below the solar surface to a few Gauss in the corona (away from active regions). Despite the high magnetic field strength in lower layers, it is the immense gas pressure that dominates the plasma motion in these regions. Looking at the plasma beta β (ratio of gas pressure and magnetic pressure), β is generally larger than unity below the solar surface and changes to values below one at the photosphere, decreasing rapidly in the chromospheric layer. The magnetic field strength varies

Figure 2.1: The atmospheric layers of the Sun (not to scale)

over several orders of magnitude at any one height, depending on the horizontal location. In active regions the magnetic field reaches up to a few thousand Gauss, while the background field is estimated to be a few tens of Gauss. The corona shows mainly two characteristic magnetic field topologies; zones where both 'ends' of the magnetic field lines are attached to the Sun and zones where field lines reach far out into space, interacting with the interplanetary magnetic field before returning to the opposite polarity at the Sun. Locally the latter type seems to be field lines of a magnetic monopole, hence 'open'. Such field lines are predominantly found in polar regions and are a typical feature of 'coronal holes'. From open field line regions fast solar wind constantly emerges, featuring velocities of $400 - 800 \, \mathrm{km \, s^{-1}}$, while closed magnetic field line regions produce a slower solar wind, with velocities on the order of $200 - 400 \, \mathrm{km \, s^{-1}}$.

2.2 3D Reconnection

The basic concept of 3D reconnection in connection with solar eruptions has been introduced by Giovanelli (1946), who pointed out the likely existence of neutral points in the chromosphere. Reconnection is a process that restructures the magnetic field and converts stored magnetic energy into kinetic energy (particle acceleration), bulk flow and heat, with the purpose of transferring the system into a lower energy state.

Reconnection is fundamentally different in 2D and 3D. One of the most significant differences between these two cases is that 3D reconnection can occur in entire volumes (called *diffusion regions*) and does not require that the magnetic field vanishes at a so-called X-type null-point, in contrast to 2D reconnection. Studies of 3D reconnection have changed the understanding and definition of reconnection. It is now defined as a non-ideal process in which

$$\mathbf{B} \times (\nabla \times \mathbf{R}) \neq 0, \tag{2.1}$$

4

where **B** is the magnetic field and **R** symbolizes the violation term of the ideal Ohm's law (Schindler, Hesse, and Birn, 1988), which contains all possible contributions from the Hall effect, the Petersen effect, as well as normal and anomalous resistivity. Schindler, Hesse, and Birn (1988) describe this requirement as 'breakdown of magnetic connection due to a localized non-idealness'. Magnetic connection had been defined many years before by Newcomb (1958), who called it the necessary and sufficient condition for magnetic field line-preservation. Equation (2.1) states that reconnection occurs if field lines do not follow the plasma. Note that this is a weaker constraint than flux conservation, as shown in Kulsrud (2005). Equivalent to Equation (2.1) Hesse and Schindler (1988) define reconnection as

$$\int E_\parallel ds \neq 0, \tag{2.2}$$

where $E_\parallel$ is the parallel electric field component with respect to the magnetic field direction. In reconnection regions the electric field is hence no longer zero in the frame co-moving with the plasma, but there is a local electric field present. Locally the plasma is said to be non-ideal, which implies that the frozen-in flux theorem is no longer valid. The reconnection rate, which describes how violent a reconnection process is, is directly deduced from the reconnection definition as the maximum value of the integral over the parallel electric field along a magnetic field line (Hesse, Forbes, and Birn, 2005). $E_\parallel$ is of high importance for the acceleration of particles. It can arise for example from instabilities in the reconnection region, which set in as a result of flows that lead to a thinning of the current sheet, which consequently goes unstable. Such a process could for instance be triggered by shearing of photospheric magnetic field lines or by magnetic flux emergence from below the photosphere.

Another difference between 2D and 3D reconnection is the types of instabilities that are possible. 2D instabilities can suddenly get overwhelmed by 3D instabilities in a 3D experiment (e.g. Dahlburg and Einaudi, 2002).

For these reasons I focus in the course of this thesis on 3D reconnection, which is still heavily under investigation, while the 2D case is more well established.

Reconnection is happening over an immense range of different scales; the large scales, on the order of tens of Mm, which can be described by magnetohydrodynamics (MHD), determine the overall magnetic field structure and thus the locations of reconnection. At the small, kinetic scales, on the order of mm to cm, the mechanism of particle acceleration and energy transfer is specified. Numerically this latter scale may be represented by particle-in-cell (PIC) simulations. Thin, unstable current sheets with typical thicknesses on the order of kinetic scales may then provide important sites of reconnection.

Numerical studies of reconnection have shown that there are mainly three different reconnection scenarios possible in 3D: non-null reconnection, null-point reconnection and separator reconnection (Pontin, 2011). In the first paper of this thesis (Baumann, Galsgaard, and Nordlund, 2012), referred to as active region experiment, reconnection takes place in the vicinity of a magnetic null-point. The general geometry is sketched in Figure 2.2. Such null-points are part of the magnetic skeleton, which also includes the spine and fan-plane (Priest and Titov, 1996a). The spine passes through the null-point, where the fan-plane separates the two connectivity domains. The fan-plane is therefore also called a separatrix surface. Spine- and fan-reconnection are defined according to

5

Figure 2.2: Magnetic 3D reconnection null-point topology

where a current builds up during reconnection; in spine-reconnection a current is present in the spine, while fan-reconnection shows a current in the fan-plane. The orientation of the fan and spine is defined by the eigenvectors of ∇B_{null}, where B_{null} can be estimated to lowest order using a Taylor expansion at the null-point

$$B_{null} = B_{Jacobi}(\mathbf{s_0} - \mathbf{s}) \tag{2.3}$$

where B_{Jacobi} is the Jacobi matrix of the magnetic field at the null-point s_0. In case that the eigenvalues of the fan-plane are equal the field lines in the fan-plane are isotropically distributed, while unequal eigenvalues results in an anisotropy of the field lines, which concentrate towards the eigenvector with the largest eigenvalue. A summary of the different types of 3D null-points can be found in Parnell *et al.* (1996).

In case that a magnetic skeleton experiences for instance shearing, a current can build up either in the fan-plane or along the spine. If the current forms along the spine the field lines in the fan-plane form spirals and the fan and spine are inclined towards each other by 90 degrees. If a current is present in the fan-plane the inclination will no longer be 90 degrees (Birn and Priest, 2007, pg. 63 – 64). Combinations of these two cases are possible as well. In the active region experiment of this thesis the fan current dominates and therefore the spine and the fan surface are not orthogonal to each other.

2.2.1   Observational Signatures of Reconnection

As the magnetic field in the solar corona is weak compared to the photosphere, direct measurements of the coronal magnetic field are generally difficult. One possibility to extract information is by conducting extrapolations of the magnetic field of the photosphere into the corona. The photospheric magnetic field is usually measured by making use of the Zeemann effect. The longitudinal Zeeman effect can be turned directly into images of the component of the magnetic field along the line of sight by using circular polarization filters, and by utilizing in addition the linear polarization caused by the transverse Zeeman effect one can create vector magnetograms. In order to carry out a magnetic field extrapolation one needs to first make an assumption of what magnetic field one expects in this particular environment; e.g. a current free (potential) or a force free magnetic field.

The lack of exact measurements makes it difficult to confront observations directly with concepts from the theory of magnetic reconnection, such as magnetic null-points or magnetic separatrices. Hence there are also no direct observations of reconnection. The reason is the small scales of the dissipation regions as well as the low densities that are making emissions very weak and hence difficult to detect (van Driel-Gesztelyi, 2009). However, applying the previously mentioned extrapolation techniques it became apparent from the resulting magnetic field topologies that magnetic null-points are abundant in the solar corona (e.g. Régnier, Parnell, and Haynes, 2008; Longcope and Parnell, 2009). There are also various indirect evidences of reconnection, as associated processes leave direct footprints on its environment that can be observed; e.g. hot loop top emissions (Masuda *et al.*, 1994), the separation of flare ribbons (Wang *et al.*, 2003), outflow shocks and bi-directional jets (Wang, Sui, and Qiu, 2007), radio type III bursts (Manoharan *et al.*, 1996), plasmoid and plasma blob eruptions (Ohyama and Shibata, 1998; Kumar *et al.*, 2012), among numerous others (cf. van Driel-Gesztelyi (2003)).

2.3   Resistivity and Collisions in Solar Plasmas

The global coronal magnetic field is mostly force-free and well frozen into the plasma. But locally resistivity—or analogous processes leading to magnetic dissipation—must be present, since it is a requirement for reconnection to happen. Resistivity is indirectly also linked to particle acceleration, as it allows parallel electric fields to develop during the reconnection process.

Resistivity in plasmas is mainly representing particle collisions, or more precisely collisions between electrons (e) and ions (i), because the collision frequency and the cross-section for such collisions is highest, as mentioned for example by Boyd and Sanderson (2003, p.316):

$$\nu_{ei} \sim Z\nu_{ee} \gg \nu_{ii} \gg \nu_{ie}, \tag{2.4}$$

where ν are the collision frequencies and Z is the charge state (equals unity for ionized hydrogen). In a fully ionized plasma, completely dominated by Coulomb collisions, the electric resistivity, defined as the reciprocal of the conductivity σ, is the *Spitzer resistivity*.

The corona is close to being fully ionized, so the mean molecular weight μ is often assumed to be ≈ 0.6 (differing from 0.5 because of the presence of helium and heavier elements). In such a plasma the particles interact primarily via Coulomb fields (and only little via collisions with neutrals), which leads to a majority experiencing small angle scatterings. As the electron-ion collision frequency ν_{ei} goes as the particle density n_e and the electron temperature $T_e^{-3/2}$, a hot rare plasma like the corona is almost collisionless, since the collision frequency is much smaller than the plasma frequency. However, electric resistivity and hence magnetic diffusion may nevertheless occur, since there are other mechanisms than Coulomb collisions that may generate non-ideality. Anomalous resistivity is one candidate (or candidate group). Anomalous resistivity is a result of kinetic instabilities, for example in turbulent current sheets. The resistivity is then a locally variable quantity, generally depending on the local current density (Birn and Priest, 2007, p.144). But there is still little known

about this type of plasma behavior and more numerical kinetic simulations are required. However, anomalous resistivity goes beyond the scope of this thesis.

2.4 Particle Acceleration

2.4.1 Basic Equations of Particle Acceleration

The relativistic equation of motion for a charged particle in an electric field $\mathbf{E}$, a magnetic field $\mathbf{B}$, and a gravitational field giving rise to a force of gravity $\mathbf{g}$ may be written as

$$m\frac{d(\gamma\mathbf{v})}{dt} = \mathbf{g} + q(\mathbf{E} + \mathbf{v} \times \mathbf{B}), \tag{2.5}$$

where $\frac{d\mathbf{x}}{dt} = \mathbf{v}$ is the particle velocity, m its mass and γ is the Lorentz factor. Since the effect of gravity is negligible small in the solar corona over time scales of a few seconds it can be ignored for this discussion of sources of particle acceleration. The acceleration must hence be caused by the electric field $\mathbf{E}$ or the Lorentz force $\mathbf{v} \times \mathbf{B}$. To look at the kinetic energy gain of a particle with time, we take the scalar product of Equation (2.5) with $\mathbf{v}$ and receive

$$m\gamma \cdot \frac{d}{dt}(v^2) = q\mathbf{v}\mathbf{E} + \mathbf{v} \cdot (\mathbf{v} \times \mathbf{B}), \tag{2.6}$$

where the second term is zero, since $\mathbf{v} \cdot (\mathbf{v} \times \mathbf{B}) = \mathbf{B} \cdot (\mathbf{v} \times \mathbf{v})$. So we are left with

$$m\gamma \cdot \frac{d}{dt}(v^2) = q\mathbf{v}\mathbf{E} \tag{2.7}$$

which reveals that a charged particle gains (or loses) energy only if its velocity has a component along the electric field. So the amount of acceleration of a particle depends on the strength of the electric field and the angle between $\mathbf{v}$ and $\mathbf{E}$. In a magnetic field, a particle undergoes a circular motion, perpendicular to $\mathbf{B}$, called the gyro motion. The radius of the gyration is known as the gyro radius or Larmor radius and is defined by

$$r_g = \frac{v_\perp}{\omega_c} \approx \frac{v_{th}}{\omega_c} \tag{2.8}$$

where ω_c is the gyro frequency of a particle around $\mathbf{B}$, $v_\perp$ is the particle velocity component perpendicular to the magnetic field and v_{th} represents the thermal speed. A force along the magnetic field can thus accelerate particles without any interaction with the gyro motion of the particle and is thus most efficient. Hence the $E_\parallel$ is the major accelerator of particles in plasmas.

Next I give a short overview over the different sources of electric fields in the corona.

2.4.2 Particle Acceleration Mechanisms and Observational Constraints

It is widely accepted that reconnection is where particle acceleration events have their roots - both in solar flares (active region experiment) and in X-ray jets (coronal hole experiment). But besides DC electric fields, turbulence and shocks

may also contribute their share to the acceleration of particles in reconnection regions.

The energy build-up phase of the pre-eruptive fields is a process that takes many hours or even days, while the actual eruption happens on time scales of seconds or minutes. The build-up phase is likely a phase where the system is in quasi-static equilibrium, with free magnetic energy either growing or, alternatively, coming closer and closer to a state where it can be released. It is during the release phase that particle acceleration becomes most apparent, but in principle some (much lower) level of particle acceleration may take place also during the build-up phase.

With respect to particle acceleration during eruptive solar events there are several observational constraints that need to be incorporated. Here are some of the most important ones:

- Energy releases during the most powerful solar flares are on the order of 10^{25} J (10^{32} erg) (Woods, Kopp, and Chamberlin, 2006). X-ray jets show energy releases on the order of 10^{20}–10^{22} J (Shimojo and Shibata, 2000).

- Electrons are accelerated up to at least $100\,\text{MeV}$ (Aschwanden, 1999) in solar flares.

- Electron acceleration happens on time scales on the order of seconds or tens of seconds (Aschwanden, 1999) in flares and on the order of minutes in coronal jet events (Filippov, Golub, and Koutchmy, 2009).

- The electron energy distribution features a power-law above thermal energies (Kane and Anderson, 1970), sometimes it shows a broken power-law.

- The energy release often happens in sub-steps and not continuously and on time scales much shorter than that for energy injection into the corona (Aschwanden, 2002). In the case of X-ray jets, this shows up as recurring events (Chifor *et al.*, 2008).

- The impact locations of non-thermal electrons in a certain magnetic field geometry are mainly revealed by hard X-ray observations, as non-thermal particles impact dense plasma regions and radiate hard X-rays through bremsstrahlung (thick target model (Brown, 1971; Brown *et al.*, 2009)).

- The spectral index in flare events evolves according to the soft-hard-soft rule, by Parks and Winckler (1969); Kane and Anderson (1970)

A possible acceleration mechanism of particles in reconnection regions is based on large-scale DC electric fields. Particles are, at the same time as they feel the force by the electric field, also subjected to collisions with ambient particles. Dreicer (1960) defined a critical electric field value E_D, the so-called Dreicer field, for which the force resulting from the electric field and the frictional force balance. The Dreicer field is typically around $10^{-2}\,\text{V m}^{-1}$ (Anastasiadis, 2002) in the solar corona and provides a reference point for distinction between 'weak' and 'strong' electric fields.

If the frictional force is smaller than the acceleration force the associated electric field is called a super-Dreicer electric field and has $E > E_D$. Retaining

only the acceleration and collision terms the equation of motion for an electron in an external electric field may be rewritten as (Zharkova *et al.*, 2011)

$$\frac{d\mathbf{v}}{dt} = \frac{q\mathbf{E}}{m_e} - \nu_c \mathbf{v}, \tag{2.9}$$

where ν_c is the collision frequency. As previously mentioned, the electron ion collisions dominate the collision frequency, so that $\nu_c \approx \nu_{ei}$. And since ν_{ei} is $\propto v^{-3}$, this leads to

$$m_e \frac{d\mathbf{v}}{dt} = q \left(\mathbf{E} - \mathbf{E_D} \left[\frac{v_{th,e}}{v} \right]^2 \right), \tag{2.10}$$

where $v_{th,e}$ is the electron thermal speed. Litvinenko (1996) applied this case to a simple magnetic configuration of a current sheet.

On the other hand in the sub-Dreicer regime, where $E < E_D$, only the particles in the thermal velocity distribution with $v > \sqrt{\frac{E_D}{E}} \cdot v_{th,e}$ experience a velocity increase, which then reduces the electric drag force further and thus leads to electrons being accelerated freely out of the thermal distribution. This process is known as *runaway acceleration*. Particles with velocities smaller than $\sqrt{\frac{E_D}{E}} \cdot v_{th,e}$ are slowed down and remain part of the thermal velocity distribution function. In the marginal super-Dreicer case the critical velocity is at the thermal speed, meaning that all electrons with speed higher than the thermal speed are accelerated.

Although sub-Dreicer electric fields, applied to solar eruptions (e.g. Holman, 1985), can in principal explain the velocity distribution of non-thermal particles, the major problem with considering this acceleration source as the main particle accelerator in solar eruptive events is the large spatial scales required to reach the observed energy gain, which has not found support in observations.

Super-Dreicer fields are discussed in Litvinenko (1996). They are believed to be more realistic when considering particle acceleration in powerful solar eruptions.

There are two other models, which do not rely on large-scale electric fields, but in which acceleration takes place due to small scale electric fields in shocks and turbulent regions. Shocks are often seen in connection with reconnection of magnetic field lines, but it is still not known what part they play in the particle acceleration. The underlying process of shock acceleration are the first- and second-order Fermi shock acceleration mechanism (Fermi, 1949). An important constraint of shock acceleration models is the requirement for turbulence or plasma waves, which serve as a tool to get a repetitive passage of particles through the shock front. Shock acceleration in solar flares has been studied by among others Cargill (1991).

The other particle acceleration model to be considered is stochastic particle acceleration, reviewed by Miller *et al.* (1997). In general stochastic processes utilize the fact that particles gain energy in average over a certain period of time during which they are exposed to several acceleration/deacceleration sites in a turbulent environment. A frequently discussed stochastic acceleration mechanism is due to wave-particle interaction, where one idea is to use the resonance between the particles gyro radius and the wave frequency (Miller *et al.*, 1997), where the time it takes a particle to make one gyro orbit is equal to the period

of a wave. The accumulated particle energy is taken from the turbulent energy pool, which thus decreases with time if not replenished. For an overview of the different acceleration mechanism, see Miller (2000).

It is likely that in reality DC electric fields, turbulence and shocks are simultaneously present in reconnection regions, and contribute in different ways to the overall picture. Different acceleration mechanisms could dominate in different energy intervals, and for different particle species, for example.

Observations provide certain hints concerning the acceleration mechanism present. But the resolution as well as the measurement techniques set limits to the extent of understanding of the underlying physics. What we can see are mainly the consequences of accelerated particles, such as bremsstrahlung, cyclotron radiation, synchrotron radiation, and Thomson scattering. But we are not able to directly observe what leads to these energetic particles. This is why numerical simulations are very handy. They provide a way to study the physical processes in particle acceleration regions using different models whose results may then be compared to observations, and thus the underlying mechanism can be inferred.

The most common approach for particle acceleration investigations is the test particle approach (Chapter 3.2). The trajectories of test particles in a 3D reconnection topology given by Priest and Titov (1996b) has been studied for fan-reconnection as well as spine-reconnection by Dalla and Browning (2005) and Dalla and Browning (2008), respectively. Their initial conditions are coronal. They found a strong dependence of the energy gain of a test particle on its starting position. The highest acceleration appeared near the null-point, where the particles are unmagnetized and free to move according to the imposed electric field. In these studies spine-reconnection produces more high-energy particles than fan-reconnection and the steady-state is reached more quickly. On the other hand spine-reconnection did not produce jets emitted along the spine axis as they found during fan-reconnection.

These studies indicate that the DC electric field is a viable mechanism for particle acceleration in solar eruptions. But such collisionless test particle approached are only valid if on the one hand the particles speeds are high enough, so that collisions are rare, and on the other hand there is only a small particle population accelerated, so the effect of the charged particles on their accelerating electric fields is negligible. Dalla and Browning (2006) further investigated spine-reconnection, using the same potential field null-point reconnection configuration, finding two reconnection jets traveling in both directions along the spine. The initial velocity distribution is chosen to be Maxwellian. Highly accelerated particles show a strong velocity component along the magnetic field and the quasi-steady state energy distribution features a power-law tail index of -0.92. The authors conclude that the level of acceleration of these particles is strongly dependent on their angle of injection and hence on their position inside the reconnection region. It can therefore be surmised that their power-law index must be somehow dependent on the number of particles in the optimal injection position and the geometry of the magnetic field. This is what is found as well in the work presented here (see Baumann, Haugbølle, and Nordlund, 2012; Baumann and Nordlund, 2012): The magnetic field geometry, its magnitude, and the particle density are essentially the main factors to determine the power-law distribution. It is crucial though to note here that the publications by Dalla et al. use a potential magnetic field geometry (no currents), and as they require

the initially potential magnetic field to be static $\frac{dB}{dt} = 0$, there will never be currents (unlike in the experiments presented here). They do drive the boundaries in order to build up electric fields. At the locations where these electric fields are discontinuous, reconnection is assumed to take place, although non-ideal effects are not included in the model. This approach is a simplified version of solving the MHD equations, and is equivalent to saying that reconnection is taking place with infinite velocity. This may be a dangerous approach if one is interested in short timescale processes, such as the instant powerful particle acceleration in solar eruptions evidenced by hard X-ray and radio wavelength.

Another approach was taken by Rosdahl and Galsgaard (2010), who also conducted test particle simulations in connection with the formation of a solar jet., but starting from a flux emergence experiment. Further Turkmani *et al.* (2005, 2006) used an evolved MHD simulation snapshot of an MHD model in which a straight stratified coronal magnetic loop reacts to photospheric driving, together with test particles to study particle acceleration in such a turbulent environment. They showed that the applied photospheric random motion causes small scale current sheets at which particles are stochastically accelerated to relativistic energies in only a fraction of a second. Despite neglecting resistivity outside the current sheets in the MHD snapshot they conclude that the particle acceleration is clearly too high, due to the ignored back reaction of the particles onto the fields, which in fact breaks the conservation of energy; particles gain energy from the fields, but the field energy remains constant, see also the discussion of the test particle approach in Chapter 3.2.

As previously mentioned, electrons are found to be accelerated up to at least 100 MeV in solar flares, which, assuming a purely thermal source would mean that they escaped from regions with temperatures of approximately 7×10^{11} K. There have been some observations of very hot regions, such as by Masuda *et al.* (1994), but such regions are very rare and are unlikely to be the reason for the observed highly energetic particles. In fact, Lin *et al.* (2003) estimated from observations that $10\% - 50\%$ of the total released energy in eruptive solar events is contained in non-thermal electrons, while the rest is shared between non-thermal protons, plasma flow (bulk flow) and heating. MHD simulations (see Chapter 3.1) are limited to a thermal particle distribution, meaning that they cannot explain the production of non-thermal highly energetic particles. But the theory of MHD can of course account for the energy released by the plasma flow coming from a region covering several Mm or more, which kinetic effects can hardly account for. Plasma particle velocities in 3D reconnection outflow regions in MHD are a superposition of a bulk flow, accelerated by the Lorentz force ($\mathbf{j} \times \mathbf{B}$, where $\mathbf{j}$ is the electric current density) and thermal velocities, which are the result of mainly Joule dissipation in the non-ideal dissipation region, giving further rise to a high gas pressure capable of helping to accelerate plasma out of the reconnection region. Another contribution comes from slow shock structures, which are sometimes found in reconnection scenarios. But shocks are not expected to be the major accelerators of plasma in 3D reconnection regions.

To summarize, MHD simulations are an excellent choice to describe the overall magnetic field structures of a reconnection region, or in other words to provide the active region environment, but they cannot cover the entire story, down to non-ideal dissipative scales. A kinetic description is needed to understand the non-thermal part of the observed particle energies. Therefore the

approach developed in this thesis of using an MHD code to set up the 3D reconnection environment and then pass the state on to a PIC code is a new and promising way to understand solar eruptive events.

Particle Acceleration in Current Sheets

Current sheets form where magnetic field lines in adjacent regions are inclined at some angle (Ampére's law). In the corona current sheets build as a result of photospheric motions; when flux tubes emerge into pre-existing magnetic fields, or when translational motions in the photosphere push magnetic flux of different orientations towards each other. Current sheets are only maintained if there is a flow or the magnetic field is continuously deformed; otherwise the current sheets eventually diffuse away.

Assuming that reconnection is responsible for particle acceleration in eruptive coronal events and that reconnection occurs in current sheets links current sheets directly to particle acceleration. Instabilities in current sheets can trigger non-ideal plasma processes and thus lead to reconnection. But the overall current density inferred from magnetic field measurements in solar flare regions cannot, via classical resistivity, account for high enough resistive electric field to induce a reconnection event. Therefore, to drive reconnection, current sheets must consist of clusters of much smaller current sheets, providing locally a higher resistivity that then enables reconnection.

Additionally thin current sheets are prone to various instabilities, which also lead to enhancements of the resistivity. The fragmentation of current sheets, offering a possibility for multiple reconnection sites, has been investigated by using numerical experiments, leading to the conclusion that one or several governing small scale instabilities, such as the tearing instability (Shibata and Tanuma, 2001), are responsible for the suggested fragmentation. A concurrent process is the formation of magnetic islands, which may later merge by the coalescence instability (reconnection between magnetic islands). Islands shrink due to magnetic tension and finally lead to first-order Fermi acceleration of particles (Drake *et al.*, 2006a). One example of current sheet fragmentation simulations is summarized in the papers by Bárta, Büchner, and Karlický (2010) and Karlický and Bárta (2011). They show that coalescence and fragmentation of plasmoids can cause fragmentation of current sheets, which furthermore may lead to acceleration of electrons up to non-thermal energies. Further investigations on kinetic scales have been undertaken by Drake *et al.* (2006a). Such models may explain the periodic energy release seen in some solar flares, but most of the simulations performed so far showing a fragmentation of the current sheet are 2- or 2.5-dimensional. There have only been little work done in a fully 3D realistic setup. But future studies will certainly reveal the importance of plasmoids for particle acceleration.

3   COMPUTATIONAL MODELING

There is an immense range of different scales interacting in the solar atmosphere and there is still no clear understanding of how the complex non-ideal feedback from small to large scales is taking place. Magnetic reconnection is a typical example of a multi-scale process; magnetic diffusion takes place on kinetic scales (order of mm), while the overall magnetic field of the reconnection region feeding flux to the reconnection area as well as the scale of energy inflow are on the order of Mm, as illustrated in Figure 3.1. Next I provide an overview of the re-

Figure 3.1: From the gyro radius to the coronal loop size

strictions of different numerical codes when used for solar atmosphere modeling. I concentrate on the three most popular theoretical descriptions; magnetohydro-dynamics (MHD) single-fluid models, test particle models, and particle-in-cell (PIC) models. There are of course numerous others, such as multi-fluid approaches and alternative kinetic descriptions, e.g. the hybrid method (where electrons are described as a fluid and ions as single particles).

14

3.1 The MHD Approach

MHD is basically a fluid description, with an actively evolving magnetic field, while the electric field is derived from an approximate 'generalized Ohm's law'. The main constraints of this description are (e.g. Baumjohann and Treumann, 1996):

- The time scales must be much longer than characteristic time scales of individual particle motions

- The length scales of plasma variations are much larger than characteristic length scales of individual particles, such as the gyro radius

- Relativistic effects are negligible. As by point 1), only long time scales are considered, so the displacement current can be neglected.

- The plasma is in thermodynamic equilibrium, hence collision-dominated

- The plasma is treated as one fluid and single particle aspects are neglected

Although MHD codes assume collisions to be abundantly present, MHD works astonishingly well also for collisionless plasmas in low density environment, such as in the solar corona, as has been extensively demonstrated.

3.2 Test Particle Approach

The test particle approach is one way to get a first order estimate of kinetic plasma behavior on macroscopic scales. It is hence something in-between a kinetic description and a macroscopic description. It normally starts out from electromagnetic fields from an MHD simulation, or possibly an analytic expression or observations. The idea is to position charged test particles in an electromagnetic field and to integrate their trajectories, by solving their equation of motion. This method for studying the particle acceleration mechanisms is very popular. Its main requirements are (Rosdahl and Galsgaard, 2010):

- The number of accelerated particles needs to be small, so that the magnetic and electric fields associated with the moving charges are negligible.

- Collisions and other particle interactions (e.g. charge attraction or repulsion) can be neglected

- low plasma densities, so that the polarization field is weak (Siversky and Zharkova, 2009)

In test particle simulations there is, unlike in kinetic simulations, no immediate back-reaction from the particles onto the field. Siversky and Zharkova (2009) compared the test particle approach with a kinetic simulation and concluded that the magnetic field induced by moving charged particles is negligible, while the electric field induced by accelerated particles is large compared to the background field induced by reconnection. Therefore particle trajectories and energy spectra may be substantially altered even for a small number of simulated particles. Ignoring the back-reaction from particles onto the fields also means that the energy gained by the particles is not lost from the fields. An exaggerated acceleration is the consequence, as noted also by Rosdahl and Galsgaard (2010).

3.3 The Kinetic Approach

A popular kinetic approach is to use particle-in-cell (PIC) codes. PIC codes, such as the *PhotonPlasma* code, solve the Maxwell equations, containing external and self-consistent fields arising from the plasma motion,

$$-\frac{\partial \mathbf{B}}{\partial t} = \nabla \times \mathbf{E} \tag{3.1}$$

$$\epsilon_0 \mu_0 \frac{\partial \mathbf{E}}{\partial t} = \nabla \times \mathbf{B} - \mu_0 \mathbf{j}, \tag{3.2}$$

together with the relativistic equation of motion for charged particles

$$m\frac{d(\gamma \mathbf{v})}{dt} = q(\mathbf{E} + \mathbf{v} \times \mathbf{B}), \tag{3.3}$$

where ϵ_0 is the vacuum permittivity and μ_0 the vacuum permeability. PIC simulations use the phase space to describe a plasma and its temporal evolution, unlike the MHD description of a fluid, which ignores all information related to the velocity distribution. Every classical particle can be completely described by its position and momentum. In the PIC description we therefore give every particle a set of seven coordinates including its position, momentum and time. Instead of densities like in the MHD approach, distribution functions are used in kinetic simulations. This enables one to look at the statistical, kinetic information of a plasma, which is why the MHD description is also known as macroscopic and the PIC description as kinetic. MHD simulations further assume transport coefficients, while PIC codes directly allow for particle and wave particle interactions. In addition to the usual MHD wave modes PIC simulations provide the transverse electromagnetic waves / light waves. Note that PIC simulations in principle contain the complete MHD description, but that in practice the MHD limit may be prohibitively expensive.

Kinetic approaches are in principle the most exact descriptions. But there are, as well as in the other approaches, assumptions and approximations relative to the real case. Some of the general assumptions / properties of PIC codes are:

- Particles are considered to be so-called 'pseudo particles' representing many real particles, keeping the same charge to mass ratio as its components have in total.

- A particle position is represented by a probability function, a so called shape function, in order to smoothen out the charge distribution to avoid aliasing problems. Hence particles are not defined at only one position, but over about one cell.

- The positions of the fields are discrete although in reality they are continuous. However, field values can be computed at continuous locations, using interpolation between the discrete points.

In addition to these there are stability and similar constraints for explicit PIC codes, such as the *PhotonPlasma* PIC code:

- the Debye length λ_D[1] should not be smaller than about 0.3 grid cells, Δs. If the ratio of $\lambda_D/\Delta s$ is smaller, *aliasing effects* may become disturbing —

---

[1]The Debye sphere is the distance at which the thermal particle energy and the electrostatic potential energy are in balance (Baumjohann and Treumann, 1996) - see definition in appendix

depending on the shape function of the particle; the smoother the shape function, the less of a problem there is. Aliasing effects are side effects of the spatial discretization, causing artificial plasma perturbations, the result of which is heating of the plasma, leading to a growth of λ_D. This constraint for PIC simulations was introduced by Birdsall (1991) and has been widely used since (e.g. Siversky and Zharkova, 2009; Tsiklauri and Haruki, 2007; Pritchett, 2003). But already Okuda (1972) noted that depending on the ratio of the Debye sphere to the grid size numerical instabilities do or do no occur. If the Debye sphere is resolved by the computational grid there should not occur any numerical instabilities and kinetic effects can be correctly represented.

- Another requirement on the cell size is that the propagation of electromagnetic (light-) waves should be resolved, meaning that $c\Delta t < \Delta s$, where Δt is the time step.

- Δt must be smaller than (some fraction of) the orbit period of a particle (Tajima, 1986, p.59): $\omega_{ce}\Delta t < 0.35$, where ω_{ce} is the electron gyro frequency.

- A second recommendation concerning the time step is that it should resolve the Langmuir wave (plasma oscillation) evolution: $\omega_{pe}\Delta t < 1$, where ω_{pe} is the electron plasma frequency[2].

- One also needs to make sure to stay in the kinetic range and do not simulate MHD; A few grid cells Δs need to be contained in one electron skin depth δ_{skin}. Too few Δs per δ_{skin} lead to an MHD-like fluid behavior of the plasma, while too many Δs per δ_{skin} may result in uncoupling kinetic scales from the MHD behavior and hence a loss of the ability to match the large scale plasma behavior to MHD boundary and initial conditions.

- Additionally the number of particles per cell is often considered as a restrictive parameter of PIC simulations. A minimum number of 10 particles per cell turns out to be a reasonable limit in the case of the *PhotonPlasma* code – this constraint also depends on the smoothness of the shape function. Having too few particles per cell in a simulation results in single particles scattering against each other through the mechanism of the charge collection on the grid; fluctuations in the total charge per cell caused by low number statistics leads to artificial small scale electric field fluctuations.

All these recommendations and requirements have the purpose to ensure the dominance of the physical forces over the numerical (Monte Carlo) noise in PIC simulations. The noise mainly comes from the following factors: the reduced number of particles compared to reality by using pseudo-particles, the discrete spatial scale introduced by the grid, the order of the particle distribution shape function representing the particle spatially, and finally the interpolation from the particles to the grid as well as the time integration. Most requirements

[2]The plasma frequency is the frequency of charge oscillations in an ionized plasma, describing the time it takes for electrons to restore charge neutrality after a perturbation of any kind (Baumjohann and Treumann, 1996).

concern the electrons, as they are lighter and faster, they determine the time step and the cell size in the simulation.

λ_D is on the order of millimeters in the corona. The physical extents of the computational box in PIC experiments would hence be very tiny if they had to conform with the true scale requirements. On the other hand typical length scales of solar events are on the order of Mm. To study solar flares using PIC codes would thus require an immense number of cells. Additionally, the huge density and temperature ranges from below the solar surface out into the solar corona are impossible for PIC codes to cover, hence flux emergence is essentially impossible to model solely by a PIC simulation. To face the tremendous challenge of covering solar event length scales one is forced to scale the fundamental physical parameters, so that the hierarchy of (order of) length scales and velocities is retained, keeping different scales reasonably separated, but making the dynamical span small enough so that it can be resolved. This is done by modifications of the constants of nature, as discussed in the next Section.

3.4 Coupling the Different Approaches by Modifications of the Constants of Nature

One approach to combine macroscopic with microscopic scales is the test particle approach. But as previously mentioned, this approach has very tight validity limits. In order to assure self-consistent modeling of particle acceleration in solar eruptive events, a kinetic description of the plasma motion is needed. But how can we couple all the scales, from the size of a solar flare down to the electron skin depth or the current sheet width, using a single numerical code? There has so far been mainly one attempt, by Sugiyama and Kusano (2007), to couple MHD and kinetic codes into a so-called interlocked model. But including small scale kinetic domains in an MHD simulation faces several problems; among these that a low-pass filter is needed in the interface between the two domains, as only low-frequency waves may propagate in the MHD domain. These combined models are still under development as it is numerically a highly complex problem. In the present study we introduce a new method to meet the challenge of multi-scale simulations and use the method to investigate particle acceleration mechanisms in coronal reconnection regions.

The avoid confusion with respect to the term 'scaling', we make the following clear distinction:

Unit Scaling

We use the term *unit scaling* about the technique of converting physical units into units suitable for numerical codes. This is partly done with the purpose to avoid under- and overflows, partly to reveal the extent to which the results are, in a certain sense, independent of the exact physical size. The experiments hence become 'dimensionless'. Typical choices are for instance to choose the scalings of length, time and density. Fixing these three, we describe a certain physical system, and the scalings of any other physical quantity can be recovered by requiring the relation between physical quantities to remain the same. Requiring, for example, the relation between dynamic pressure, and magnetic pressure to be the same fixes the scaling of magnetic field strength. Any other

three variables may be chosen as the basis for unit scaling. In coronal MHD simulations, for example, one often chooses a typical coronal Alfvén speed, length scale and density as a basis for the scaling.

System Modifications

On the other hand there are system *modifications*, which can be performed by modifications of the constants of nature or, equivalently, modifications of the physical properties of the experiment. Here, in order to reduce the large range between microscopic and macroscopic scales, two sets of modifications are introduced. In doing so, we choose to maintain pressure equilibrium, which implies keeping the plasma beta constant:

$$\beta = \frac{P}{P_m} = \frac{2k_B \rho_m T \mu_0}{\mu m_u B^2},\qquad(3.4)$$

where m_u is the atomic mass constant, P_m the magnetic pressure, k_B the Boltzmann constant, ρ_m the mass density, T the temperature and μ the mean molecular weight.

Modification I: Micro Scales

With this modification the previously mentioned restrictions on the kinetic scales (λ_D, δ_{skin}, ω_{pe} and ω_{ce}) are loosened.

In terms of changes of the constants of nature modification I amounts to reducing the fundamental charge per particle; this increases all micro scales in proportion to the inverse of the charge per particle.

The same effect may be produced by changing physical properties of the system in the following way: First the magnetic field strength is changed by a factor $b < 1$. This changes the gyro frequency ω_{ce}. A change in the magnetic field strength must be balanced by reducing the mass density by a factor b^2, to keep the plasma beta (Equation (3.4)) constant, while keeping the temperature constant. This then leads to a change in λ_D and δ_{skin} by a factor of b^{-1} and a change in ω_{pe} by a factor of b. The ratios of the gyro and plasma frequency as well as the ratio between the skin depth and the Debye length are kept constant. These modifications further keep the acceleration of gravity unchanged, since the scale height is proportional to T/g. Also the velocities stay untouched.

Modification II: Velocities

With this modification the previously mentioned restriction on the time step by the speed of light c is loosened.

In terms of changes of the constants of nature modification II amounts to reducing the speed of light; this increases the time step allowed in numerical simulations correspondingly. A similar effect — reducing the gap between the speed of light and other speeds — may be obtained by changing the physical properties in the following way:

The temperature is increased by a factor t^2, with a corresponding increase in the acceleration of gravitation g by t^2 and a change of the sound speed v_s and thermal speed v_{th} by t. In order to keep the pressure equilibrium (Equation (3.4)), the magnetic field strength needs to be increased by a factor t. This

further leads to a change of the Alfvén speed by t. Increasing also the material speed with a factor of t one has thus reduced the gap between the speed of light and other speeds with the factor t. The kinetic scales are not left completely unchanged by this modification, as a change in the magnetic field strength has an influence on the gyro frequency, and a change of the temperature changes the Debye length. The skin depth and plasma frequency on the other hand stay constant. The bottom line is that the ratio of the skin depth to the Debye length and gyro radii is modified in exactly the same way as when changing the speed of light.

Adopted Modifications

To summarize, the spans in speed and physical scales may be reduced by changing two of the fundamental constants of nature; the speed of light and the fundamental charge per particle.

Both modifications have in fact at least partially been used before; Drake *et al.* (2005, 2006a,b) changed the speed of light to be 20 times the Alfvén speed. Siversky and Zharkova (2009) on the other hand reduced (often by a factor of 100) the particle density, which is essentially equivalent to reducing the charge per particle.

Another assumption that is often used, and which we also adopt, is a reduction of the mass ratio between ions and electrons from its normal value $m_i/m_e \approx 1836$. This decreases the range between the ion and electron micro scales (skin depths and plasma frequencies), and also reduces the electron thermal velocities. Therefore this approach is often used together with a speed of light decrease, in order to rescale the ratio of the speeds to the speed of light accordingly.

A crucial point to keep in mind when using these types of modifications is to ensure that the hierarchy of characteristic speeds, times and length scales is, to the largest extent possible, maintained. In the solar corona this hierarchy is

$$v_J < v_{th,i} \sim v_s < v_{th,e} < v_A < c, \tag{3.5}$$

where v_J is the average electron drift speed, which arises due to the electric current, $v_{th,i,e}$ is the thermal speed of protons/electrons, v_s is the speed of sound and v_A is the Alfvén speed.

For our simulations of a solar active region as well as for the coronal hole experiment we use a combination of these modifications compared to the real Sun:

- The ratio of proton mass to electron mass is changed to 18, by increasing the electron mass

- ϵ_0 is increased - thus lowering c to of the order 3800 $\mathrm{km\,s^{-1}}$. μ_0 is kept constant to leave the magnetic pressure the same.

- The elementary charge is reduced with a factor of about 10^6, in order to be able to resolve the micro scales.

In the active region experiment we additionally increase the number density: Instead of the typically used coronal value of $1 \times 10^9\,\mathrm{cm^{-3}}$ (Aschwanden, 2005), we use $128 \times 10^9\,\mathrm{cm^{-3}}$, in order to reduce the Alfvén speed (a value on the order of $1 \times 10^9\,\mathrm{cm^{-3}}$ is probably also too low in an active region).

3.5 Intersection MHD - PIC Simulation

In general the basic macroscopic moments for a one-fluid theory are: the number density n, the plasma bulk flow velocity v, the pressure tensor P and the thermal temperature T. In the *Stagger* code, the simulation provides the mass density (ρ_m) the 3-dimensional momentum (px, py, pz), the thermal energy per unit volume (e) and finally the magnetic field components (Bx, By, Bz). For the initialization of the kinetic parameters in the PIC code we make the following assumptions

$$n_{e,i} = \frac{\rho_m}{(m_e + m_i)} \tag{3.6}$$

$$P_{e,i} = \frac{e}{\rho_m}(\gamma - 1) \tag{3.7}$$

$$\equiv n_{e,i} \cdot k_B \cdot T_{e,i} \tag{3.8}$$

$$T_{e,i} = \frac{P_{e,i}}{n_{e,i}k_B} \tag{3.9}$$

$$= \frac{P_{e,i}(m_e + m_i)}{\rho_m k_B} \tag{3.10}$$

$$v_{th,e,i} = \sqrt{\frac{k_B T_{e,i}}{m_{e,i}}} \tag{3.11}$$

$$\mathbf{u}_{\mathrm{MHD}} = \frac{\mathbf{p}_{\mathrm{MHD}}}{\rho_m} \tag{3.12}$$

$$\mathbf{v}_J = \frac{1}{\mu_0} \cdot \frac{\nabla \times \mathbf{B}}{q n_e} \tag{3.13}$$

$$\mathbf{V}_e = \mathbf{u}_{\mathrm{MHD}} + \mathbf{v}_{th,e} + \mathbf{v}_J \tag{3.14}$$

$$\mathbf{V}_i = \mathbf{u}_{\mathrm{MHD}} + \mathbf{v}_{th,i} \tag{3.15}$$

$$\mathbf{E} = -\mathbf{u}_{\mathrm{MHD}} \times \mathbf{B} \tag{3.16}$$

where $n_{e,i}$ is the electron and ion density, P is the gas pressure, p_{MHD} are the MHD bulk momenta, u_{MHD} the MHD bulk speeds and $T_{e,i}$ the electron and ion temperatures. v_J is the average electron speed required to carry the electric current (to simplify the initialization the electric current is assumed to initially be carried only be the electrons).

For the PIC simulations an initially Maxwellian plasma is assumed, due to the MHD assumption of a collisional system (system time is long compared with the collision time $\frac{1}{\nu}$). The velocity distribution function $f(\mathbf{v})$ is therefore the general Maxwell distribution function

$$f(\mathbf{r}, \mathbf{v}) = n(\mathbf{r}) \left(\frac{m}{2\pi k_B T(\mathbf{r})} \right)^{3/2} \exp\left(\frac{-m(\mathbf{v} - \mathbf{u}_{\mathrm{MHD}})^2}{2k_B T(\mathbf{r})} \right) \tag{3.17}$$

$$\propto \exp\left(-\frac{(\mathbf{v} - \mathbf{u}_{\mathrm{MHD}})^2}{v_{th}(\mathbf{r})^2} \right), \tag{3.18}$$

which thus gives a measure of the spread of the Maxwellian.

The dependence on the position $\mathbf{r}$ arises due to the chosen photosphere-corona temperature and density profile from the MHD simulations. If the electrons and ions were given the same initial bulk velocity there would be no initial
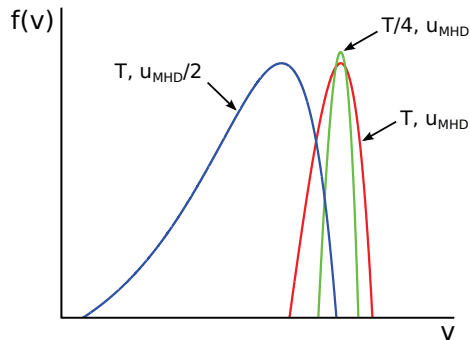
Figure 3.2: Maxwell distribution in a log-log plot: With changing bulk speed the peak shifts sidewards and changes the shape of the distribution, while a change in temperature changes the width and hence shape of the distribution function.

electric current, and there would be a large initial imbalance in Ampere's law, with a transient electric field causing a rapid increase in electric current and with the current carried mainly by the electrons, since the electrons move much faster than the heavier ions. To avoid this artificial perturbation in the beginning of the experiment, the electron velocity is initialized including an electric current speed:

$$\mathbf{j} = n_e q_e \mathbf{V_e} + n_i q_i \mathbf{V_i} \tag{3.19}$$
$$\nabla \times \mathbf{B} \approx \mu_0 \mathbf{j}, \tag{3.20}$$

where q_i is the ion charge. Assuming that $n_e = n_i$ and that, because of the larger inertia of the ions, $V_i \approx \mathbf{u}_{\mathrm{MHD}}$ we are left with

$$\mathbf{V_e} = \mathbf{u}_{\mathrm{MHD}} + \frac{\nabla \times \mathbf{B}}{\mu_0 n_e q_e}. \tag{3.21}$$

This setup provides an electric current from the very beginning of the simulation. A similar velocity initiation has been used in the interlocked model by Sugiyama and Kusano (2007). In principal one should also give ions a weak opposite speed component, but since the initial state inherited from MHD can never be completely consistent with the PIC model we do not bother to do this.

In addition to the setup parameters mentioned so far, in case of a stratified MHD simulation snapshot the densest part is removed, for the sake of code stability, as well as for the fact that we are only interested in the reconnection region in the solar corona. It is of course of high importance to still cover MHD scales with the PIC cut-out, so the experiment does not lose its relation to the solar active region environment.

The magnetic field is directly taken from the MHD snapshot. But the electric field of the PIC simulation is initialized using only the advective electric field $-\mathbf{u}_{\mathrm{MHD}} \times \mathbf{B}$ from the MHD snapshot, for the following reason:

$E_\parallel$ can only build up in non-ideal processes. In MHD simulations this parallel electric field is included as a resistivity term $\mathbf{E}_{\mathrm{res}} = \eta \mathbf{j}$. The resistivity η in numerical MHD simulations is imposed to handle instabilities which are caused by the high order operators in steep gradient areas such as current sheets and

shocks, while the real physical viscosity and resistivity length scales and hence the scales at which the parallel electric fields forms in diffusion regions, are taking place on kinetic length scales. These real solar diffusion scales are NOT resolved by MHD length scales. So the resistivity in MHD simulations is artificially high, and should not be directly incorporated into the PIC simulations. This ensures that any $E_\parallel$ that develops in the PIC simulations is created self-consistently.

In particle-in-cell codes (PIC) codes steep gradients also occur, but are automatically limited by the smoothing caused by the interpolations to and from the grid to the particle positions. This can also be seen as a non-ideal term, since particles are moved according to the Lorentz force, which is a result of the electric and magnetic fields produced by the weighted charge and current distribution of the neighboring particles. Hence particles feel each other indirectly over the grid, but two particles in the same cell do not interact directly with each other. Hence the only real physical resistivity in PIC simulations are the particle collisions as implemented in the *PhotonPlasma* PIC code as part of this thesis in the Coulomb scattering routine.

3.6 Initialization of the Magnetic Field in Numerical Experiments

As mentioned earlier in this document, only the photospheric magnetic field can routinely be measured at high resolution. The highly complex coronal field hence needs to be reconstructed. In general there are three fairly different approaches to simulate the magnetic field of pre-eruptive regions of the corona. One is to use a simplified magnetic field geometry, which resembles the observations on large scales. Such a numerical models in regard to solar active regions have been introduced by Baum and Bratenahl (1980), who positioned four flux cells in the photosphere, essentially four point magnetic charges or monopoles. These represent cuts through magnetic flux tubes emerging into the atmosphere. The magnetic field resulting from this construct show separator and separatrix field lines. More recent, improved studies that have used the model of sub-photospheric sources are Demoulin, Henoux, and Mandrini (1994) or Priest, Bungey, and Titov (1997); Aulanier, Pariat, and Démoulin (2005); Santos, Büchner, and Otto (2011). Santos, Büchner, and Otto (2011), for example, started from a force-free potential field and imposed photospheric boundary motions in order to build up currents.

A more elaborated way is magnetic field extrapolation from magnetograms obtained from observations. The simplest approach here is the potential field extrapolation, assuming $\nabla \times \mathbf{B} = 0$, or force-free field extrapolations[3], assuming $\nabla \times \mathbf{B} = \alpha \mathbf{B}$ (and called *linear force-free* if α is constant in space). The potential field extrapolations employed for the active region experiment were performed by using a Fast Fourier Transform potential extrapolation method. Numerical studies of solar flare events in the solar corona making use of this technique have been performed by Masson *et al.* (2009); this was one of the first MHD simulations to use realistic boundary and initial conditions in order

---

[3]Force-free, because the magnetic force on the plasma is zero $\mathbf{j} \times \mathbf{B} = 0$, hence there are only field-aligned currents possible.

to simulate a solar flare event. The active region experiment presented here (Baumann, Galsgaard, and Nordlund, 2012) uses the same technique of extrapolation of the magnetic field from an observed magnetogram. In cases where vector magnetograms are available, a related approach can be to make a linear or non-linear force-free field extrapolation, as done by Baker *et al.* (2009), who investigated the resulting magnetic topology in comparison with observations.

The third method I would like to mention here is one where results are extracted from a flux emergence simulation. The simulation is for example initiated with a twisted and unstable flux tube, initially positioned below the photosphere, which then emerges into the solar corona and interacts with a constant, pre-existing coronal magnetic field. This approach is used in the coronal hole experiment presented in this thesis. It has previously been used by e.g. Archontis *et al.* (2004, 2005) and Moreno-Insertis, Galsgaard, and Ugarte-Urra (2008). Archontis and Hood (2008); Gontikakis, Archontis, and Tsinganos (2009) went even a step closer to reality and simulated first the flux emergence of one flux tube to get a more realistic coronal magnetic field, into which then a second magnetic flux tube emerged.

3.7   The *PhotonPlasma* Particle-In-Cell Code

For all performed PIC simulations discussed in this thesis the *Photon-Plasma* code (Haugbølle, 2005; Hededal, 2005) has been used. The Photon-Plasma code solves the Maxwell equations

$$-\frac{\partial \mathbf{B}}{\partial t} \quad = \quad \nabla \times \mathbf{E} \tag{3.22}$$

$$\epsilon_0\mu_0\frac{\partial \mathbf{E}}{\partial t} \quad = \quad \nabla \times \mathbf{B} - \mu_0\mathbf{j}, \tag{3.23}$$

together with the relativistic equation of motion for charged particles

$$m\frac{d(\gamma\mathbf{v})}{dt} \quad = \quad q(\mathbf{E} + \mathbf{v} \times \mathbf{B}) \tag{3.24}$$

on a staggered Yee lattice (Yee, 1966). The code is fully three-dimensional and uses a 2nd order leapfrog scheme for the progression in time, with 6th order spatial differencing. The electric and magnetic fields on the grid are interpolated to the particle positions using a cubic scheme that involves the 64 nearest mesh points. The particle positions and velocities are updated using the Vay particle-pusher (Vay, 2008). The electric currents are calculated using a new 6th order version of the Esirkepov charge conservation method (Esirkepov, 2001).

There is an option in the code to include particle-interactions via Coulomb scattering, which is especially valuable in the solar chromosphere. As the two main experiments introduced here are both taking place in a coronal environment, the scattering option has generally not been used, except in control experiments that showed only marginal differences. Additional code options (also not used here) are Compton scattering, pair creation and annihilation, multiple species treatment, e.g. to include neutrals and heavier ions.

We use SI units, scaled so the unit of length is $1\,\mathrm{km}$, the unit of time is $0.1\,\mathrm{s}$, and the unit of density is $10^{-12}\,\mathrm{kg\,m^{-3}}$. The same code units are used for the active region as well as the coronal hole experiment.

3.8 The *Stagger* MHD Code

The MHD *Stagger* code is a compressible MHD code, which solves the resistive MHD equations

$$\frac{\partial \rho_m}{\partial t} = -\nabla \cdot (\rho_m \mathbf{u}) \tag{3.25}$$

$$\frac{\partial (\rho_m \mathbf{u})}{\partial t} = -\nabla \cdot (\rho_m \mathbf{u}\mathbf{u} + \underline{\underline{\tau}}) - \nabla P$$
$$+ \mathbf{j} \times \mathbf{B} + \rho_m \mathbf{g} \tag{3.26}$$

$$\frac{\partial e}{\partial t} = -\nabla \cdot (e\mathbf{u} + \mathbf{f_e}) - P\nabla \cdot \mathbf{u}$$
$$+ Q_J + Q_\nu \tag{3.27}$$

$$\frac{\partial \mathbf{B}}{\partial t} = -\nabla \times \mathbf{E} \tag{3.28}$$

$$\mathbf{j} = \nabla \times \mathbf{B} \tag{3.29}$$

$$\mathbf{E} = -\mathbf{u} \times \mathbf{B} + \eta \mathbf{j} \tag{3.30}$$

$$Q_J = \eta j^2 \tag{3.31}$$

$$\nabla \cdot \mathbf{B} = 0 \tag{3.32}$$

$$P = (\gamma - 1)e \tag{3.33}$$

$$\tau_{ij} = -\nu_{ij} \rho_m S_{ij} \tag{3.34}$$

$$S_{ij} = \frac{1}{2} \left(\frac{\partial u_i}{\partial x_j} + \frac{\partial u_j}{\partial x_i} \right) \tag{3.35}$$

$$Q_\nu = \rho_m \sum_{ij} \nu_{ij} S_{ij}^2 \tag{3.36}$$

$$\mathbf{f_e} = -\nu_e \rho_m \nabla (e/\rho_m) \tag{3.37}$$

where $\mathbf{u}$ is the bulk velocity, e the thermal energy per unit volume and ν_{ij} represents coefficient of viscosity, symmetric in ij. In some MHD codes the viscosity is assumed to be constant while in others the viscosity is supplied implicitly, through the methods used to ensure numerical stability. In the *Stagger* code the viscosity is instead defined explicitly by

$$\nu = \Delta s \left(\nu_1 c_f + \nu_2 |\mathbf{u}| + \nu_3 \Delta s \, | - \nabla \cdot \mathbf{u}|_+ \right), \tag{3.38}$$

where $\nu_1 = 0.005 - 0.02$, $\nu_2 = 0.005 - 0.02$, and $\nu_3 = 0.2 - 0.4$ are dimensionless coefficients that provide dissipation for fast mode waves (ν_1), advective motions (ν_2), and shocks (ν_3). $| - \nabla \cdot \mathbf{u}|_+$ denotes the positive part of the rate of compression $-\nabla \cdot \mathbf{u}$. c_f is the fast mode speed defined by $c_f = \sqrt{(B^2 + \gamma P)/\rho_m}$.

The resistivity η is analogously defined by

$$\eta = \Delta s \left(\nu_1 c_f + \nu_2 |\mathbf{u}| + \nu_3 \Delta s \, | - \nabla \cdot \mathbf{u}_\perp|_+ \right), \tag{3.39}$$

where $\mathbf{u}_\perp$ is the component of the velocity perpendicular to $\mathbf{B}$, and where the expression scaled by ν_3 prevents electric current sheets from becoming numerically unresolved. The resulting magnetic grid Reynolds numbers are on the order of a few in current sheets, as required to keep such structures marginally resolved. η is very small in the solar corona, but is still present, in particular in
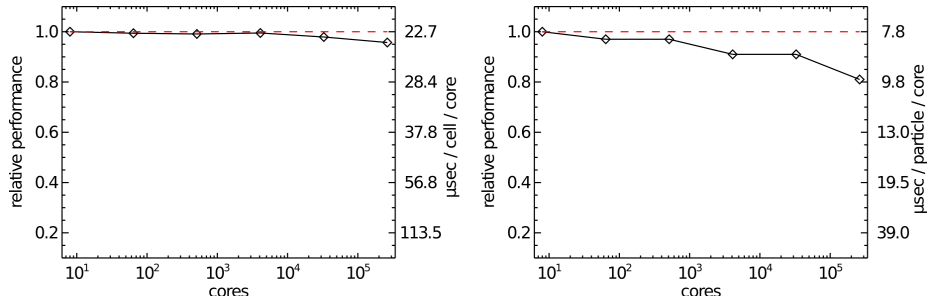
Figure 3.3: Weak Scaling plot for the MHD *Stagger* code (left) and the PIC *PhotonPlasma* code (right) for up to 262 k cores on the JUGENE supercomputer (see also Table 3.1).

reconnection regions. The overall scaling with Δs makes sure that advection, waves, shocks and current sheets are resolved by a few grids cells, independent of the mesh size. Handing resistivity this way minimizes the resistivity overall, as in smooth regions the resistivity is very small and only in steep gradient regions it is enhanced. Further in these MHD Equations S_{ij} is the shear tensor, τ_{ij} the viscous stress tensor and $\mathbf{f_e}$ is a weak diffusive flux of thermal energy needed for numerical stability. The term Q_v represents viscous dissipation, turning kinetic energy into heat, while Q_J is the Joule dissipation, responsible for converting magnetic energy into heat. And finally γ represents the ratio of specific heats, being 5/3 in our simulations, which means that we assume a monoatomic, ionized plasma (no neutrals or molecules included). This is a common approach for coronal plasma, since the temperature is very high and the density is low, the formation of neutral atoms and molecules is unimportant.

The high conductivity and the low plasma beta (10^{-3}, Aschwanden, 2005) lead, together with Equation (3.26) to the conclusion, that in most of the corona electric currents are flowing in directions nearly parallel to the magnetic field.

We include the force of gravity in both the MHD and PIC experiments.

3.9 The Performance of the *Stagger* and the *PhotonPlasma* Codes

Almost all simulations have been run in parallel on the JUGENE IBM Blue-Gene/P supercomputer at Forschungs-Zentrum Jülich (F-ZJ) in Germany. The *Stagger* code uses 23 microseconds per zone update per core on JUGENE, almost independently of the number of cores, as shown in Figure 3.3. The *PhotonPlasma* code uses 7 microseconds per particle update per core on JUGENE. Generally it can be said that the codes show good strong scaling (scaling at constant total problem size) and excellent weak scaling (scaling at constant problem size per core) on the JUGENE cluster. On JUGENE the code scales from 8 to 262 k cores with 82% efficiency, while the *Stagger* code scales with 96% efficiency from 8 to 262 k cores, at constant problem size per core.

Extensive scaling tests were performed. More information can be found at http://comp.astro.ku.dk/Twiki/view/CompAstro/JugeneNotes

Table 3.1: Scaling results

Cores	1	8	64	512	4096	32768	262144
sec/cell (MHD)		22.71	22.84	22.91	22.82	23.19	23.73
sec/particle (PIC)	7.04	7.81	8.09	8.05	8.61	8.57	9.70

4   ACTIVE REGION PLASMA ACCELERA-TION

The active region experiment consists of two parts: An MHD simulation and an associated PIC simulation. The goal of this active region experiment is to investigate the acceleration mechanism responsible for the particle acceleration in solar flares and other solar eruptive events. The numerical experimental setup is illustrated in Figure 4.1.

4.1   MHD Simulation

We choose a solar flare event which has previously been investigated both observationally as well as numerically by Masson *et al.* (2009). As a vector magnetogram was not available for this solar C-flare[1] event on 16th November 2002, and hence a nonlinear force-free extrapolation not possible, the numerical experiment starts out from a potential magnetic field extrapolation of a magnetogram from the Michelson Doppler Imager (MDI) instrument on The Solar and Heliospheric Observatory (SOHO) satellite (Scherrer *et al.*, 1995)[2]. The cut-out contains 185 x 110 data points. Each horizontal Fourier transform component of the potential is set to be exponentially decreasing in the direction away from the boundary, with amplitude factors of the form $\exp{(-zk_{x,y})}$, where z is the vertical coordinate. The magnetic field is then computed from the gradient of the potential, using the same differential operators as in the MHD code. This ensures that the magnetic field numerically satisfies $\nabla \times \mathbf{B} = 0$; i.e., that it is current free. Subsequently the numerical divergence $\nabla \cdot \mathbf{B}$ is computed; while analytically this should vanish numerically there is generally a small residual. This is iteratively removed by solving for a correction $\delta\Phi$ of the potential which has $\Delta(\delta\Phi) = \nabla \cdot \mathbf{B}$. This ensures that we start with a numerically $\nabla \cdot \mathbf{B}$ clean magnetic field (apart from some small scale noise due to truncation errors). Although the magnetic field in the coronal region is clearly non-potential, a potential field configuration is in most cases a reasonable representation of the overall topology of the magnetic field, while variations in for instance the magnetic field line loop height or the connectivity in weak magnetic field regions may occur (Régnier, 2012).

---

[1] C-flares typically release energies of about 3.6×10^{30} ergs (Kretzschmar, 2011).

[2] The MDI instrument is looking at the Doppler shift in right and left circularly polarized light from the Ni I $\lambda6768$ Å absorption line which forms in about 200 – 300 km above the photosphere (Georgobiani *et al.*, 2000). These MDI measurements provide a full-disk line-of-sight magnetic field every 96 minutes with a resolution of 4 arcseconds and a total field of view of 34 x 34 arcminutes (Scherrer *et al.*, 1995). The accuracy of the magnetic field data is about about 20 G.
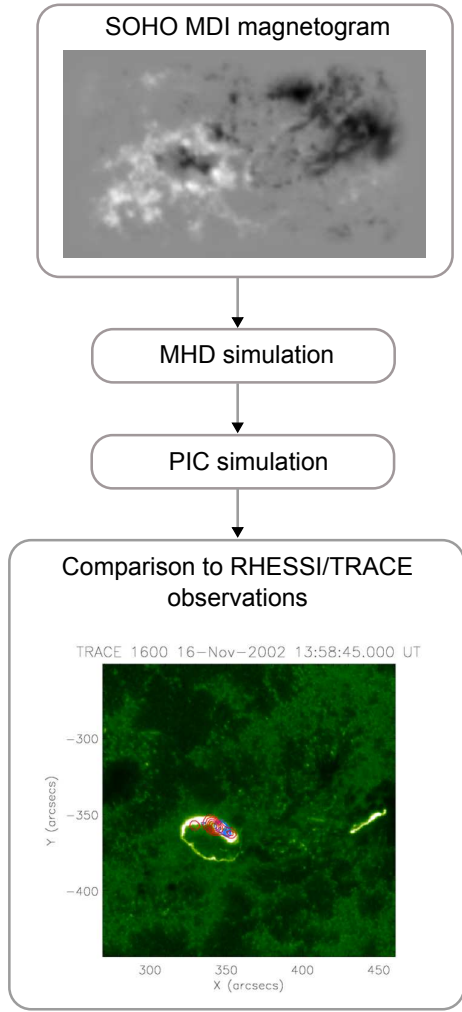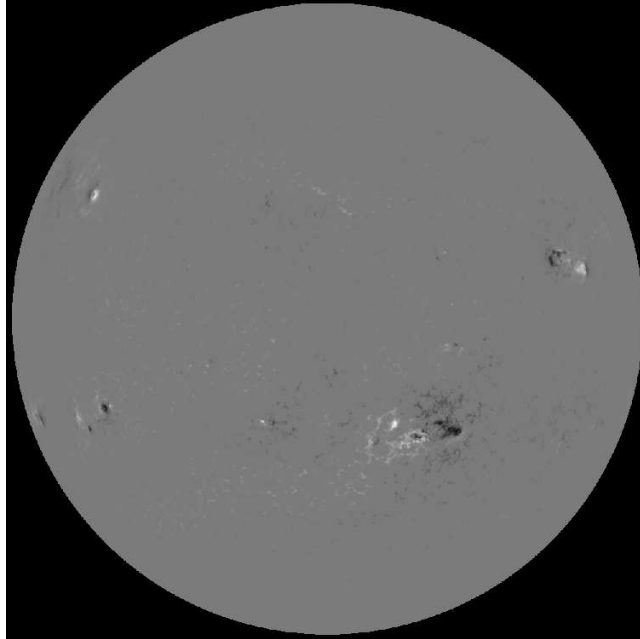
Figure 4.1: Active region experiment sketch

In case that the magnetic field is derived from a magnetogram, as in the active region experiment, the simulation setup is fully defined, with zero initial electric current (because the magnetic field is potential) and zero bulk velocity (since we have no other information). We used a magnetogram (see Figure 4.2a) taken at about 8 hours before the flare occurrence observed by the Transition Region and Coronal Explorer (TRACE), SOHO (Masson *et al.*, 2009) and RHESSI (Reid, 2011) (Figure 4.3a). This gives the simulation time to build up currents as a result of the driving motion we apply after some initial relaxation phase at the photospheric boundary. The applied driving motion at the bottom boundary represents the horizontal photospheric motions in the chosen active region observed by SOHO during the given time period. Driving is needed in order to build up currents and free magnetic energy in the system. The pattern used — deliberately chosen identical to the one used by Masson *et al.* (2009) — is shown in Figure 4.2b. Note that using the line-of-sight data of an active region which is away from the solar meridian causes a projection effect, which may cause some differences in the magnetic fields geometry. This is partially taken into account in the setup of the simulation, using a deprojection that cancels the foreshortening and skewing of the magnetogram. The contamination of the line of sight magnetic field by horizontal components cannot easily be removed.
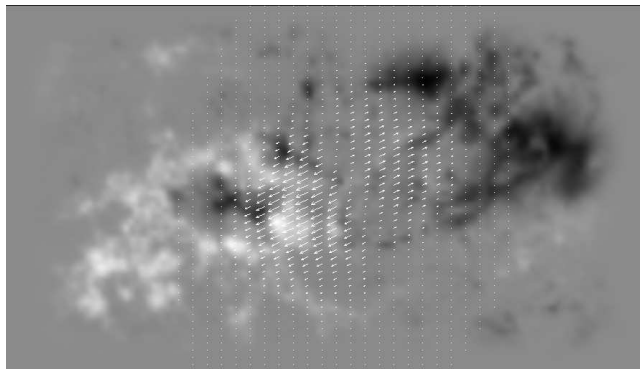
The magnetic feature seen in the solar observatory magnetogram in Figure 4.2a are thought to be a result of emerging flux tubes which rise up to the photosphere from the convection region (Caligari, Moreno-Insertis, and Schussler, 1995) due to the convection and the gas pressure. The hard X-rays emission shown in Figure 4.3b is most probably a result of electrons accelerated to non-thermal energies, which impact the much denser chromosphere and therewith produce bremsstrahlung. Soft X-rays on the other hand are thought to be from bremsstrahlung of electrons with thermal speeds as well as from atomic lines. In the non-thermal thick target model by Brown (1971) it is assumed that the soft X-ray spectra electrons are a consequence of the evaporation of hot plasma, which is heated by electrons that have previously been accelerated at the reconnection region and then impacted the chromosphere at the foot-points of the coronal loops. The model was subsequently improved and an update was published in Brown *et al.* (2009). Even if the electrons collide with thermal protons in the surrounding already before impacting the denser chromosphere the chromospheric emission will dominate because of the proportionality of bremsstrahlung to the ambient density.

Due to a 'parasitic' magnetic field polarity (the small region of black polarity immersed in the larger scale region with white polarity in the left hand side part of the magnetogram) the extrapolation of our chosen magnetogram leads to a 3D magnetic null-point topology, containing a fan-plane with a dome-shaped structure and a spine, surrounded by a much stronger magnetic field that extends to larger heights in the corona.

The 3D MHD simulations using the *Stagger* MHD code are performed on a box size of 175 x 100 x 62 Mm, covered by a stretched mesh of dimensions 896 x 512 x 320, with a cell size of about 80 km covering a reasonably larger region around the null-point. The boundaries at top and bottom are mainly chosen to be closed, while they are periodic on the sides. We conduct two kind of numerical MHD simulations: Stratified atmosphere experiments and constant temperature-density experiments. Additionally we modify the driving speed

(a) MDI full-disk image, 16th November 2002, 06:27 UT

(b) Lowest boundary vertical magnetic field after 0.001 sec after start of an active region experiment MHD run. A windowing function is initially employed, which conduced to have periodic boundary conditions for the Fast Fourier Transform potential extrapolation. Overplotted is the driving velocity pattern applied to photospheric boundary.

Figure 4.2: Full-disk SOHO magnetogram and applied velocity driving pattern

(a) TRACE observations at 1600 Å combined with the SOHO magnetogram (Masson *et al.*, 2009). Reproduced by permission of the AAS and the author.

(b) RHESSI X-ray observations at energies of (blue - soft) 12–25 keV (> 50%) and (red - hard) 25–100 keV (> 50%) overplotted on a TRACE image (Reid, 2011).

Figure 4.3: Observations of the solar C-flare event in AR 10191 on 16th November 2002

and look into its influence on the results. The driving speed is varied by a factor of 6 and even its smallest magnitude is at least 6.6 times larger than the corresponding, observed plasma motions ($\approx 0.5\,\mathrm{km\,s^{-1}}$), for reasons of limited computing time. It is of high importance to keep the driving speed well below the Alfvén velocity v_A and the sound speed v_s, because the magnetic structure and the plasma needs to have enough time to adapt to the new magnetic geometry and should not be haled by the driver. With this we assure an almost force free state at all times in the simulation, meaning that the current is well aligned with the magnetic field.

The driving velocity distribution at the bottom boundary leads to a relative shear of the main two different magnetic flux domains — inside and outside the dome-shaped fan-plane — and gives rise to a thin current sheet in the fan-plane separating these domains. This is the location at which also the diffusive electric field peaks. Reconnection takes place close to the null-point in the separatrix surface. The null-point itself is disrupted with increasing displacement (product of simulation time and amplitude of the average applied driving velocity) by the shearing motion and stretches into a 'weak magnetic field region'. The distortion of the magnetic field further leads to an electric field buildup. The advective electric field, $\mathbf{u} \times \mathbf{B}$, shows generally a higher magnitude than its diffusive counterpart $\eta\mathbf{j}$. With increasing boundary displacement the diffusive electric field close to the null-point increases in a characteristic run with a driving speed of $v_{drive} = 10\,\mathrm{km\,s^{-1}}$ up to around $50\,\mathrm{V\,m^{-1}}$, which corresponds to about $20\,\mathrm{V\,m^{-1}}$ with solar amplitude driving, since the diffusive electric field in current sheets relates as

$$E_{\mathrm{CS}} \propto \phi \propto v^{1/2}. \tag{4.1}$$

to the speed v (Baumann, Galsgaard, and Nordlund, 2012), where Φ is the angle formed by the field lines on each side of the current sheet, while the experimental driving speed is estimated to be 20 times larger than the real photospheric plasma motions. The advective electric field on the other hand experiences a much stronger increase, reaching values of about $900\,\mathrm{V\,m^{-1}}$, which, under the assumption of slow enough driving ($v_{drive} < v_A$), corresponds to $45\,\mathrm{V\,m^{-1}}$. Hence the electric field increase can be traced back to the energy input brought into the system by the boundary motion.

The systems in the presented experiments goes through different near-potential states, so that the evolution of the magnetic energy versus the boundary displacement is nearly perfectly identical for all stratified as well as non-stratified runs and the dissipation represents only a small fraction of the magnetic energy input rate. The rate of change of magnetic energy is almost constant in the beginning of the simulation, but as the work input from the lower boundary looses efficiency due to the angle between the boundary and the magnetic field lines approaching 90 degrees as well as a reduced amount of flux available for displacement, it begins to decrease. The system only stores a tiny amount of free magnetic energy on top of the potential energy, which cannot be countervailed by dissipation. The dissipation is shown in Baumann, Galsgaard, and Nordlund (2012) to be to lowest order proportional to the driving speed. Dissipation itself is suggestive of parallel electric fields, as the current in the corona is well aligned with the magnetic field. The parallel electric field $E_\parallel$ is of high interest in conjunction with particle acceleration.

Comparing the evolution with increasing boundary displacement of the non-

stratified and stratified cases leads to the following observation: The density profiles of all non-stratified simulation runs develop congruently with increasing displacement, independent of the driving speed as long as it is well below the Alfvén and sound speed, in which case also the dissipation normalized to the average driving speed at a given boundary displacement is almost superposable. Otherwise, if the ratio between Alfvén and driving speed is approaching unity, the dissipation level deviates perceptibly from the asymptotic behavior of the non-stratified runs. Advancing in time, the null-point in the stratified case moves up faster than in the non-stratified runs, due to dense material (over 1000 times denser than in the non-stratified cases) slowly rising from the lower boundary through the transition region into the corona. This behavior is physical as long as the driving at the photospheric boundary is sufficiently slow. If it is comparable to or faster than the sound speed the global plasma motion changes significantly and discrepancies from the common asymptotic behavior of all other conducted runs occur, in the magnetic dissipation behavior as well as in the magnetic energy evolution. In conclusion, the stratified simulation runs are much more sensitive to the driving speed than non-stratified runs, which initially have a constant density.

In Baumann, Galsgaard, and Nordlund (2012) it is further shown that the total dissipation is approximately independent of the thickness ΔL of the current sheet and hence approximately independent of the grid size, as the numerical models generally resolve current sheets down to a few grid cells. The total dissipation only depends on the change in magnetic field across the current sheet and the current sheet extent A_{CS}, where the current sheet covers a volume of $V_{CS} = \Delta L \cdot A_{CS}$. This results in the important conclusion, that the diffusive electric field as well as the total amount of dissipation is to a lowest order independent of the amount of numerical resistivity.

3D MHD simulations based on observed solar magnetogram of active regions have previously been performed by Masson *et al.* (2009), on a mesh of 237 x 201 x 201, which in fact inspired the MHD part of the experiment presented here. Javadi *et al.* (2011) investigated the heating mechanism of the corona in bright points using an potential field extrapolation of a SOHO magnetogram. But in general simulations based on extrapolations of photospheric magnetic fields are rare, although magnetograms have been used extensively to investigate 3D reconnection topologies (Close *et al.*, 2003; des Jardins *et al.*, 2009), as well as in test particle studies (Arzner and Vlahos, 2006). Arzner and Vlahos (2006) performed a linear force-free magnetic field extrapolation and traced electrons in this time-independent field configuration in order to deduce from their energy spectra the emission spectra. They used a test particle approach (see Section 3.2), where again no back-reactions from the particles onto the fields was included, unlike the experiment introduced in the next Section.

4.2   PIC Simulation

For the *Photon-Plasma* PIC code simulations an evolved (2 h 40 min of real solar time into an MHD simulation) and scaled (according to the guidelines in Section 3.4) MHD simulation dataset with a driving speed of $20\,\mathrm{km\,s^{-1}}$ serves as a starting point. A set of PIC simulations utilizing an MHD simulation data cut-out of size 44 x 25 16 Mm on a uniform mesh with up to 2518 x 1438 x 923
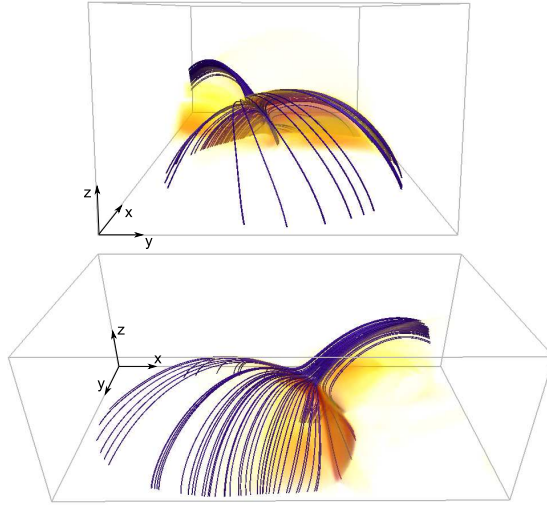
Figure 4.4: Initial PIC simulation snapshot. The blue lines represent the magnetic field lines and the semitransparent volume illustrates the highest electric current density (yellow-lower and orange-highest)

grid points and cell sizes down to $17.5\,\mathrm{km}$ are performed. About 30 real time solar seconds are covered. The velocities of the 20 electrons and 20 protons per cell and the fields are initialized as described in Section 3.5. The boundaries of the computational box are fixed for the fields and open for particles. The initial magnetic field configuration carried over from the MHD simulation is shown in Figure 4.4. A strong current sheet can be seen on the side of the dome, where the driving motion in the MHD simulation has been applied.

Systematic electric fields build up in the fan-plane, where the current sheet is located and the electric current density peaks. The current sheet is a consequence of the shearing of the outer and inner fan-plane magnetic field lines, which arose mainly from the applied boundary motion during the MHD simulations, which is still partially maintained by the chosen boundary conditions; new particles created in the ghost cells are specified according to the MHD snapshot parameters. Similar to the diffusive electric field in the MHD simulation, which is not inherited by the PIC simulation, an $E_\parallel$ component builds up quickly, with peak values in the current sheet, equivalent to the location of the diffusive electric field in the MHD simulations. The overall magnitudes of the electric field, being on the order of $20 - 200\,\mathrm{mV\,m^{-1}}$, are generally far below the one from the MHD simulations, after the modifications described in Section 3.4 have been rescaled according to the following equation, providing the energy-charge relation of a particles that experiences a DC electric field acceleration

$$q\,E\,L = \mu_0^{-2} \left(\frac{\Delta B}{\Delta L} \right)^2 \frac{m_e}{2n^2q^2}, \tag{4.2}$$

where L is the distance covered by the electron with mass m_e. The right hand side of Equation (4.2) can be reformulated by replacing the ΔL with the typical current sheet thickness and expressing the magnetic field change ΔB with help

35

of the Alfvén speed to show that all its parameters are determined by macroscopic quantities. This leads to the conclusion that the electric field is inversely proportional to the elementary charge per particle, which was the main modified natural constant in the different simulation runs. The systematic DC electric field, which is mostly parallel to the magnetic field inside the current sheet, causes particles to experience a strong acceleration parallel to the magnetic field as long as they remain inside the current sheet. Most non-thermal particles are located inside the current sheet and win energies of about $4\,\mathrm{keV}$ in just a few seconds, as a result of the DC electric field. Their energy distribution converges in only a couple of seconds to a stable power-law with $dN/dE \sim E^{-1.75}$ (N is the number of particles per unit energy), showing the efficiency of the acceleration. This is a somewhat harder electron distribution compared to what is observed in the real Sun, where the (absolute value of the) index is reported to be ≥ 2 (Krucker *et al.*, 2010).

As the current sheet area only makes up a small fraction of the domain, most particles are not significantly accelerated. The thermal electron distribution is preserved by (the majority of) the particles which do not enter the acceleration region of the current sheet and hence remain in the Maxwellian distribution, as they were initialized. The current sheet is mainly maintained by the particles in the lowest part of the non-thermal particle energy distribution. On the other hand up to 50% of the total energy resides in the power-law tail of the energy distribution, while there is only a fraction of 5% of all particles. This low particle number assures that the polarization electric field does not become large.

The power-law index is presumably a consequence of the DC systematic electric field in the fan-plane and is just as the energy cut-off likely determined by the magnetic field geometry. The fastest electrons reach velocities on the order of $10\,\mathrm{keV}$. As the simulation takes place several hours before the C-flare occurrence in this particular active region, we expect higher particle energies during the flare event. Additionally one needs to keep in mind that we simulate 'quiescent' times, which becomes clear from the MHD simulations that did not result in a solar flare, due to the insufficient amounts of free energy available to the system. Nevertheless, the nature of the particle acceleration mechanism is likely to be the same also during the solar flare event. In fact, the lower boundary impact area of non-thermal particles in the simulation collected over a time interval of five seconds is shown in Figure 4.5. Non-thermal electrons are to a large extent responsible for the observed hard X-ray signatures, shown as red contours for this specific solar flare event in Figure 4.3, which correlates rather well with the impact area of the non-thermal particles in our numerical experiment.

The different modifications of the natural constants turn out to result in similar electric fields in the current sheet as well as nearly equivalent power-law indices, as long as the initial temperature is kept sufficiently low. Their thermal distributions are almost congruent, independent of the type of modifications applied. Increasing the temperature drowns the non-thermal distribution, although the electric field range in the current sheet remains about the same.

Solar flares are in general believed to be triggered by shearing and twisting motions (Amari *et al.*, 1996) at the photospheric boundary or by MHD instabilities, such as the kink instability (Kliem, Titov, and Török, 2004). But it is also known from observations that the *photospheric* flux distribution does not change much during the eruptive event itself, which implies that the coronal

Figure 4.5: Impact area of non-thermal electrons in a cut-out of the simulation box. Additionally magnetic field lines passing close to the null-point are over-plotted.

magnetic field must be in a highly non-potential state before the flare starts.

We used the method of applying shearing motions at the boundary and although the applied speeds are exaggerated compared to the observed photospheric speeds the system could not reach a state in which a solar eruption is possible. However, this does not prevent us from studying the particle acceleration mechanism, since the overall magnetic structures during the flare event are already established several hours prior to the eruption. And, as shown, the impact area of the particles accelerated to non-thermal energies in our simulations are similar to what is observed for this particular event.

5 CORONAL HOLE PLASMA ACCELERATION

The solar jet experiment presented in this Chapter is similarly to the active region experiment a continuation of an MHD simulation using the *Photonplasma* PIC code. Instead of starting from a magnetogram as in the previous experiment, the second of the mentioned main approaches (see Chapter 3.6) to simulate the coronal magnetic field is used: A flux emergence simulation.

Simulating a flux emergence process from several Mm below the photosphere to several tens of Mm into the corona is computationally a challenging task, as the density changes by a factor of more than 1×10^8. The low density in the corona directly constrains the time-step through the Alfvén speed for explicit MHD codes and hence leads to expensive simulations. In addition to these constraints, the presence of shocks often observed in such simulations provokes the necessity to handle the resistivity and viscosity accordingly to keep the simulation stable.

There has been a lot of work done in the context of simulating flux emergence events. I do not want to go into a detailed review of this work here, as we mostly concentrate on the particle acceleration aspect of the PIC simulation and use the emerging flux rope method more as a tool to create a characteristic arrangement of the coronal magnetic field. I refer to the two reviews of Hood, Archontis, and MacTaggart (2011) and Moreno-Insertis (2007) for further details on flux emergence simulations.

The jet experiment presented here is similar to the flux emergence simulation conducted by Moreno-Insertis, Galsgaard, and Ugarte-Urra (2008), whose setup is motivated by observations on March 10, 2007, by the HINODE satellite in a coronal hole region. Solar eruptive events are often associated with emerging photospheric flux (e.g. Jiang *et al.*, 2007). In this case a jet appeared in the EIS and XRT observations simultaneously to an emergence of a magnetic bipole at the photosphere. The EIS instrument is capable of providing information on velocity and density and therefore gives a convenient occasion for comparisons to and setting of initial conditions of numerical simulations.

The main difference to the simulation by Moreno-Insertis, Galsgaard, and Ugarte-Urra (2008) is the much higher spatial resolution, partly due to the implementation of a stretched mesh in all three directions. The results of the flux emergence experiment by Moreno-Insertis, Galsgaard, and Ugarte-Urra (2008) are briefly summarized in the next section.

5.1 Emerging Flux Tube as Initiator of a Coronal Jet

The jet experiment makes use of the emergence of a buoyant subphotospheric magnetic flux tube to form bipolar magnetic spots, leading to the formation of arch-shaped current sheets containing reconnection sites from which high velocity plasma outflows — so-called hot plasma jets — emerge. The flux tube, positioned in the solar interior at the start of the simulation, is cylindrical and twisted, analogously to the one defined in Fan (2001). The twist of the flux tube is a necessity, in order to allow the flux tube to retain its form, as shown by Abbett, Fisher, and Fan (2000). The twisted property of magnetic flux tubes is also confirmed by observations (e.g. Caligari, Moreno-Insertis, and Schussler, 1995). The magnetic flux tube is initially in pressure equilibrium with its surrounding. As the magnetic field of the tube (internal) is much stronger than the background magnetic field (external), we may write

$$P_{ext} = P_{int} + P_{m,int} = P_{int} + \frac{B^2}{2\mu_0}. \tag{5.1}$$

Assuming an ideal gas law $P = \frac{\rho_m k_B T}{\mu m_u}$ and $T_{ext} = T_{int}$, we conclude that, because of the additional magnetic pressure term, the gas density inside the tube must be lower than in its surrounding. Hence there is a buoyancy force acting against the tension force of the magnetic field of the flux tube. If a density perturbation at the center of the flux tube is introduced, the tube rises due to the gas pressure difference between the inside and outside of the flux rope and extends against the force of gravity and the tension force from the bending magnetic field of the flux tube, as discussed in Archontis *et al.* (2004).

When approaching the photosphere the flux tube slows down. Here the plasma beta becomes of the order of unity, which suddenly causes the magnetic pressure to win in importance. The magnetic pressure of the tube acts now against the gas and magnetic pressure of the surrounding, and the tube expands rapidly into the rare corona. The penetrating emerging flux at the photosphere causes a destabilization of the coronal magnetic field, which leads to the formation of current sheets and reconnection regions at the interface of the two connectivity domains. The background magnetic field and the flux tube magnetic field are chosen to become almost exactly anti-parallel at their first encounter. Subsequent flux emergence of the twisted magnetic field leads to several reconnection events. From the main reconnection region two hot plasma jets are expelled as a result of the gas pressure gradient (causing velocities on the order of the local sound speed) and as a result of the Lorentz force (causing velocities on the order of the local Alfvén speed).

5.2 The MHD Experiment

The fully 3D resistive, compressible MHD simulation, is performed using the *Stagger* code, including gravity, but not taking into account radiative cooling and heat conduction effects. The experiment covers a vertical physical height of 32.5 Mm and horizontally extends to 33.8 Mm and 38.1 Mm in the x and y directions respectively. The numerical grid, of size 512^3, is non-uniform in all
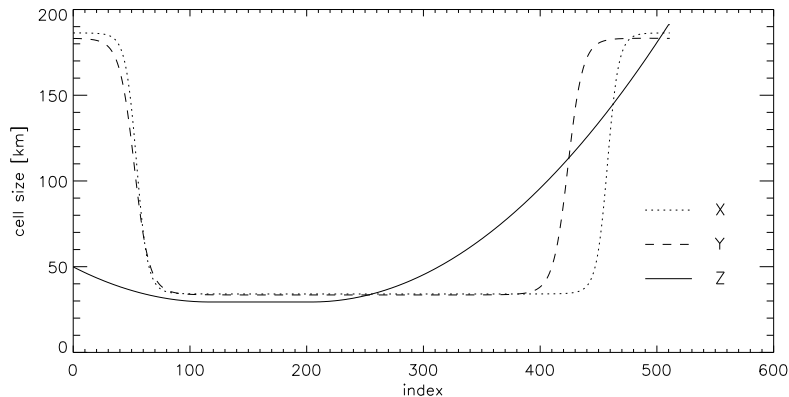
Figure 5.1: Cell sizes in km for all three axis against the indices. The z axis is the height.

three directions. Its minimal grid spacing of (x_{min}, y_{min}, z_{min})=(34.1, 33.5, 29.4) km is centered around the region, in which later in the experiment reconnection will take place. Figure 5.1 visualized the stretching of the mesh. The boundaries are periodic in x and y and closed/damped in the vertical direction.

A simple, stratified atmospheric profile is imposed, see Figure 5.2, in which the lowest 3.7 Mm of the total computational box height are still below the photosphere. From the lower boundary of the photosphere to the transition region extends a 2 Mm "chromosphere", in which the temperature is assumed to be constant at $\approx 5.6 \times 10^4$ K. Above that there is a steep temperature gradient, representing the transition region, with a physical height of 2 Mm. On top of that resides the corona, covering about 24.8 Mm with an initially constant temperature of around 2.2×10^6 K. The density of the corona is about $6 \times 10^8 \mathrm{cm}^{-3}$, an order of magnitude smaller than what is estimated from active regions (Aschwanden, 2005), consistent with the fact that the model represents a coronal hole region of the Sun.

In order to obtain a hydrostatic background profile we start by setting a one dimensional temperature profile as a function of height. From

$$\frac{dP}{dz} = -\rho_m g \tag{5.2}$$

and

$$\rho_m = \mu \cdot m_u \cdot \frac{P}{k_b \cdot T} \tag{5.3}$$

we integrate Equation (5.2) to obtain the pressure and further receive from Equation (5.3) the density. On top of that we define a constant background magnetic field of magnitude 3.3 Gauss, featuring an inclination of 65 degrees in the yz-plane. The flux tube is positioned along the y-axis, 1.7 Mm below the photosphere and has a maximum magnetic field strength of 1000 Gauss. The imposed background magnetic field is present throughout the entire box, representing the open magnetic field in which plasma can actually reach into the interplanetary space; i.e., a typical magnetic field configuration of coronal holes.
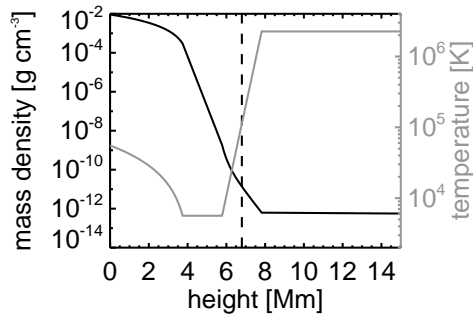
40

Figure 5.2: Atmospheric profile. The mass density (black) and the temperature (gray) are plotted against the box height in Mm. The dashed line represents the lower end of the cut-out used for the PIC simulation.

This overall field does not significantly influence the flux tube motion below the photosphere, since it is much below the magnetic field strength of the flux tube and the plasma motion is dominated by the gas pressure.

In addition to the high density plasma emerging into the corona from lower heights, rendering the particle densities horizontally highly inhomogeneous, there is a steep vertical particle density gradient, due to the initial stratification profile applied. Passing such an evolved MHD dataset to the PIC code would result in strong fluctuations in the electric field, as pseudo-particles with different weights move into low density regions, causing sudden increases in the charge density, which hence lead to strong fluctuations of the electric field. These kind of numerical fluctuations would disturb the investigation of the acceleration mechanism at work. We therefore cut away the lower, very dense parts of the MHD simulation domain (see dashed line in Figure 5.2[1]) before passing a subregion of the MHD dataset of extent 22 x 22 x 22 Mm to the PIC code. Even after cutting away the lower parts of the MHD dataset this experiment is, due to the highly varying number densities in the horizontal direction, numerically more challenging with respect to keeping numerical noise low, in comparison to the active region experiment discussed before.

At the specific time of the MHD simulation where a snapshot is passed on to the PIC code the dense plasma enclosed in the flux rope has almost completely been reconnected and ejected out of the reconnection region. Some of it also drained off along the magnetic field lines as a result of gravity. The jet velocities are of the order $400 - 800 \, \text{km s}^{-1}$.

The interface between the MHD and PIC simulation is again treated as described in Chapter 3.5. The boundaries are left open for particles and fixed for the fields. Figure 5.3 shows the initial magnetic field configuration, together with the current sheet that extents along the flux rope, where reconnection with the overlying (green) magnetic field is taking place. To the left of the flux rope in the left hand side panel of Figure 5.3 a turbulent area has developed as a consequence of down flowing material interacting with material ejected from the reconnection site. To the right of the flux rope a new connectivity

---

[1]Note, that Figure 5.2 shows the initial atmospheric profile, while an evolved state of the MHD simulation is used as PIC simulation input.
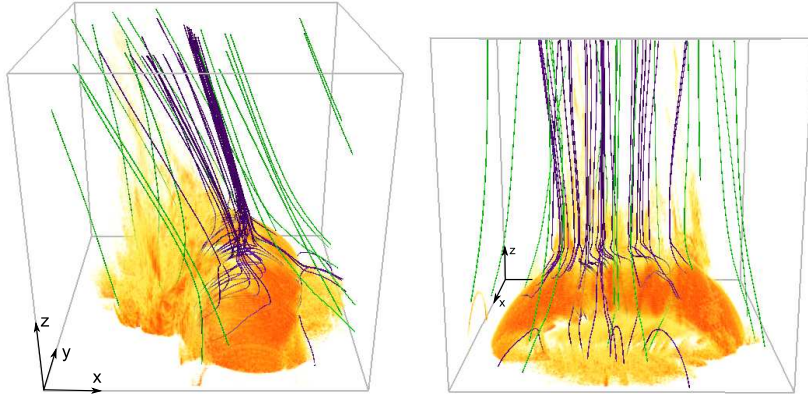
Figure 5.3: PIC simulation initial state. Magnetic field lines in blue are chosen to be close to the low magnetic field region, while the green field lines highlight the overlying coronal magnetic field. The electric current sheet density is shown in a semitransparent volume covering from yellow (low) to red (high) in intensity.

domain has formed by newly reconnected magnetic field lines, as described in Moreno-Insertis, Galsgaard, and Ugarte-Urra (2008, region 3, Figure 2).

Mainly two different grid dimensions are used; 400^3 and 800^3. The mesh is uniform and the cell sizes are 55 km and 27.5 km. Up to 7.5 seconds of solar time are simulated, with 20 particles per cell per species. In order to resolve microscopic scales of the plasma, the charge density, the speed of light as well as the proton-to-electron mass ratio have been modified, see Chapter 3.4. Two modification sets are introduced here, which differ by a factor of two in the choice of the elementary charge. The Debye length and skin depth are resolved by four cells in the current sheet, while one gyro radius contains several tens of cells in that area. The diffusive electric field ($E_{res} = \eta \mathbf{j}$ from the MHD simulation, where η is the locally defined resistivity and $\mathbf{j}$ the current density) contains the $E_{\parallel}$. A comparison of the locations of E_{res} and the self-consistently established $E_{\parallel}$ in the PIC simulation shows that both peak in the dome-shaped current sheet between the two connectivity domains. As a consequence, a non-thermal electron energy tail distribution builds up in the reconnection region, featuring a power-law index of $\frac{dN}{dln(E)}$ in the range -0.6 – -0.7. The overall distribution shows several peaks already from the beginning, mainly as a result of the two different plasmas flowing into the reconnection region; on one hand there is the low density but high temperature coronal plasma and on the other hand there is the cool, dense plasma contained in the flux rope. These are transferred to the PIC simulation through the bulk flow. In addition to that, the distribution coming from the currents in the MHD snapshot is added to this superposition of energy distribution functions (current drift velocity, as in Equation (3.20)).

The main acceleration mechanism is found to, also in this case, be a systematic, slowly fluctuating electric field peaking in the current sheet. The electric field is mainly directed along the magnetic field. The current sheet thickness is hence determining in particular the shape of the non-thermal energy distribution, by limiting the number of particles that can enter it. Particles which have once reached the current sheet are accelerated and therefore contribute a

share to the current density required by the magnetic field geometry. Due to the low magnetic field strength, their gyro radius is increased, so that they may feel differently oriented electric field areas during one gyration period. This may drop them out of the current sheet, which gives rise to a need for new particles entering this region to become accelerated, in order to maintain the electric current.

Jets have been observed in several different wavelengths, of which X-ray jets are the largest jet events. Jets are in general following magnetic field lines and there is an entire zoo of different jets reaching speeds from about $10 \, \text{km} \, \text{s}^{-1}$ to about $1000 \, \text{km} \, \text{s}^{-1}$, with an average of 150–$200 \, \text{km} \, \text{s}^{-1}$, and releasing energies on the order of 10^{27}–10^{29} ergs (e.g. Shimojo *et al.*, 1996; Shimojo and Shibata, 2000; Bain and Fletcher, 2009; Savcheva *et al.*, 2007). Shibata *et al.* (1994) concluded from observations of an active region that, similarly to solar flare plasma eruptions, solar jets must be driven by reconnecting magnetic fields. PIC simulations of reconnection region which give rise to strong outflow jets have been previously performed by Karimabadi, Daughton, and Scudder (2007) and Shay, Drake, and Swisdak (2007)), who focused their simulations on the small diffusion region. On large scales, using the test particles approach, Rosdahl and Galsgaard (2010) investigated the charged particle motion in a dataset of a flux emergence experiment. Apart from the already mentioned studies by Archontis *et al.* (2005) and Moreno-Insertis, Galsgaard, and Ugarte-Urra (2008), Gontikakis, Archontis, and Tsinganos (2009) conducted a similar simulation, but with two successive flux emergence events, spatially close enough that reconnection takes place between them. A current sheet formed, at which outer edge reconnection jets with local Alfvén velocities on the order of $100 \, \text{km} \, \text{s}^{-1}$ occur, which nicely compare with the presented TRACE observations. Pariat, Antiochos, and DeVore (2009) introduced a model for solar polar jets with a follow-up article (Pariat, Antiochos, and DeVore, 2010) explaining among numerous simulation outcomes, the intermittency of jets.

6 SUMMARY AND CONCLUSIONS

This work has focused on providing the first steps towards bridging the immense gap between microscopic scales (generation of resistivity) and macroscopic scales (generation of magnetic eruptive phenomena) on the Sun. A primary goal has been to study the mechanism of particle acceleration in different magnetic environments of the solar atmosphere. Hence, offering a method for coupling MHD and PIC models is one of the novel cornerstones of this project.

Kinetic simulations covering fully realistic scales of solar phenomena will never be possible, even on the largest supercomputer ever to be built. However, as shown in the present thesis, this challenge can be faced by making the dynamical span small enough to be resolved, while still keeping the different scales reasonably well separated, and retaining as much as possible of the ordering in the hierarchy of length and times scales.

Nonetheless, in the process of obtaining the results presented here over 50 million BlueGene/P core hours were spent, in simulations with up to 136 billion particles and 3.5 billion cells. A single simulation produced up to 5 Terabytes of data, the analysis of which was naturally a challenge, also from the hardware point of view. The access to such extensive resources was rendered possible through a John von Neumann Institute for Computing (NIC) grant, and through a subsequent Partnership for Advanced Computing in Europe (PRACE) grant. Due to the very successful scaling results obtained on the current system (with up to 2^{18} processors being used in parallel), it is expected that the performance of the simulation codes remains excellent even on systems with millions of cores, allowing investigations with even higher resolutions in the future.

The MHD active region experiment made use of an increase in driving speed when compared to reality, saving large amounts of computing power and making it possible to simulate the long buildup phase ahead of large solar eruptions. It was demonstrated that, as long as the driving speed remains smaller than the local Alfvén speed and sound speed, the results are essentially equivalent, and can be scaled to solar values. The restriction on velocities was shown to be more severe in simulations with a stratified atmosphere than in simulations with an initially constant density. However, if the constraints are complied with, stratified and non-stratified simulation runs show striking similarities.

The experiments were started from a potential extrapolation of a SOHO magnetogram, providing the main aspects of the magnetic topology of this particular solar active region. Despite the exaggerated driving, no flare like event emerged. It can be concluded that with the applied boundary driving, with only horizontal motions, and with a mainly compressive character, not enough free energy can be stored in the system to cause a sudden and powerful energy release. Therefore, flux emergence or twisting motions must have been present

44

in the real Sun, simultaneously with the observed horizontal motion.

The level of dissipation in the current sheet was shown to be, to lowest order, independent of the numerical resolution. Within the limits of the resolution we can afford the currents sheets we obtain are essentially monolithic, but we assume that at higher resolutions large scale current sheets will tend to fragment and break up.

The subsequent PIC simulations of this solar active region event are the first of a kind to study self-consistent particle acceleration in a realistic topology. The specifically chosen active region has been used because of its well defined topology, which has previously been investigated by Masson *et al.* (2009). The coupling between MHD and PIC simulations was implemented by using the magnetic fields from the MHD dataset, while only the advective electric field was passed on to the PIC setup. The fields were held fixed at the boundaries. Particles were initially given velocities that consist of the MHD bulk speed, a random thermal velocity, and component related to the electric current. The boundaries were chosen to be open for particles, so they can leave and enter the computational domain freely from a surrounding layer where the initial values are maintained.

A major finding from these investigations is the formation of a power-law of accelerated electrons, which turned out to be the result of a systematic ('DC') electric field particle acceleration mechanism, predominantly present in the current sheet of the fan-plane. A similar result was obtained in the coronal hole experiment, even though the magnetic field geometries are quite different. While the low magnetic field region in the active region experiment is localized to a small volume near a magnetic null-point, in the coronal hole experiment it extends over the entire reconnection region, as reflected by the occurrence of several null-points. The guide field in this reconnection geometry is very small, unlike in the active region experiment, where the guide field is dominating in the fan-plane current sheet. Another difference between the experiments is the enormous density contrasts related to the emergence of dense material from sub-photospheric layers in the coronal hole experiment, which leads to numerical noise, especially in the electric field. The coronal hole experiment further includes a turbulent region, which we speculate, given sufficiently high spatial resolution and sufficiently long simulation times, might be able to host stochastic acceleration sites.

Despite the diverseness, the two types of experiments investigated showed a similar behavior with respect to particle acceleration. We take that as evidence indicating that the power-law nature of the non-thermal particle distribution is very robust, and that the DC acceleration mechanism may be a generic source of at least the lower energy part of the non-thermal particle distribution, independent of the drastic modifications of natural constants applied to the parameter setup of the PIC simulations.

The modifications change the magnitudes of the simulation quantities in a way which can be subjected to scaling arguments, in order to estimate the corresponding solar values. Further investigations are needed to test more carefully to what extent such modification leave the underlying physics qualitatively unchanged. However, some results seem to be of such a fundamental nature that they are likely to be true, independent of the physical modifications.

It was shown, for example, that significant DC electric fields can exist, even in a collisionless environment, without being completely short-circuited by feed-

back effects (polarization electric field). This is due to the limited time particles can stay in the accelerating electric field and hence due to the limited number of particles accelerated to non-thermal energies. The reason for this is that particles get lost from the current sheet, either by following magnetic field lines that do not stay in the current sheet — this is particularly the case in the active region experiment — or because they enter a region with a very weak magnetic field, as they do in the coronal hole experiment.

In the Sun (and in numerical experiments with sufficient resolution) the thickness of current sheets is likely to be controlled by kinetic effects on microscales, and that, together with the small scale magnetic field topology and its evolution then sets constraints on how many, how much and how long particles are accelerated in the current sheet electric field. The electric field itself is a necessity, as it ensures a net charged particle flux in the current sheet, as required by the associated magnetic field configuration. The power-law is hence presumably a consequence of the probability for a particle to stay in the current sheet for a certain time.

In Section 2.4.2 the most important observational constraints for solar eruptions were listed. Some of them are consistent with the results obtained in the numerical experiments; e.g. the non-thermal energy-tail featuring a power-law electron energy distribution, a fast electron acceleration process, and the correlation of the impact regions of non-thermal particles with the X-ray emission images. However, the energies of the non-thermal electrons obtained in the two PIC simulations are rather at the lower end of the observed non-thermal distributions, hence contain only a fraction of the high-energy particles estimates of solar flares.

We speculate that the DC electric field explains the lower energy power-law, up to energies of a few hundred keV in the Sun, while its steeper extension part is presumably of another origin, such as stochastic acceleration. The current study is, despite the huge resources that have been available, still bound by numerical constraints that necessarily limit the explorations of parameter space, and basically prevent a study of stochastic particle acceleration mechanisms. Higher resolution and longer duration simulations are needed to resolve turbulent structures.

We expect that particular care must be taken when choosing the mass ratio between electrons and ions when studying stochastic acceleration, since the mass ratio probably plays an important role in producing the observed differences in energy gain. Studying stochastic acceleration is furthermore difficult because a larger number of particles are needed. The steeper power-laws observed at high energies means a very tiny probability of finding particles in this energy domain.

For now it can be concluded that the low energy part of the power-law electron distribution in eruptive solar events is very likely due to DC electric field acceleration.

BIBLIOGRAPHY

Abbett, W.P., Fisher, G.H., Fan, Y.: 2000, The Three-dimensional Evolution of Rising, Twisted Magnetic Flux Tubes in a Gravitationally Stratified Model Convection Zone. *Astrophys. J.* **540**, 548 – 562. doi:10.1086/309316.

Amari, T., Luciani, J.F., Aly, J.J., Tagger, M.: 1996, Very Fast Opening of a Three-dimensional Twisted Magnetic Flux Tube. *Astrophys. J. Lett.* **466**, L39. doi:10.1086/310158.

Anastasiadis, A.: 2002, Acceleration of solar energetic particles: the case of solar flares. *Journal of Atmospheric and Solar-Terrestrial Physics* **64**, 481 – 488. doi:10.1016/S1364-6826(02)00003-2.

Archontis, V., Hood, A.W.: 2008, A Flux Emergence Model for Solar Eruptions. *Astrophys. J. Lett.* **674**, L113 – L116. doi:10.1086/529377.

Archontis, V., Moreno-Insertis, F., Galsgaard, K., Hood, A., O'Shea, E.: 2004, Emergence of magnetic flux from the convection zone into the corona. *Astron. Astrophys.* **426**, 1047 – 1063. doi:10.1051/0004-6361:20035934.

Archontis, V., Moreno-Insertis, F., Galsgaard, K., Hood, A.W.: 2005, The Three-dimensional Interaction between Emerging Magnetic Flux and a Large-Scale Coronal Field: Reconnection, Current Sheets, and Jets. *Astrophys. J.* **635**, 1299 – 1318. doi:10.1086/497533.

Arzner, K., Vlahos, L.: 2006, Gyrokinetic electron acceleration in the force-free corona with anomalous resistivity. *Astron. Astrophys.* **454**, 957 – 967. doi:10.1051/0004-6361:20064953.

Aschwanden, M.J.: 1999, Particle Acceleration and Kinematics in Solar Flares and the Solar Corona. In: Wilson, A., *et al.*(eds.) *Magnetic Fields and Solar Processes*, *ESA Special Publication* **448**, 1015.

Aschwanden, M.J.: 2002, Particle acceleration and kinematics in solar flares - A Synthesis of Recent Observations and Theoretical Concepts (Invited Review). *Space Sci. Rev.* **101**, 1 – 227. doi:10.1023/A:1019712124366.

Aschwanden, M.J.: 2005, *Physics of the Solar Corona. An Introduction with Problems and Solutions (2nd edition)*.

Aulanier, G., Pariat, E., Démoulin, P.: 2005, Current sheet formation in quasi-separatrix layers and hyperbolic flux tubes. *Astron. Astrophys.* **444**, 961 – 976. doi:10.1051/0004-6361:20053600.

Bain, H.M., Fletcher, L.: 2009, Hard X-ray emission from a flare-related jet. *Astron. Astrophys.* **508**, 1443 – 1452. doi:10.1051/0004-6361/200911876.

Baker, D., van Driel-Gesztelyi, L., Mandrini, C.H., Démoulin, P., Murray, M.J.: 2009, Magnetic Reconnection along Quasi-separatrix Layers as a Driver of Ubiquitous Active Region Outflows. *Astrophys. J.* **705**, 926 – 935. doi:10.1088/0004-637X/705/1/926.

Bárta, M., Büchner, J., Karlický, M.: 2010, Multi-scale MHD approach to the current sheet filamentation in solar coronal reconnection. *Advances in Space Research* **45**, 10 – 17. doi:10.1016/j.asr.2009.07.025.

Baum, P.J., Bratenahl, A.: 1980, Flux linkages of bipolar sunspot groups - A computer study. *Solar Phys.* **67**, 245 – 258. doi:10.1007/BF00149805.

Baumann, G., Nordlund, Å.: 2012, Particle-In-Cell Simulation of Electron Acceleration in Solar Coronal Jets. *ArXiv e-prints.*

Baumann, G., Galsgaard, K., Nordlund, Å.: 2012, 3D Solar Null Point Reconnection MHD Simulations. *ArXiv e-prints.*

Baumann, G., Haugbølle, T., Nordlund, Å.: 2012, Kinetic modeling of particle acceleration in a solar null point reconnection region. *ArXiv e-prints.*

Baumjohann, W., Treumann, R.A.: 1996, *Basic space plasma physics.*

Birdsall, C.K.: 1991, Particle-in-cell charged-particle simulations, plus Monte Carlo collisions with neutral atoms, PIC-MCC. *IEEE Transactions on Plasma Science* **19**, 65 – 85. doi:10.1109/27.106800.

Birn, J., Priest, E.R.: 2007, *Reconnection of magnetic fields : magnetohydrodynamics and collisionless theory and observations.*

Boyd, T.J.M., Sanderson, J.J.: 2003, *The Physics of Plasmas.*

Brown, J.C.: 1971, The Deduction of Energy Spectra of Non-Thermal Electrons in Flares from the Observed Dynamic Spectra of Hard X-Ray Bursts. *Solar Phys.* **18**, 489 – 502. doi:10.1007/BF00149070.

Brown, J.C., Turkmani, R., Kontar, E.P., MacKinnon, A.L., Vlahos, L.: 2009, Local re-acceleration and a modified thick target model of solar flare electrons. *Astron. Astrophys.* **508**, 993 – 1000. doi:10.1051/0004-6361/200913145.

Caligari, P., Moreno-Insertis, F., Schussler, M.: 1995, Emerging flux tubes in the solar convection zone. 1: Asymmetry, tilt, and emergence latitude. *Astrophys. J.* **441**, 886 – 902. doi:10.1086/175410.

Cargill, P.J.: 1991, The interaction of collisionless shocks in astrophysical plasmas. *Astrophys. J.* **376**, 771 – 781. doi:10.1086/170325.

Chifor, C., Young, P.R., Isobe, H., Mason, H.E., Tripathi, D., Hara, H., Yokoyama, T.: 2008, An active region jet observed with Hinode. *Astron. Astrophys.* **481**, L57 – L60. doi:10.1051/0004-6361:20079081.

Close, R.M., Parnell, C.E., Mackay, D.H., Priest, E.R.: 2003, Statistical Flux Tube Properties of 3D Magnetic Carpet Fields. *Solar Phys.* **212**, 251 – 275.

Dahlburg, R.B., Einaudi, G.: 2002, MHD unstable modes in the 3D evolution of 2D MHD structures and the diminished role of coalescence instabilities. *Physics Letters A* **294**, 101 – 107. doi:10.1016/S0375-9601(02)00027-0.

Dalla, S., Browning, P.K.: 2005, Particle acceleration at a three-dimensional reconnection site in the solar corona. *Astron. Astrophys.* **436**, 1103 – 1111. doi:10.1051/0004-6361:20042589.

Dalla, S., Browning, P.K.: 2006, Jets of Energetic Particles Generated by Magnetic Reconnection at a Three-dimensional Magnetic Null. *Astrophys. J. Lett.* **640**, L99 – L102. doi:10.1086/503302.

Dalla, S., Browning, P.K.: 2008, Particle trajectories and acceleration during 3D fan reconnection. *Astron. Astrophys.* **491**, 289 – 295. doi:10.1051/0004-6361:200809771.

Demoulin, P., Henoux, J.C., Mandrini, C.H.: 1994, Are magnetic null points important in solar flares ? *Astron. Astrophys.* **285**, 1023 – 1037.

des Jardins, A., Canfield, R., Longcope, D., McLinden, E., Dillman, A.: 2009, Signatures of Magnetic Stress Prior to Three Solar Flares Observed by RHESSI. *Astrophys. J.* **693**, 886 – 893. doi:10.1088/0004-637X/693/1/886.

Drake, J.F., Shay, M.A., Thongthai, W., Swisdak, M.: 2005, Production of Energetic Electrons during Magnetic Reconnection. *Physical Review Letters* **94**(9), 095001. doi:10.1103/PhysRevLett.94.095001.

Drake, J.F., Swisdak, M., Che, H., Shay, M.A.: 2006a, Electron acceleration from contracting magnetic islands during reconnection. *Nature* **443**, 553 – 556. doi:10.1038/nature05116.

Drake, J.F., Swisdak, M., Schoeffler, K.M., Rogers, B.N., Kobayashi, S.: 2006b, Formation of secondary islands during magnetic reconnection. *Geophys. Res. Lett.* **33**, 13105. doi:10.1029/2006GL025957.

Dreicer, H.: 1960, Electron and Ion Runaway in a Fully Ionized Gas. II. *Physical Review* **117**, 329 – 342. doi:10.1103/PhysRev.117.329.

Esirkepov, T.Z.: 2001, Exact charge conservation scheme for Particle-in-Cell simulation with an arbitrary form-factor. *Computer Physics Communications* **135**, 144 – 153. doi:10.1016/S0010-4655(00)00228-9.

Fan, Y.: 2001, The Emergence of a Twisted Ω-Tube into the Solar Atmosphere. *Astrophys. J. Lett.* **554**, L111 – L114. doi:10.1086/320935.

Fermi, E.: 1949, On the Origin of the Cosmic Radiation. *Physical Review* **75**, 1169 – 1174. doi:10.1103/PhysRev.75.1169.

Filippov, B., Golub, L., Koutchmy, S.: 2009, X-Ray Jet Dynamics in a Polar Coronal Hole Region. *Solar Phys.* **254**, 259 – 269. doi:10.1007/s11207-008-9305-6.

Georgobiani, D., Kosovichev, A.G., Nigam, R., Nordlund, Å., Stein, R.F.: 2000, Numerical Simulations of Oscillation Modes of the Solar Convection Zone. *Astrophys. J. Lett.* **530**, L139 – L142. doi:10.1086/312490.

Giovanelli, R.G.: 1946, A Theory of Chromospheric Flares. *Nature* **158**, 81–82. doi:10.1038/158081a0.

Gontikakis, C., Archontis, V., Tsinganos, K.: 2009, Observations and 3D MHD simulations of a solar active region jet. *Astron. Astrophys.* **506**, L45–L48. doi:10.1051/0004-6361/200913026.

Haugbølle, T.: 2005, Modelling Relativistic Astrophysics at the Large and Small Scale. PhD thesis, Niels Bohr Institute [astro-ph/0510292].

Hededal, C.: 2005, Gamma-Ray Bursts, Collisionless Shocks and Synthetic Spectra. PhD thesis, Niels Bohr Institute [astro-ph/0506559].

Hesse, M., Schindler, K.: 1988, A theoretical foundation of general magnetic reconnection. *J. Geophys. Res.* **93**, 5559–5567. doi:10.1029/JA093iA06p05559.

Hesse, M., Forbes, T.G., Birn, J.: 2005, On the Relation between Reconnected Magnetic Flux and Parallel Electric Fields in the Solar Corona. *Astrophys. J.* **631**, 1227–1238. doi:10.1086/432677.

Holman, G.D.: 1985, Acceleration of runaway electrons and Joule heating in solar flares. *Astrophys. J.* **293**, 584–594. doi:10.1086/163263.

Hood, A.W., Archontis, V., MacTaggart, D.: 2011, 3D MHD Flux Emergence Experiments: Idealized models and coronal interactions. *ArXiv e-prints*.

Javadi, S., Büchner, J., Otto, A., Santos, J.C.: 2011, About the relative importance of compressional heating and current dissipation for the formation of coronal X-ray bright points. *Astron. Astrophys.* **529**, A114. doi:10.1051/0004-6361/201015614.

Jiang, Y.C., Chen, H.D., Li, K.J., Shen, Y.D., Yang, L.H.: 2007, The Hα surges and EUV jets from magnetic flux emergences and cancellations. *Astron. Astrophys.* **469**, 331–337. doi:10.1051/0004-6361:20053954.

Kanamori, H.: 1978, Quantification of Earthquakes. *Nature* **271**, 411–414. doi:10.1038/271411a0.

Kane, S.R., Anderson, K.A.: 1970, Spectral Characteristics of Impulsive Solar-Flare X-Rays ???? 10 KeV. *Astrophys. J.* **162**, 1003. doi:10.1086/150732.

Karimabadi, H., Daughton, W., Scudder, J.: 2007, Multi-scale structure of the electron diffusion region. *Geophys. Res. Lett.* **34**, 13104. doi:10.1029/2007GL030306.

Karlický, M., Bárta, M.: 2011, Successive Merging of Plasmoids and Fragmentation in a Flare Current Sheet and Their X-Ray and Radio Signatures. *Astrophys. J.* **733**, 107. doi:10.1088/0004-637X/733/2/107.

Kliem, B., Titov, V.S., Török, T.: 2004, Formation of current sheets and sigmoidal structure by the kink instability of a magnetic loop. *Astron. Astrophys.* **413**, L23–L26. doi:10.1051/0004-6361:20031690.

Kretzschmar, M.: 2011, The Sun as a star: observations of white-light flares. *Astron. Astrophys.* **530**, A84. doi:10.1051/0004-6361/201015930.

Krucker, S., Hudson, H.S., Glesener, L., White, S.M., Masuda, S., Wuelser, J.-P., Lin, R.P.: 2010, Measurements of the Coronal Acceleration Region of a Solar Flare. *Astrophys. J.* **714**, 1108 – 1119. doi:10.1088/0004-637X/714/2/1108.

Kulsrud, R.M.: 2005, *Plasma physics for astrophysics.*

Kumar, P., Cho, K.-S., Bong, S.-C., Park, S.-H., Kim, Y.H.: 2012, Initiation of Coronal Mass Ejection and Associated Flare Caused by Helical Kink Instability Observed by SDO/AIA. *Astrophys. J.* **746**, 67. doi:10.1088/0004-637X/746/1/67.

Lin, R.P., Krucker, S., Hurford, G.J., Smith, D.M., Hudson, H.S., Holman, G.D., Schwartz, R.A., Dennis, B.R., Share, G.H., Murphy, R.J., Emslie, A.G., Johns-Krull, C., Vilmer, N.: 2003, RHESSI Observations of Particle Acceleration and Energy Release in an Intense Solar Gamma-Ray Line Flare. *Astrophys. J. Lett.* **595**, L69 – L76. doi:10.1086/378932.

Litvinenko, Y.E.: 1996, Particle Acceleration in Reconnecting Current Sheets with a Nonzero Magnetic Field. *Astrophys. J.* **462**, 997. doi:10.1086/177213.

Longcope, D.W., Parnell, C.E.: 2009, The Number of Magnetic Null Points in the Quiet Sun Corona. *Solar Phys.* **254**, 51 – 75. doi:10.1007/s11207-008-9281-x.

Manoharan, P.K., van Driel-Gesztelyi, L., Pick, M., Demoulin, P.: 1996, Evidence for Large-Scale Solar Magnetic Reconnection from Radio and X-Ray Measurements. *Astrophys. J. Lett.* **468**, L73. doi:10.1086/310221.

Masson, S., Pariat, E., Aulanier, G., Schrijver, C.J.: 2009, The Nature of Flare Ribbons in Coronal Null-Point Topology. *Astrophys. J.* **700**, 559 – 578. doi:10.1088/0004-637X/700/1/559.

Masuda, S., Kosugi, T., Hara, H., Tsuneta, S., Ogawara, Y.: 1994, A loop-top hard X-ray source in a compact solar flare as evidence for magnetic reconnection. *Nature* **371**, 495 – 497. doi:10.1038/371495a0.

Miller, J.A.: 2000, Particle Acceleration in Solar Flares. In: Martens, P.C.H., Tsuruta, S., Weber, M.A. (eds.) *Highly Energetic Physical Processes and Mechanisms for Emission from Astrophysical Plasmas*, *IAU Symposium* **195**, 277.

Miller, J.A., Cargill, P.J., Emslie, A.G., Holman, G.D., Dennis, B.R., LaRosa, T.N., Winglee, R.M., Benka, S.G., Tsuneta, S.: 1997, Critical issues for understanding particle acceleration in impulsive solar flares. *J. Geophys. Res.* **102**, 14631 – 14660. doi:10.1029/97JA00976.

Moreno-Insertis, F.: 2007, Three-dimensional numerical experiments of flux emergence into the corona. In: Shibata, K., Nagata, S., Sakurai, T. (eds.) *New Solar Physics with Solar-B Mission*, *Astronomical Society of the Pacific Conference Series* **369**, 335.

Moreno-Insertis, F., Galsgaard, K., Ugarte-Urra, I.: 2008, Jets in Coronal Holes: Hinode Observations and Three-dimensional Computer Modeling. *Astrophys. J. Lett.* **673**, L211 – L214. doi:10.1086/527560.

Newcomb, W.A.: 1958, Motion of magnetic lines of force. *Annals of Physics* **3**, 347 − 385. doi:10.1016/0003-4916(58)90024-1.

Ohyama, M., Shibata, K.: 1998, X-Ray Plasma Ejection Associated with an Impulsive Flare on 1992 October 5: Physical Conditions of X-Ray Plasma Ejection. *Astrophys. J.* **499**, 934. doi:10.1086/305652.

Okuda, H.: 1972, Nonphysical Noises and Instabilities in Plasma Simulation due to a Spatial Grid. *Journal of Computational Physics* **10**, 475. doi:10.1016/0021-9991(72)90048-4.

Pariat, E., Antiochos, S.K., DeVore, C.R.: 2009, A Model for Solar Polar Jets. *Astrophys. J.* **691**, 61 − 74. doi:10.1088/0004-637X/691/1/61.

Pariat, E., Antiochos, S.K., DeVore, C.R.: 2010, Three-dimensional Modeling of Quasi-homologous Solar Jets. *Astrophys. J.* **714**, 1762 − 1778. doi:10.1088/0004-637X/714/2/1762.

Parks, G.K., Winckler, J.R.: 1969, Sixteen-Second Periodic Pulsations Observed in the Correlated Microwave and Energetic X-Ray Emission from a Solar Flare. *Astrophys. J. Lett.* **155**, L117. doi:10.1086/180315.

Parnell, C.E., Smith, J.M., Neukirch, T., Priest, E.R.: 1996, The structure of three-dimensional magnetic neutral points. *Physics of Plasmas* **3**, 759 − 770. doi:10.1063/1.871810.

Pontin, D.I.: 2011, Three-dimensional magnetic reconnection regimes: A review. *Advances in Space Research* **47**, 1508 − 1522. doi:10.1016/j.asr.2010.12.022.

Priest, E.R., Titov, V.S.: 1996a, Magnetic Reconnection at Three-Dimensional Null Points. *Royal Society of London Philosophical Transactions Series A* **354**, 2951 − 2992. doi:10.1098/rsta.1996.0136.

Priest, E.R., Titov, V.S.: 1996b, Magnetic Reconnection at Three-Dimensional Null Points. *Royal Society of London Proceedings Series A* **354**, 2951 − 2992.

Priest, E.R., Bungey, T.N., Titov, V.S.: 1997, The 3D topology and interaction of complex magnetic flux systems. *Geophysical and Astrophysical Fluid Dynamics* **84**, 127 − 163. doi:10.1080/03091929708208976.

Pritchett, P.L.: 2003, Particle-in-Cell Simulation of Plasmas - A Tutorial. In: Büchner, J., Dum, C., Scholer, M. (eds.) *Space Plasma Simulation, Lecture Notes in Physics, Berlin Springer Verlag* **615**, 1 − 24.

Régnier, S.: 2012, Magnetic Energy Storage and Current Density Distributions for Different Force-Free Models. *Solar Phys.* **277**, 131 − 151. doi:10.1007/s11207-011-9830-6.

Régnier, S., Parnell, C.E., Haynes, A.L.: 2008, A new view of quiet-Sun topology from Hinode/SOT. *Astron. Astrophys.* **484**, L47 − L50. doi:10.1051/0004-6361:200809826.

Reid, H.: 2011, private communication. In: *private communication*.

Rosdahl, K.J., Galsgaard, K.: 2010, Test particle acceleration in a numerical MHD experiment of an anemone jet. *Astron. Astrophys.* **511**, A73. doi:10.1051/0004-6361/200913541.

Santos, J.C., Büchner, J., Otto, A.: 2011, Development of electric currents in a magnetic field configuration containing a magnetic null point. *Astron. Astrophys.* **525**, A3. doi:10.1051/0004-6361/201014758.

Savcheva, A., Cirtain, J., Deluca, E.E., Lundquist, L.L., Golub, L., Weber, M., Shimojo, M., Shibasaki, K., Sakao, T., Narukage, N., Tsuneta, S., Kano, R.: 2007, A Study of Polar Jet Parameters Based on Hinode XRT Observations. *PASJ* **59**, 771.

Scherrer, P.H., Bogart, R.S., Bush, R.I., Hoeksema, J.T., Kosovichev, A.G., Schou, J., Rosenberg, W., Springer, L., Tarbell, T.D., Title, A., Wolfson, C.J., Zayer, I., MDI Engineering Team: 1995, The Solar Oscillations Investigation - Michelson Doppler Imager. *Solar Phys.* **162**, 129 – 188. doi:10.1007/BF00733429.

Schindler, K., Hesse, M., Birn, J.: 1988, General magnetic reconnection, parallel electric fields, and helicity. *J. Geophys. Res.* **93**, 5547 – 5557. doi:10.1029/JA093iA06p05547.

Shay, M.A., Drake, J.F., Swisdak, M.: 2007, Two-Scale Structure of the Electron Dissipation Region during Collisionless Magnetic Reconnection. *Physical Review Letters* **99**(15), 155002. doi:10.1103/PhysRevLett.99.155002.

Shibata, K., Tanuma, S.: 2001, Plasmoid-induced-reconnection and fractal reconnection. *Earth, Planets, and Space* **53**, 473 – 482.

Shibata, K., Nitta, N., Strong, K.T., Matsumoto, R., Yokoyama, T., Hirayama, T., Hudson, H., Ogawara, Y.: 1994, A gigantic coronal jet ejected from a compact active region in a coronal hole. *Astrophys. J. Lett.* **431**, L51 – L53. doi:10.1086/187470.

Shimojo, M., Shibata, K.: 2000, Physical Parameters of Solar X-Ray Jets. *Astrophys. J.* **542**, 1100 – 1108. doi:10.1086/317024.

Shimojo, M., Hashimoto, S., Shibata, K., Hirayama, T., Hudson, H.S., Acton, L.W.: 1996, Statistical Study of Solar X-Ray Jets Observed with the YOHKOH Soft X-Ray Telescope. *PASJ* **48**, 123 – 136.

Siversky, T.V., Zharkova, V.V.: 2009, Particle acceleration in a reconnecting current sheet: PIC simulation. *Journal of Plasma Physics* **75**, 619. doi:10.1017/S0022377809008009.

Sugiyama, T., Kusano, K.: 2007, Multi-scale plasma simulation by the interlocking of magnetohydrodynamic model and particle-in-cell kinetic model. *Journal of Computational Physics* **227**, 1340 – 1352. doi:10.1016/j.jcp.2007.09.011.

Tajima, T.: 1986, Plasma physics via computer simulation C.K. Birdsall and A.B. Langdon, McGraw-Hill, New York, 1985. xxiii + 479 pages. US $45. *Computer Physics Communications* **42**, 151 – 152. doi:10.1016/0010-4655(86)90240-7.

Tsiklauri, D., Haruki, T.: 2007, Magnetic reconnection during collisionless, stressed, X-point collapse using particle-in-cell simulation. *Physics of Plasmas* **14**(11), 112905. doi:10.1063/1.2800854.

Turkmani, R., Vlahos, L., Galsgaard, K., Cargill, P.J., Isliker, H.: 2005, Particle Acceleration in Stressed Coronal Magnetic Fields. *Astrophys. J. Lett.* **620**, L59 – L62. doi:10.1086/428395.

Turkmani, R., Cargill, P.J., Galsgaard, K., Vlahos, L., Isliker, H.: 2006, Particle acceleration in stochastic current sheets in stressed coronal active regions. *Astron. Astrophys.* **449**, 749 – 757. doi:10.1051/0004-6361:20053548.

van Driel-Gesztelyi: 2003, *Observational signatures of magnetic reconnection.*

van Driel-Gesztelyi, L.: 2009, Magnetic reconnection and energy release on the Sun and solar-like stars. In: *IAU Symposium*, *IAU Symposium* **259**, 191 – 200. doi:10.1017/S1743921309030440.

Vay, J.-L.: 2008, Simulation of beams or plasmas crossing at relativistic velocity. *Physics of Plasmas* **15**(5), 056701. doi:10.1063/1.2837054.

Wang, H., Qiu, J., Jing, J., Zhang, H.: 2003, Study of Ribbon Separation of a Flare Associated with a Quiescent Filament Eruption. *Astrophys. J.* **593**, 564 – 570. doi:10.1086/376360.

Wang, T., Sui, L., Qiu, J.: 2007, Direct Observation of High-Speed Plasma Outflows Produced by Magnetic Reconnection in Solar Impulsive Events. *Astrophys. J. Lett.* **661**, L207 – L210. doi:10.1086/519004.

Woods, T.N., Kopp, G., Chamberlin, P.C.: 2006, Contributions of the solar ultraviolet irradiance to the total solar irradiance during large flares. *Journal of Geophysical Research (Space Physics)* **111**, 10. doi:10.1029/2005JA011507.

Yee, K.: 1966, Numerical solution of inital boundary value problems involving maxwell's equations in isotropic media. *IEEE Transactions on Antennas and Propagation* **14**, 302 – 307. doi:10.1109/TAP.1966.1138693.

Zharkova, V.V., Arzner, K., Benz, A.O., Browning, P., Dauphin, C., Emslie, A.G., Fletcher, L., Kontar, E.P., Mann, G., Onofri, M., Petrosian, V., Turkmani, R., Vilmer, N., Vlahos, L.: 2011, Recent Advances in Understanding Particle Acceleration Processes in Solar Flares. *ArXiv e-prints.*

A APPENDIX: NOTATION AND DEFINITIONS

Notation

$\mathbf{B}$	magnetic field
c	speed of light
$\mathbf{E}$	electric field
$\mathbf{E_D}$	Dreicer electric field
$E_{\parallel}$	electric field component parallel to the magnetic field
$\mathbf{E_{res}}$	resistive electric field
E_{CS}	electric field in current sheet
e	thermal energy per volume
$\mathbf{g}$	gravitational field
$\mathbf{j}$	electric current density
k_B	Boltzmann constant
$m_{e,i}$	electron and proton mass
m_u	atomic mass constant
N	number of particles
$n_{e,i}$	electron and proton particle density
P	gas pressure
P_m	magnetic pressure
p_{MHD}	MHD bulk momenta
$-q_e = q_i$	electron and proton charge
Q_J	Joule dissipation
Q_v	viscous dissipation
Z	charge state
$r_{g,e,i}$	electron and ion gyro radius
S_{ij}	shear tensor
$T_{e,i}$	electron and proton temperature
t	time
u_{MHD}	MHD bulk speed
$V_{e,i}$	PIC average speed
$\mathbf{v}$	particle velocity
v_A	Alfvén speed
v_J	electric current drift speed
v_s	sound speed
v_{drive}	driving speed of boundary motion
$v_{th,e,i}$	electron and proton thermal speed

β	plasma beta
γ	adiabatic index or Lorentz factor
$\delta_{skin,e,i}$	electron and proton skin depth
Δs	cell size
Δt	time step in simulations
ΔL	current sheet thickness
ϵ_0	vacuum permittivity
η	resistivity
λ_D	Debye length
μ	mean molecular weight
μ_0	vacuum permeability
ν_{ij}	viscosity
ν_c	collision frequency
ν_{ei}	electron-ion collision frequency
ρ_m	mass density
ρ_q	charge density
σ	plasma conductivity
τ_{ij}	viscous stress tensor
Φ	angle between field lines on each side of the current sheet
$\omega_{c,e,i}$	electron and proton gyro frequency
$\omega_{p,e,i}$	electron and proton plasma frequency

Definitions and Equations (SI units)

$$
\begin{aligned}
c &= \frac{1}{\sqrt{\epsilon_0 \cdot \mu_0}} \\[2mm]
\rho_m &= n_e m_e + n_i m_i \\[2mm]
\rho_q &= q_i n_i + q_e n_e \\[2mm]
P_m &= \frac{B^2}{2\mu_0} \\[2mm]
P &= n k_B T \\[2mm]
&= \frac{\rho_m k_B T}{\mu\, m_u} \\[2mm]
&= \rho_m R T \\[2mm]
T &= \frac{m\, v_{th}^2}{3 k_B} \\[2mm]
\mathbf{j} &= q_e n_e \mathbf{V_e} + q_i n_i \mathbf{V_i} \\[2mm]
\beta &= \frac{P}{P_m} \\[2mm]
&= \frac{2\mu_0 n k_B T}{B^2} \\[2mm]
\lambda_{D,e} &= \sqrt{\frac{\epsilon_0 k_B T_e}{n_e \cdot q_e^2}} \\[2mm]
&= \frac{v_{th,e}}{\omega_{pe}} \\[2mm]
v_s &= \sqrt{\gamma \cdot \frac{P}{\rho_m}} \\[2mm]
&= \sqrt{\gamma \cdot \frac{k_B T}{m}} \\[2mm]
v_A &= \frac{B}{\sqrt{\mu_0 \cdot \rho_m}} \\[2mm]
\omega_{ce,ci} &= \frac{q_{e,i} \cdot B}{m_{e,i}} \\[2mm]
\omega_{pe,pi} &= \sqrt{\frac{n_{e,i} \cdot q^2}{m_{e,i} \cdot \epsilon_0}} \\[2mm]
\delta_{skin,e} &= \frac{c}{\omega_{pe}} \\[2mm]
&= \sqrt{\frac{m_e \epsilon_0 c^2}{n_e q_e^2}} \\[2mm]
&= \sqrt{\frac{m_e}{\mu_0 n_e q_e^2}}
\end{aligned}
\tag{A.1}
$$

$$
\begin{aligned}
v_{th,e,i} &= \sqrt{\frac{3k_B \cdot T_{e,i}}{m_{e,i}}} \\
\mathbf{v}_J &= \frac{\nabla \times \mathbf{B}}{\mu_0 n_e q_e} \\
r_{g,e,i} &= \frac{m_{e,i} \cdot v_\perp}{|q_{e,i} \cdot B|} \\
&\approx \frac{v_{th,i}}{\omega_{ci}}
\end{aligned}
$$

Maxwell equations

$$
\begin{aligned}
\nabla \times \mathbf{B} &= \mu_0 \mathbf{j} + \mu_0 \epsilon_0 \frac{\partial \mathbf{E}}{\partial t} \\
\nabla \times \mathbf{E} &= -\frac{\partial \mathbf{B}}{\partial t} \\
\nabla \cdot \mathbf{B} &= 0 \\
\nabla \cdot \mathbf{E} &= \frac{\rho_q}{\epsilon_0}
\end{aligned}
$$

B APPENDIX: PUBLICATIONS

Article 1: Active region MHD experiment

3D Solar Null Point Reconnection MHD Simulations

G. Baumann[1] · **K. Galsgaard**[1] · **Å. Nordlund**[1]

Abstract Numerical MHD simulations of 3D reconnection events in the solar corona have improved enormously over the last few years, not only in resolution, but also in their complexity, enabling more and more realistic modeling. Various ways to obtain the initial magnetic field, different forms of solar atmospheric models as well as diverse driving speeds and patterns have been employed. This study considers differences between simulations with stratified and non-stratified solar atmospheres, addresses the influence of the driving speed on the plasma flow and energetics, and provides quantitative formulae for mapping electric fields and dissipation levels obtained in numerical simulations to the corresponding solar quantities. The simulations start out from a potential magnetic field containing a null-point, obtained from a Solar and Heliospheric Observatory (SOHO) magnetogram extrapolation approximately 8 hours before a C-class flare was observed. The magnetic field is stressed with a boundary motion pattern similar to — although simpler than — horizontal motions observed by SOHO during the period preceding the flare. The general behavior is nearly independent of the driving speed, and is also very similar in stratified and non-stratified models, provided only that the boundary motions are slow enough. The boundary motions cause a build-up of current sheets, mainly in the fan-plane of the magnetic null-point, but does not result in a flare-like energy release. We conclude that the most likely reason for the flare energy release was the additional flux emergence that occurred near the flare site.

Keywords: Sun — corona — magnetic reconnection — magnetic null-point

1. Introduction

There have been different attempts to initialize the magnetic field of the photosphere and corona for numerical simulations; amongst others by elimination of the complex observed small scale structure by the use of several photospheric magnetic monopole sources (Priest, Bungey, and Titov, 1997), by flux emergence experiments (Archontis *et al.*, 2004), as well as by extrapolation (e.g. Masson *et al.*, 2009) of solar observatory magnetograms, e.g. from SOHO. The latter type has typically been used together with potential extrapolations, for simplicity

---

[1] Niels Bohr Institute, Juliane Maries Vej 30, 2100
København Ø, Denmark email: gbaumann@nbi.ku.dk

reasons as well as due to the limited availability of vector magnetograms. As potential magnetic fields contain no free magnetic energy, these cannot directly be used for explaining how flare events take place and where the released energy arises from. Therefore, to use a potential magnetic field as the basis for an investigation of a flare event, the field must be stressed into a state where it contains sufficient free magnetic energy to account for the energy release event. There are different ways by which this may be accomplished. A simple approach is to impose boundary motions that resemble the ones derived from observations (Bingert and Peter, 2011; Gudiksen and Nordlund, 2002). An alternative, more challenging approach is to stress the system by allowing additional magnetic flux to enter through photospheric magnetic flux emergence (Fan and Gibson, 2003). In the solar context both of these process take place simultaneously, while experiments typically concentrate on a single type of stressing, in order to investigate in detail its influence on the dynamical evolution of the magnetic field.

The present investigation is an extension of the work done by Masson *et al.* (2009). They studied the evolution preceding a specific flare event observed with SOHO, starting by taking a magnetogram from about 8 hours before the flare and deriving a potential magnetic field. Due to the presence of a 'parasitic' magnetic polarity, the resulting magnetic field contains a magnetic null-point. From the motions of observed magnetic fragments a schematic photospheric velocity flow was constructed, and was used to stress this initially potential magnetic field. The imposed stress distorts the magnetic field, causing electric currents to build up in the vicinity of the magnetic null-point. The magnetic dissipation associated with the electric current allows a continuous reconnection to take place. The boundary driving together with the reconnection causes the null-point to move. The locations of the magnetic dissipation agree qualitatively with the locations of flare emission in various wavelength bands, which may be seen as evidence supporting a close association between reconnection at the magnetic null-point and the observed C-class flare.

The Masson *et al.* (2009) paper raises many interesting questions, some of which we attempt to answer in the present paper. We therefore let the same observations provide the basis for deriving a potential initial magnetic field, and employ the same imposed boundary stressing of the magnetic field, using the setup to investigate the impact of varying the amplitude of the driving speed, as well as the impact of allowing the experiment to take place in a gravitationally stratified setting.

The paper is organized as follows: In Section 2 we list the equations we solve, and briefly describe the numerical methods used to solve them. In Section 3 we give an overview of the different numerical experiments, in Section 4 we present and discuss the results, and finally in Section 5 we summarize the main results and conclusions.

2. Methods

The simulations have been performed using the fully 3D resistive and compressible *Stagger* MHD code (Nordlund and Galsgaard, 1997a).

The following form of the resistive MHD equations are solved in the code:

$$\frac{\partial \rho}{\partial t} = -\nabla \cdot (\rho \mathbf{u}) \tag{1}$$

$$\frac{\partial (\rho \mathbf{u})}{\partial t} = -\nabla \cdot (\rho \mathbf{u}\mathbf{u} + \underline{\underline{\tau}}) - \nabla p$$
$$+\mathbf{j} \times \mathbf{B} + \rho \mathbf{g} \tag{2}$$

$$\frac{\partial e}{\partial t} = -\nabla \cdot (e\mathbf{u} + \mathbf{f_e}) - p\nabla \cdot \mathbf{u}$$
$$+Q_J + Q_\nu \tag{3}$$

$$\frac{\partial \mathbf{B}}{\partial t} = -\nabla \times \mathbf{E} \tag{4}$$

$$\mathbf{j} = \nabla \times \mathbf{B} \tag{5}$$

$$\mathbf{E} = -\mathbf{u} \times \mathbf{B} + \eta \mathbf{j} \tag{6}$$

$$Q_J = \eta j^2 \tag{7}$$

$$\nabla \cdot \mathbf{B} = 0 \tag{8}$$

$$p = (\gamma - 1)e \tag{9}$$

$$\tau_{ij} = -\nu_{ij}\rho S_{ij} \tag{10}$$

$$S_{ij} = \frac{1}{2}\left(\frac{\partial u_i}{\partial x_j} + \frac{\partial u_j}{\partial x_i}\right) \tag{11}$$

$$Q_\nu = \rho \sum_{ij} \nu_{ij} S_{ij}^2 \tag{12}$$

$$\mathbf{f_e} = -\nu_e \rho \nabla(e/\rho) \tag{13}$$

where ρ is the mass density, $\mathbf{u}$ the bulk velocity, p the pressure, $\mathbf{j}$ the current density, $\mathbf{B}$ the magnetic field, g the acceleration of gravity, e the thermal energy per unit volume and η the resistivity. S_{ij} is the shear tensor, τ_{ij} the viscous stress tensor and $\mathbf{f_e}$ is a weak diffusive flux of thermal energy needed for numerical stability. The term Q_v represents viscous dissipation, turning kinetic energy into heat, while Q_J is the Joule dissipation, responsible for converting magnetic energy into heat.

The solution to the MHD equations is advanced in time using an explicit 3rd order predictor-corrector procedure (Hyman, 1979).

The version of the Stagger MHD code used here assumes an ideal gas law and includes no radiative cooling and heat conduction. The variables are located on different staggered grids, which allows for conservation of various quantities to machine precision. The staggering of variables has been chosen so $\nabla \cdot \mathbf{B}$ is among the quantities conserved to machine precision. Interpolation of variables between different staggered grids is handled by using 5th order interpolation. In a similar way spatial derivatives are computed using expressions accurate to 6th order. To minimize the influence of numerical diffusion dedicated operators are used for calculating both viscosity and resistivity. The viscosity is given by

$$\nu = \Delta d \left(\nu_1 c_f + \nu_2 |\mathbf{u}| + \nu_3 \Delta d \left| - \nabla \cdot \mathbf{u} \right|_+\right), \tag{14}$$

where Δd is the mesh size and $\nu_1 = 0.005 - 0.02$, $\nu_2 = 0.005 - 0.02$, and $\nu_3 = 0.2 - 0.4$ are dimensionless coefficients that provide a suitable amount of dissipation of fast mode waves (ν_1), advective motions (ν_2), and shocks (ν_3). The expression $|-\nabla \cdot \mathbf{u}|_+$ denotes the positive part of the rate of compression $-\nabla \cdot \mathbf{u}$. c_f is the fast mode speed defined by $c_f = \sqrt{(B^2 + \gamma p) \cdot \rho^{-1}}$.

The resulting grid Reynolds numbers, $\Delta d \, c_f / \nu$, are on the order of $50 - 200$ in regions with smooth variations, while in the neighborhood of shocks they are of the order of a few. The corresponding expression for the resistivity is

$$\eta = \Delta d \left(\nu_1 c_f + \nu_2 |\mathbf{u}| + \nu_3 \Delta d \, |-\nabla \cdot \mathbf{u}_\perp|_+ \right), \tag{15}$$

where $\mathbf{u}_\perp$ is the component of the velocity perpendicular to $\mathbf{B}$, and where the expression scaled by ν_3 prevents electric current sheets from becoming numerically unresolved. The resulting magnetic grid Reynolds numbers are of the order a few in current sheets, as required to keep such structures marginally resolved.

The overall scaling with Δd ensures that advection patterns, waves, shocks and current sheets remain resolved by a few grids, independent of the mesh size.

The advantage of these three-part expressions for the viscosity and the resistivity, compared to having constant viscosity and resistivity is that constant values would have to be chosen on the order of the largest of these three term, in order to handle shocks and current sheets. In the rest of the volume the viscosity and resistivity would then be orders of magnitude larger than needed. As demonstrated in (Kritsuk *et al.*, 2011) the results are quite similar to state of the art codes that use local Riemann solvers. Such codes also have dissipative behavior on the scale of individual cells – no numerical code is 'ideal' in the sense that it presents solutions corresponding to zero resistivity.

In this article we refer to the $-\mathbf{u} \times \mathbf{B}$-term in the induction equation as the advective electric field, while its counterpart $\eta \mathbf{j}$ is referred to as the diffusive electric field.

3. Simulations

The experimental setup is inspired by the work by Masson *et al.* (2009). Our study sets out from a Fast Fourier Transform potential extrapolation applied to a level 1.8 SOHO/Michelson Doppler Imager magnetogram (Scherrer *et al.*, 1995) from November 16, 2002 at 06:27 UT, 8 hour prior to a C-class flare occurrence in the AR10191 active region. The extrapolation leads to a 3D magnetic null-point topology with a clear fan and spine structure (Green, 1989; Priest and Titov, 1996). In order to allow periodic boundary conditions in the potential field extrapolation we applied a windowing function to the SOHO cut-out of the active region AR10191, which decreases the field close to the boundary towards zero. This cut-out from the complete solar disk SOHO data differs slightly from the one used by Masson *et al.* (2009). As a result, in our case the null-point is initially located at a height of about 4 Mm above the magnetogram, while in their case the null-point is located at a height of only 1.5 Mm above the magnetogram. The change in null position places our null-point in the corona proper and allows

Table 1. Simulation runs. In the stratified runs min and max values are given in brackets. 'Boundary' refers to the plasma flow boundary condition at the lower boundary. Runs with a stratified atmosphere are denoted with an 'S', while 'O' stands for open boundary.

Run	boundary	max. driving $[\mathrm{km\,s^{-1}}]$	density $[\mathrm{cm^{-3}}]$	temperature [K]
1	closed	3.33	6.8×10^{12}	5.0×10^5
1O	open	3.33	6.8×10^{12}	5.0×10^5
2	closed	6.67	6.8×10^{12}	5.0×10^5
3	closed	10	6.8×10^{12}	5.0×10^5
4	closed	20	6.8×10^{12}	5.0×10^5
1S	closed	3.33	$[4.5\times10^{10},\ 9.1\times10^{15}]$	$[8000, 1\times10^6]$
3S	closed	10	$[4.5\times10^{10},\ 9.1\times10^{15}]$	$[8000, 1\times10^6]$
4S	closed	20	$[4.5\times10^{10},\ 9.1\times10^{15}]$	$[8000, 1\times10^6]$

us to perform affordable simulations with stratified atmospheres, while at the same time it does not influence the nature of the current sheet formation, and still successfully describes a typical solar-like magnetic field geometry.

Numerically, a magnetic field derived from a potential extrapolation is not necessarily divergence free, and we therefore initially apply a divergence cleaning procedure, which removes the divergence (as measured by our specific numerical stretched mesh derivative operators) by iteratively applying a correction obtained from solving the Poisson equation

$$\Delta\delta\Phi = -\nabla \cdot \mathbf{B}. \tag{16}$$

The structure of the resulting initial magnetic field is illustrated in Figure 1a and 1b, showing a strong overall magnetic field and a weaker fan-spine structure close to the photospheric boundary, which is separately illustrated in Figure 2. Note, that the field lines of the fan-spine topology were selected specifically to show the topology, and that the density of the field lines is therefore not representative of the magnetic flux density.
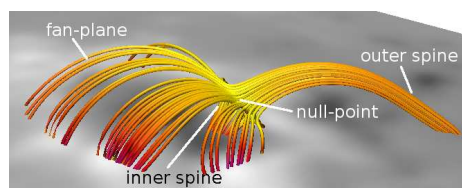
We performed two types of simulations; one type in which we imposed a 1-D gravitationally stratified atmosphere profile, and a second type with constant density and temperature. The density and temperature profiles are shown in Figure 3, and a summary of the simulation runs may be found in Table 1.

The magnetic fields are in all cases anchored at the vertical boundaries, which due to boundary conditions also prevent plasma from flowing in and out. The exception to this is run 1O, in which instead constant pressure is assumed at the lower boundary, and plasma flows through the boundary are allowed. Only minor differences were found between the open and closed boundary cases.

An imposed horizontal velocity field is introduced at the lower boundary of the computational box. This schematic velocity field is based on the motions of magnetic fragments observed by SOHO in the active region. These fragments
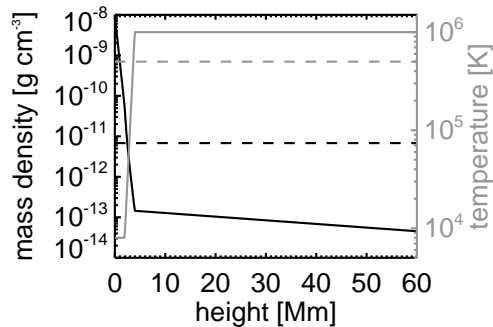
Figure 1. Magnetic field resulting from the FFT extrapolation of the SOHO magnetogram taken on November 16, 2002. The region shown here is the entire computational box, having an extent of $60 \times 175 \times 100$ Mm. The slice represents the vertical component of the magnetic field. Black is the negative polarity, white is positive.

Figure 2. Zoom in of Figure 1 (upper drawing) to the fan-spine topology, excluding the large scale field. The volume below the fan-plane is referred to as 'the dome'.

Figure 3. Mass densities are presented in black, temperatures in gray. The solid line shows the 1D mass density and temperature profiles as a function of height x [Mm] of all stratified runs. The dashed line illustrates the constant mass density and temperature of run 1, run 1O, run 2 run 3 and run 4.

outline the fast relative motions observed prior to the flare in the active region and correlate with the observed flux emergence process described by Masson *et al.* (2009). We used and implemented the description of the velocity pattern provided in this reference. In order not to produce initial transients the velocity field at the bottom boundary is slowly ramped up, over a period of about 100 s, by using a hyperbolic tangent function, and is afterwards kept constant. A variety of driving speeds have been employed, ranging from values similar to those used by Masson *et al.* (2009) to values about 6 times lower. We compare and discuss their influence in Section 4.

In general, it is important to keep the driver velocity well below the Alfvén velocity of the magnetic concentrations, because the magnetic structure and the plasma need to have enough time to adapt to the changing positions of the magnetic field lines at the boundary. Ideally, to allow gas pressure to equalize along magnetic fields, in response to compressions and expansions imposed by the boundary motions, the driver velocity should also be small compared to the sound speed in the coronal part of the model. This condition is generally fulfilled in all experiments, since the coronal sound speed is on the order of $100 \, \text{km s}^{-1}$, while our driving speeds are considerably smaller than that.

With these conditions we assure an almost force free state at all times in the simulation, which implies that the electric current is well aligned with the magnetic field. Nevertheless, the line-tied motions of magnetic field lines imposed by the lower boundary motions causes the creation of a current sheet in which magnetic reconnection takes place.

The maximal velocity of around $20 \, \text{km s}^{-1}$ that we applied exceeds the actual velocities measured in the active region by a factor of about 40, while it is at the same time clearly sub-Alfvénic. This speed up, which is similar to the one used by Masson *et al.* (2009), has the desirable effect that we can cover a larger solar time interval; a simulated time interval of 12 minutes then corresponds to 8 hours of real solar time. In our slowest cases (1S, 1, and 1O), the simulated time is more than an hour, and the driving speed ($3.33 \, \text{km s}^{-1}$) is approaching realistic solar values.

Figure 4. Cell sizes in km for all three axis plotted against the grid indices. X is the height.
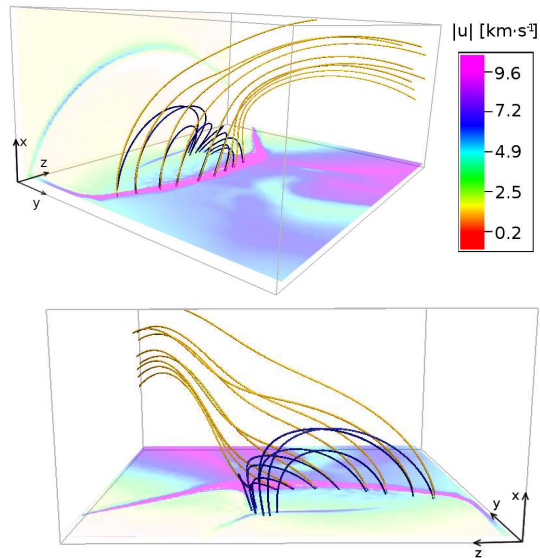
The simulated region has a size of $62 \times 175 \times 100$ Mm, where our x axis points in the direction normal to the solar surface. The computational box is covered by a stretched grid of dimensions $320 \times 896 \times 512$, with a minimum cell size of ≈ 80 km maintained in a relatively large region around the null-point. The grid size is smaller than 85 km over a $8\, x50\, x\, 30$ Mm region, which includes the entire fan-plane and its intersection with the lower boundary. The distributions of cell sizes over grid indices are illustrated in Figure 4. In the initial setup, the null-point is located at height index x = 50.

4. Results and Discussions

As mentioned above, the field extrapolation based on the SOHO magnetogram leads to a fan-spine topology of the magnetic field, illustrated in Figure 2. This structure is surrounded by a stronger magnetic field, which extents to much larger heights into the corona. We concentrate in the present study on the small fan-spine structure, which forms as a consequence of a generally positive polarity in the active region AR10191 hosting a small ('parasitic') negative polarity region. The overlying magnetic field lines, including the ones forming the fan-plane, are anchored in the photosphere and build together with the spine a rather stable magnetic field structure, keeping the plasma from expanding into the upper corona.

We simulate the motion of magnetic field lines located between the large scale negative and positive polarity — hence outside the fan-spine structure — which on November 16, 2002 moved a large amount of magnetic flux towards the east side[1] (left hand side in Figure 1) of the dome, which we define as the volume confined by the fan-plane. This translational motion at the photospheric boundary is represented in our experiment by a boundary motion ('driver'), which is applied at the lower boundary of our computational box. The boundary motions lead to an eastward directed motion of the magnetic field lines outside

---

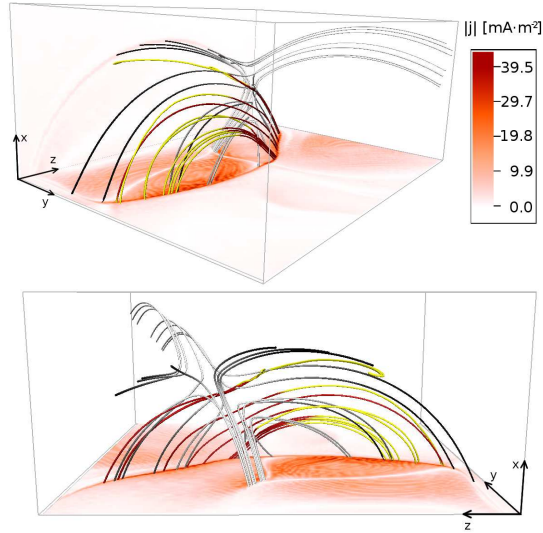[1] We use as reference system the solar coordinate system.

Figure 5. Magnetic field lines connecting to the inside (dark blue) and to the outside (orange) of the fan-plane. The bottom slice shows the bulk speed at a height of about 1.4 Mm. The snapshot is taken at a displacement D = 2.12 Mm in the experiment run 3. The box size is $10 \times 16 \times 22$ Mm.

the dome and to magnetic plasma being pushed against the west periphery of the fan-spine structure. Especially in the stratified case, a part of this flow extends upward along the magnetic field lines toward the neighborhood of the null-point and the outer spine.

The displacement of field lines, particularly outside of the fan-plane, introduces a misalignment between the inner and outer spine (see also Figure 2). Figure 5 shows the field line shear at a nominal 'boundary displacement' (simulation time times the amplitude of the average applied boundary velocity), D = 2.12 Mm after the start of run 3, which has a driving speed of about $10 \, \text{km s}^{-1}$. Choosing the displacement instead of the simulation time has the advantage that at a given displacement, all runs have experienced about the same energy input from the work introduced by the boundary driving and are hence comparable. The angle ϕ, designating the difference of the direction between the inner magnetic field lines (in dark blue) and the outer magnetic field lines (in orange) with respect to the fan-plane, is still quite small. The quasi-transparent slices show the bulk speed, which is high just outside the fan-plane, where plasma is pushed up by the driver. Magnetic field lines closely approaching the null-point run just below this high bulk flow layer.

The applied photospheric driving motion indirectly moves the fan-plane foot points at the west side of the fan-spine structure, causing a slight shear between the inner and the outer field lines of the fan-plane to arise due to a different stress level of these two flux systems. The magnetic flux system inside the dome experiences a compression of about 5 times the surrounding gas pressure when the magnetic flux system west to the dome has moved towards it. This leads to
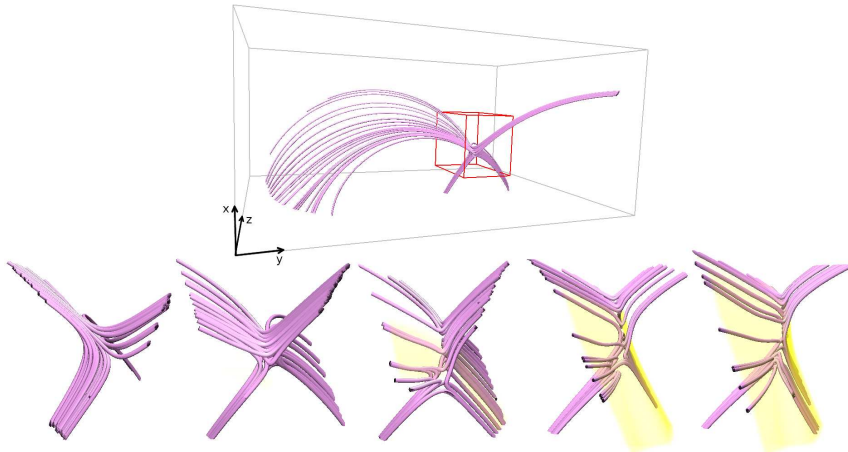
Figure 6. The electric current (red–yellow) flowing antiparallel to the magnetic field lines (black–gray). The color gradient along the streamlines indicates the flow direction (going from red to yellow) and the magnetic field orientation (going from black to gray). The slices show the electric current density of run 3. D = 2.66 Mm and the box size is $10 \times 16 \times 22$ Mm.

a large stress close to the null-point, on the east side of the outer spine, where the magnetic field as a consequence reconnects with the surrounding field in order to reach a lower energy state. A thin current sheet forms in the fan-plane, with the largest electric current densities occurring closest to the driver, where the shear of the field lines is largest. The magnitude of the electric current is lower in the neighborhood of the null-point. At the null-point itself the effect is to disrupt the structure of the null in such a way that the two spine axes move apart, as seen also in other single null investigations (Pontin, Bhattacharjee, and Galsgaard, 2007; Galsgaard and Pontin, 2011). Figure 6 shows the streamlines and direction of the highest electric current in run 3 at D = 2.66 Mm. We find that the electric current is mostly anti-parallel to the magnetic field lines in the fan-plane.

A partial outcome of the reconnection is seen in the motion of the inner spine, which is not being moved directly by the applied photospheric driver, but nevertheless moves at the photospheric level a significant absolute distance of about 4.5 Mm in the simulation, corresponding to a speed of about $4.7 \, \mathrm{km \, s^{-1}}$. The motion is nearly linear in space and time. A second signature is the character of the displacement of the outer spine relative to the position of the inner spine.

The initial null-point area, connecting the inner and outer spine, stretches with increasing displacement into a 'weak field region', where the magnetic field strength is very low. This initiates an electric current that passes through the fan-plane, causing the ratio of the smallest to largest fan-eigenvalues to decrease (Parnell *et al.*, 1996). In this case the null almost adopts a 2D structure. This is illustrated in Figure 7. We discuss the relation of this inner and outer spine distance to the electric field at the end of section 4.1.
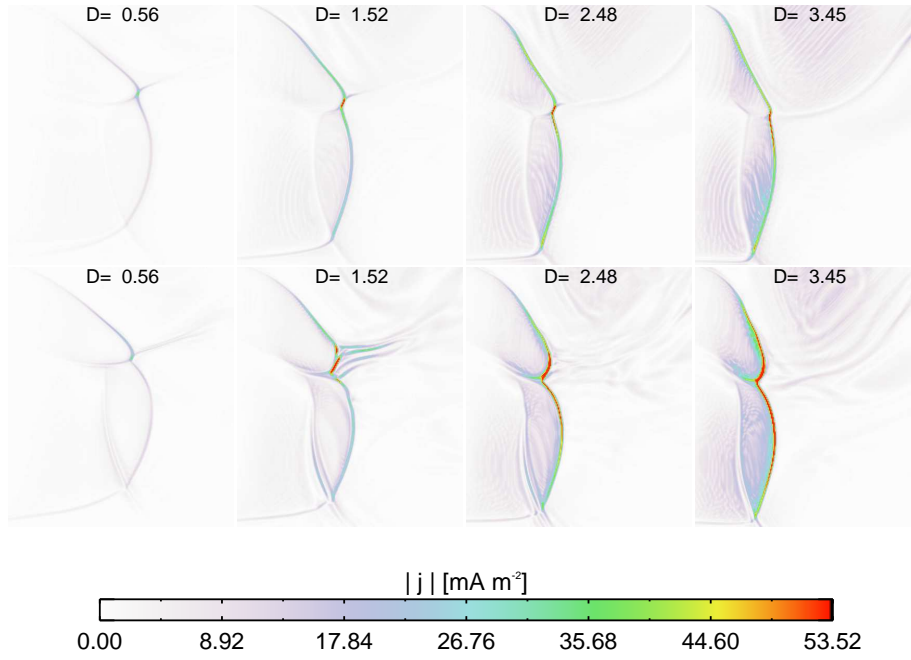
Figure 7. Relative motion of inner and outer spine for run 3. The top panel shows the cutout region for D = 0.02 Mm and the lower panel shows approximately the same selected region for D = 0.02, 0.52, 1.05, 1.59, 2.12 Mm. The yellow volume shows the highest electric current density, which is located in the fan-plane.
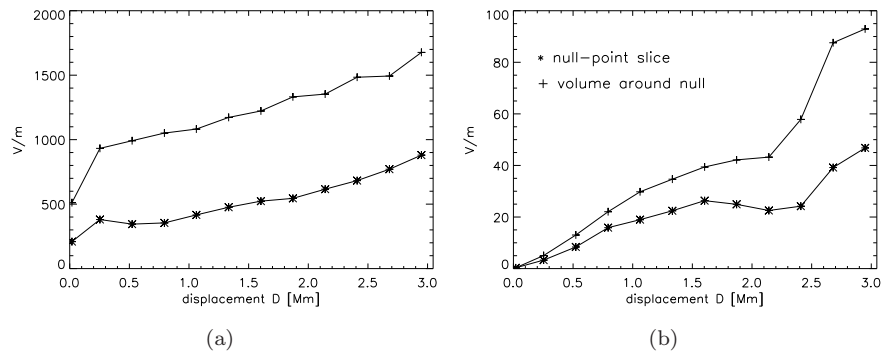
4.1. Time evolution of the diffusive electric field

The diffusive part of the electric field ($\eta\mathbf{j}$) included in the induction equation is responsible for both changing the magnetic field topology and for transforming magnetic energy into Joule dissipation in the MHD picture. In the Sun the diffusive electric field component parallel to the magnetic field is responsible for particle acceleration (Arzner and Vlahos, 2006). It is therefore of particular interest to see how this field evolves with the boundary displacement, and to find out where it concentrates and how large values it reaches. Figure 8 illustrates the electric current accumulation in the fan-plane and along the spine axes of the magnetic null. This behavior is representative for all stratified and non-stratified runs. In the code the resistivity is not a simple constant, as specified by Equation 14, allowing diffusion to be locally increased where dissipation is needed to keep structures from becoming unresolved, while at the same time allowing a minimal amount of diffusion in regions where the magnetic field is smooth. Images of the diffusive electric field are therefore not exact replicas of images of the electric current, but since the resistivity is generally near its largest value in current sheets there is a close correspondence.

The diffusive electric field is found to be concentrated in the fan-plane and to have its local peak in the region where the fan-spine intersection is distorted. However, large values occur over a significant fraction of the fan-plane, as is the case for the electric current density. It is only the parallel diffusive electric field that gives rise to both magnetic reconnection and particle acceleration and its magnitude indicates how violent these processes can be (Schindler, Hesse, and Birn, 1988). In our simulations the advective electric field ($-\mathbf{u} \times \mathbf{B}$), associated with the bulk plasma motion in the fan-plane and along the spine axis is much stronger (Figure 9a) than its diffusive counterpart, but since it is perpendicular

Figure 8. Current density in y-z slice for constant density run 4 (upper row) and stratified atmosphere run 4S (lower row) at a height of x = 3.22 Mm and different displacements D.

to the magnetic field this component causes no magnetic dissipation, and cannot be associated with particle acceleration.
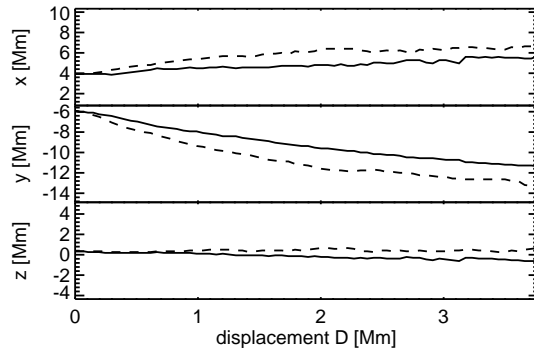

(a)   (b)

Figure 9. Maximum advective electric field (a) and average diffusive electric field calculated over those grid points, at which the electric field amplitude is within 10 percent of the maximum field in a slice of 2 grid cells thickness (b) of the cutout region at the respective height of the null-point (*) and in the total cutout region 10 × 16 × 22 Mm around the null-point, including the fan-plane (+) in run 3.

When determining the values of the diffusive electric field one finds that the peak values in the vicinity of the null-point are increasing with growing displacement (see Figure 9b), going from initially zero to on the order of $50\,\mathrm{V\,m^{-1}}$, while in the fan-plane the diffusive electric field reaches more than $90\,\mathrm{V\,m^{-1}}$ at D = $2.92\,\mathrm{Mm}$. However, as shown below (cf. Equation 22), to estimate the analogous solar electric field, the simulation value should be reduced with a factor equal to the square root of the factor (about 20 for run 3) by which the boundary driving is exaggerated; here we obtain $E \approx 90/\sqrt{20}$, or about $20\,\mathrm{V\,m^{-1}}$. Considering our more benign conditions, this is consistent with Pudovkin *et al.* (1998), who find typical electric fields to be of the order of $100 - 300\,\mathrm{V\,m^{-1}}$ under flaring conditions. Electrons accelerated along the entire current sheet, with an extent of about $15\,\mathrm{Mm}$ (see Figure 6), could nevertheless gain energies of up to about $300\,\mathrm{MeV}$ in our case. Of interest is also the shape of the average diffusive electric field increase in the vicinity of the null-point, plotted in Figure 9b as a (*)-line. Its progression shows an almost identical behavior as a plot of the increasing distance between the inner and outer spine (see Figure 7) plotted against the displacement (plot not presented here).

4.2. Comparison of stratified and non-stratified simulations

Since the null-point is an essential node of the magnetic skeleton, we use it as a reference point for our investigation of the influence of the density profile on the temporal changes of the magnetic field. Here we compare simulation run 4S, which has a stratified atmosphere, with simulation run 4, which has a constant chromosphere-like density and temperature atmosphere (see, Table 1). Figure 10 shows the position of the null-point, connecting the fan-plane and spine magnetic field lines, in all three directions versus the boundary displacement D. In the

Figure 10. Null-point position in Mm in the coordinate system of the experiment. The vertical coordinate is x, and the two horizontal coordinates are y and z. The solid line shows the constant density run 4, while the dashed line represents the stratified run 4S.

stratified case the very dense plasma (9×10^{15} cm^{-3}) at the bottom of the box gives rise to a low Alfvén speed ($\mathrm{v}_A = B/\sqrt{\mu_0 \rho_m}$), meaning that the higher density impedes the propagation of the boundary disturbance into the box. But once the disturbances reach beyond the transition region the ambient density

has fallen drastically, and the dense plasma from the lower atmosphere starts spreading out faster and pushes the null-point up. The velocity gradient induced by the large density change causes strong dissipation and in some regions a disruption into multiple smaller current sheets, which can also be seen in the electric current density comparison in Figure 8, showing $|\mathbf{j}|$ for runs 4 and 4S.

In the non-stratified runs the amount of plasma that moves upwards along the magnetic field lines into the corona and contributes to pushing the null-point upwards is much reduced, as seen in Figure 10.

For all runs we find a significant null-point motion (about 1–2 Mm in x, 6 Mm in y and 1 Mm in z) due to the applied driving motion on the bottom boundary, which is comparable to the relative motion of the inner spine.

4.3. The influence of boundary conditions

The driver of the magnetic field evolution is the boundary motion. The magnetic field displacements imposed by the boundary motions have a large influence on the spatial structure of the magnetic skeleton, consisting of null-points, separatrix surfaces (such as the fan-plane), separators, sources and flux domains (e.g. Parnell, Haynes, and Galsgaard, 2008, and references therein). The skeleton itself is a very robust structure, which does not change from a topological point of view, but the detailed appearance of it changes with boundary displacement, as already shown by the analysis of the null-point motion.

In Figure 11b we compare the density profiles of the closed runs 1, 2, 3 and 4 and the open boundary run 1O. The figure shows that all non-stratified closed flow boundary runs develop a similar density profile: A certain expansion or compression of a region connected to the closed boundary leads to the same density profile, regardless of the driving speed.
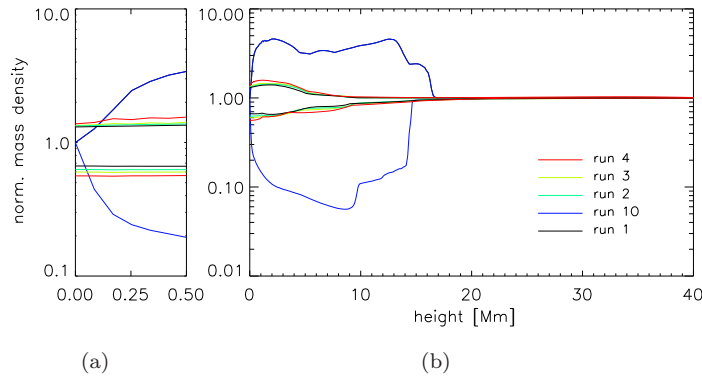
The initial sound speed is about $83\,\mathrm{km\,s^{-1}}$ for the non-stratified runs, while being much lower—on the order of $10\,\mathrm{km\,s^{-1}}$—in the lower parts of the stratified runs. The sound speed influences among other things the in- and outflows at open boundaries.

Figure 11a illustrates that the closed boundary conditions influence particularly the lowest density layer, where regions with low and high density build up and cannot be emptied nor filled by plasma out- and inflow. This is not very important for the dynamics of the system, but is also not very solar-like. In the open case, there is a continuous mass exchange and pressure equalization at the boundaries, in which case it is crucial that the sound speed is well above the driving speed, so that the system has time to approach pressure balance.

The low sound speed in the stratified case poses a very tight restriction on the driving speed, in order to avoid exaggerating the effects of inertia. On the other hand there is a clear advantage of having stratification: it provides a pool of mass for the corona to communicate with; the large amount of mass at low temperature acts as a buffer, due to the low Alfvén and sound speed.

Overall, Figure 11b confirms that the density contrast is mainly caused by volume changes, which arise from the imposed boundary motions. If these volume changes happen sufficiently slowly relative to the Alfvén and sound speed, the driving speed loses its importance for the results (but not for the computational cost of obtaining them!).

Figure 11. Density profile min and max over each slice in height for the closed non-stratified simulations, normalized to the asymptote: run 1, run 2, run 3 and run 4 and the open non-s-tratified run 1O. (a) is a zoom in of the first 0.5 Mm of plot (b). The displacement of each run is taken to be from the snapshot closest to D = 1.02 Mm.
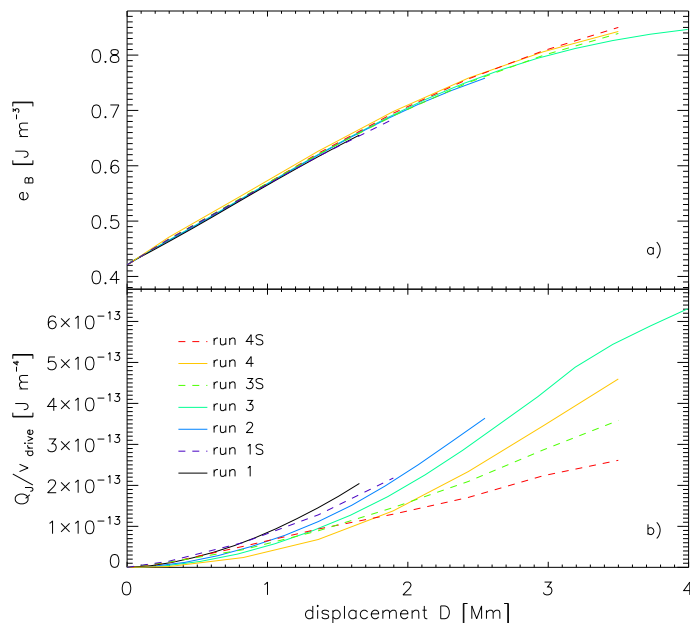
4.4. Energy dissipation

Magnetic energy brought into the system by photospheric driving cannot only move the system into another potential state but can also be stored on top of the evolving potential configuration, in case that the integrated dissipation rate cannot compensate for the work done on the system that goes into non-potential energy.

The rate of change of magnetic energy density $e_B = B^2/2$ is described by Equation 17. A change of electromagnetic energy can be caused by a divergence of the Poynting flux F_P, a conversion into bulk kinetic energy by the Lorentz work W_L, or by conversion to heat through Joule dissipation Q_J.

$$\frac{\partial e_B}{\partial t} = -\nabla \cdot (F_P) - W_L - Q_J. \tag{17}$$

The Lorentz work is defined by $W_L = -\mathbf{u} \cdot (\mathbf{j} \times \mathbf{B})$. Joule dissipation, $Q_J = \mathbf{E}_\eta \cdot \mathbf{j} = \eta \mathbf{j}^2$, primarily takes place in the strong current sheets. Electric currents flow mainly along the magnetic field in the corona and therefore Q_J is a suitable indicator for locations at which a significant component of the electric field parallel to the magnetic field may form. This parallel electric field can accelerate charged particles along the magnetic field lines, resulting e.g. in the brightening of flare ribbons.

The evolutions of the magnetic energy and the Joule dissipation normalized to the average driving speed are summarized in a plot covering several simulation runs in Figure 12. The first thing to notice is that the evolution of the magnetic energy, when expressed in terms of the boundary displacement D, is practically identical in all of the runs. The reason for this is that most of the boundary work goes directly into increasing the potential magnetic energy, while only a small amount goes into free magnetic energy. From Figure 12b is seen that the dissipation increases with increasing displacement. This shows that an increasing amount of free energy becomes available through the build up of current
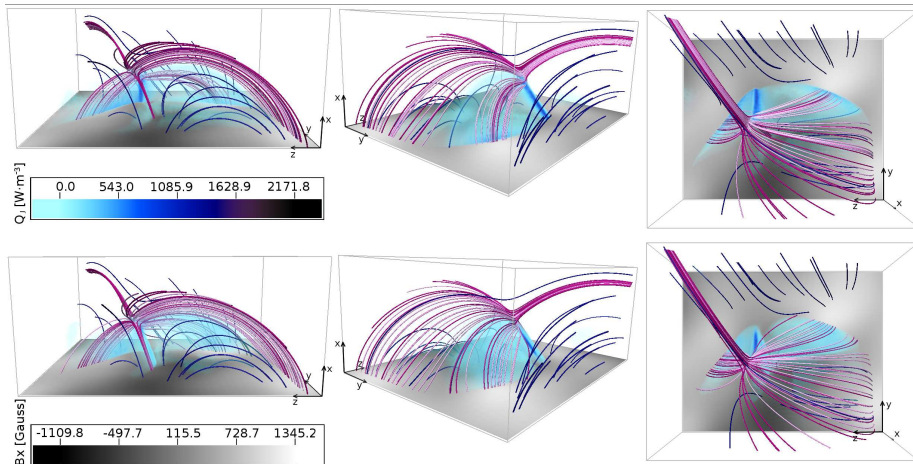
Figure 12. Comparison of the average magnetic energy a) and average magnetic dissipation normalized by the average boundary driving speed of each run b) for constant density runs (solid lines) and stratified runs (dashed lines) in the cutout of approximate size 10 x 16 x 22 Mm.

structures in the null-point fan-plane as the experiment progresses. The small amount of dissipation also hints that the total free energy in the system is small in comparison to the change of energy in the changed potential magnetic field.

The normalization of the magnetic dissipation by average driving speed employed in Figure 12b brings the curves showing the evolution of magnetic dissipation for all the different runs together into a relatively tight set of parallel relations. This illustrates that, to lowest order, the rate of magnetic dissipation, at any given value of the displacement, is proportional to the driving velocity and to the rate of boundary displacement.

The dissipation curves corresponding to the different experiments follow the same general trend, although with some differences, in particular between the stratified and non-stratified cases. The dissipation is generally higher for the stratified cases than for the non-stratified runs during early times and lower during late times. The exception is run 1S, the run with the lowest driving speed, which agrees closely with the non-stratified cases with the slowest driving speed.

The deviations from this common asymptotic behavior are likely consequences of the low Alfvén speeds in the dense layers of the stratified models, causing the dissipation in the stratified runs to be initially high due to their higher densities at low heights compared to the constant density cases. Later, when the motions

Figure 13. The highest joule dissipation of run 1 in the top row and run 1S in the lower row is shown as a semitransparent volume rendering at about D = 0.82 Mm. The box size is $10 \times 16 \times 22$ Mm. The field lines represent magnetic field lines passing closest to the null point (purple), in the close surrounding of the null-point (magenta) and the overlying strong magnetic field (dark blue). The slice on the lower boundary shows the bx magnetic field component.

introduced by the driver reach greater heights, where the mass density is lower than in the constant density runs, the stratified runs generally display a lower dissipation.

We note in this context also that the viscous dissipation in the system is much smaller than the Joule dissipation, as is expected in a coronal environment.

The results summarized in Figure 12 illustrate that for a quantitatively accurate estimate of properties related to the magnetic dissipation it is essential to drive in a way which is compatible with the ordering of characteristic speeds in the Sun; i.e., to keep the boundary speed smaller than the Alfvén speed, and to scale the quantities down in proportion to the speed-up factor used in the driving.

For the non-stratified runs we compute initial Alfvén speeds of $70 - 1400\,\mathrm{km\,s^{-1}}$ at the lower boundary, which is clearly higher than the driving speed of all runs. So we expect, as is also shown by Figure 12, a similar dissipation increase with increasing displacement, after some initial differences due to the driving speed differences.

In the stratified atmosphere runs the Alfvén speed increases with height. At the lower boundary the initial Alfvén speed is approximately $5 - 200\,\mathrm{km\,s^{-1}}$, where the minimum value falls below the driving speed used in runs 3S and 4S. Run 1S is just at the edge of being driven slower than the minimum Alfvén speed and indeed gives results which are similar to the non-stratified case run 1. Figure 13 shows that the stratified and non-stratified cases are nevertheless distinguishable. The volume renderings show the Joule dissipation normalized by the driving speed, for run 1 (upper panel) and run 1S (lower panel). The locations of the dissipation maxima agree nicely, but the dissipation maxima differ by a factor of about 1.8, being higher in the stratified run 1S.

In summary, we find that the ratio of the driving speed to the Alfvén speed has a noticeable impact on the dissipation level and, as Figure 12 illustrates, that the stratified simulations tend to display a progressive growth of deviations from the common asymptotic relations defined by the non-stratified runs, unless the driving speed is small compared to both the local Alfvén speed and the sound speed.

However, these are relatively small deviations, compared to the lowest order effect, which is a proportionality of the magnetic dissipation and the driving speed. The reason for this proportionality lies in the scaling behavior of dissipation in current sheets, which is explored in the next subsection.

4.5. Scaling of magnetic dissipation in the current sheet

As illustrated by Figure 5, the magnetic field line orientations on the two sides of the fan-plane only differ by a small amount. This means that the electric current carried by the current sheet, whose thickness (on the order of a few grid cells in the present numerical model) we denote with Δs, is much less than the maximal electric current density $2B/\Delta s$ that would result from a complete reversal of the magnetic field orientation across the current sheet. The electric current density in the current sheet (CS) is in fact on the order of

$$j_{\mathrm{CS}} \sim \Delta B \, \Delta s^{-1} \approx sin(\phi)B_{\mathrm{CS}}\Delta s^{-1} \approx \phi B_{\mathrm{CS}}\Delta s^{-1}, \tag{18}$$

for small ϕ, where B_{CS} is a typical strength of the magnetic field just outside the current sheet, and ϕ is an angle characterizing the difference of direction of field lines on the two sides of the current sheet.

A fundamental question is now how the total dissipation in the current sheet, and hence the average rate of reconnection in the structure, depends on factors such as the numerical resolution and rate of work done at the boundary. By construction the code keeps current sheets just barely resolved. A change in numerical resolution is thus directly mapped into a proportional change of the current sheet thickness Δs. This behavior is obtained by making η essentially proportional to the grid size (cf. Equation 15). To a first order approximation both B_{CS} and ϕ are independent of Δs. By Equation 18 the electric current density is inversely proportional to Δs, and the magnetic dissipation rate per unit volume Q_J therefore scales as

$$Q_{\mathrm{CS}} = \eta j_{CS}^2 \sim \Delta B^2 \Delta s^{-1} = \phi^2 B_{CS}^2 \Delta s^{-1}. \tag{19}$$

To obtain the total dissipation in the current sheet this needs to be multiplied with the volume of the current sheet,

$$V_{\mathrm{CS}} \sim A_{\mathrm{CS}}\Delta s. \tag{20}$$

where we denote by A_{CS} the total area of the current sheet. We thus conclude that the total dissipation is

$$Q_{\mathrm{CS}}V_{\mathrm{CS}} \sim \Delta B^2 A_{\mathrm{CS}}, \tag{21}$$

and hence is, to lowest order, *independent of* Δs and the resistivity in the current sheet. Note that, as a consequence of ϕ being small, reconnection in the current sheet can proceed without requiring super-Alfvénic outflow velocities from the current sheet.

Estimating now the diffusive electric field in the current sheet we find that it scales as

$$E_{\mathrm{CS}} = \eta_{\mathrm{CS}} j_{\mathrm{CS}} \propto \Delta B = \phi B_{\mathrm{CS}}, \tag{22}$$

again independent of Δs, but proportional to the change of magnetic field direction across the current sheet and hence proportional to ϕ.

Generally the work done by the boundary must go into an increase in magnetic energy (potential plus free magnetic energy), or into kinetic energy or ohmic dissipation. In the present case the magnetic dissipation is able to keep up with the free energy input, and the system essentially goes through a series of equilibrium states. As Figure 12 shows, the total magnetic energy only depends on the displacement and not on the driving speed itself, while the dissipation is essentially proportional to how fast we drive at the boundary, thus $Q_{\mathrm{CS}} \propto v$ (Equation 19) and hence $v \propto \phi^2$. So we conclude with the help of Equation 22 that the magnitude of the parallel electric field along the current sheet is essentially proportional to the square-root of the driving speed,

$$E_{\mathrm{CS}} \propto \phi \propto v^{1/2}. \tag{23}$$

This dissipation-driving speed relation is not an artifact of the chosen numerical method; the scaling of η with Δs is generic to all numerical methods, and serves to ensure that higher numerical resolution can be used to reach larger magnetic Reynolds and Lundquist numbers.

With much higher rates of stressing, or with much higher numerical resolution, the current sheet may need to fragment and enter a turbulent regime, in order to support the required amounts of dissipation and reconnection in the face of increasing constraints by the thinness of the current sheets. This is a process that is by now well understood to be able to take over when the need arises (Galsgaard and Nordlund, 1996; Nordlund and Galsgaard, 1997b; Gudiksen and Nordlund, 2005; Berger and Asgari-Targhi, 2009; Bingert and Peter, 2011; Ng, Lin, and Bhattacharjee, 2011; Pontin, 2011).

We thus conclude that, provided that conditions that apply equally to both numerical simulations and the Sun are fulfilled, neither the total magnetic dissipation in a current sheet structure, nor the diffusive part of the electric field depend, to lowest order, on the electrical resistivity—or for that matter on the precise mechanism that sets the level of the electrical resistivity.

4.6. Triggering of rapid energy release

As in Masson *et al.* (2009) there is no significant and sudden relaxation of the system, with an energy release that could correspond to a flare, even though the simulations cover enough solar time to get across the observed flaring event. Looking at the potential part of the magnetic field at different displacement

steps in the simulations, we find steadily increasing magnetic potential energies, and most of the build-up of magnetic energy seen in the experiment actually goes into increasing the potential rather than the non-potential part of the magnetic energy. As discussed above, the magnetic dissipation is able to keep up with varying levels of boundary work, with a residual amount of free energy scaling approximately linearly with the driving speed. The stress in the system is demonstrably moderate, even with our exaggerated driving speed, and we therefore cannot expect boundary motions of the type applied here to be able to explain violent events similar to the observed solar flare.

We consider three possibilities for this difference in behavior between these MHD simulations and the Sun:

i) The limited resolution of the numerical experiment is preventing an instability from occurring that would otherwise trigger a flare-like event

ii) A flare-like event would occur if taking into account kinetic effects (e.g. by using particle-in-cell simulations)

iii) A flare-like event could take place, with MHD alone, but would require for instance an additional flux emergence event in addition to the slow and systematic boundary motion implemented here and in Masson *et al.* (2009)

As demonstrated above, numerical resolution does not to a first order determine the level of dissipation in current sheets, once they are reasonably well resolved. Indeed, by the arguments in the preceding subsection we expect the level of stress (as measured for example by the angle ϕ) caused by the type of motions we employ in the current investigation to be *smaller* in the Sun (by a factor of e.g. $\approx \sqrt{7} \approx 2.5$ relative to our runs 1, 1O and 1S, and it is thus very unlikely that the flare was triggered by accumulation of stress from this type of boundary motion.

An MHD-instability could in principle occur at a later point in time than to where our runs go; but as demonstrated by our experiments even a driving speed that is highly exaggerated relative to the solar value is not able to build up sufficient free energy to account for a C-class flare: The maximum *total* magnetic energy in the entire simulated domain of our experiment is on the order of 2×10^{30} ergs, of which only a very small fraction is free energy. Estimates of C-flare emission are larger than even our potential energy (Kretzschmar, 2011), and hence the free energy available in our model is not sufficient to power a C-class flare. As discussed above, the level of stress is expected to be essentially proportional to the driving speed, and is expected to be largely independent of the level of resistivity, and hence it is unlikely that more stress would build up in the Sun than in these numerical simulations.

Figure 14, which is representative of all runs, illustrates that the rate of change of magnetic energy increases in the beginning, as a result of the work done by the lower boundary. This energy input looses efficiency as the angle between the field lines and the driving boundary approaches 90 degrees. Additionally, since the driving pattern location is fixed, the applied stress becomes less and less efficient, as the flux in this particular region is gradually removed. The dissipation is small compared to the rate of change of magnetic energy, implying that the dissipated free energy only makes up a tiny fraction compared to the

Figure 14. The average rate of change of magnetic energy for run 3 is plotted as a solid line, and the dissipation divided by the average driving speed is shown as a dashed line. Both are restricted to the cutout of approximate size 10 x 16 x 22 Mm used previously

potential energy. This is in agreement with Figure 5, which illustrates that the shear of the magnetic field lines in the current sheet is not very large, even with our exaggerated driving speed. Hence the reconnection is rapid enough to keep the boundary work at a given displacement at an approximately constant level, and to keep the system in a near potential state. We are thus far away from an instability to occur and it is improbable to achieve one at a later point of the experiment.

By similar arguments kinetic effects are not expected to have a major influence on the macroscopic dissipation behavior and reconnection rate. This is consistent with the findings by Birn *et al.* (2005), which show that the same amounts of energy release take place for the same type of reconnection event, independent of the dissipation mechanism. It also shows that there are only small differences in the time scales of the event going from MHD to PIC simulations. These results are entirely consistent with the current sheet scaling arguments presented above, since they hold true independent of the nature of the dissipation mechanism.

We thus conclude that additional external forcing, such as the additional flux emergence mentioned in the third alternative above, is the most likely explanation for the observed solar flare. This conclusion is consistent with the fact that all observational evidence associates flaring either with new flux emergence, or with magnetic configurations that evolve into states that are decidedly MHD-unstable; i.e., ones in which lower energy states become accessible and where dissipative effects make it possible to reach those lower energy states and dynamic instabilities therefore develop. In such dynamic events both of the above two points are still true; things are really kinetic on a small scale, but evolve essentially according to MHD on large scales.

5. Conclusions

The main topic of the presented work is a study of the influence of the driving speed for stratified and non-stratified atmosphere models used to simulate 3D reconnection events in the solar corona. The major findings are:

- Sufficiently low driving speeds lead to similar plasma behavior, including similar evolution of the magnetic energy density and the Joule dissipation (after compensating for the expected effects of the different driving speeds).
- The magnetic dissipation and the diffusive electric field — capable of accelerating charged particles — are both, to lowest order, independent of the plasma resistivity, and hence depend only weakly on the grid resolution in numerical experiments.
- When driving is taking place sufficiently slowly the rate of magnetic dissipation increases linearly with the boundary driving speed while the diffusive electric field increases as the square root of the driving speed.
- The driving speed has a larger impact on the general plasma behavior in the cases with stratified atmospheres, while its influence is minor for non-stratified runs with closed flow boundary conditions, if compared at the same boundary motion displacements.
- The sound speed compared to the driving speed determines the exchange of plasma at the boundaries. Voids can be filled in open boundary runs, while pressure differences at the boundary are carried along in the closed boundary cases. This is not an issue in the stratified runs, due to the large reservoirs of relatively cold gas in the vicinity of the lower boundary. On the other hand the lower information speeds there set severe restrictions on the driving speed.

Our investigations suggest that the applied driver is unlikely to be able to provide a flare-like energy release in the simulations (as well as in the Sun). In fact, based on a comparison of the available free energy in our model with estimates from observations of C-class flares we anticipate that additional magnetic flux emergence served as the triggering mechanism of the observed sudden energy release in the C-class flare that occurred here.

References

Archontis, V., Moreno-Insertis, F., Galsgaard, K., Hood, A., O'Shea, E.: 2004, Emergence of magnetic flux from the convection zone into the corona. *Astron. Astrophys.* **426**, 1047 – 1063. doi:10.1051/0004-6361:20035934.

Arzner, K., Vlahos, L.: 2006, Gyrokinetic electron acceleration in the force-free corona with anomalous resistivity. *Astron. Astrophys.* **454**, 957 – 967. doi:10.1051/0004-6361:20064953.

Berger, M.A., Asgari-Targhi, M.: 2009, Self-organized Braiding and the Structure of Coronal Loops. *Astrophys. J.* **705**, 347 – 355. doi:10.1088/0004-637X/705/1/347.

Bingert, S., Peter, H.: 2011, Intermittent heating in the solar corona employing a 3D MHD model. *Astron. Astrophys.* **530**, A112. doi:10.1051/0004-6361/201016019.

Birn, J., Galsgaard, K., Hesse, M., Hoshino, M., Huba, J., Lapenta, G., Pritchett, P.L., Schindler, K., Yin, L., Büchner, J., Neukirch, T., Priest, E.R.: 2005, Forced magnetic reconnection. *Geophys. Res. Lett.* **32**, 6105. doi:10.1029/2004GL022058.

Fan, Y., Gibson, S.E.: 2003, The Emergence of a Twisted Magnetic Flux Tube into a Preexisting Coronal Arcade. *Astrophys. J. Lett.* **589**, L105 – L108. doi:10.1086/375834.

Galsgaard, K., Nordlund, Å.: 1996, Heating and activity of the solar corona 1. Boundary shearing of an initially homogeneous magnetic field. *J. Geophys. Res.* **101**, 13445 – 13460. doi:10.1029/96JA00428.

Galsgaard, K., Pontin, D.I.: 2011, Steady state reconnection at a single 3D magnetic null point. *Astron. Astrophys.* **529**, A20. doi:10.1051/0004-6361/201014359.

Green, J.M.: 1989, Geometrical properties of 3d reconnecting magnetic fields with nulls. *J. Geophys. Res.* **93**, 8583.

Gudiksen, B.V., Nordlund, Å.: 2002, Bulk Heating and Slender Magnetic Loops in the Solar Corona. *Astrophys. J. Lett.* **572**, L113 – L116. doi:10.1086/341600.

Gudiksen, B.V., Nordlund, Å.: 2005, An Ab Initio Approach to the Solar Coronal Heating Problem. *Astrophys. J.* **618**, 1020 – 1030. doi:10.1086/426063.

Hyman, J.M.: 1979, A method of lines approach to the numerical solution of conservation laws. In: *Advances in Computer Methods for Partial Differential Equations - III*, 313 – 321.

Kretzschmar, M.: 2011, The Sun as a star: observations of white-light flares. *Astron. Astrophys.* **530**, A84. doi:10.1051/0004-6361/201015930.

Kritsuk, A.G., Nordlund, Å., Collins, D., Padoan, P., Norman, M.L., Abel, T., Banerjee, R., Federrath, C., Flock, M., Lee, D., Li, P.S., Müller, W.-C., Teyssier, R., Ustyugov, S.D., Vogel, C., Xu, H.: 2011, Comparing Numerical Methods for Isothermal Magnetized Supersonic Turbulence. *Astrophys. J.* **737**, 13. doi:10.1088/0004-637X/737/1/13.

Masson, S., Pariat, E., Aulanier, G., Schrijver, C.J.: 2009, The Nature of Flare Ribbons in Coronal Null-Point Topology. *Astrophys. J.* **700**, 559 – 578. doi:10.1088/0004-637X/700/1/559.

Ng, C.S., Lin, L., Bhattacharjee, A.: 2011, High-Lundquist Number Scaling in Three-Dimensional Simulations of Parker's Model of Coronal Heating. *ArXiv e-prints*.

Nordlund, A., Galsgaard, K.: 1997a, A 3D MHD code for Parallel Computers. Technical report, Niels Bohr Institute.

Nordlund, A., Galsgaard, K.: 1997b, Topologically Forced Reconnection. In: Simnett, G.M., Alissandrakis, C.E., Vlahos, L. (eds.) *European Meeting on Solar Physics*, *Lecture Notes in Physics, Berlin Springer Verlag* **489**, 179. doi:10.1007/BFb0105676.

Parnell, C.E., Haynes, A.L., Galsgaard, K.: 2008, Recursive Reconnection and Magnetic Skeletons. *Astrophys. J.* **675**, 1656 – 1665. doi:10.1086/527532.

Parnell, C.E., Smith, J.M., Neukirch, T., Priest, E.R.: 1996, The structure of three-dimensional magnetic neutral points. *Physics of Plasmas* **3**, 759 – 770. doi:10.1063/1.871810.

Pontin, D.I.: 2011, Three-dimensional magnetic reconnection regimes: A review. *Advances in Space Research* **47**, 1508 – 1522. doi:10.1016/j.asr.2010.12.022.

Pontin, D.I., Bhattacharjee, A., Galsgaard, K.: 2007, Current sheet formation and nonideal behavior at three-dimensional magnetic null points. *Physics of Plasmas* **14**(5), 052106. doi:10.1063/1.2722300.

Priest, E.R., Titov, V.S.: 1996, Magnetic Reconnection at Three-Dimensional Null Points. *Royal Society of London Philosophical Transactions Series A* **354**, 2951 – 2992. doi:10.1098/rsta.1996.0136.

Priest, E.R., Bungey, T.N., Titov, V.S.: 1997, The 3D topology and interaction of complex magnetic flux systems. *Geophysical and Astrophysical Fluid Dynamics* **84**, 127 – 163. doi:10.1080/03091929708208976.

Pudovkin, M.I., Zaitseva, S.A., Shumilov, N.O., Meister, C.-V.: 1998, Large-Scale Electric Fields in Solar Flare Regions. *Solar Phys.* **178**, 125 – 136.

Scherrer, P.H., Bogart, R.S., Bush, R.I., Hoeksema, J.T., Kosovichev, A.G., Schou, J., Rosenberg, W., Springer, L., Tarbell, T.D., Title, A., Wolfson, C.J., Zayer, I., MDI Engineering Team: 1995, The Solar Oscillations Investigation - Michelson Doppler Imager. *Solar Phys.* **162**, 129 – 188. doi:10.1007/BF00733429.

Schindler, K., Hesse, M., Birn, J.: 1988, General magnetic reconnection, parallel electric fields, and helicity. *J. Geophys. Res.* **93**, 5547 – 5557. doi:10.1029/JA093iA06p05547.

Article 2: Active region PIC experiment

KINETIC MODELING OF PARTICLE ACCELERATION IN A SOLAR NULL POINT RECONNECTION REGION

G. Baumann[1], T. Haugbølle[2,1] and Å. Nordlund[1,2]

[1] *Niels Bohr Institute, University of Copenhagen, Juliane Maries Vej 30, DK-2100 Copenhagen, Denmark*
[2] *Centre for Star and Planet Formation, Natural History Museum of Denmark, University of Copenhagen, Øster Voldgade 5-7, DK-1350 Copenhagen, Denmark*

gbaumann@nbi.ku.dk

ABSTRACT

The primary focus of this paper is on the particle acceleration mechanism in solar coronal 3D reconnection null-point regions. Starting from a potential field extrapolation of a SOHO magnetogram taken on 2002 November 16, we first performed MHD simulations with horizontal motions observed by SOHO applied to the photospheric boundary of the computational box. After a build-up of electric current in the fan-plane of the null-point, a sub-section of the evolved MHD data was used as initial and boundary conditions for a kinetic particle-in-cell model of the plasma. We find that sub-relativistic electron acceleration is mainly driven by a systematic electric field in the current sheet. A non-thermal population of electrons with a power-law distribution in energy forms, featuring a power-law index of about -1.75. This work provides a first step towards bridging the gap between macroscopic scales on the order of hundreds of Mm and kinetic scales on the order of cm in the solar corona, and explains how to achieve such a cross-scale coupling by utilizing either physical modifications or (equivalent) modifications of the constants of nature. With their exceptionally high resolution — up to 135 billion particles and 3.5 billion grid cells of size $17.5 \, \mathrm{km}$ — these simulations offer a new opportunity to study particle acceleration in solar-like settings.

Subject headings: Corona — DC electric field — particle acceleration — Sun

1. Introduction

During solar flares an enormous amount of energy is released, in particular in the form of highly energetic non-thermal electrons. It is generally accepted that the underlying release mechanism is magnetic reconnection. In connection with a reconnecting current sheet, strong large-scale electric fields can build up (Liu et al. (2009) and references therein), leading to direct acceleration of particles beyond thermal velocities, while fluctuating electric fields created by reconnection and other dynamic events can lead to stochastic acceleration (e.g. Miller et al. 1996, 1997; Petrosian et al. 2006).

During the last decade high resolution observations of solar magnetic fields from several so-lar space missions and ground-based observations, such as YOHKOH, SOHO, TRACE, RHESSI, HINODE, STEREO, SDO and SST (e.g. Longcope et al. 2005; Ko et al. 2003; Milligan et al. 2006; Priest & Schrijver 1999; Sui et al. 2004; Aulanier et al. 2007; Kumar et al. 2011; Jess et al. 2008) have brought new insights and substantial support for existing solar flare and CME models.

Additionally, new three-dimensional coronal magnetic reconnection and acceleration models (e.g. Priest & Titov 1996; Vlahos et al. 2004) as well as the rapid expansion of computing resources for large scale simulations (Isobe et al. 2007; Galsgaard & Pontin 2011; Toriumi & Yokoyama 2012) have opened up a new chapter in the understanding of the formation of current sheets and particle acceleration sites in three dimensional reconnec-

tion regions. But what is lacking is an interconnected understanding of how microscopic plasma physics scales interact and exchange information with macroscopic large-scale magnetohydrodynamics (MHD) scales in the solar atmosphere. MHD scales provide the environment for particle acceleration to happen, but it is unclear how the complex non-linear feedback from much smaller scales onto the overall behavior of the plasma above the solar surface is handled by nature.

Most studies have made use of the fact that the temporal evolution of the large-scale magnetic field in the solar atmosphere can to a first approximation be described by compressible MHD. But fluid approaches are limited to thermal particle distributions, which is not sufficient to describe the kinetic aspects of magnetic reconnection that convert magnetic field energy into particle kinetic energy. A proper description of such processes requires taking into account the back reaction of kinetic processes on the large scale dynamics. Nevertheless, test particle MHD simulations, (e.g. Turkmani et al. 2005, 2006; Browning et al. 2010; Dalla & Browning 2005, 2008; Rosdahl & Galsgaard 2010), give a good idea of the overall acceleration region framework. In such simulations MHD fields evolve independently of the motion of the test particles. There is no immediate backreaction from the accelerated particles onto the fields, which is potentially a serious limitation, since especially the changes of the electric field that would be induced by the accelerated particles can be large compared to the background field induced by magnetic reconnection (Siversky & Zharkova 2009). The lack of feedback can lead to an exaggerated particle acceleration, as has been noted by for example Rosdahl & Galsgaard (2010), since there is no limitation for the energy gain of particles. Furthermore, kinetic instabilities can be of importance for the fast reconnection onset in solar flares, and more generally for the evolution of the current sheets in reconnection regions (Bárta et al. 2010). There is therefore a need for realistic self-consistent kinetic simulations to examine micro scale processes in plasmas and to be able to properly take into account backreactions from the particles to the fields.

The main challenge for kinetic simulations on scales of solar events is the enormous dynamic range involved. Explicit particle-in-cell (PIC) simulations have to resolve characteristic kinetic scales and are restricted to very small physical sizes, due to limitations that arise from conditions for code stability as well as from resolution criteria. These computational restrictions have so far prevented investigations of the coupling of kinetic to MHD scales using kinetic simulations, and have thus prevented self-consistent modeling of particle acceleration in solar flares. There has mainly been one interlocked model attempt e.g. by Sugiyama & Kusano (2007), but the complexity of the problem limits the applicability of such attempts significantly. In the present study we introduce a new method to meet the challenge of multi-hierarchy simulations and use the method to investigate particle acceleration mechanisms in a solar reconnection event using ultra large scale kinetic modeling.

In Section 2 we describe the numerical methods and their implementation, while in Section 3 we introduce the experimental setup and list the most important simulations we performed, indicating their relative roles and importance. In Section 4 we present and discuss the results, and in Section 5 we summarize the results, present our conclusions, and give an outlook onto future work.

2. Methods

We perform PIC simulations using the *Photon-Plasma* code (Haugbølle 2005; Hededal 2005), which solves the Maxwell equations

$$-\frac{\partial \mathbf{B}}{\partial t} = \nabla \times \mathbf{E} \qquad (1)$$

$$\epsilon_0 \mu_0 \frac{\partial \mathbf{E}}{\partial t} = \nabla \times \mathbf{B} - \mu_0 \mathbf{J}, \qquad (2)$$

together with the relativistic equation of motion for charged particles

$$m \frac{d(\gamma \mathbf{v})}{dt} = q(\mathbf{E} + \mathbf{v} \times \mathbf{B}) \qquad (3)$$

on a staggered Yee lattice (Yee 1966). We use SI units, scaled so the unit of length is $1\,\mathrm{km}$, the unit of time is $0.1\,\mathrm{s}$, and the unit of density is $10^{-12}\,\mathrm{kg}$ m^{-3}.

The Lorentz force is computed by interpolation of the electromagnetic fields $\mathbf{E}$ and $\mathbf{B}$ from the mesh to the particle positions, employing a cubic scheme using the 64 nearest mesh points. The code integrates the trajectories of protons and

electrons moving in the electromagnetic field with a Vay particle mover (Vay 2008). The charge density ρ is determined by weighted averaging of the particles to the mesh points using the same cubic scheme as for the field to particle interpolation, to avoid self forces. The currents are found using a new 6th order version of the Esirkepov charge conservation method (Esirkepov 2001) that is consistent with the field solver[1]. The field equations are solved on the mesh using an implicit 2nd order in time and 6th order in space method. Because the solver is charge conserving and the fields properly staggered, Gauss' law is obeyed and the **B** field is kept divergence free to numerical precision.

The boundaries of the domain are fixed for the magnetic fields and open for particles. Particles can escape and new particles are added to the box from 'ghost cells' outside the physical boundaries, where the conditions are specified from values in the MHD snapshot. In the current short duration kinetic simulations the field values in the boundaries are held fixed. In longer duration simulations they could be made time dependent by performing interpolations in time between MHD snapshots. See also Haugbølle et al. (2012).

Below we introduce for the first time a modification of the elementary charge q, in addition to and analogous to the well known speed of light (c) modification that has previously been used in many cases (e.g. Drake et al. 2006). Since all the micro-scales (gyro radii, skin depths, Debye lengths) are inversely proportional to the charge per particle, one can increase the micro-scales until they are resolvable on macroscopic scales by decreasing the charge per particle sufficiently.

While changing the ratio of micro- to macro-scales by a large amount may appear to be a very drastic approach, the method can be defended on both qualitative and quantitative grounds: From a qualitative point of view it may be argued that as long as one retains a proper ordering of non-dimensional parameters, as discussed in more detail below, one should expect to see essentially the same qualitative behavior, albeit with (possibly large) differences in quantitative aspects. From a quantitative point of view one can indeed at-tempt to predict how these quantitative aspects depend on the modifications of q and c, to be able to extrapolate—at least to order of magnitude—to values that would be typical in the unmodified system.

Adopting this approach enables us to perform explicit PIC simulations of large scale plasmas. With the parameter values used here we resolve the electron skin depth δ_e with at least 3.8 grid cells and the Debye length with at least 0.3 grid cells. For the time stepping we use a Courant condition of 0.4, considering the light crossing time in a grid cell as well as the local plasma frequency.

3. Simulations

In order to investigate the particle acceleration mechanism around a 3D reconnection region, we started out with a Fourier transform potential extrapolation of a Solar and Heliospheric Observatory/Michelson Doppler Imager magnetogram from 2002 November 16 at 06:27:00 UT, 8 hour prior to a C-flare occurrence in the AR10191 active region. This is similar to the setup by Masson et al. (2009). As there is no vector magnetogram available for this event, a non-linear force-free extrapolation has not been feasible. The potential field magnetic configuration arising from the extrapolation showed mainly two connectivity regions, separated by a dome-shaped 'fan-surface' (Craig et al. 1997), each including a spine structure, which is the symmetry line intersecting the fan at the magnetic null-point.

We define the inner spine as the spine intersecting with the solar surface inside the dome-like surface delimited by the fan-plane, while the outer spine reaches up into the corona before returning to the photosphere several tens of Mm away from the null-point (cf. Figure 1). The magnetic field lines in the fan-plane meet at the magnetic null-point, which is located at about 4 Mm above the photospheric boundary.[2] The dome-like fan-plane is a typical feature of a parasitic polarity magnetic null-point topology originating when a vertical dipole field emerges into a magnetic field configuration of opposite magnetic polarity. For

---

[1] The original Esirkepov method, just like most other charge conserving schemes in the literature, is only consistent with a 2nd order field solver.

[2] For computational reasons we tapered off the vertical magnetic field towards the boundaries of our horizontally periodic MHD model, and the height of the null-point is therefore different from the case in Masson et al. (2009).

an elaborated description of the observations of this solar flare event, see Masson et al. (2009).

We previously conducted fully 3D resistive compressible MHD simulations using the *Stagger* MHD code (Nordlund & Galsgaard 1997) on a box size of $175 \times 100 \times 62$ Mm and a stretched $896 \times 512 \times 320$ grid with a minimum cell size of ≈ 80 km in a region around the null-point (Baumann et al. 2012). In most cases the initial particle density and temperature were set to the constant values of 6.8×10^{12} cm^{-3} and 5×10^5 K, neglecting gravity, analogously to Masson et al. (2009). The boundaries were chosen to be closed at the bottom and top, and periodic on the sides. Assuming, as did Masson et al. (2009), that the strong horizontal motions observed by SOHO during the considered time interval was the driver of the reconnection event, we simulated the plasma motion caused by these motions by using essentially the same elliptically shaped driver at the photospheric boundary of the box as was used by Masson et al. (2009), applying velocity amplitudes ranging from 3.33 to 20 km s^{-1} and a horizontal shape function schematically representing the observed photospheric motion. The enhanced driving speed, compared to observations, led to a significant reduction of the simulation time, while it was still sub-Alfvénic and thus left the overlying plasma and magnetic field enough time to adapt to the displacement.

The line-tied photospheric boundary motions indirectly reshuffled the fan-spine geometry at its foot-points by a pressure increase onto the fan-plane, which caused a relative displacement of the magnetic field lines inside and outside the fan plane of the magnetic null point, respectively, resulting in the formation of a current sheet in the fan-plane. The displacement of field lines also causes a relative displacement of the two spines, which then leads to magnetic reconnection at the null-point and a growing resistive electric field in the fan-plane. A detailed description of the MHD simulations and their results are published in a companion paper (Baumann et al. 2012).

For the present study we used an MHD simulation with an initial particle density of 6.8×10^{12} cm^{-3}, a temperature of 5×10^5 K and an applied driving speed of 20 km s^{-1}. After 240 seconds of simulated solar time the null-point area showed clearly enhanced current densities parallel to the

magnetic field, indicating that a dissipative process was taking place. We choose this as the starting point for the 3D relativistic PIC simulation. To minimize computational constraints due to the plasma frequency we rescale the density from the essentially chromospheric value of 6.8×10^{12} cm^{-3} used by Masson et al. (2009) partway towards values more characteristic of an active region corona, so that it becomes instead 1.28×10^{11} cm^{-3}.

Figures 1a and 1b illustrate the initial PIC simulation setup, by showing the chosen cut-out of a snapshot from the MHD simulation, as seen along the x and y axis respectively. The outer spine extends to the right of Figure 1b, while the fan-surface spreads out over the rest of the area. Due to the initial difference in the fan-plane eigenvalues (Masson et al. 2009) a slight asymmetry in the fan-surface is noticeable. The inner spine can be recognized inside the volume spanned by the fan-plane field lines in Figure 1a.

For the kinetic simulations we use the *Photon-Plasma* code on a uniform grid. A cut-out of the MHD simulation box with dimensions $44 \times 25 \times 16$ Mm is chosen for a set of simulations, covering cell sizes from 70 km down to 17.5 km corresponding to uniform grids with up to $2518 \times 1438 \times 923$ cells. The simulations are generally performed with 20 particles per species per cell, covering up to 30 solar seconds. We neglect gravitation, since the aim of this study is mainly to assess the electron acceleration mechanism, for which the influence of the gravitational force is negligible. The initial ion velocities consist of two components; a random thermal velocity drawn from a Maxwellian distribution plus the bulk velocity from the MHD simulation. For the electron velocities, we use the sum of a random thermal velocity drawn from a Maxwellian distribution, the bulk velocity and the velocity due to the initial electric current. The initial electric field is simply taken as the convective electric field from the MHD simulation, which will be self-corrected by the system after the first few time-steps of the kinetic simulation, by adapting the electric field as well as the electric current to balance the system. An overview of the relevant simulations may be found in Table 1.

4

3.1. Modifications to the System

It is common in MHD and PIC simulations to convert physical units into numerically more convenient code units. Such a rescaling leaves the simulated physical situation completely unaffected and all parameters can easily be rescaled back to physical units at any time. Because they leave the ratio of scales unaffected these kinds of conversions between units of measurement are not sufficient to allow explicit PIC codes to address the multi-scale issues discussed below.

Magnetic reconnection is a typical example of multi-scale physics, where microscopic scales interact with and couple to macroscopic scales. While kinetic scales in the solar corona are on the order

(a)

(b)
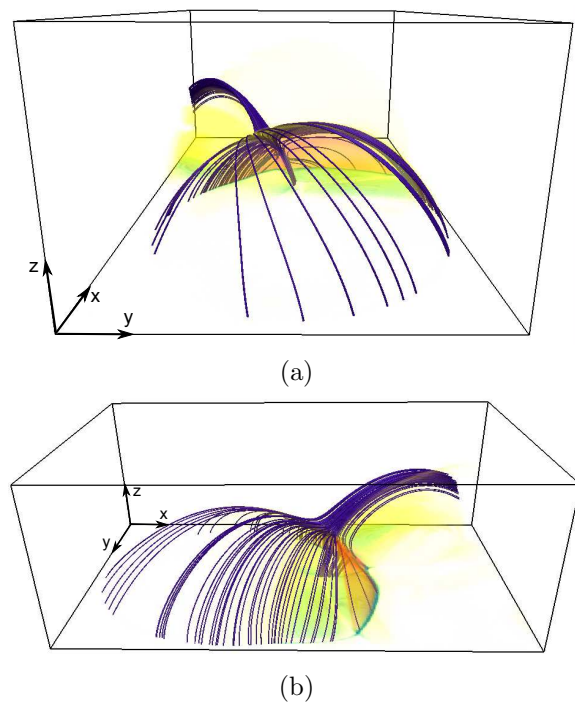
Fig. 1.— Initial state of the PIC code simulation; a cut-out of size 44×25×16 Mm of an evolved MHD simulation snapshot. a) Seen along the x-axis and b) along the y-axis. Shown are magnetic field lines (purple), the maximum current density at the lower boundary (blue) and the electric current density as a semitransparent direct volume rendering (yellow for lowest value, orange for highest value).

of mm, coronal structures such as the ones investigated here have scales on the order of tens of Mm. This range of spatial scales is impossible to cover by explicit kinetic simulations — now as well as in the foreseeable future. Explicit PIC codes are subject to a number of numerical stability constraints. For the code that we use here, one of them is that the Debye length, defined as $\lambda_D = \sqrt{\epsilon_0 k_B T / n_e q_e^2}$, where k_B is the Boltzmann constant, T the temperature, ϵ_0 the vacuum permittivity, n_e the electron density and q_e the electron charge, should be at least on the order of a fraction of a grid cell Δs:

$$0.3\,\Delta s \lesssim \lambda_D. \qquad (4)$$

In addition there are also stability constraints on the time step set by the speed of light and the plasma frequency

$$\Delta t < \Delta s / c, \qquad (5)$$

$$\Delta t \lesssim 2/\omega_p. \qquad (6)$$

In summary, code stability requires that the time step needs to approximately resolve the light-wave and plasma wave propagation and that the grid spacing should not severely under-resolve the electron Debye length. When these conditions are marginally fulfilled in the global simulation domain they are typically (except for the speed of light condition) fulfilled with a good margin in most computational cells, which helps to improve the accuracy of the numerical solution.

Additionally we need to fulfill the following approximate equality:

$$\delta_{skin} \approx \text{a few} \cdot \Delta s. \qquad (7)$$

This requirement arises to ensure a reasonably faithful representation of the plasma, as employing too few grid cells per skin depth suppresses sub-skin depth plasma behavior, while, for a fixed number of grid cells, having too many grid cells per skin depth results in a model where the kinetic scales and the MHD scale are not sufficiently separated, and consequently the MHD behavior is lost. Given these constraints, we would require approximately one septillion (1×10^{24}) grid cells for an unmodified simulation to simultaneously resolve the microscopic and macroscopic scales in the problem. This fundamental constraint notwithstanding, bridging the large scale difference is in fact

approachable. One can either change some of the physical properties (e.g. the magnetic field strength or the plasma density) or, equivalently, modify some of the constants of nature. As long as such modifications of the physical properties of the system do not change the large scale behavior, they may be helpful by decreasing the gap between microscopic and macroscopic scales.

We first introduce two possible sets of modifications of the physical properties which conduce to decrease the large gap between the micro scales and the macro scales, using three modification parameters, which are closely related to each other, so that only two of them are so to speak free parameters, while the third one is a result thereof. One of the reasons for this is an MHD variable constraint; we wish to maintain the relative importance of magnetic and fluid pressure, i.e., we wish to keep the plasma beta parameter unchanged in each type of modification. The goal is to change micro scales, which cause the previously mentioned numerical constraints, i.e. increasing the Debye length λ_D, decreasing the span of velocities (equivalent to decreasing the speed of light), and decreasing the plasma frequency. In modification of type A we change the magnetic field strength by a factor $b < 1$, implying a change in the density to keep the pressure balance. This increases the length scales (λ_D, the gyro radius r_g and the skin depth δ_{skin}) and at the same time reduces the frequencies (ω_p and the gyro frequency ω_g) by the same factor, while leaving the temperature and hence the sound speed v_s and Alfvén speed v_A of the system unchanged.

Modifications of type B address the macroscopic speed ratios. We start by changing the temperature by a factor t^2, which then leads to an increase in the acceleration of gravity g by the same factor. The consequences of this modification are that speeds increase by a factor t, while the length and frequency ratios are forced to be changed to achieve these required modifications, which means that for this type of change one cannot maintain the micro scale ratios.

These modifications of physical properties are equivalent to changing the constants of nature q and c; the unit of charge and the speed of light. Then q^{-1} determines the ratio between micro and macro scales through the charge density and c^{-1} influences the ratio of the speeds. μ_0 needs to

be kept constant, in order to keep the magnetic pressure and hence the plasma beta unchanged, hence ϵ_0 is the parameter that needs to be modified. Here is a summary of these two types of modifications:

A: PHYSICAL CHANGES: $B \sim b, \rho \sim b^2, T =$ constant
CONSEQUENCES: $\lambda_D \sim \delta_{skin} \sim r_g \sim b^{-1}, \omega_p \sim \omega_g \sim b, v_A \sim v_s \sim v_{th} =$ constant

B: PHYSICAL CHANGES: $T \sim t^2, g \sim t^2, B \sim t, \rho =$ constant
CONSEQUENCES: $\lambda_D \sim t$, but $\delta_{skin} \sim \omega_p =$ constant, $v_A \sim v_s \sim v_{th} \sim t$

The idea of modifying the constants of nature has previously been employed. Drake et al. (2006) reduced in their approach the speed of light c, while Siversky & Zharkova (2009) reduced the particle density, which has the same effect on the micro-scales as lowering the charge per particle. In fact, one can show that changes of on the one hand temperature and particle density, and on the other hand changes of the speed of light and the charge per particle, have similar effects: Decreasing the speed of light or increasing the temperature (squared) both reduce the ratio of the speed of light to the thermal speed, and decreasing the particle density or the charge per particle both increase the ratio of micro- to macro-scales (adjusting at the same time the magnetic field so as to keep the plasma beta the same). So, in that sense, our changes of the speed of light and the electric charge per particle effectively corresponds to simulating a coronal region with a very high temperature and a very low particle density.

Apart from the modifications discussed above, a reduction of the ratio of the electron to proton mass from 1836 to 18 is used. This is done to decrease the gap between the ion and electron plasma frequency and skin depths to acceptable values. It is a standard trick in PIC simulations, and mass ratios above 16 are normally considered enough to separate the two scales.

Decreasing the ratio between the different speeds (e.g. by lowering the speed of light) are generally motivated by an assumption that if the speeds are nevertheless much smaller than the speed of light, one expects only very marginal changes in the dynamics, while the savings in com-

puting time (which scales as the speed of light) are considerable.

Changing the charge per particle with a large amount (on the order of 10^6 here) is more drastic, but is necessary to bring micro scales into a realm that is resolvable with current computing resources. To lowest order, such a change of scales is not expected to change the magnetically dominated dynamics dramatically; charged particles are still forced to move essentially along magnetic field lines, with gyration orbits oriented in essentially the same manner with respect to the large scale structures. What changes is exactly what is required to change, namely the ratios between micro and macro scales. Any effect that depends on this ratio then changes in an in principle predictable fashion, and one can, a posteriori, attempt to compensate for this, when analyzing and discussing the results, as is done below in Section 4.2.

A crucial point when modifying the constants of nature is to ensure that the hierarchy of characteristic speeds, times and length scales are, to the largest extent possible, kept as in the real average coronal environment. For the characteristic speeds this hierarchy is

$$v_d < v_{th,p} \sim v_s < v_{th,e} < v_A < c, \qquad (8)$$

where v_d is the average electron drift speed that arises due to the electric current, $v_{th,p(e)}$ is the thermal speed of protons(electrons), v_s is the speed of sound, v_A is the Alfvén speed, and c is the speed of light. For the corona the values of these inequalities can be approximated by the following numbers [km s^{-1}]:

$$0.002 < 90 < 3\,900 < 12\,000 < 300\,000 \qquad (9)$$

We performed several simulation runs with different physical resolutions and modifications of q and c, while measuring everything in scaled SI units (unit of length = 1 km, unit of time = 0.1 s, and unit of mass density = 10^{-12} kg m^{-3}).

In Table 1 the typical initial run parameters for a subset of the different simulations performed are summarized. The influence of the modifications of the physical properties in different simulations on our results are investigated in Section 4.2 and 4.5. In contrast to MHD simulations of a solar event, the magnitude of the parameters of a scaled PIC simulation cannot be directly compared to observationally obtained values, since the modifications of the constants of nature have an influence on the magnitudes of the parameters. But estimating what the corresponding solar values would be is possible, by careful rescaling.

4. Results and Discussion

There are several objectives with these experiments, but the most important one is to establish whether any particle acceleration (i.e., production of non-thermal particles) takes place in the experiments and if so, what the main particle acceleration mechanism at work is. As we demonstrate and discuss below, non-thermal particles are indeed being produced. Their energy distributions are approximate power-laws, with slopes similar to the slopes inferred from observations of the bulk of sub-relativistic accelerated electrons in magnetic reconnection events in the solar corona.

Most importantly the presented simulations manifest the main electron accelerator as being a systematic electric field, which evolves relatively slowly, and which we therefore characterize as being essentially a 'direct current' (DC) electric field. This does not mean that the field is completely stationary, nor that time evolution is unimportant. What it does mean is that we can demonstrate that power-law distributions of electrons can be created even by nearly stationary electric fields, as a result of basically geometric factors, and without reliance on a recursive process in time. Such systematic electric fields occur in our experiments in connection with the strong current sheets that build up as a consequence of the imposed stress on the magnetic field.

In the beginning of the simulations we observe a strong increase in the electric current density and the electric field in the fan-plane, close to the location where the relative inclinations between the magnetic field lines of the two conductivity domains—the inner and outer fan-plane area—are largest, but also close to the inner spine. Due to the boundary conditions chosen we see a motion of the inner spine as well as a relative motion between the inner and outer spines, where their relative distance increases with increasing stress and decreases as the system relaxes, as discussed also in Baumann et al. (2012). The photospheric

Table 1: Summary of simulation runs.

Run	Δs [km]	$\delta_e/\Delta s$	Δt	$r_g/\Delta s$	$\lambda_D/\Delta s$	c [km s^{-1}]	v_J [km s^{-1}]	# cells	# part.	t [s]
1S	70	5	0.0072	0.24	0.4	3900	28	54 M	2.1 B	21
2M	35	10	0.0036	0.48	0.8	3900	28	427 M	17 B	17
3M	35	5	0.0036	0.2	0.4	3900	32	427 M	17 B	30
4M	35	5	0.0013	0.2	0.2	7800	32	427 M	17 B	17
5L	17.5	5	0.0018	0.1	0.4	3900	22	3.4 B	136 B	12
3M$_T$	35	5.5	0.0036	0.77	1.3	3900	63	427 M	17 B	12
2M$_T$	35	11	0.0036	1.55	2.6	3900	67	427 M	17 B	12

NOTE.—We use the median values of the entire domain for all ratios of parameters/Δs, where Δs is the cell size, $\delta_e = c/\omega_{pe}$ the skin depth, ω_{pe} the plasma frequency, $\lambda_D = v_{th}/\omega_{pe}$ the Debye length, $r_L \approx v_{th,e}/\omega_{ce}$ the gyro radius, ω_{ce} the electron gyro frequency, $v_J = J/(qn)$ is the electron current velocity, and Δt the time step. The simulated time is given in solar seconds. The runs with the attribute T have twice the temperature compared to the other simulations runs.

boundary motion triggers magnetic reconnection at the null-point by adding shear between the inner and the outer magnetic field lines of the fan surface, which causes stress on the system that can only be reduced by dissipative processes, including magnetic reconnection. The resulting current sheet after 8 seconds of solar time in simulation run 3M is shown in Figure 2, which also shows the location of the non-thermal high energetic particles (arrows), located in the current sheet of the fan-plane outlined by magnetic field lines, coinciding with the location of an enhanced electric field and E∥B̂. The semitransparent light blue surface depicts the highest electric current density, which is located in the fan-plane. A fraction of the high-energetic electrons move through the null-point up along the outer spine. Due to the increasing magnetic field strength with increasing distance from the null, these particles will essentially follow the magnetic field lines, and will, unless reflected by a magnetic mirroring effect, likely impact the solar surface where the strongly bent outer spine intersects with the photosphere. The other (larger) fraction of non-thermal particles passes the null-point and impacts the photosphere on the northeast side of the fan-plane (to the left in Figure 2). A comparison of this impact region with the observations of this event reveals several similarities, as discussed in Section 4.4. The electrons in the fan-plane experiences a strong acceleration parallel to the magnetic field inside the current sheet while approaching the null-point.

4.1. The Occurrence of Electric Fields in MHD and PIC Experiments

A systematic electric current develops in the fan-plane as a result of the photospheric driver, which introduces a near discontinuity in direction of the magnetic field in the two regions with different connectivity; outside and inside the fan plane. This occurs already in the MHD experiment, where the electric current **J** is identically equal to $\nabla \times \mathbf{B}$ (disregarding constant factors), and where the corresponding electric field in the local reference frame, here called the *diffusive electric field*, is given by an Ohm's law of the type $\mathbf{E}_\eta = \eta \mathbf{J}$, where η is a numerical resistivity.

Apart from rapid fluctuations (on plasma frequency time scales) a similar equality between $\nabla \times \mathbf{B}$ and the electric current **J** must also hold in the PIC experiment. Because the PIC simulations are collisionless one would perhaps expect that the diffusive part of the electric field, initially not inherited from the MHD simulation (only the advective, $-\mathbf{u} \times \mathbf{B}$, part is kept in the PIC initial condition), would remain negligibly small. The results of our experiment shows, however, that this is not the case. Instead of remaining small, the diffusive electric field actually grows in magnitude, although it generally remains much lower (after taken into account the modifications as per Section 4.2) than in the MHD simulation from which the PIC simulations where started.

On closer inspection the reason for the growth of the electric field becomes obvious: The charged
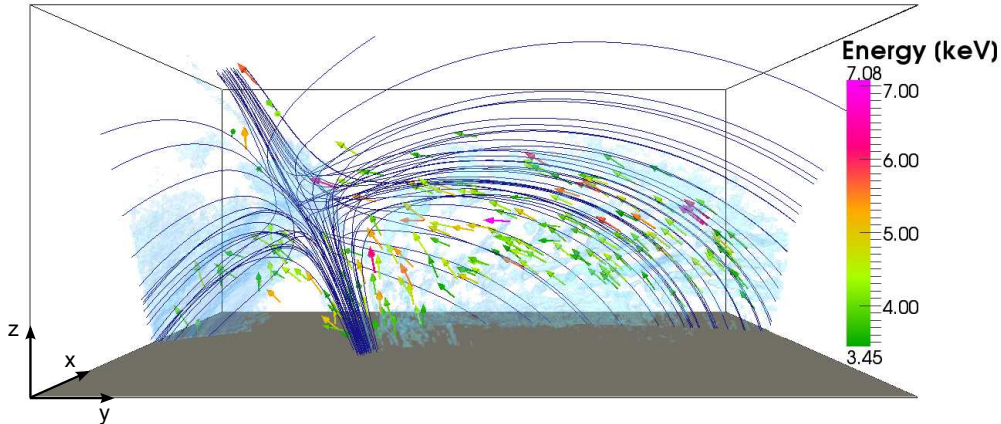
Fig. 2.— A random selection of non-thermal particles (arrows with color indicating their energy) in the current sheet (semi-transparent light blue), which is located in the fan-plane, together with the magnetic field (dark blue) for run 3M. The spine of the topological structure stretches into the left upper corner (outer spine) and reaches down into the center of the dome-shaped fan-plane (inner spine).

particles that carry the electric current — this is primarily the electrons — cannot go where-ever they want by following the slightest whim of a tiny electric field (in the frame of reference moving with the current). Instead, they are in general forced to follow magnetic field lines. But even along field lines the charged particle motions are not unhindered; already modest (local or global) increases of the magnetic field can force a charged particle to become reflected. In addition, systematic or fluctuating cross-field components of the electric field may cause charged particles to drift away from its initial field line, especially in low magnetic field strength regions, and in regions with significant shear of magnetic field lines; i.e., precisely in regions with significant net electric currents.

In particular, it is clear from the very definition of the concept that magnetic reconnection causes a continuously on-going change of magnetic connectivity, and that this change occurs exactly in the place where the largest electric current needs to be maintained.

The component of the electric field along B, $E\|\hat{B}$, corresponds closely to the diffusive electric field in MHD when considering the corona. $E\|\hat{B}$ is plotted together with the magnitude of E in $V\,m^{-1}$ for runs 1S, 2M, 3M, 5L, $2M_T$ and $3M_T$ in Figure 3. In the snapshot from the MHD run used for the PIC simulations, we find diffusive electric field values of about $29\,V\,m^{-1}$ and a total electric field

of $1666\,V\,m^{-1}$. A comparison of the locations of high diffusive electric fields in the MHD with regions of high $E\|\hat{B}$ in the PIC simulations show, that the peak values can be found in both cases in the current sheet, while when comparing the advective electric fields, it reveals that, unlike in MHD case, the PIC advective electric fields peak again in the current sheet. In the MHD case this quantity is high in most of the domain around the null-point, while in the PIC case it is only high inside the current sheet. Both differences (magnitude and peak location of the advective electric field) are presumably a consequence of lowering the elementary charge, imposed by the modifications. The lower the charge, the higher the speeds of the (lightest) particles have to be in order to maintain the same electric current, set by the magnetic field geometry. Therefore the diffusive as well as the advective electric field adapt to higher values in the PIC simulations, particularly in the current sheet. As previously mentioned, our modifications of the constants of nature prevent us from directly comparing these electric field values to the values obtained in the MHD simulations. But, as shown in the next section, we are able to make a qualified guess as to what the PIC electric fields would be in the real solar case, which we further compare to the MHD electric fields. While most medium resolution runs (cf. Table 1) show comparable electric fields (Figure 3), with differences

of a factor of 2–3, run 1S is under-resolved, and clearly disagrees with all other simulation runs.

Charged particles moving in a realistic (non-smooth) electro-magnetic field effectively experience a 'resistance', and a non-negligible, systematic electric field is needed to maintain the electric current **J** consistent with $\nabla \times \mathbf{B}$, as required by the Maxwell equations. Below we demonstrate that, at least in our numerical experiment, it is this systematic electric field that is mainly responsible for the particle acceleration. We then argue that, since the same phenomena must occur in the real solar case, a similar particle acceleration mechanism must be at work there.

4.2. The DC Electric Field as the Particle Accelerator

The systematic electric field which develops across the fan-plane peaks where the electric current density is largest. This is where particles are mainly being accelerated and where the major contribution to the power-law energy distribution population presented in Section 4.5 comes from. Its origin is the tendency for an imbalance between the current density and the curl of the magnetic field, which occurs as a consequence of the dissipative reconnection processes. As magnetic field lines are reconnected, the charged particles that
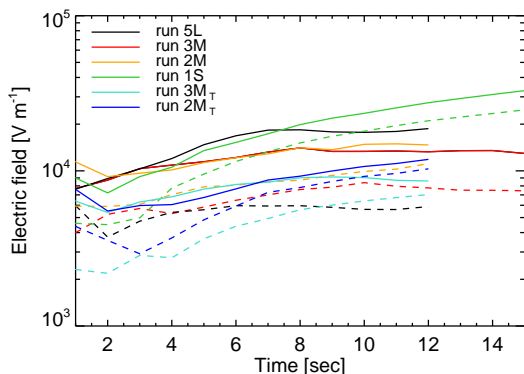
Fig. 3.— Average magnitude of the largest total electric field (solid) and E∥B̂ (dashed) calculated on a cut-out around the null-point with dimensions $13 \times 21 \times 16$ Mm over the number of grid points covering 1 Mm for runs 2M, 3M and 5L and the higher temperature runs $2M_T$ and $3M_T$.

flow along them become 'misdirected' and need to be replaced by the acceleration of new particles that are now, instead of the previous ones, situated correctly with respect to the magnetic field and its curl.

Tracing particles with kinetic energies in the high-energy tail and interpolating the fields to the particle position in time steps of 0.003 seconds for 5 solar seconds in run 3M, the direct correlation between a continuous energy gain for electrons and a negative electric field component in the direction of motion is apparent. These non-thermal particles are primarily found in regions close to, or inside, the current sheet of the fan-plane, where the electric current density is highest. In Figure 4, seven representative non-thermal particles that gain energy during approximately 4 seconds are shown. Similar plots, but for particles that loose energy, are shown in Figure 5. Electrons starting from the right hand side of the current sheet feel first a very diffuse and rapidly changing electric field, due to a fragmentation of the current sheet, which first develops there. This behavior is evident when looking at the green energy bump around time 5 seconds in the first panel of Figure 4. In such fluctuating regions there is a constant competition between the dominance of the perpendicular electron movement in-between the strong E∥B patches and the parallel motion inside an E∥B region. But once a particle is inside a current filament the velocity is mostly directed oppositely to the electric field, and electrons then experience a rapid acceleration, due to which the perpendicular energy relative to the magnetic field becomes negligible and the electrons move almost parallel to the magnetic field (c.f. the cos(pitch angles) in Figure 4 and Figure 5). The gyro radius is permanently very small (on the order of $3 - 8$ km), meaning that electrons tightly follow the magnetic field lines. When particles approach the null-point (marked by the cross-hair in the graphics), their gyro radius naturally grows, as $r_g \propto v_\perp \cdot B^{-1}$. At the same time the magnetic field is weak enough that the electrons are no longer strongly confined to the magnetic field lines, and they are instead directly accelerated by the electric field, rather independent of their orientation relative to the magnetic field. Particles entering the region close to the strongest current sheet may also experience a modest growth in gyro radius, as the magnetic

field there is rather weak.

Small scale regular oscillations which can especially be seen in the E∥v and in the cos(pitch angle) in the panels of Figures 4 and 5 occur at a frequency of about $7.65\,\mathrm{s}^{-1}$, which is of the order of the plasma frequency.
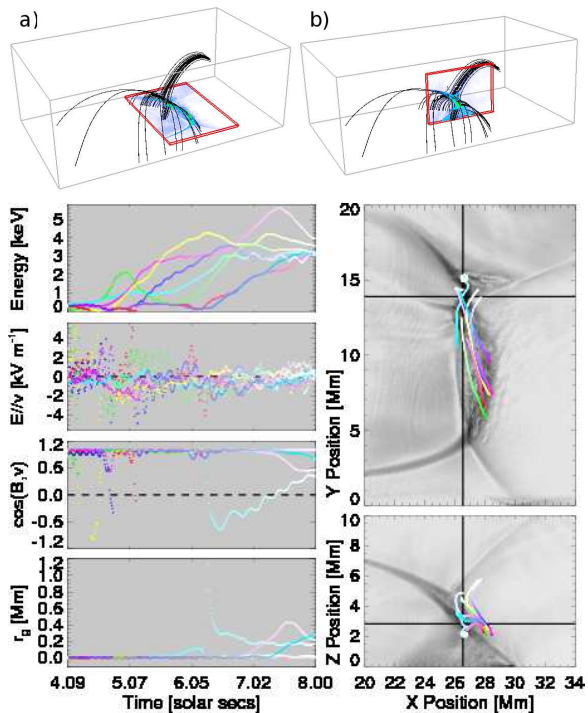

Fig. 4.— Random particles from the power-law energy tail of run 3M, which gain energy. r_g is the gyro radius, $cos(B, v)$ the cosine of the pitch angle and E∥v the electric field component pointing in the direction of the particle velocity. The background images in the two panels to the right are the sum over electric current density slices. The upper panel shows the sum of xy-slices from a height of $2.5\,\mathrm{Mm}$ to $2.9\,\mathrm{Mm}$ illustrated in a) (see top of figure), while the lower panel has xz-slices averaged over $12.6\,\mathrm{Mm}$ to $13.4\,\mathrm{Mm}$ in the y-direction as shown in b). Both are taken at $t = 6\,\mathrm{s}$ and raised to the power 0.5 to enhance the visibility of the fine structures. The null-point is located at $[26.5, 13.9, 2.8]\,\mathrm{Mm}$, plotted as a cross-hair. Note that the particle trajectories are projected onto these planes, and that the dynamics changes slightly during the time interval. Therefore the trajectories are seen at a slight displacement.
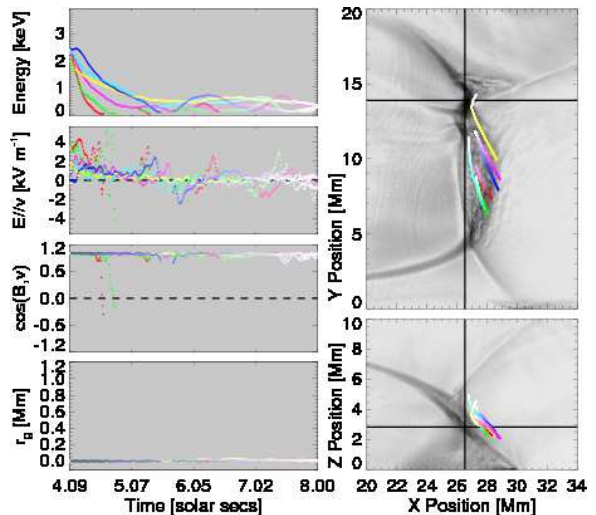
Fig. 5.— Analog to Figure 4, but for random particles from the power-law energy tail of run 3M, which lose energy.

We provide in Figure 3 as well as in Figure 4 and 5 electric field values which are affected by our modifications of the constants of nature. We therefore need to address how to transform these values back, in order to make them comparable to the MHD simulation results as well as to observations.

For this purpose we start out with the force that an electron with charge q and mass m_e experiences when moving in an electric field E, assuming that the DC electric field is the main particle accelerator $F = q E = m_e a$. We further neglect the displacement current since the accelerating electric field – ignoring small scale turbulence – is persistent. At time t and after having covered a distance $L = \frac{1}{2} a t^2$ the electron has a velocity v of

$$v = a t = (2La)^{1/2} = \left(\frac{2LqE}{m_e}\right)^{1/2} \qquad (10)$$

The electric current has to balance the magnetic field through Ampère's law

$$J = \mu_0^{-1} \nabla \times B \approx \mu_0^{-1} \frac{\Delta B}{\Delta L}, \qquad (11)$$

where ΔB is the typical change in the magnetic field across the current sheet and ΔL is the thickness of the current sheet. The current is generated

by moving the electrons

$$J = nvq = n \left(\frac{2Lq^3E}{m_e} \right)^{1/2}, \qquad (12)$$

where n is the particle density. Using the above two expressions for J we obtain an equation for the total energy gain of a single particle due to the electric field

$$q\,E\,L = \mu_0^{-2} \left(\frac{\Delta B}{\Delta L} \right)^2 \frac{m_e}{2n^2q^2}. \qquad (13)$$

Given that this acceleration only happens inside the current sheet the expression can be interpreted as the maximal acceleration a single electron can obtain, if it moves continuously inside the current sheet over the distance L.

To relate Equation 13 to our simulations and real observations, we need the scaling of ΔB and the current sheet thickness ΔL. ΔL is determined by stability constraints, as instabilities diffuse the current away, in case it shrinks below a certain thickness ΔL. There have been several studies in 2D and 2.5D on the current sheet thickness concluding that ΔL is comparable to the size of the diffusion region, as noted in laboratory experiments by Ji et al. (2008), as well as in PIC simulations by Hesse et al. (2001). But these magnetic geometries are not directly comparable to our case, in which most of the diffusion takes place in the current sheet rather than around an idealized magnetic X-point geometry. In fact, very little is known about the thickness of 3D fan-plane current sheets. We therefore cover here the most probable cases. We assume the smallest length scale over which a coherent large scale plane of current can be maintained is either the electron gyro radius r_g in the magnetic field or the electron skin depth.

$$\Delta L \approx \frac{m_e v_{th,e}}{qB} \qquad \text{(gyro radius)} \qquad (14)$$

$$\Delta L \approx \left(\frac{m_e}{\mu_0 nq^2} \right)^{1/2} \qquad \text{(skin depth)} \qquad (15)$$

(if ΔL is instead of the order of the ion gyro radius it would be larger than the estimate in Eq. 14 by a factor $(m_p/m_e)^{1/2}$, which is about a factor of 4 in our case). If we rewrite ΔB as a fractional change in the magnetic field $\Delta B = \epsilon_B B$, and express B

and ΔB in terms of the Alfvén speed v_A in the plasma

$$v_A^2 = \frac{B^2}{\mu_0 nm_p} = \frac{\Delta B^2}{\epsilon_B^2 \mu_0 nm_p} \qquad (16)$$

two elegant expressions emerge for Equation 13, defining the maximal electron energy generated by the DC acceleration

$$q\,E\,L = \epsilon_B^2 \frac{E_A^2}{E_{th,e}}, \quad (\Delta L \sim \text{gyro radius}) \quad (17)$$

$$q\,E\,L = \epsilon_B^2 E_A, \qquad (\Delta L \sim \text{skin depth}) \quad (18)$$

where $E_A = \frac{1}{2}m_p v_A^2$ is the "kinetic Alfvén energy", which is needed to move information in the system, and $E_{th,e} = \frac{1}{2}m_e v_{th,e}^2$ is the thermal energy of the electrons. If the current sheet thickness is related to the gyro radius, then the higher the temperature the smaller the acceleration of an individual particle. A higher temperature is also reflected in a larger gyro radius, but the total energy available for acceleration induced by Ampère's law is the same, and hence there must be more, but lower energy, particles in a thicker current sheet. On the other hand, if the current sheet thickness is related to the electron skin depth the maximum energy should be independent of the temperature. Note that the right hand side of Equations 17 and 18 only contains macroscopic fluid parameters.

Equations 17 and 18 provide an estimate of the electric field and at the same time predict what the maximum resulting particle energies would be if we were able to run without reducing the charge per particle; the charge times the electric field magnitude is to lowest order a constant and hence our modifications in charge are reflected in a q_{mod} times too large electric field, where typically $q_{mod} \approx 2 \times 10^6$. Equations similar to 17 or 18 are what we expect to be able to test in the future. As for now the numerical resolution is not sufficient for an experiment to resolve typical gyro radii with enough grid cells, while simultaneously resolving the large scale plasma.

In the current experiments the current sheet thickness is essentially determined by the grid spacing, and is generally a few times Δs; about an order of magnitude larger than the typical electron gyro radii, and about half an order of magnitude larger than the typical proton gyro radii. If, at the same elementary charge per particle q, we were able to increase the numerical resolution in order

to resolve the gyro radii and the current sheet became correspondingly thinner, then according to Equation 13 the maximum energy gain would increase with the square of the ΔL factor, so with 1 – 2 orders of magnitude.

We conclude that a conservative estimate of the current sheet electric field in the Sun would be smaller by at most the factor (about 2×10^6) by which the elementary charge per particle has been reduced, and it could possibly be 1 – 2 orders of magnitude larger. Taking $4000\,\mathrm{V\,m^{-1}}$ as a typical magnitude of the electric field in our experiments, we thus come up with a conservative estimate on the order of $2\,\mathrm{mV\,m^{-1}}$ for the solar electric field in a situation analogous to the one we model (which is *not* a flaring situation). Using a less conservative estimate based on the argument of numerical resolution, the electric field is on the order of 20 – $200\,\mathrm{mV\,m^{-1}}$. In comparison electric fields *during* solar flares are inferred to be on the order of thousands of $\mathrm{V\,m^{-1}}$ (Qiu et al. 2002).

4.3. Magnetic Field Geometry versus Power-law Distribution

As the current sheet channels make up a very small fraction of the domain, most particles will not exhibit the correct angle to exactly pass through an acceleration channel, but will instead be deflected by the magnetic field, ending up outside the current sheet without undergoing a continued acceleration. Hence most particles are *not* continuously accelerated. The electric current itself is mainly carried by the lowermost part of the power-law distribution, as illustrated in Figure 6, which shows the contributions from the particles to the electric current density from three equally large regions of log(energy) of the power-law tail of run 5L. The particles of the lowest bin are most probably in constant exchange with the thermal particle distribution. Figure 7 sets the power-law tail in relation to the bulk flow and the thermal particles. The power-law tail dominates over the thermal contribution with respect to contributions to the electric current density. About 0.2% of all electrons in the computational box make up the non-thermal electrons high-energy tail of the distribution. 5% of the total electron energy is carried by the power-law tail particles, while most of this energy is in the most energetic particles of the power-law tail, as illustrated in Figure 8. But,

if we only consider particles with a negative vertical velocity, thus moving towards the bottom of the box, and additionally reside in a zone on the lower quarter of the box of $1.9 \times 10^{11}\,\mathrm{km^3}$ (from approximately 0.175 – 1.750 Mm above the bottom boundary), the energy share coming from the power-law tail amounts to over 50% and we find more than 5% of all particles in the high-energy tail population in run 5L, while the total number of electrons in this cut-out is about 1.52×10^7. These are the particles that on the real sun would be decelerated in the chromosphere, leaving an imprint in the form of observable bremsstrahlung emission.

4.4. Comparison with Observations

Considering the observations of this particular reconnection event, in addition to the bright ribbons observed in Hα and UV at the intersection of the fan and the chromosphere (Masson et al. 2009), the chromospheric foot points of the interchange reconnection region show also soft and hard X-ray signatures in the area northwards of the null-point, presumably originating from bremsstrahlung (H. Reid, private communication). This coincides well with the impact region of the power-law electrons in our simulation which travel along the fan-plane and finally hit the lower
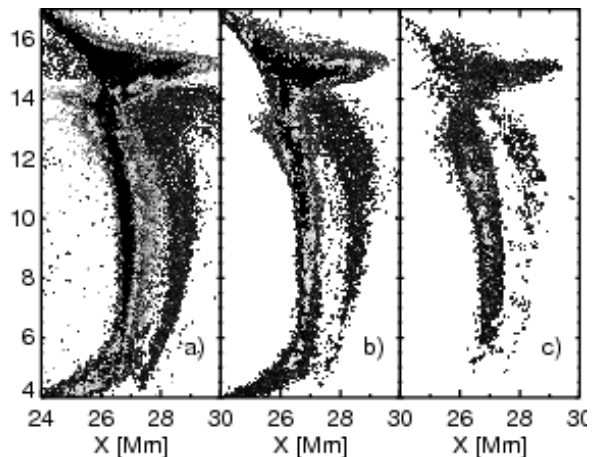

Fig. 6.— Run 5L: Power-law tail electric current density (J) contributions from particles within the energy range of a) $4.3 \times 10^{-22} < e < 1.4 \times 10^{-21}$, b) $1.4 \times 10^{-21} < e < 4.4 \times 10^{-21}$ and c) $e > 4.4 \times 10^{-21}$ in [a.u.].
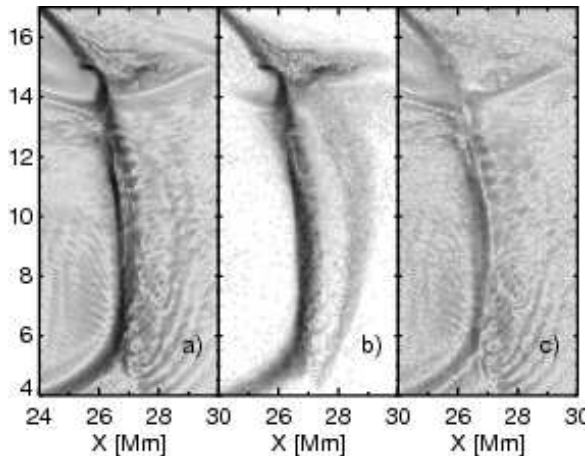
Fig. 7.— The electric current density arising from a) bulk flow b) the power-law tail particles and c) the thermal particles in run 5L.
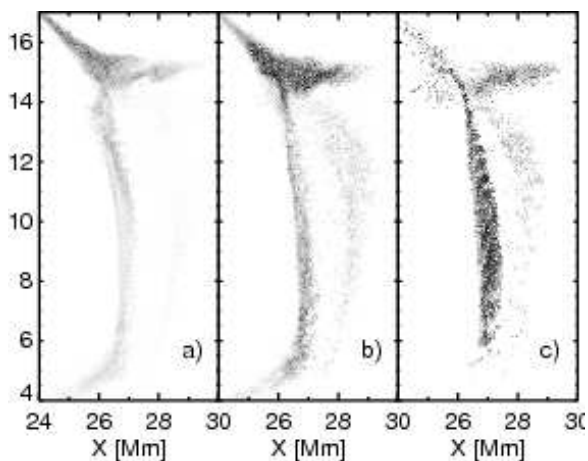

Fig. 8.— Run 5L: Power-law tail energy (e) contributions from particles within the energy range of a) $4.3\times10^{-22} < e < 1.4\times10^{-21}$, b) $1.4\times10^{-21} < e < 4.4\times10^{-21}$ and c) $e > 4.4\times10^{-21}$ in [a.u.].

boundary. Figure 9 shows the non-thermal electron energies at their impact regions on the lower boundary of the box accumulated over t = 4 – 9 seconds. The small difference in the location of the peak intensity compared to observations (Masson et al. 2009) can at least partly be explained by the driving pattern, which is of course only an approximation to the real photospheric boundary motion. A second reason may be the overall magnetic field at the start of the simulation, which is an outcome of an MHD simulation, which was again initialized from a potential field extrapolation.

However, our electron energies are clearly lower than what is needed for the observed emission spectra to be produced. Hence it is important to emphasize that we do not model the observed flare event, but rather the pre-flare phase. One reason is that we use an MHD state taken at a time well before the flare event. Another reason is, as shown in Baumann et al. (2012), that the boundary driver in the MHD simulations, representing the observed horizontal magnetic field motion in the active region, does not provide enough shear and stress to the system to result in an abrupt
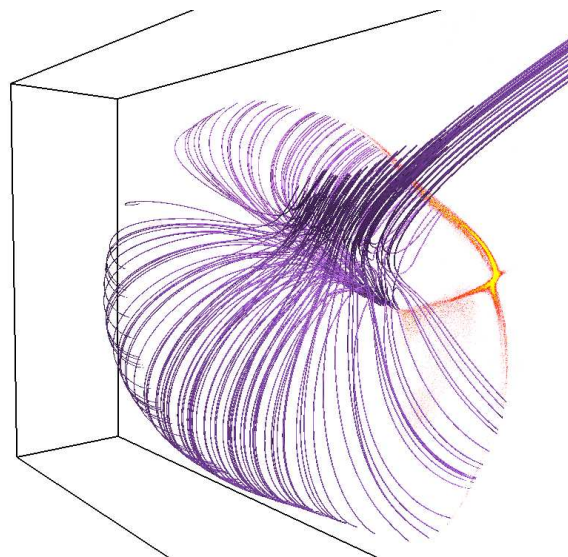
Fig. 9.— Impact area of non-thermal electrons from run 5L. Shown is the electron energy (from orange increasing to yellow) added up at the lower boundary over a period of 5 sec. Additionally magnetic field lines (purple) passing close to the null-point are plotted.

energy release. Despite that, we expect the qualitative nature of the acceleration mechanism to be the same in the flare phase as in its pre-phase. This is supported by the fact that the highly accelerated flare electrons are observed to impact at essentially the same locations as the non-thermal particles in the simulation.

4.5. The Energy Distribution and the Influence of the Modifications

Looking at the energy histogram of the same particles considered in Section 4.3; downward moving in a cut-out of the lower part of the simulation box (see top illustration in Figure 10), we find a Maxwell-Boltzmann distribution combined with a $dN/d\ln E = EdN/dE$ power-law index of about -0.78, corresponding to a dN/dE distribution power-law index of -1.78 (see Figure 10). A power-law index of -1.78 implies that the electric current resulting from the power-law population is mainly carried by the low energy electrons, while the kinetic energy is mainly carried by the highest energy constituents, visualized in Figure 8. The color code in Figure 10 shows the temporal evolution of the energy distribution function for downward-moving particles in the cut-out. The power-law index for the full simulation box is similar. Figure 10 further shows that the tail slope rapidly converges toward the power-law index of about -1.78, indicating an impulsive acceleration of electrons. The weak, apparently non-thermal tail present in the distribution function from the very beginning (dark blue line), does not share origin with the power-law tail that is created dynamically at later times. It arises due to the electric current in the MHD current sheet (the initial electron velocities are drawn randomly from a Maxwellian distribution, shifted with a systematic velocity to maintain the local electric current density). It is entirely due to the high values of the drift velocity necessitated by our rescaled units, but does not influence the later creation of accelerated particles; they appear also in tests where the electrons are not given a systematic initial velocity.

A comparison of the different electron energy distributions from the simulation runs, listed in Table 1, may be found in Figure 11 and Figure 12. For these plots all electrons in the full simulation domain are used. The histograms are not normal-
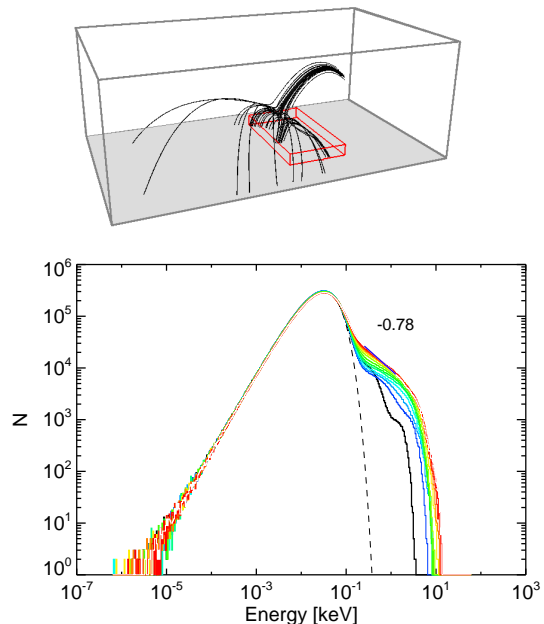

Fig. 10.— Energy distribution of run 5L covering 12 solar secs (from dark blue to red) and being obtained from 1.52×10^{7} electrons in a volume of $1.9 \times 10^{11}\,\mathrm{km^3}$ shown in the illustration above the plot. Δt is $1\,\mathrm{solar\ sec}$. The dashed line represents a Maxwell-Boltzmann distribution fit.
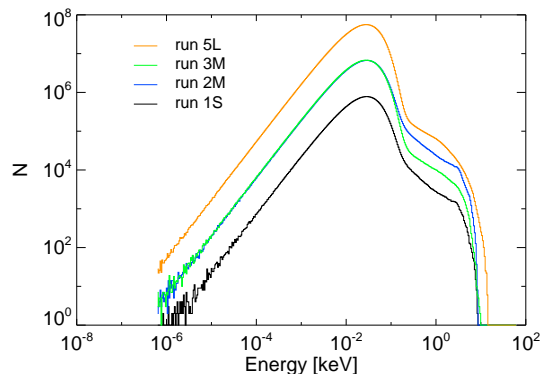

Fig. 11.— Energy histogram for all electrons in the full box for different simulation runs at time $\mathrm{t} = 12\,\mathrm{sec}$.

15

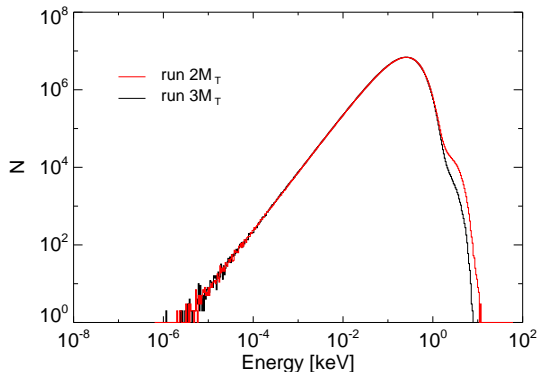Fig. 12.— Energy histogram for all electrons in the full box at time t = 12 sec for the simulation runs with double the temperature of the runs presented in Figure 11.

ized by the number of particles in order to allow for a better power-law index comparison between the different runs. The thermal distribution is the same for all simulations having initially the same temperature profile and it is stable over at least 12 solar seconds, as shown as an example in run 5L, Figure 10. The non-thermal energy tail part quickly approaches a power-law index of about -1.75 for all runs, independently of their resolution. The power-law itself is mainly a consequence of the DC systematic electric field particle acceleration and together with the cutoff of the energy histogram presumably a result of the available electric potential difference in the system, which is determined by the current sheet thickness. The thickness, on the other hand, is controlled by the magnetic field geometry and its evolution.

For simulations with initially a higher temperature (see Figure 12) the non-thermal part of the energy distribution drowns in the thermal part. With a plasma beta in the corona << 1, a change in the temperature is not expected to significantly change the overall electric field (also see Figure 3) and thereby the maximum energy that can be gained by a particle.

Comparing our power-law index to observations shows that our electron power-law index is slightly harder than what is indicated by observations, where it is often > 2. There have been a number of test particle investigations of current sheets, such as Turkmani et al. (2006); Wood &

Neukirch (2005); Zharkova & Gordovskyy (2005) finding similar electron power-law indices - and even slightly harder. But such comparisons are dangerous, as the these studies were conducted using the test particle approach and the latter additionally assumed a simplified 3D magnetic and electric field configuration, presumably having a significant influence on the power-law index as partially studied by Zharkova & Gordovskyy (2005).

5. Conclusions

In this study of a pre-flare 3D reconnection region near a 3D magnetic null point in the solar corona the main electron acceleration mechanism has been shown to be the parallel electric field, building up as a consequence of the magnetic reconnection and dissipation close to the null-point and in the fan-plane current sheet. We estimate from the simulation results the average electric field in this quiescent region to be on the order of $20 - 200\,\mathrm{mV\ m^{-1}}$ in the Sun, which is significantly smaller (2 – 3 orders of magnitude) than what has been found in MHD simulations (Baumann et al. 2012), but still sufficient to create a noticeable non-thermal electron power-law tail. We also present a discussion of the expected dependency of the electric field on the modified elementary charge per particle; showing that the product $E \cdot q$ is expected to be conserved to lowest order. The verification of this relation must be left for future studies due to the current restrictions on computational resources.

The different modification options given in this article serve to reduce the ratio between micro and macro scales. The main parameter change used to increase micro scales is a reduction of the elementary charge per particle, essentially equivalent to a reduction of the particle density.

From studies of the locations of the non-thermal electrons and of their acceleration paths we conclude that the magnetic field geometry and its temporal evolution are likely to be the main factors controlling the power-law index measured in this experiment. We further show that in the lower part of the computational box the electron energy is predominantly in the non-thermal component, with a particle impact area that correlates well with the observations by TRACE, SOHO and

RHESSI. In spite of the modifications of the constants of nature necessary to make this experiment possible we expect that the physical processes in the experiment are qualitatively similar to those in the real Sun, and we therefore see these kinds of studies as a very valuable tool for studying the coupling between kinetic and MHD scales in semi-realistic models.

In the future we hope to strengthen our findings with even higher resolution simulations, and we additionally plan to study the temporal dependence of the power-law index by employing longer simulation runs, which would at the same time provide an opportunity to study ion acceleration.

REFERENCES

Aulanier, G., Golub, L., DeLuca, E. E., Cirtain, J. W., Kano, R., Lundquist, L. L., Narukage, N., Sakao, T., & Weber, M. A. 2007, Science, 318, 1588

Bárta, M., Büchner, J., & Karlický, M. 2010, Advances in Space Research, 45, 10

Baumann, G., Galsgaard, K., & Nordlund, Å. 2012, ArXiv e-prints

Baumann, G., Galsgaard, K., & Nordlund, Å. 2012, Sol. Phys., 000, 000

Browning, P. K., Dalla, S., Peters, D., & Smith, J. 2010, A&A, 520, A105

Craig, I. J. D., Fabling, R. B., & Watson, P. G. 1997, ApJ, 485, 383

Dalla, S., & Browning, P. K. 2005, A&A, 436, 1103

—. 2008, A&A, 491, 289

Drake, J. F., Swisdak, M., Che, H., & Shay, M. A. 2006, Nature, 443, 553

Esirkepov, T. Z. 2001, Computer Physics Communications, 135, 144

Galsgaard, K., & Pontin, D. I. 2011, A&A, 529, A20

Haugbølle, T. 2005, PhD thesis, Niels Bohr Institute [astro-ph/0510292]

Haugbølle, T., Frederiksen, J. T., Baumann, G., & Nordlund, Å. 2012, in preparation

Hededal, C. 2005, PhD thesis, Niels Bohr Institute [astro-ph/0506559]

Hesse, M., Birn, J., & Kuznetsova, M. 2001, J. Geophys. Res., 106, 3721

Isobe, H., Miyagoshi, T., Shibata, K., & Yokoyama, T. 2007, in Astronomical Society of the Pacific Conference Series, Vol. 369, New Solar Physics with Solar-B Mission, ed. K. Shibata, S. Nagata, & T. Sakurai, 355

Jess, D. B., Mathioudakis, M., Crockett, P. J., & Keenan, F. P. 2008, ApJ, 688, L119

Ji, H., Ren, Y., Yamada, M., Dorfman, S., Daughton, W., & Gerhardt, S. P. 2008, Geophys. Res. Lett., 35, 13106

Ko, Y.-K., Raymond, J. C., Lin, J., Lawrence, G., Li, J., & Fludra, A. 2003, ApJ, 594, 1068

Kumar, P., Cho, K.-S., Bong, S.-C., Park, S.-H., & Kim, Y. H. 2011, ArXiv e-prints

Liu, W. J., Chen, P. F., Ding, M. D., & Fang, C. 2009, ApJ, 690, 1633

Longcope, D. W., McKenzie, D. E., Cirtain, J., & Scott, J. 2005, ApJ, 630, 596

Masson, S., Pariat, E., Aulanier, G., & Schrijver, C. J. 2009, ApJ, 700, 559

Miller, J. A., Cargill, P. J., Emslie, A. G., Holman, G. D., Dennis, B. R., LaRosa, T. N., Winglee, R. M., Benka, S. G., & Tsuneta, S. 1997, J. Geophys. Res., 102, 14631

Miller, J. A., Larosa, T. N., & Moore, R. L. 1996, ApJ, 461, 445

Milligan, R. O., Gallagher, P. T., Mathioudakis, M., Bloomfield, D. S., Keenan, F. P., & Schwartz, R. A. 2006, ApJ, 638, L117

Nordlund, A., & Galsgaard, K. 1997, A 3D MHD code for Parallel Computers, Tech. rep., Niels Bohr Institute

Petrosian, V., Yan, H., & Lazarian, A. 2006, ApJ, 644, 603

Priest, E. R., & Schrijver, C. J. 1999, Sol. Phys., 190, 1

Priest, E. R., & Titov, V. S. 1996, Royal Society of London Proceedings Series A, 354, 2951

Qiu, J., Lee, J., Gary, D. E., & Wang, H. 2002, ApJ, 565, 1335

Rosdahl, K. J., & Galsgaard, K. 2010, A&A, 511, A73

Siversky, T. V., & Zharkova, V. V. 2009, Journal of Plasma Physics, 75, 619

Sugiyama, T., & Kusano, K. 2007, Journal of Computational Physics, 227, 1340

Sui, L., Holman, G. D., & Dennis, B. R. 2004, ApJ, 612, 546

Toriumi, S., & Yokoyama, T. 2012, ArXiv e-prints

Turkmani, R., Cargill, P. J., Galsgaard, K., Vlahos, L., & Isliker, H. 2006, A&A, 449, 749

Turkmani, R., Vlahos, L., Galsgaard, K., Cargill, P. J., & Isliker, H. 2005, ApJ, 620, L59

Vay, J.-L. 2008, Physics of Plasmas, 15, 056701

Vlahos, L., Isliker, H., & Lepreti, F. 2004, ApJ, 608, 540

Wood, P., & Neukirch, T. 2005, Sol. Phys., 226, 73

Yee, K. 1966, IEEE Transactions on Antennas and Propagation, 14, 302

Zharkova, V. V., & Gordovskyy, M. 2005, Space Sci. Rev., 121, 165

Article 3: Coronal hole experiment

Particle-In-Cell Simulation of Electron Acceleration in Solar Coronal Jets

G. Baumann and Å. Nordlund

Niels Bohr Institute, Juliane Maries Vej 30, 2100 København Ø, Denmark

gbaumann@nbi.ku.dk

ABSTRACT

We investigate electron acceleration resulting from 3D magnetic reconnection between an emerging, twisted magnetic flux rope and a pre-existing weak, open magnetic field. We first follow the rise of an unstable, twisted flux tube with a resistive MHD simulation where the numerical resolution is enhanced by using fixed mesh refinement. As in previous MHD investigations of similar situations the rise of the flux tube into the pre-existing inclined coronal magnetic field results in the formation of a solar coronal jet. A snapshot of the MHD model is then used as an initial and boundary condition for a particle-in-cell simulation, using up to half a billion cells and over 20 billion charged particle. Particle acceleration occurs mainly in the reconnection current sheet, with accelerated electrons displaying a power law dN/dE distribution with an index of about -1.65. The main acceleration mechanism is a systematic electric field, striving to maintaining the electric current in the current sheet against losses caused by electrons not being able to stay in the current sheet for more than a few seconds at a time.

Subject headings: Sun: corona — Acceleration of particles — Sun: magnetic topology

1. INTRODUCTION

Solar jets have been shown to be triggered by magnetic reconnection, similarly to solar flares, while their released energy is much below what is set free in a medium sized flare event, and the time scales are usually shorter. Nevertheless their high frequency of occurrence make them a significant contributor to the solar ejecta, particularly in the solar wind originating from coronal holes. Solar jets feature upflow velocities of more than $150 \, \mathrm{km \, s^{-1}}$ (Savcheva et al. 2007; Chifor et al. 2008) and are observed at from EUV down to X-ray wavelengths primarily in coronal holes (Kamio et al. 2007), but also in active regions (Chifor et al. 2008). Observational data of solar jets has mainly been provided by YOHKOH (Shibata et al. 1992; Shimojo et al. 1996), SOHO (Innes et al. 1997), HINODE (Chifor et al. 2008), TRACE (Alexander & Fletcher 1999) and SDO (Srivastava & Murawski 2011).

A test particle study of particle acceleration in a solar jet MHD snapshot has previously been performed by Rosdahl & Galsgaard (2010). As these authors were careful to point out, test particle studies are subject to severe limitations, in that neglecting the back reaction of the accelerated particles on the electric field is only justified if the number of accelerated particles is small. Here we present results from performing fully self-consistent particle-in-cell (PIC) simulations in essentially the same initial setup.

In Section 2 we describe the implementation of the experiment and the simulations performed. In Section 3 the results are presented and discussed. Finally, in Section 4 conclusions are drawn and an outlook is given onto future work.

2. SIMULATIONS

This solar jet experiment starts out with a fully 3D resistive compressible MHD simulation of a twisted emerging flux rope, which is initially positioned at 1.7 Mm below the photosphere.

The setup is similar to the one used by Moreno-Insertis et al. (2008). A constant magnetic field of strength 3.3 Gauss is imposed on the entire volume of the computational box, featuring an inclination of 65 degrees in the yz-plane. The maximum magnetic field strength of the flux rope is slightly higher than 1000 Gauss and hence much larger than the background magnetic field. The atmosphere is initially in hydrostatic equilibrium with a 1D atmospheric profile similar to the one used in Archontis et al. (2005), but with slightly different initial parameter values: The sub-photospheric temperature at the bottom is 5.5×10^4 K, with a maximum mass density ρ of about 9×10^{-6} g cm^{-3} at a depth of 3.7 Mm below the surface. The "chromosphere" has a constant temperature of about 5600 K and the corona starts out with T = 2.2×10^6 K and $\rho = 6 \times 10^{-16}$ g cm^{-3}, as illustrated in Fig. 1.

The simulations are performed using the *Stagger* MHD code, as in Moreno-Insertis et al. (2008), assuming an ideal gas law and neither taking heat conduction nor radiative cooling into account. Viscosity and resistivity are locally defined, depending mainly on the velocity gradient, in order to provide a suitable (to maintain code stability), but minimal amount of dissipation. A numerical mesh with 512^3 cells covers a box with physical extents of $33.8 \times 38.1 \times 32.5$ Mm. The mesh is non-uniform in all directions, with a minimal mesh spacing of $(x_{min}, y_{min}, z_{min})=(0.034, 0.034, 0.030)$ Mm around the reconnection region,
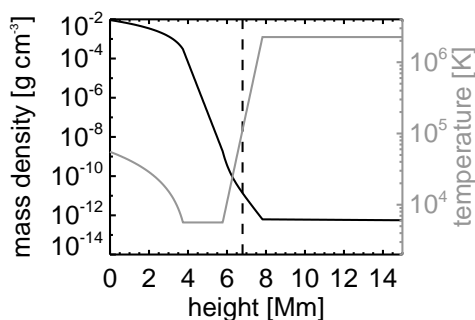

Fig. 1.— 1D atmospheric profile for the MHD simulations. The dashed vertical lines shows the lower cut in height for the sub-domain used for the PIC simulations.

and with mesh spacing less than 10% larger than that in a region of size $12.5 \times 10.7 \times 5.1$ Mm. We refer to the z coordinate as the direction normal to the solar surface.

Despite the slightly denser corona compared to the previously performed simulations by Moreno-Insertis et al. (2008), the overall evolution of the experiment is the same: The twisted flux tube is made buoyantly unstable by applying a density perturbation at its center, which causes it to rise up into the much rarer corona, against the Lorentz force from the bending tube, while expanding as described in Archontis et al. (2004). Above the photosphere the expansions of the magnetic flux rope, now due to the high magnetic pressure, continues rapidly as more and more flux reaches coronal heights. At the same time the corona is locally pushed upwards, where plasma as well as magnetic flux emerges (cf. Archontis et al. 2005). The interaction between the two magnetic field domains defined by the corona and the flux rope leads to a destabilization of the field configuration and causes the formation of a thin dome-shaped current sheet where the magnetic field lines are most inclined relative to each other. As in Moreno-Insertis et al. (2008), magnetic field lines of the two domains end up being nearly anti-parallel at their first encounter, which makes their interaction maximally powerful. The sheet is subject to ohmic dissipation, causing it to reach temperatures as high as about 8×10^6 K. Reconnection gradually occurs between the field lines of the twisted tube and the ambient coronal magnetic field. Due to this restructuring of the magnetic field, several distinct flux domains form in the corona, as shown in Moreno-Insertis et al. (2008) (see their Fig. 2). A hot plasma jet pair emerges from the high temperature and gas pressure region of the reconnection region, propagating sidewards together with the expelled reconnected magnetic field lines. The plasma in the jets is fed to the reconnection side from both sides of the current sheet; the region below supplies dense and cold photospheric plasma, while the plasma coming from above is much hotter and rarer coronal plasma.

After a large fraction of the dense plasma enclosed in the flux rope has been reconnected and ejected in form of plasma jets, as well as drained off along the magnetic field lines due to gravity acting on the heavy sub-photospheric gas, we initialize

the particle-in-cell (PIC) experiment with a cut-out of size $22 \times 22 \times 22$ Mm from the MHD simulation. The reconnection process nevertheless continues expelling coronal low-density plasma and reconnecting field lines from both connectivity domains. Starting from this situation, the density of plasma outflow from the reconnection region is reduced, but at the same time the smaller mass may be accelerated to higher velocities.

The PIC simulations are performed using the *Photon-Plasma* code (Haugbølle 2005; Hededal 2005), which solves the Maxwell equations together with the relativistic equation of motion for charged particles. We fix the magnetic fields to the values given by the MHD dataset at the boundaries, and leave the boundaries open for particles to exit or enter (Haugbølle et al. 2012). To initialize the electric field in the PIC simulation, only the advective electric field ($\mathbf{u} \times \mathbf{B}$, where $\mathbf{u}$ is the bulk speed) is passed on. The particles are initially given a random thermal velocity drawn from a Maxwellian distribution, plus the bulk velocity from the MHD simulation. Electron velocities consist of additionally the velocity due to the initial electric current

$$v_{\mathrm{J}} = \frac{1}{\mu_0 q n} (\nabla \times \mathbf{B}), \qquad (1)$$

where the magnetic field $\mathbf{B}$ and the density n are provided by the MHD snapshot dataset. The jet velocity of this specific MHD dataset is at that point in time on the order of $400 - 800 \, \mathrm{km \, s^{-1}}$. These jets are dominated by the thermal motion in this high temperature and low magnetic field region.

We conducted several PIC runs with grid dimensions of 400^3 and 800^3 cells on a uniform grid with cell sizes of 55 km and 27.5 km respectively, in each case with 20 particles per species (protons and electrons) per cell, simulating up to 7.5 solar seconds.

To minimize computational constraints, the MHD snapshot is cut at 1.1 Mm below the bottom of the corona, hence in the transition region, shown as a dashed line in Fig. 1. This limits the density span to a factor of 4×10^4, small compared to the span of about 2×10^{10} covered by the MHD simulation, but still large for a PIC simulation.

In order to make the plasma micro-scales marginally resolvable in the computational box

the charge per particle is reduced, and to ease the time step constraint from the propagation of electro-magnetic waves the speed of light is reduced, as explained in Baumann et al. (2012).

The run names denote the grid dimension as well as the type of modification; q1 and q2 are for two different modifications, only differing in the choice of the elementary charge by a factor of 2. The electron skin depth in the current sheet is thus resolved with about $5 - 10$ grid cells. The electron gyro radius varies between a fraction of a cell in the flux tube interior to many cells inside the current sheet — because of the near cancellation of oppositely directed magnetic fields there are several dynamically evolving null points inside the current sheet.

In additional to these stratified atmosphere simulation runs, control runs with a constant density of $3 \times 10^{-15} \, \mathrm{g \, cm^{-3}}$ were also performed. Both types of runs show similar overall results.

3. RESULTS AND DISCUSSION

During the MHD flux emergence simulation a diffusive electric field $\mathbf{E}_{\mathrm{res}} = \eta \mathbf{j}$, where η is the resistivity and $\mathbf{j}$ the current density, builds up in the reconnection region, approximately cospatial with the current sheet. The parallel (in relation to the magnetic field) electric field $E_{\parallel}$ is part of the diffusive (non-ideal) electric field, and provides information on the rate of reconnection as well as on favored regions for particle acceleration. The diffusive component of the electric field is, unlike the advective electric field ($\mathbf{v} \times \mathbf{B}$), not inherited by the PIC code, but builds up self-consistently. Fig. 2 compares the location of the diffusive electric field component for the chosen snapshot of the MHD simulations with the $E_{\parallel}$ field of the PIC simulation 0.5 sec after start. The electric fields reach in general much higher magnitudes in the MHD simulations compared to the PIC simulations.

The $E_{\parallel}$ field is the most efficient particle accelerator, since its force acts on the particles without being affected by the purely perpendicular particle gyro motion. Its maximum is located inside the current sheet, equivalent to the diffusive electric field E_{res} in the MHD simulation. Accelerated electrons (see purple and green dots in Fig. 3) are located in the plasma outflow regions of the reconnection region. The fastest velocities are
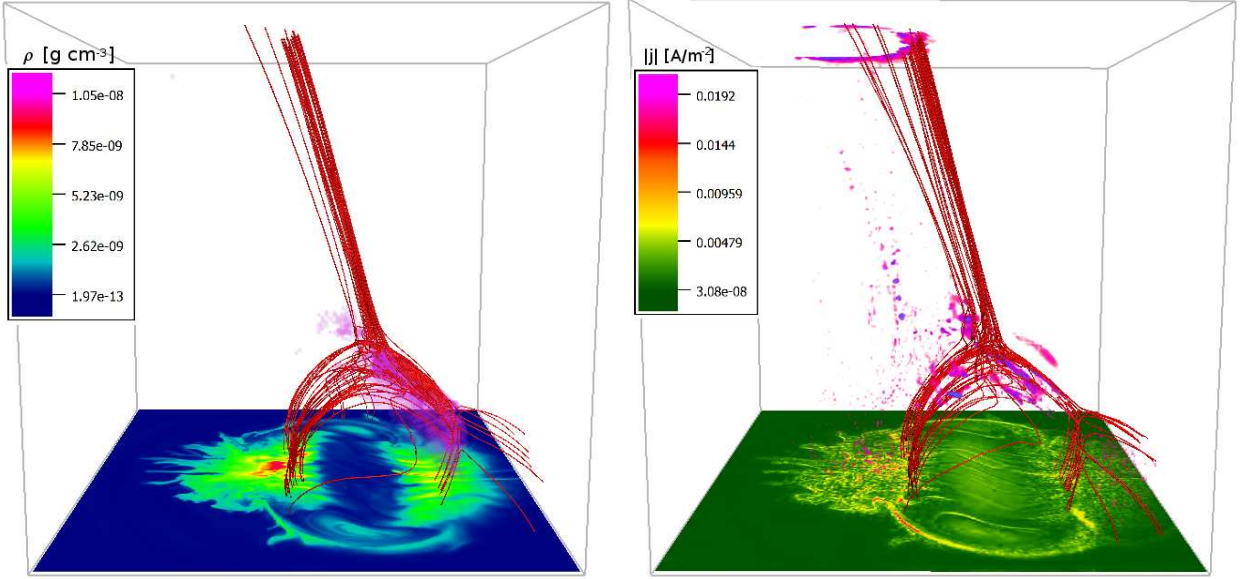
Fig. 2.— Magnetic field lines (red) together with a) the diffusive electric field $\mathbf{E}_{\mathrm{res}} = \eta\mathbf{j}$ in the PIC cut-out of the MHD snapshot dataset (purple volume) and the charge density plane at the bottom of the box — note the low density inside the flux rope, as explained in the last section — and b) the $E_\parallel$ field 0.5 sec after start of the PIC simulation in Run q1-400^3 (purple), together with the current density plane at the bottom of the box.

much above the escape velocity, being on the order of $3000\,\mathrm{km\,s^{-1}}$, while the average speed is about $150\,\mathrm{km\,s^{-1}}$ being approximately the observed average speed of X-ray jets. The lower plane of the PIC simulation visualization in Fig. 2 shows the electric current density. At the bottom center of this figure resides the flux rope, whose twisted field lines are indicated by the strongest electric current pattern. Additionally, to the left of the flux rope signature, the current sheet features a turbulent structure. This is the result of fast up and down flowing plasma, as can be seen in Fig. 3, in which upward moving electrons are shown in purple and downward moving electrons are shown in green.

By tracing particles that win energy over a time period of a second it becomes clear, see Fig. 4, that the acceleration mechanism is a systematic DC electric field, particularly present in the proximity of the current sheet, and mainly directed parallel to the magnetic field. However, since the magnetic field is very weak in the current sheet area particles are almost decoupled from the magnetic field lines, as can further be seen in their pitch angle fluctuations in the third panel to the left in Fig. 4.

Note that in Fig. 4 the electric field fluctuations of the second panel on the left are to a large extent Monte Carlo noise, due to low numbers of particles per cell. This has been verified with a control experiment using twice the number of particles per cell. Further, the background electric current density image is not exactly at the particle positions, which results in a slight projection offset.

Only a limited number of particles happen to be close enough to the current sheet to be efficiently accelerated by the $E_\parallel$, thus being able to contribute to the electric current required by the magnetic field topology. After experiencing a certain amount of acceleration, they get expelled from the current sheet, as they follow magnetic field lines which leave the current sheet region. The particles lost from the current sheet are replaced by new particles, which again need to be accelerated. Since the magnetic field in the reconnection region is very low, due to the chosen initial background magnetic field geometry, it is easy for electrons to get misguided, as they are no longer tightly attached to their magnetic field lines and therefore may encounter different electric field structures on
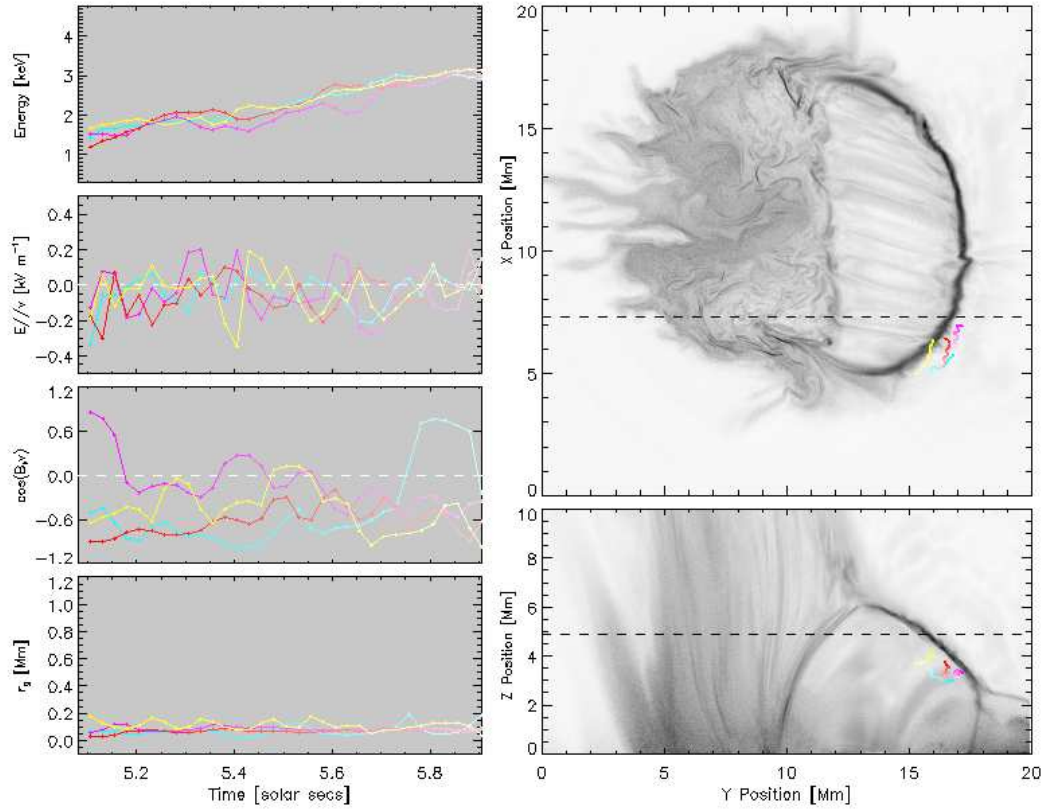
4

Fig. 4.— Four random electrons are traced in run q2-800³ during one second. Their projected positions are plotted in the slices to the right, together with the electric current density (raised to the power 0.5 to enhance fine structures) in yz- and an yx-planes. The black dashed lines in the right images show the cut in the respective direction for the other image. Additionally the gyro radius r_g of the particles, their cosine of the pitch angle $\cos(B, v)$ and the electric field they feel in the direction of motion E‖v are plotted.
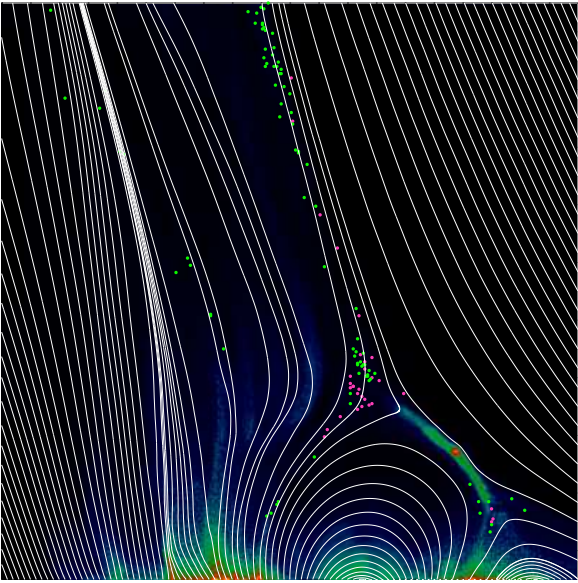
Fig. 3.— Electrons that win energy over a time interval of 2.5 sec, about 4.5 sec after the start of the simulation run q1-400³ are presented together with the magnetic field lines (white) and the electric current density as contour plot (blue-green-red for increasing current density) in a yz-plane. Particles with velocities directed upward are colored purple, while downward moving electrons are green.

their large gyro radius trajectories.

The systematic parallel electric field building up in the current sheet is capable of accelerating particles up to non-thermal velocities. Fig. 5 presents the energy histogram of electrons located in a cut-out of 19.0 x 13.2 x 6.5 Mm around the reconnection region. The initial energy distribution is shown by the dashed line. It is primarily a superposition of the two different plasma inflow domains of the reconnection area passed to the PIC code through the bulk velocity; one of coronal origin, hence at higher temperatures and lower densities, and another one from plasma emerging from the flux rope, hence at lower temperatures and higher densities. To this the drift speed from particles in the current sheet is added, as defined by Equation 1. The power-law forming in the high-energy tail of the Maxwell-Boltzmann distribution typically features a $dN/d\ln(E)$ index of around -0.6 to -0.7 for all three simulations. While the
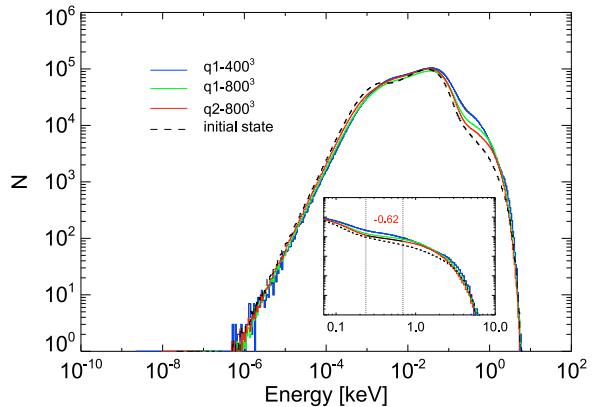

Fig. 5.— Electron energy histogram at t = 4 sec in keV, for particles in a cut-out of size 19.0 x 13.2 x 6.5 Mm around the reconnection region, for three different runs: 400 and 800 defines the mesh size, q1 and q2 are the modification done to the elementary charge. The black dashed curve illustrates the initial particle distribution. The zoom-in plot is a cut-out of the power-law tail between which dashed lines a power-law is fitted.

distribution does not change for the two high-resolution runs, it does change with resolution.

The independence of the power-law index on the modification of natural constants (cf. Baumann et al. 2012) can be seen in Fig. 5, by comparison of the q1-800³ and q2-800³ runs, between which the only difference is a doubling of elementary charge per particle. The energy power-law distribution appears unaltered. Increasing the elementary charge from the modification q1 to q2 just implies a lower net particle flux, as the current density is pre-defined by the magnetic field and needs to be retained.

4. CONCLUSIONS

On the basis of an MHD jet experiment, similar to the one conducted by Moreno-Insertis et al. (2008), but using stretched meshes to obtain higher spatial resolution, we have used particle-in-cell simulations to study the acceleration of charged particles in the 3D reconnection region of a solar coronal jet. This is the first fully 3D kinetic model of particle acceleration in the context of solar jets.

A strong correlation is found between a slowly evolving DC electric field located inside the current sheet and the location of the accelerated particles. The magnetic field is weak and chaotic inside the current sheet, with several magnetic null-points coming and going during the experiment. Most of the particles that are accelerated are quickly lost from the current sheet, only to be replaced by new particles, which again need to be accelerated. The systematic electric field required to constantly accelerate new particles is, in effect, a dissipative ('resistive', non-ideal) electric field, sustained even though the plasma particles in this experiment are collisionless.

The distribution of accelerated particles over energy forms a power-law tail at the high-energy side of the initial Maxwell-Boltzmann distribution, with a dN/dE power-law index of about -1.6 to -1.7.

In the future, with increasing available computational resources, we hope to be able to resolve turbulent regions sufficiently, and for a sufficiently long time, to enable a study of stochastic particle acceleration, expected to be able to accelerate particles to much higher energies.

ACKNOWLEDGMENTS

REFERENCES

Alexander, D., & Fletcher, L. 1999, Sol. Phys., 190, 167

Archontis, V., Moreno-Insertis, F., Galsgaard, K., Hood, A., & O'Shea, E. 2004, A&A, 426, 1047

Archontis, V., Moreno-Insertis, F., Galsgaard, K., & Hood, A. W. 2005, ApJ, 635, 1299

Baumann, G., Haugbølle, T., & Nordlund, Å. 2012, ArXiv e-prints

Chifor, C., Young, P. R., Isobe, H., Mason, H. E., Tripathi, D., Hara, H., & Yokoyama, T. 2008, A&A, 481, L57

Haugbølle, T. 2005, PhD thesis, Niels Bohr Institute [astro-ph/0510292]

Haugbølle, T., Frederiksen, J. T., Baumann, G., & Nordlund, Å. 2012, in preparation

Hededal, C. 2005, PhD thesis, Niels Bohr Institute [astro-ph/0506559]

Innes, D. E., Inhester, B., Axford, W. I., & Wilhelm, K. 1997, Nature, 386, 811

Kamio, S., Hara, H., Watanabe, T., Matsuzaki, K., Shibata, K., Culhane, L., & Warren, H. P. 2007, PASJ, 59, 757

Moreno-Insertis, F., Galsgaard, K., & Ugarte-Urra, I. 2008, ApJ, 673, L211

Rosdahl, K. J., & Galsgaard, K. 2010, A&A, 511, A73

Savcheva, A., Cirtain, J., Deluca, E. E., Lundquist, L. L., Golub, L., Weber, M., Shimojo, M., Shibasaki, K., Sakao, T., Narukage, N., Tsuneta, S., & Kano, R. 2007, PASJ, 59, 771

Shibata, K., Ishido, Y., Acton, L. W., Strong, K. T., Hirayama, T., Uchida, Y., McAllister, A. H., Matsumoto, R., Tsuneta, S., Shimizu, T., Hara, H., Sakurai, T., Ichimoto, K., Nishino, Y., & Ogawara, Y. 1992, PASJ, 44, L173

Shimojo, M., Hashimoto, S., Shibata, K., Hirayama, T., Hudson, H. S., & Acton, L. W. 1996, PASJ, 48, 123

Srivastava, A. K., & Murawski, K. 2011, A&A, 534, A62